Experimental Study on the Role of Flow Large-Scale Circulating Structures in Poiseuille and Rayleigh-Bénard Convection

by

Sina Kashanj

A thesis submitted in partial fulfillment of the requirements for the degree of

Doctor of Philosophy

in

Mechanical Engineering

Department of Mechanical Engineering
University of Alberta

Abstract

This dissertation is an experimental study of the influence of flow rolling structures, especially large-scale circulation (LSC), on heat and mass transfer of Rayleigh-Bénard convection (RBC) and Poiseuille and Rayleigh-Bénard convection (PRBC). These two phenomena are buoyancy-driven flows paradigms in thermofluid systems where natural and mixed convection are dominant in both natural and engineered systems. RBC is important for studying various natural phenomena in a geophysical and astrophysical context, such as atmospheric circulation, ocean currents, and even the dynamics within the Earth's mantle. PRBC is also important in engineering applications where forced and natural convection coexist such as design and optimization of heat exchangers, such as those in Stirling engines, solar thermal systems, and HVAC technologies.

Investigations were conducted experimentally using optical measurement techniques such as particle image velocimetry (PIV) and laser-induced fluorescence (LIF) thermometry. To visualize and quantify the velocity field and flow rolling structures 2D and 3D domains a 3D scanning technique was employed. Furthermore, to visualize and measure the temperature field and estimate the heat transfer coefficient i.e. the Nusselt number, in the 2D fluid domain, planar laser-induced fluorescence (PLIF) was used and developed to achieve further enhanced temperature sensitivity. Time-resolve 3D measurement of the temperature field was also achieved by a scanning approach, which is a significant advancement in the context of temperature measurement in fluid flows.

By applying 2D PIV and a combinatorial vortex detection algorithm, it was found that in RBC flow within a unit aspect ratio convection cell, the formation of a smaller number of flow rolling structures increased the momentum transfer. This inverse correlation between the number of flow rolling structures and the momentum transfer highlights the importance of controlling the formation and development of LSC. Lateral confinement of the convection cell was found to be a controlling parameter that can suppress the elliptical instability which is responsible for the breakup of the LSC and the formation of the sloshing regime where multiple LSC structures form and heat transfer decreases. With a laterally confined convection cell, experiments revealed that increasing the Rayleigh number leads to the formation of a prolonged twisting regime. In this regime, increasing the Rayleigh number leads to an increase in the number of twists of the LSC structure, yet keeping a single LSC which leads to optimized heat transport.

Within this condition, it is found that only a single thermal plume generates a constant frequency responsible for driving the LSC and the temperature fluctuations. It was found that within RBC, LSC has a key role in heat transport and can be manipulated for heat transfer enhancement. In PRBC flow, which is a case with more similarity in engineering applications, experimental examination of temperature and velocity field showed that LSC is not developed within the PRBC flow within a channel with limited length. However, findings suggest that by applying LSC to the flow, heat transfer can be enhanced significantly while the flow regime is in the mixed convection regime. These findings highlight the significant influence of LSC in heat and momentum transfer, which could be a solution for heat transfer enhancement in engineering applications where natural and mixed convection are dominant.

Preface

This thesis is based on the original research conducted by Sina Kashanj. The experimental work and methodologies outlined in this document were developed and carried out in the Optical Diagnostics Group laboratory, under the supervision of Professor David S. Nobes. This work was funded by future energy systems (FES) and Natural Sciences and Engineering Research Council of Canada (NSERC). A significant portion of the research findings presented in this thesis has been published in peer-reviewed journals and conferences, as detailed in the following paragraphs.

Chapter 2 investigates the role of flow rolling structures on momentum transfer in Rayleigh-Bénard convection. The research presented in this chapter has been published in *Physics of Fluids* (2024) under the title *“Experimental evidence on the correlation between the flow rolling structures and momentum transfer in turbulent Rayleigh-Bénard convection”* (J-3). Aspects of this work were also presented at the *CSME Conference* (C-8).

Chapter 3 explores the effect of convection cell confinement on the properties of large-scale circulating structures in Rayleigh-Bénard convection. The findings from this chapter are based on the paper *“Prolonged Twisting Regime in a Lateral Confined Mesoscale Rayleigh-Bénard Convection”* (J-4), which is in preparation for submission to *Physical Review Letters*. Relevant sections of this study were also presented at the *14th International Symposium on Particle Image Velocimetry* (C-7) in Chicago and at the *20th International Symposium on Laser and Imaging Techniques* (C-6) in Lisbon.

Chapter 4 looks into the temperature field and its oscillations in confined Rayleigh-Bénard convection. The research has been published in *Physics of Fluids* (2024) as *“Temperature field of non-Oberbeck-Boussinesq Rayleigh-Bénard convection in a low aspect ratio cell”* (J-2).

Chapter 5 contrasts 2D and 3D measurement techniques for investigating the temperature field and heat transfer in confined Rayleigh-Bénard convection. This chapter is based on the work published in *Experiments in Fluids* (2023) as *“Application of 4D two-colour LIF to explore the temperature field of laterally confined turbulent Rayleigh-Bénard convection”* (J-1). Some of the details were also presented at the *76th Annual Meeting of the APS Division of Fluid Dynamics* (C-4), and at the *20th International Symposium on Laser and Imaging Techniques* (C-6).

Chapter 6 explores the flow and temperature properties in Poiseuille-Rayleigh-Bénard convection. The results from this chapter have been submitted for review to *Experiments in Fluids* as *“Determination of Nusselt number in Poiseuille-Rayleigh-Bénard Convection Using Simultaneous Temperature PLIF and PIV”* (J-5). Various aspects of this work were also presented at the *American Society of Thermal and Fluids Engineers (ASTFE)* (C-5), the *International Symposium on Flow Visualization* (C-3), and the *21st International Symposium on Laser and Imaging Techniques* (C-1).

Chapter 7 looks into the influence of inducing LSC into PRBC flow on heat transfer enhancement. The outcomes of this research were presented at the *21st International Symposium on Laser and Imaging Techniques* (C-2).

Journal Publications

J-1 Sina Kashanj and David S. Nobes. “Application of 4D two-colour LIF to explore the temperature field of laterally confined turbulent Rayleigh–Bénard convection.” *Experiments in Fluids* 64.3 (2023): 46.

J-2 Sina Kashanj, and David S. Nobes. “Temperature field of non-Oberbeck-Boussinesq Rayleigh-Bénard convection in a low aspect ratio cell”, *Physics of Fluids*, 2024; 36 (4): 047110.

J-3 Sina Kashanj, and David S. Nobes. “Experimental evidence on the correlation between the flow rolling structures and momentum transfer in turbulent Rayleigh-Bénard convection.” *Physics of Fluids*, 2024, 36, 107101.

J-4 Sina Kashanj, and David S. Nobes. “Prolonged Twisting Regime in a Lateral Confined Mesoscale Rayleigh-Bénard Convection.” (Ready for submission).

J-5 Sina Kashanj, and David S. Nobes. “Application of simultaneous PIV and PLIF in studying Poiseuille-Rayleigh-Bénard convection." (Under review).

Conference publications and presentations

C-1 Sina Kashanj, and David S. Nobes. "Enhancing Sensitivity And Quantifying Uncertainty Of Volumetric Two-Colour Two-Dye Laser-Induced Fluorescence Thermometry Of Aqueous Solutions.", 2024, *21st International Symposium on the Applications of Laser and Imaging Techniques to Fluid Mechanics., Lisbon, Portugal.*

C-2 Sina Kashanj, and David S. Nobes. “Simultaneous Two-Colour Two-Dye Thermometry PLIF And PIV To Determine The Nusselt Number In Steady And Oscillatory Poiseuille-Rayleigh-Bénard Convection.”, 2024, *21st International Symposium on the Applications of Laser and Imaging Techniques to Fluid Mechanics., Lisbon, Portugal.*

C-3 Sina Kashanj, and David Nobes. “Application of 3D LIF and PIV in studying Poiseuille-Rayleigh-Bénard convection.”, 2023, *International Symposium on Flow Visualization., Delft, Netherlands*.

C-4 Sina Kashanj, and David S. Nobes. “Dancing of Thermal plumes; A 4D Visualization of Temperature field of Rayleigh-Bénard convection.”, 2023, *76th Annual Meeting of the APS Division of Fluid Dynamics, Washington, DC, USA.*

C-5 Sina Kashanj, and David Nobes. “Role of Large-Scale Circulating Structures in Mixed Convection of Poiseuille-Rayleigh-Bénard Convection”, 2023, *American Society of Thermal and Fluids Engineers (ASTFE), Oregon, USA.*

C-6 Sina Kashanj, Y. Saffar, R. Sabbagh, D. S. Nobes, “Calculation of the Nusselt number from temperature and velocity data obtained from enhanced 3D two-colour LIF and 3D PTV in a Rayleigh-Bénard convection cell.”, 2022, *20th International Symposium on the Applications of Laser and Imaging Techniques to Fluid Mechanics., Lisbon, Portugal.*

C-7 Sina Kashanj, and David Nobes. “Application of simultaneous time-resolved 3-D PTV and Two Colour LIF in Studying Rayleigh-Bénard Convection.” *14th International Symposium on Particle Image Velocimetry*. Vol. 1. No. 1. 2021., *Chicago, USA.*

C-8 Sina Kashanj, and David S. Nobes. “Investigation into the onset of turbulent Rayleigh-Bénard convection using time-resolved 2-D particle image velocimetry.”, *CSME*, 2021. *Prince Edward Island, Canada.*

Acknowledgment

I would like to sincerely thank my supervisor, Prof. David S. Nobes, for his support, guidance, and knowledge throughout my PhD. His patience and thoughtful advice have been invaluable, both in shaping the direction of my research and helping me navigate the many challenges along the way. I am grateful for the opportunity to learn from him and for his continued encouragement.

I also extend my thanks to my thesis committee members, Prof. Andrew Martin and Prof. Seama Koohi, for their helpful feedback, insightful suggestions, and constructive critique. I would like to thank Pof. Lars Zigan and Prof. Morris Flynn for their insightful questions and suggestions.

A big thank you goes to my lab mates and friends for their collaboration and support over the years. In particular, I would like to acknowledge Dr. Reza Sabbagh, Dr. Lisa Kinsale, and Dr. Guillermo Bessa for their advice and assistance during my studies.

I want to express my heartfelt gratitude to my beloved wife, Yeganeh, for her support and patience. Her presence has been a source of strength and balance during the most challenging times. A special thanks goes to my family. My parents, Mina and Mehrdad, have always believed in me and encouraged me to pursue my goals. Their love and guidance have been invaluable throughout my life. Finally, I want to express my heartfelt gratitude to my sister, Sarina, for supporting me during my life and believing in me all along.

Table of Contents

Abstract ii

Preface iv

Journal Publications vi

Conference publications and presentations vii

Acknowledgment viii

List of Figures xviii

List of Tables xxx

Chapter 1: Introduction 1

1.1 Motivation 1

1.2 Thesis scope 3

1.3 Thesis structure 6

1.4 References 7

Chapter 2: Role of flow rolling structures on momentum transfer in Rayleigh-Bénard convection 9

2.1 Introduction 10

2.2 Methodology 15

2.2 Experimental condition 22

2.3 Results and discussion 28

2.4 Conclusion 48

2.5 References 49

Chapter 3: Effect of convection cell confinement on the properties of the large-scale circulating structures in Rayleigh-Bénard convection 53

3.1 Introduction 54

3.2 Experimental approach 56

3.3 Properties of different flow modes 57

3.4 Twisted regime and restriction of elliptical instability 61

3.5 Conclusion 64

3.6 References 65

Chapter 4: Temperature field and its oscillations in confined Rayleigh-Bénard convection 67

4.1 Introduction 68

4.2 Methodology 77

4.3 Results and Discussion 84

4.4 Conclusion 115

4.5 References 117

Chapter 5: 2D vs 3D measurement of the temperature field and heat transfer in confined Rayleigh-Bénard convection 125

5.1 Introduction 126

5.2 Two-colour PLIF 130

5.3 Results and discussion 144

5.4 Conclusion 155

5.5 References 156

Chapter 6: Flow and temperature properties in Poiseuille-Rayleigh-Bénard convection ... 161

6.1 Introduction 162

6.2 Fluid Test Rig 172

6.3 Experiment Condition 174

6.4 Optical Configuration 178

6.5 Simultaneous configuration 180

6.6 Results and discussion 185

6.7 Conclusion 201

6.8 References 202

Chapter 7: Inducing LSC in Poiseuille-Rayleigh-Bénard convection for heat transfer enhancement 207

7.1 Introduction 208

7.2 Methodology 209

7.3 Results and discussion 215

7.4 Conclusion 222

7.5 References 223

Chapter 8: Conclusion 224

Future work 228

Appendix A: Uncertainty Estimation 242

Random Uncertainty in PIV 242

Systematic Uncertainty (Bias) in PIV 243

Total Uncertainty in PIV 243

Velocity in RBC with $\Gamma = 1/10$ 244

Velocity in RBC with $\Gamma = 1$ 245

Velocity in PRBC 246

Uncertainty Estimation in PLIF (Temperature Measurement) 247

Random Uncertainty in PLIF 247

Systematic Uncertainty (Bias) in PLIF 248

Total Uncertainty in PIV 248

Temperature in RBC with $\Gamma = 1/10$ 249

Temperature in PRBC 250

Appendix B: Fluid Test Rig Drawing 252

List of Figures

Figure 2-1. Schematic of the optical measurement system used to apply time-resolved 2C2D PIV and a render of the solid model of the RBC enclosure used for the experiment. 16

Figure 2-2. (a) An image of the experimental setup showing the convection cell. (b) A rendering of the convection cell showing its components. (c) Schematic of the convection cell showing the boundary conditions and convection cell dimensions. 17

Figure 2-3. (a) Temperature map of the surface of the solid horizontal boundary of the heat exchanger of the convection cell captured by an IR camera. (b) The temperature profile of the solid boundary along two lines of $x/h = 0$ and $z/h = 0$. 19

Figure 2-4. (a)-(c) The process for detecting flow rolling structures of the mean flow of the developed RBC flow showing the mean wind at the center and two small corner rolling structures. (a) Mean vorticity field. (b) Regions of interest. (c) Ellipses showing the detected rolling structures of the mean flow. For the developed flow, (d)-(f) shows the flow rolling structure detection process of an instantaneous flow field with high number of rolling structures. (d) Instantaneous vorticity field after a short time after the start of convection, $t/tf = 8$. (e) Regions of interest. (f) Ellipses showing the detected rolling structures of the instantaneous flow. Red and blue colours show the CCW and CW rolling structures respectively. 21

Figure 2-5. Schematic of the streamline of a vortex segmented by n number of points αi which is used to define the winding angle shows the angle between two lines of $Pi - 1 - Pi$ and $Pi - Pi + 1$. 22

Figure 2-6. Shows the statistical convergence of the spatial average velocity magnitude of S2 (red) and S3 (blue) during the period of the examination. 23

Figure 2-7. The diagram shows the height of the enclosure, h, versus the temperature difference, ΔT to classify the Oberbeck-Boussinesq (OB) from non-Oberbeck-Boussinesq (NOB) condition in Rayleigh-Bénard flow. The asterisk indicates the current work. This diagram is after Horn and Shishkina [30]. 27

Figure 2-8. The velocity magnitude map of the two states of (a) S2 and (b) S3. 29

Figure 2-9. (a) Normalized mean horizontal velocity, $uxtg\alpha\Delta TH$ along the vertical axis of the convection cell at the center, $xh = 0$. (b) Normalized mean vertical velocity, $uytg\alpha\Delta TH$ along the horizontal axis of the convection cell at $yh = 0$. (c) instantaneous normalized horizontal velocity, $uxg\alpha\Delta TH$ along $xh = 0$ axis. (d) Instantaneous normalized vertical velocity, $uyg\alpha\Delta TH$along $xh = 0$ axis. 31

Figure 2-10. The probability density function (PDF) of (a) and (b) normalized horizontal velocity, $uxg\alpha\Delta TH$ of S2 and S3 and (c) and (d) normalized vertical velocity $uyg\alpha\Delta TH$ of S2 and S3. The schematics at the top left side of the plots indicate the direction of LSC. In (a) and (b) the red colour shows the region near the bottom (hot) wall and the blue colour shows the region near the top (cold) wall. In (c) and (d), the red colour shows the region where thermal plumes are rising and the blue colour shows the region where they are falling. 32

Figure 2-11. The probability density function (PDF) of (a) normalized horizontal velocity, $uxg\alpha\Delta TH$ and (b) normalized vertical velocity, $uyg\alpha\Delta TH$ of S1. 34

Figure 2-12. Isometric, front, and back view of the time-reconstructed Q-criterion > 0.1 iso-surfaces of (a)-(c) S1, (d)-(f) S2, and (g)-(i) S3 during $\Delta t/tf = 0 - 315$. Red and blue iso-surfaces represent the CCW and CW rolling structures. (a), (d), and (g) show the isometric view. (b), (e), and (h) show the front view, and (c), (f), and (i) show the back view of this 3D map. 37

Figure 2-13. Instantaneous vorticity field of the three states of (a) S1 (Multimedia available online), (b) S2 (Multimedia available online), and (c) S3 (Multimedia available online). The temporal evolution of the vorticity field can be seen in the multimedia. 39

Figure 2-14. Normalized size distribution of the CW and CCW flow rolling structures during (a) S1, (b) S2, (c) S3, (d) two different modes of S1. 39

Figure 2-15. (a) Variation of time average Reynolds number, Re and its standard deviation, $Restd$ versus the three states. (b) Variation of the temporal and spatial average of the rolling structure size, $A*$ and its standard deviation, $Astd*$ versus the three states. (c) Variation of the normalized number of the large-scale circulating structure (LSC) and the small-scale rolling structure (SSR) versus the three states of S1, S2, and S3. 40

Figure 2-16. A plot of the Reynolds number (black line), Re, and the number of the rolling structures (blue line), n, versus the dimensionless time interval, Δttf, after the start of convection, S1. The dashed red line at $\Delta ttf = 190$ divides the plot into two modes with high variation (light red region), Mode 1 and low variation (light blue region), Mode 2 based on the threshold of the squared coefficient of variance of Reynolds number, $CV = 10\ \%$. Contours show the vorticity field at (a) $\Delta ttf \approx 8$ (b) $\Delta ttf \approx 16$ (c) $\Delta ttf \approx 31$. (d) Plot of the variation of the number of the LSC during the first state, S1. 41

Figure 2-17. Temporal variation of the squared coefficient of variance of Reynolds number SCV of the first state, S1. Highlighted point at $\mathrm{P}(190{,}10)$ indicates the point in which the SCV reach to 10 %. 42

Figure 2-18. Plot of the variation of the number of LSC, number of rolling structures, and Reynolds number, for (a) S2 and (b) S3. The areas with light blue colour in $n-\Delta ttf$ and $Re-\Delta ttf$ are highlighted for better visualization of these two plots. 44

Figure 2-19. Cross-correlation function between the signal of the kinetic energy-based Reynolds number and the number of the rolling structures for states of (a) S1 Mode1, (b) S1 Mode2, (c) S2, and (d) S3. 47

Figure 3-1. Evolution of three velocity components normalized by the free-fall velocity, i.e., vertical velocity $uz2x,zuf2$, horizontal velocity, $ux2x,zuf2$, and velocity magnitude $uz2+ux2x,zuf2$ over period of $t=1300$ s. Rayleigh number is varying from (a) $Ra=2.3\times107$, (b) 5.6×107, and (c) 8.8×107. Movie 3 in the supplementary material indicates the temporal development this plot along with the 2D temporal evolution of the velocity and relevant properties for the three investigated Rayleigh number. 58

Figure 3-2. Velocity vectors and velocity magnitude of the mean velocity during the quasi-steady state for (a) $Ra=2.3\times107$, (b) 5.6×107, and (c) 8.8×107. The in-depth variation of the flow properties is depicted for more information in Movie 2 in the supplementary materials. 60

Figure 3-3. For three Rayleigh numbers of (a) $Ra=2.3\times107$, (b) 5.6×107, and (c) 8.8×107, this figure is showing the horizontal velocity magnitude, $ux2+uy2xuf2$, in comparison with the vertical velocity $uz2xuf2$. $\omega x2+\omega y2x\omega f2$ is also showing the enstrophy profile all along the vertical axis spatially averaged along the horizontal plane i.e. $x-y$. 63

Figure 4-1. Schematic of the beginning of the convection and developed flow in RBC. (a) shows the start of the convection, (b) developed flow and formation of LSC, (c) Mean flow and highlighted high Reynolds stress and kinetic energy regions, (d) Mean flow and temperature map. 70

Figure 4-2. (a) Schematic of the convection cell of RBC with boundary conditions. (b) The RBC flow cell and optical measurement system. 78

Figure 4-3. (a) Normalized calibration of the Fluorescein and Kiton red each fitted with a linear function. (b) The ratiometric calibration graph of the ratiometric Fluorescein-Kiton red fitted with an exponential function. 79

Figure 4-4. Schematic of the optical measurement system used for applying two-colour PLIF. 81

Figure 4-5. Variation of the (a) Rayleigh number, Ra, (b) Prandtl number, Pr, and (c) falling time, tf within the three examined cases; $Ra1$, $Ra2$, and $Ra3$. This has been plotted for the parameters at the maximum temperature, TH, minimum temperature, Tc, and the mean temperature, T. 83

Figure 4-6. Height to temperature difference diagram indicating the validity range for OB assumption after Horn and Shishkina [49]. The red and blue colours indicate valid OB and NOB regions, respectively. The triangles are showing the three different cases that have been investigated in this paper. 84

Figure 4-7. Instantaneous temperature map of RBC at the beginning of the convection at $t \approx 8$ s for (a) $Ra1$, (b) $Ra2$, (c) $Ra3$. The aspect ratio of the temperature field has been adjusted for a better visualization. 85

Figure 4-8. Temperature variation along the x-axis at two vertical location of (a) $y *=$ 0.875 and (b) $y *= 0.125$ lines for the three cases of $Ra1$, $Ra2$, and $Ra3$. Temperature is non-dimensionalized as $T *= T - T\Delta T$ is based on the maximum, $TH = 45$ °C and minimum, $TC =$ 5 °C temperatures. 86

Figure 4-9. Temporal evolution of the temperature for (a) $Ra1$, (b) $Ra2$, (c) $Ra3$. Plots show the horizontal mean temperature at the bottom boundary, $T * x *, y * \approx 0$, top boundary, $T * x *$ $, y * \approx 1$, and the spatial mean temperature, $T * x *, y *$. 89

Figure 4-10. Spatio-temporal map of the temperature evolution for $Ra1$. (a) Shows the evolution of temperature in vertical direction, y-axis. (b) Shows the evolution of temperature along x-axis. For better visualization of the temperature map, the colour bar shows the dimensionless temperature, $T *$ variation from -0.5 to 0.25. 91

Figure 4-11. Spatio-temporal map of the temperature evolution for $Ra2$. (a) Shows the evolution of temperature in vertical direction, y-axis. (b) Shows the evolution of temperature along x-axis.. 94

Figure 4-12. Spatio-temporal map of the temperature evolution for $Ra3$. (a) Shows the evolution of temperature in vertical direction, y-axis. (b) Shows the evolution of temperature along x-axis...**Error! Bookmark not defined.**

Figure 4-13. Power spectra of the horizontal mean temperature, Tx oscillation at three different vertical locations of bottom, top, and middle, $y * \approx 0, 1, y *=$ of the convection cell for three different Rayleigh numbers of (a)-(c) $Ra1$, (d)-(f) $Ra2$, and (g)-(i) $Ra3$. 97

Figure 4-14. Instantaneous temperature fields for three different Rayleigh numbers of (a) $Ra1$, (b) $Ra2$, and (c) $Ra3$. The aspect ratio of the temperature field has been adjusted for a better visualization. 100

Figure 4-15. (a)-(c) Variation of the peak of the power spectra along the x-axis at three different vertical direction of bottom, top, and middle, $y *\approx 0{,}1, y *= 0.5$ of the convection cell for three different Rayleigh numbers of (a) $Ra1$, (b) $Ra2$, and (d) $Ra3$. (d)-(f) Corresponding frequency of the peak of the power spectra along the x-axis at the same vertical direction of bottom, top, and middle, $y *\approx 0{,}1, y *= 0.5$ for (d) $Ra1$, (e) $Ra2$, and (f) $Ra3$. In (a)-(c) the y-axis of each plot is adjusted for better visualization of the variation of frequency of each Rayleigh number. 103

Figure 4-16. Variation of the peak of the power spectra of horizontally mean temperature, Tx oscillation along the y-axis for three different Rayleigh numbers of (a) $Ra1$, (c) $Ra2$, and (e) $Ra3$. The y-axis of each plot is adjusted for better visualization of the variation of the power spectra due to the significant difference of its value in different Rayleigh numbers.................................... 105

Figure 4-17. Variation of the correspondent frequency to the peak of the power spectra of horizontally mean temperature, Tx oscillation along the y-axis for Rayleigh numbers of $Ra1$, $Ra2$, and $Ra3$.. 106

Figure 4-18. Temperature cross-correlation between the horizontally mean temperatures, Tx between hot and cold boundaries and their auto-correlations for three different Rayleigh numbers of (a) $Ra1$, (b) $Ra2$, and (c) $Ra3$. The black line is indicating the cross-correlation function between the temperature of the hot and cold boundary, red and blue lines are showing the auto-correlations just for comparison the auto-correlation function with the cross-correlation function. 109

Figure 4-19. Probability Density Functions (PDF) of the normalized temperature distributions for different Rayleigh numbers of (a) $Ra1$, (b) $Ra2$, (c) $Ra3$. 110

Figure 4-20. Plot of the temperature skewness, ST' and flatness, FT' versus Rayleigh number. 112

Figure 4-21. Variation of the center temperature for three cases of $Ra1$, $Ra2$, and $Ra3$. Error bar shows the standard deviation of temporal deviation. 113

Figure 4-22. Probability Density Functions (PDF) of the normalized logarithm of the thermal dissipation distributions for different Rayleigh numbers of (a) $Ra1$, (b) $Ra2$, (c) $Ra3$............ 114

Figure 5-1. Signal of a temperature sensitive fluorescent dye (one-colour) showing the rise of the thermal plumes in an enclosure heated from below. Colour bar indicates the temperature range after applying the temperature calibration. 131

Figure 5-2. (a) Temperature sensitivity of Fl and Fl 27, excited with 532 nm and 488 nm laser, (b) Temperature sensitivity of Kr, collected with $589\ \text{nm} < \lambda < 625\ \text{nm}$ band pass filter and with long pass, $\lambda > 600\ \text{nm}$ filter. 135

Figure 5-3. A plot of the absorption and emission signal variation with wavelength of Fl and Kr (after [27]). Different colours show the different filter wavelength range and the laser wavelength. 136

Figure 5-4. Two-colour PLIF signals and optics diagram. 137

Figure 5-5. Normalized intensity-temperature calibration graph. (a) One colour, Fl and Kr calibration, (b) Ratiometric intensity-temperature graph. Error bars in (a) indicates the standard deviation of the intensity of fluorescence signal in different depths. 138

Figure 5-6. Schematic of the optical measurement system used to apply 4D two-colour LIF. 140

Figure 5-7. Schematic diagram of the three signals produced to synchronize the two scanning mirrors and the cameras. 141

Figure 5-8. (a) Variation of the emitted light of Kr (top) and Fl (bottom) along (a) $x/w = 0$ and (b) $y/h = 0$ lines. 143

Figure 5-9. (a) Temperature distribution on the copper surface of the hot heat exchanger. (b) Rendering of the solid model of the slender rectangular RBC cell. (c) Schematic of the dimensions and boundary conditions of the RBC test cell. 144

Figure 5-10. Instantaneous planar temperature fields at three different planes of (a) $zw = -0.3$, (b) $zw = 0$, and (c) $zw = 0.3$. 145

Figure 5-11. Evolution of the temperature iso-surfaces of $T *= -0.3, -0.15, 0, 0.15, 0.3$ in the slender RBC for five different time instances. 147

Figure 5-12. Temporal evolution of the hot and cold regions at three different planes of (a) $zw = -0.3$ (b) $zw = 0$ (c) $zw = 0.3$. 148

Figure 5-13. (a) Temporal volumetric evolution of the hot and cold regions. (b) The absolute values of the correlation coefficient, Chc of the two hot and cold regions for different planes and the volumetric measurement. 149

Figure 5-14. (a) Evolution of the spatial average of the temperature field, $T*$ (b) $T*$ versus time on each plane. 150

Figure 5-15. Dimensionless heat transfer, Nusselt number, Nu distribution on (a) hot boundary and (b) cold boundary for $ttf = 22, 42, 57, 97$. 152

Figure 5-16. Evolution of spatial averaged Nusselt number for both hot and cold boundaries. 153

Figure 5-17. Comparison of spatial averaged Nusselt number, Nux, z with $Nuz = 0, Nuz = -0.3$, and $Nuz = 0.3$ for (a) hot boundary and (b) cold boundary. 154

Figure 6-1. Schematic of the Poiseuille-Rayleigh-Bénard convection flow in a channel. (a) Shows the side view of the channel and the flow develops along the channel in x-direction. (b) Indicates the cross-section of the developed flow for $x/H \approx \infty$ forming the large-scale circulation. The channel is heated from below with the constant temperature, TH, while the side and top walls are in adiabatic condition. $U\infty$, also indicates the flow Poiseuille flow along x-direction. 163

Figure 6-2. Schematic of temperature measurement uncertainty in a fluid, showing the discrepancy between the real surface temperature $Ts - real$ and the measured temperature $Ts - measured$ due to the sensor's location within the solid layer and the resulting temperature deviation Δz. 167

Figure 6-3. The schematic showing the temperature distribution near a solid boundary with constant temperature distribution of Ts, indicating the temperature gradient in vertical direction, y-axis, identifying the magnitude of the vertical heat transfer from the solid boundary to the fluid flow. 169

Figure 6-4. (a) Model of the designed fluid test rig, (b) us the actual test section of the fluid test rig, and (c) indicates the field of view (FOV) used for this study. 174

Figure 6-5. For the field of view indicated in the model of the fluid test rig in (a), the experiment conditions are shown schematically in (b). 177

Figure 6-6. Absorption and emission spectra of Sodium Fluorescein and Rhodamine B, with the laser wavelength and optical filters used for applying simultaneous PLIF and PIV. A zoomed view of the image of the seeding particles is shown to highlight is relative high signal to noise ratio. The signal of the SFL along the x-axis is shown with the standard deviation of 2.1 counts is also shown at the left bottom to highlight the relatively low noise of the collected florescent signal. 180

Figure 6-7. Schematic of the optical system for simultaneous PIV and PLIF measurements, illustrating the use of a laser sheet, dichroic mirror, filters, and two cameras to capture velocity and temperature fields independently. 181

Figure 6-8. Image of the real experimental setup showing the fluid test rig, illumination/excitation unit and the imaging unit. 183

Figure 6-9. (a) The image of the components of the illumination/excitation unit. (b) The image of the components of the imaging unit. 184

Figure 6-10. (a) Temporal evolution of the dimensionless mean temperature variation, $T - T\infty TH - T\infty$, during $\Delta t = 400$ s of measurement of the flow with $Ri = \infty$ i.e. $Re = 0$ and $Ra = 4.5 \times 105$. (b) Temporal evolution of the dimensionless mean velocity magnitude, $(ux2 + uz2)uf2$ during $\Delta t = 400$ s of measurement of the flow with $Ri = \infty$ i.e. $Re = 0$ and $Ra = 4.5 \times 105$. 187

Figure 6-11. (a) Temporal evolution of the dimensionless second moment of velocity in z-direction, $uz2uf$, during $\Delta t = 400$ s of measurement of the flow with $Ri = \infty$ i.e. $Re = 0$ and $Ra = 4.5 \times 105$. (b) Temporal evolution of the dimensionless second moment of velocity in x-direction, $ux2uf$, during $\Delta t = 400$ s of measurement of the flow with $Ri = \infty$ i.e. $Re = 0$ and $Ra = 4.5 \times 105$. 188

Figure 6-12. Probability density function (PDF) of the normalized streamwise, uz/uf and lateral, uz/uf velocities for the flow with $Ri = \infty$ i.e. $Re = 0$ and $Ra = 4.5 \times 105$. (a) and (b) indicates the PDF of the normalized streamwise velocity, ux/uf for the start of the convection from $t = 0$ s to $t = 218$ s and $t = 0$ s to $t = 400$ s, respectively. (c) and (d) indicates the PDF of the normalized vertical velocity, ux/uf for the start of the convection from $t = 0$ s to $t = 218$ s and $t = 0$ s to $t = 400$ s, respectively. 190

Figure 6-13. (a) The normalized instantaneous vorticity field, $\omega *$ for $Ri = \infty$ at the time step of $t = 50$ s. (b) The normalized temperature field, $T *$ for $Ri = \infty$ at the time step of $t = 50$ s. 191

Figure 6-14. (a) The normalized instantaneous vorticity field, $\omega *$ for $Ri = \infty$ at the time step of $t = 50$ s. (b) The normalized temperature field, $T *$ for $Ri = \infty$ at the time step of $t = 266$ s. 192

Figure 6-15. (a) Temporal evolution of the dimensionless vertical mean temperature gradient, $-\partial T * \partial z *$, during $\Delta t = 400$ s of measurement of the flow with $Ri = \infty$ i.e. $Re = 0$ and $Ra = 4.5 \times 105$. (b) Temporal evolution of the dimensionless vertical convection, $uz * T *$ during $\Delta t = 400$ s of measurement of the flow with $Ri = \infty$ i.e. $Re = 0$ and $Ra = 4.5 \times 105$. (c) Temporal evolution of Combination of temperature gradient and vertical convection, $uz * T * -\partial T * \partial z *$ within the same condition of (a) and (b). 194

Figure 6-16. Temperature profile of the dimensionless mean temperature $T - T\infty TH - T\infty$ along the vertical axis, z-direction at the center, $x/H = 0$, for Richardson numbers, Ri, listed in the figure from $Ri = 2.2$ to $Ri = \infty$. 196

Figure 6-17. Velocity profile of the dimensionless mean horizontal velocity, ux/ux along the vertical axis, z-direction at the center, $x/H = 0$, for Richardson numbers, Ri, listed in the figure from $Ri = 2.2$ to $Ri = \infty$.. 198

Figure 6-18. Mean heat transfer coefficient components of PRBC flow with the Richardson number from $Ri = 2.2$ to $Ri = \infty$. Red circles indicate the vertical temperature gradient term, while the blue circles show the vertical convection term. Red and Blue rectangles indicate the vertical temperature gradient term and vertical convection term, respectively for the $Ri = \infty$ when the flow is developed, $t > 218$ s. Error bars indicate the standard deviation. 200

Figure 7-1. (a) Rendering of the solid model of the fluid test rig designed and fabricated to generate the PRBC flow. (b) Depicts the test section properties and the field of view, FOV in $x - y$ plane; FOV. (c) The real image of the test section. 210

Figure 7-2. CAD model of the designed swirler for generating large-scale circulating structures. 211

Figure 7-3. (a) Schematic of the optical measurement system used to apply two-colour two-dye PLIF. (b) Shows the test section and emitted light from the two-dye while it is illuminated by the 532 nm laser sheet. (c) Indicates the illuminated test section visualized by a long-pass (orange) filter. 213

Figure 7-4. Temperature map of the PRBC flow at the test section height of $z = 9$ mm. $Ra = 4.5 \times 105$ and $Re = 0$. (a) $t \approx 6$ s (b) $t \approx 28$ s.. 214

Figure 7-5. Variation of the mean heat transfer coefficient, $\partial T * y \partial z *$along the x-axis for the case with the swirler highlighted as SW with red colour and base case PRBC highlighted in blue colour. 217

Figure 7-6. Spatio-temporal mean heat transfer for Richardson numbers of $Ri = 2.2$, 3.2, and 5 for the basic PRBC highlighted in red and the PRBC with swirler highlighted in blue. The error bar indicates the spatio-temporal standard deviation of the heat transfer coefficient................. 218

Figure 7-7. Instantaneous temperature fields near the bottom boundary (hot wall) for basic case of PRBC flow when the flow is fully developed and for the Richardson number of $Ri = 2.2$. 220

Figure 7-8. Instantaneous temperature fields near the bottom boundary (hot wall) for basic case of PRBC flow with the swirler and for the Richardson number of $Ri = 2.2$. 221

List of Tables

Table 2-1. Variation of the flow properties of the RBC flow according to the temperature of the hot and cold boundaries in comparison to the mean temperature. 26

Table 2-2. Correlation, cross-correlation function, and de- lay time of the cross-correlation of the two signal of kinetic energy-based Reynolds number and number of the rolling structures for the investigated regimes of S1, S2, and S3. 45

Table 3-1. Flow properties for the three investigated Rayleigh numbers of $Ra1 = 2.3 \times 107$, $Ra2 = 5.6 \times 107$, and $Ra3 = 8.8 \times 107$. 62

Table 4-1. Properties of the three different examined RBC cases. 82

Table 4-2. Frequency of the horizontally mean temperature oscillation. 99

Table 5-1. Fluorescent dye pairs and experimental specifications used to apply two-colour PLIF. 133

Table 5-2 Fluorescent dyes and experimental specifications used to apply one-colour or two-colour PLIF. 134

Table 5-3 Properties of the fluorescent dyes used in two-colour LIF. 135

Table 6-1. Flow properties of the PRBC investigated flow. 176

Table 6-2. Flow properties of the PRBC investigated flow. 178

Table 7-1. Flow properties of the PRBC investigated flow. 215

Table 7-2. Mean heat transfer coefficient for the basic PRBC and the PRBC with swirler. The enhancement is also listed for all the studied Richardson numbers... 218

Chapter 1: Introduction

1.1 Motivation

Convection, a fundamental mechanism for heat transfer, occurs in different regimes: natural, forced, and mixed convection [1]. While significant advances have been made in forced convection, particularly in enhancing heat transfer through various techniques such as surface modifications and active flow control, much less attention has been given to mixed and natural convection regimes [1]. These regimes i.e. natural and mixed, are relevant in systems where external driving forces are minimal, and the convective process is driven by buoyancy effects, as seen in solar collectors, building cooling systems, and liquid cooling of electronic components [1]. Additionally, in atmospheric science, the study of natural convection is critical for understanding phenomena such as cloud formation, where the buoyancy and thermally driven plumes impacts weather patterns [2]. Despite its importance, natural convection is challenging to model due to the unsteady and complex flow structures, including the formation of random thermal plumes that interact with the bulk flow, influencing momentum and heat transport properties [2].

Rayleigh-Bénard convection (RBC) is a paradigm for studying wall-bounded natural convection [3]. One of the most important characteristics of RBC is the formation of large-scale circulation (LSC), which plays an important role in governing the heat and momentum transfer within the system [4]. Recent studies have revealed that in slender convection cells, multiple LSCs can form, and there appears to be an inverse correlation between the number of LSCs and the efficiency of heat and momentum transfer [5], [6]. However, this correlation has only been observed under specific conditions, particularly within the Boussinesq approximation and for low Prandtl number fluids, e.g., gaseous fluids [5], [6]. In contrast, experiments conducted with higher

Prandtl number fluids, such as water, have shown that this inverse correlation is either weak or nonexistent [2], [7]. While initial observations supporting the inverse relationship between LSC formation and heat transfer were based on numerical simulations, subsequent studies involving higher Prandtl number fluids employed both experimental and computational methods [6], [7]. These findings demonstrate the complexity of LSC behavior and suggest that the interplay between flow structures and transport properties may vary significantly depending on fluid properties and boundary conditions. Therefore, understanding the influence of LSC on heat and momentum transfer remains a key objective, especially in systems that deviate from idealized conditions.

Poiseuille-Rayleigh-Bénard convection (PRBC) occurs within the mixed convection regime, where both forced and natural convection contribute to the flow dynamics [8]. PRBC represents a more complex variant of Rayleigh-Bénard convection, where the flow occurs in a channel that is heated from below [9]. While PRBC shares certain similarities with RBC, the introduction of an additional dimension such as the channel's length, makes the flow dynamics significantly more complex [9]. In PRBC, the flow along the channel interacts with the thermal plumes that rise due to buoyancy [10]. The presence of both a forced flow along the channel and natural convection driven by temperature differences introduces new challenges in predicting heat transfer behavior [10]. Unlike in RBC, where LSCs form as a function of time, in PRBC, their formation also depends on the channel’s length [10]. Both numerical and experimental studies have demonstrated that LSC formation in PRBC can significantly enhance the heat transfer, but only when the channel length is sufficiently long [10]. This highlights a limitation for engineering applications, where the available geometry often restricts the length of the channel, thereby limiting the potential for heat transfer enhancement.

1.2 Hypothesis

This work hypothesizes that LSC has a key role in convection heat transfer of the wall-bounded natural and mixed convection, e.g. RBC and PRBC flows, and they can be controlled and manipulated to enhance the heat transfer within these two regimes.

Based on this hypothesis, several key questions regarding Rayleigh-Bénard convection (RBC) and Poiseuille-Rayleigh-Bénard convection (PRBC) will be addressed. I) In relatively high Prandtl number conditions i.e. working fluid of water, and under non-Oberbeck-Boussinesq conditions, what is the organization of the flow structures in RBC, and why does the large-scale circulation (LSC) not exhibit the inverse correlation with momentum transfer typically observed in low Prandtl number flows? II) What mechanism(s) lead to the breakdown of a single LSC into multiple LSCs or small-scale flow rolling structures, and how can lateral confinement of the convection cell help preserve a single LSC? III) What are the dynamics of thermal plumes and the distribution of temperature in a laterally confined convection cell? IV) Is the 2D observation of temperature properties in such cells valid when compared to 3D observations? V) In PRBC flow, with a limited channel length, how are the flow and temperature fields organized, and does an LSC form under these conditions? VI) Can the observations from RBC be applied to induce LSC in PRBC flows, potentially harnessing this mechanism as a heat transfer enhancement technique in engineering applications?

1.3 Thesis scope

In Chapter 2, the experimental investigation focuses on the organization of flow structures in Rayleigh-Bénard convection under high Prandtl number conditions, using water as the working fluid and within a non-Oberbeck-Boussinesq regime. By applying particle image velocimetry

(PIV) to capture the velocity field, this chapter seeks to understand why large-scale circulation do not show the inverse correlation with momentum transfer, as observed in low Prandtl number fluids. A combinatorial vortex detection algorithm is employed to identify and quantify the size of flow rolling structures. This approach allows for a detailed analysis of how smaller-scale rolling structures contribute to momentum transfer and how their influence differs from that of the larger LSCs under these conditions.

In Chapter 3, the focus is on the mechanism that leads to the breakdown of a single large-scale circulation into multiple LSCs or smaller-scale flow rolling structures within Rayleigh-Bénard convection. This chapter employs experimental techniques, including 3D scanning particle image velocimetry, to explore how lateral confinement of the convection cell influences LSC stability. The severe lateral confinement, with an aspect ratio of 1/10, alters the flow dynamics, suppressing the formation of elliptical instabilities that would otherwise disrupt a single LSC. By investigating how lateral confinement can preserve or destabilize an LSC, the chapter highlights the role of geometric constraints in controlling the flow structure, revealing the conditions under which a single LSC is maintained.

In Chapter 4, the focus is on exploring the dynamics of thermal plumes and temperature distribution in a laterally confined Rayleigh-Bénard convection cell under non-Oberbeck-Boussinesq conditions. Using water as the working fluid, the study employs time-resolved two-colour planar laser-induced fluorescence to capture the detailed evolution of the temperature field over time. This chapter addresses how lateral confinement influences the behavior of thermal plumes, their development, and their interactions with the boundaries of the cell. By investigating the spatial and temporal temperature distribution, the research aims to reveal the impact of confinement on the overall temperature field, with an emphasis on whether the lateral constraints affect the vertical symmetry of the thermal plumes and the temperature field. This chapter contributes to understanding how such confinement alters the thermal and flow structures in RBC, providing insight into the complex dynamics of plume formation and temperature distribution and oscillation.

In Chapter 5, the study focuses on developing a 3D time-resolved approach to validate the accuracy of 2D observations in laterally confined Rayleigh-Bénard convection and to determine the differences in the physics. Using 3D laser-induced fluorescence thermometry, this chapter aims to investigate whether the temperature properties captured in 2D provide a complete and accurate representation of the complex flow dynamics observed in 3D. By comparing the spatial and temporal variations in temperature fields between 2D and 3D measurements, the research explores the limitations of planar observations and reveals potential discrepancies in heat transfer and plume behavior that may be overlooked in 2D. The goal of this chapter is to critically assess whether 2D measurements can be relied upon for accurately characterizing the physics of RBC, or if a full 3D time-resolved approach is necessary for a complete understanding of the system.

In Chapter 6, the study focuses on Poiseuille-Rayleigh-Bénard convection with limited channel length, addressing how flow and temperature fields are organized under these conditions and whether large-scale circulation forms. Through the use of simultaneous planar laser-induced fluorescence and particle image velocimetry, this chapter explores the complex interactions between buoyancy-driven thermal plumes and the imposed horizontal shear flow within the mixed convection regime. The limited channel length introduces unique challenges, as the development of LSC typically requires a much longer channel. The research aims to determine how the restricted geometry affects both the flow structure and the heat transfer coefficient, considering both a vertical temperature gradient and a vertical convection of flow.

In Chapter 7, the research explores whether observations from Rayleigh-Bénard convection can be applied to induce large-scale circulation in Poiseuille-Rayleigh-Bénard convection and whether this can be leveraged as a heat transfer enhancement technique. This chapter uses planar laser-induced fluorescence to examine the temperature field and heat transfer distribution along the heated surface of the channel in PRBC flow. A custom-designed swirler component is introduced at the inlet of the cross flow to promote the formation of large-scale flow structures. The heat transfer performance of the system with the swirler is then compared to the basic case without the swirler, assessing the effectiveness of LSC formation in enhancing thermal transport. The investigation aims to demonstrate how insights from RBC can be applied to mixed convection systems like PRBC to optimize heat transfer in wall-bounded flow within mixed convection regime.

1.4 Thesis structure

This thesis was prepared in a paper-based format. Hence, except for the last chapter, each chapter either published or under review as a journal paper. Each chapter starts with an abstract description of the main purpose of the chapter and a graphical abstract, relevant to that specific chapter. The references are inclusive to each chapter for convenience. Based on the layout of thesis, some overlap between the introduction and references can be observed.

References

[1] B. Adrian, CONVECTION HEAT TRANSFER. John Wiley and Sons, Inc, 2013.

[2] G. Ahlers, S. Grossmann, and D. Lohse, “Heat transfer and large scale dynamics in turbulent Rayleigh-Bénard convection,” Rev Mod Phys, vol. 81, no. 2, pp. 503–537, 2009, doi: 10.1103/RevModPhys.81.503.

[3] I. V. Miroshnichenko and M. A. Sheremet, “Turbulent natural convection heat transfer in rectangular enclosures using experimental and numerical approaches: A review,” Renewable and Sustainable Energy Reviews, vol. 82, no. December 2016, pp. 40–59, 2018, doi: 10.1016/j.rser.2017.09.005.

[4] R. Krishnamurti and L. N. Howard, “Large-scale flow generation in turbulent convection,” Proceedings of the National Academy of Sciences, vol. 78, no. 4, pp. 1981–1985, Apr. 1981, doi: 10.1073/PNAS.78.4.1981.

[5] L. Zwirner, A. Tilgner, and O. Shishkina, “Elliptical Instability and Multiple-Roll Flow Modes of the Large-Scale Circulation in Confined Turbulent Rayleigh-Bénard Convection,” Phys Rev Lett, vol. 125, no. 5, Jul. 2020, doi: 10.1103/PhysRevLett.125.054502.

[6] E. P. Van Der Poel, R. J. A. M. Stevens, and D. Lohse, “Connecting flow structures and heat flux in turbulent Rayleigh- Bénard convection,” Phys Rev E Stat Nonlin Soft Matter Phys, vol. 84, no. 4, pp. 1–4, 2011, doi: 10.1103/PhysRevE.84.045303.

[7] H. D. Xi and K. Q. Xia, “Flow mode transitions in turbulent thermal convection,” Physics of Fluids, vol. 20, no. 5, pp. 1–15, 2008, doi: 10.1063/1.2920444.

[8] Z. Wang, H. Xu, C. Chen, G. Hong, Z. Song, and Y. Zhang, “Numerical analysis of Poiseuille-Rayleigh-Bénard convection in supercritical carbon dioxide,” Nuclear Engineering and Technology, vol. 54, no. 9, pp. 3540–3550, Sep. 2022, doi: 10.1016/j.net.2022.04.010.

[9] R. Taher, M. M. Ahmed, Z. Haddad, and C. Abid, “Poiseuille-Rayleigh-Bénard mixed convection flow in a channel: Heat transfer and fluid flow patterns,” Int J Heat Mass Transf, vol. 180, Dec. 2021, doi: 10.1016/j.ijheatmasstransfer.2021.121745.

[10] D. G. Osborne and F. P. Incropera, “Laminar, mixed convection heat transfer for flow between horizontal parallel plates with asymmetric heating,” 1985.

Chapter 2: Role of flow rolling structures on momentum transfer in Rayleigh-Bénard convection

In this chapter the flow structures of the RBC flow in a convection cell with unit aspect ratio is investigated by using PIV to visualize the flow field and measure the velocity. A combinatorial algorithm was used to quantify the size of the flow rolling structures and investigate their evolution in different states of the flow and examine their correlation with momentum transfer. Experiments were conducted for Prandtl number of $Pr = 7$ and Rayleigh number of $Ra = 5.3 \times 10^7$.*

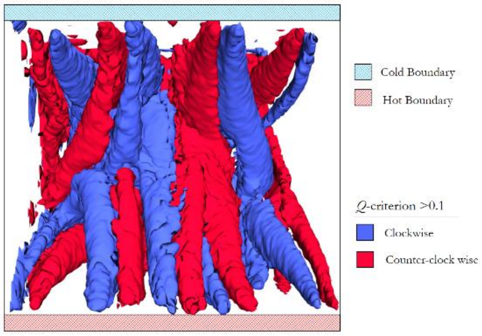

Graphical abstract for Chapter 2

---

*This chapter is published as: Sina Kashanj, and David S. Nobes. “Experimental evidence on the correlation between the flow rolling structures and momentum transfer in turbulent Rayleigh-Bénard convection.” *Physics of Fluids*, 2024, 36, 107101.

2.1 Introduction

Buoyancy-driven flow in an enclosure heated from below and cooled from above is known as Rayleigh-Bénard convection (RBC) [1]. RBC is an idealized flow system used to study the flow and heat transfer of a wide spectrum of phenomena and applications. To understand the physics of the complex convective flows that occur in nature, such as the flow inside planets and their atmospheric flows, this simple system has been a focus of investigation [2, 3]. In engineering, RBC can be studied to investigate the natural convective turbulent flow in closed systems [2]. RBC can also be employed in biomedical science applications for DNA polymerase chain reaction purposes [4, 5].

Controlling parameters of RBC are defined as the Rayleigh number, $Ra \equiv ag\Delta TH^3/\nu\kappa$, the Prandtl number, $Pr \equiv \nu/\kappa$, aspect ratio of the enclosure, $\Gamma \equiv w/H$, where α is the thermal expansion coefficient, w and H are the width and height of the convection cell respectively, g is gravitational acceleration, ν is kinematic viscosity, κ is thermal diffusivity of the fluid, and $\Delta T = T_H - T_C$ is the temperature difference between the hot, T_H , and cold, T_C, horizontal boundaries [6, 7]. In RBC, convection occurs by exceeding the Rayleigh number above a critical value [6]. In this critical Rayleigh number condition, convection is initiated by the rise and fall of the thermal plumes [8]. After the initiation of the convection, the development of turbulent flow leads to the formation of an unsteady large-scale circulation structure known as “LSC” or ”mean wind” which was found initially by Krishnamurti and Howard [9] using experimental visualization of the RBC flow.

It has been found that in slender enclosures (confined in both depth and width), $\Gamma < 1$ more than one LSC may form [10]. This effect of the enclosure aspect ratio on the number of LSC has led to recent studies investigating the correlation between the number of the LSC and heat and momentum transport [10–12]. Experimental investigations on the effect of slenderness of the convection cell with working fluid of water implied that the heat and momentum transfer in RBC is either insensitive to the number of LSC [13–16], or it has a very small effect, 0.5% [11, 17]. Further investigations were conducted by applying 2D and 3-dimensional (3D) direct numerical simulation (DNS) to examine directly the effect of the number of LSC on the heat and momentum transfer [18–21]. Results of DNS showed that there is a strong inverse correlation between the number of LSC and the heat and momentum transfer for relatively low Prandtl number e.g., the working fluid of air, $Pr = 0.7$. However, this inverse correlation was poorly observed for higher Prandtl numbers e.g., the working fluid of water, $Pr = 5$. Hence, it remains unclear whether at higher Prandtl numbers there is a relation between the flow structure and heat/momentum transfer.

The flow state of an RBC can be divided into condensed and uncondensed based on the presence of coherent flow structures [22]. While in the condensed state, the thermal plumes and small rolling structures are suppressed by the flow of the mean wind and join the wall shear flow. In the uncondensed state, rolling structures are more mobile and contribute to the flow in central regions as well [18, 22]. The probability of the formation of the uncondensed flow state is higher for higher Prandtl numbers [18]. This is due to the lower thermal diffusivity of the high Prandtl number fluids which leads to the formation of thermal plumes with higher energy and longer lifetimes [18].

The lateral confinement of the convection cell is another parameter that influences the scale of the flow structures. For example, in [20], it can be seen that the severe slenderness of the enclosure, $\Gamma = 0.125$, suppressed the small-scale rolling structures and only large-scale circulating structures can be observed in the flow field. Hence, it can be seen that they reported a significant correlation between the number of LSC with heat and momentum transfer. While in RBC convection cells with larger aspect ratios [18, 19] small-scale rolling structures can be observed along the LSC where a weaker correlation was reported compared to [20]. As a result, it can be hypothesized that in turbulent RBC with higher Prandtl numbers where small-scale rolling structures exist, small rolling structures also affect the heat and momentum transport. Evidence for this effect can be found in the work of Chen et al. [23] who investigated the elimination of corner rolling structures for an RBC flow of $Pr = 7$ and $Ra = 7.56 \times 10^8$. They showed that for a semiconfined rectangular enclosure eliminating the corner rolling structures using chamfered corners leads to an $20~\%$ increase in the Reynolds number. Yet the effect of the small-scale rolling structures has not been studied directly.

A specific situation in which rolling structures smaller than the LSCs could have a substantial role is after the onset of convection during the development of the flow to the formation of coherent LSCs. Xi et al. [8] showed that the time it takes for the coherent LSCs to appear is in the same order of magnitude as the time it takes for the flow to stabilize and reach an asymptotic state. The effect of small-scale rolling structures is probably more significant for fluids with large Prandtl numbers (e.g., water in comparison to the air) due to the higher probability of formation of unstable and uncondensed rolling structures [8] by the formation of thermal plumes with lower thermal diffusivity and higher energy [18].

Another condition that may lead to the formation of persistent high-energy thermal plumes is the non-Oberbeck-Boussinesq (NOB) condition due to the significant temperature difference between the thermal boundaries of the RBC convection cell. The non-Oberbeck-Boussinesq Rayleigh-Bénard convection refers to a fluid dynamic scenario where the fluid properties, such as density, viscosity, and thermal conductivity, vary significantly with temperature. This situation is more realistic than the Oberbeck-Boussinesq (OB) approximation, which assumes these properties are constant except for the density variation with temperature that drives buoyancy [24]. In OB Rayleigh-Bénard convection, this simplification leads to a linear relationship between buoyancy and temperature, facilitating mathematical and numerical analyses by reducing the system's complexity. However, the NOB approach accounts for the temperature dependence of fluid properties, introducing nonlinearities that more accurately reflect natural phenomena, such as atmospheric convection, oceanic flows, and the convection in the Earth's mantle. In this condition, the effect of temperature difference on density variation is significant [24]. Although NOB can affect the whole physics of flow in RBC, from direct numerical simulation it was shown that at a Prandtl number of $Pr = 0.71$ and Rayleigh number in the range of $3 \times 10^6 < Ra < 5 \times 10^9$, the effect of NOB on heat and momentum transfer is as low as $2\ \%$ even for a severe temperature difference of 240 ℃ [24].

In terms of the flow structure, under the same conditions, it was found that the flow structure and velocity field at the NOB condition are very similar to OB RBC [24]. For a Prandtl number of $Pr = 4.3$ and Rayleigh number of $Ra = 6.9 \times 10^8$, the flow structure of the RBC was visualized and compared at the NOB condition of $\Delta T = 40$ ℃ with the OB condition of $\Delta T = 9.6$ ℃ [25]. Since the temperature difference was different in OB and NOB conditions, the Rayleigh number and Prandtl number of the OB condition was slightly different to the NOB condition and equal to $Ra = 6.7 \times 10^8$, $Pr = 7.2$ [25]. Similarly, the flow structure and velocity field between the OB and NOB RBC were also reported in this case. However, a higher kinetic energy of developed LSC was observed due to high-temperature difference indicating a more chaotic flow in NOB RBC.

Although there are similarities between the OB and NOB RBC flow, some characteristics have been specified to the NOB RBC making it distinguishable from OB RBC flow. It is established that in OB RBC the vertical thermal profile consists of the thermal boundary layer near the horizontal walls and the temperature at the center which is equal to the mean temperature of the horizontal walls, i.e. $(T_H + T_C)/2$ [26]. However, in NOB RBC the temperature profile between the horizontal walls is much more complicated, deviating from the mean temperature of the horizontal walls [26–28]. In terms of the kinetic boundary layer, it has been found that while the kinetic boundary layer of the horizontal boundaries is symmetric, in NOB RBC it deviates to an asymmetry with a thicker boundary layer near the bottom(hot) wall [29, 30]. There is also some evidence highlighting differences in the flow structures such as the LSC and corner rolling structures [31, 32]. In OB RBC, a stagnation region is developed by developing the LSC. For NOB RBC, it has been found that this stagnation region moves from the center [31]. Furthermore, the two corner rolling structures are similar in OB RBC, but in NOB RBC they have different properties adding to the asymmetries of NOB RBC flow [31].

It has been confirmed that in Rayleigh-Bénard convection with the Prandtl number of the working fluid of air, and within the OB condition, there is an inverse correlation between the number of LSCs and the heat and momentum transfer [20]. However, there is some evidence that at high Prandtl numbers, e.g. working fluid of water, the inverse correlation between the number of LSCs and the heat and momentum transfer does not exist [19]. By hypothesizing the importance of small-scale rolling structure, we explore the flow rolling structures and their influence on momentum transfer in an RBC flow with relatively high Prandtl number, $Pr = 7$ and within NOB condition. The NOB condition is made by considering a relatively high temperature difference of $\Delta T = 30$ ℃ which leads to a Rayleigh number of $Ra = 5.3 \times 10^7$. The convection cell of the RBC is a cubical enclosure with unit aspect ratio, $\Gamma = 1$, a paradigm often studied in RBC flows [2]. The investigation of the flow rolling structures has been taken in three different states of the flow. The first state is considered from the start of the convection which has been observed to be unsteady and hence is a developing state. The second state is the developed RBC flow. The third state, is a developed flow, the same as the second state but with a different rotation direction of the LSC occurring due to the flow reversal in RBC flow. This state is considered to be investigated to confirm the results of the second state and also to see if the flow reversal has any influence on the characteristics of the flow rolling structures. Investigations have been taken experimentally by capturing the whole field velocity of the flow using 2C2D time-resolved particle image velocimetry (PIV). To detect the flow rolling structures and estimate their size, a combinatorial vortex detection algorithm has been employed. Using this methodology, we examine: I) The velocity field and compare its properties with OB RBC and previous NOB RBC studies; II) The flow rolling structures properties with a focus on their size, and III) The correlation between the flow rolling structures and the momentum transfer.

2.2 Methodology

To measure the velocity and visualize and quantify the flow structures, a time-resolved 2C2D PIV was employed. A schematic of the optical measurement system used to apply PIV is illustrated in Figure 2-1. An 8-bit CMOS camera (Flare 12M125, IO Industries Inc.) with a maximum frame rate of 220 fps and resolution of 2048×2048 pixels was utilized to capture the whole convection cell. To illuminate the seeded flow field, a continuous Argon-ion laser was used operating at 488 nm wavelength. As is shown in Figure 2-1, scanning mirrors were employed to generate the laser sheet (scanning mirror2). Another mirror, Mirror1 was also employed to control the location of the laser sheet in the z-direction of the convection cell at $z = 0$. A biconvex lens 3 was also used to collimate the laser sheet. Neutrally buoyant hollow glass spheres with a diameter of 18 μm were used as seeding particles. A relaxation time was implemented before the start of the experiment to ensure that the flow had achieved a stationary condition. Examination of the processed PIV data after the relaxation time showed that the motion of the seeding particles was negligible before the start of the experiment. PIV processing was applied by a multi-pass algorithm with a minimum interrogation window size of 32×32 pixels using commercial software (DaVis 8.2, LaVision GmbH).

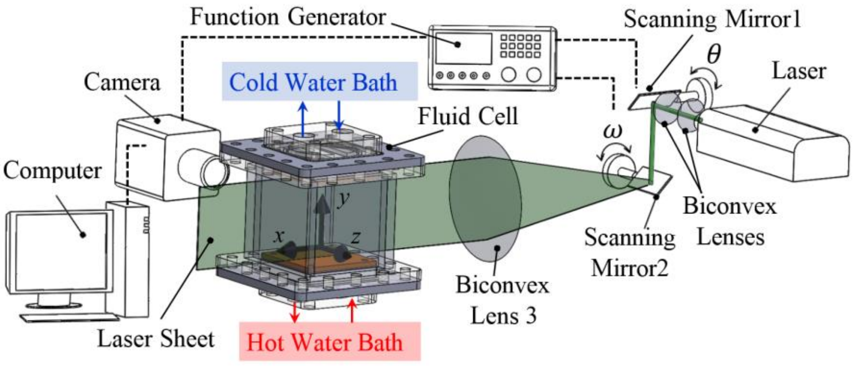

Figure 2-1. Schematic of the optical measurement system used to apply time-resolved 2C2D PIV and a render of the solid model of the RBC enclosure used for the experiment.

A schematic of the convection cell of the RBC with unit aspect ratio, $\Gamma = 1$, and the dimensions of $50 \times 50 \times 50$ mm3 is shown in Figure 2-2. The test section was made from an acrylic sheet with a thickness of 6.35 mm that had a low thermal conduction coefficient of 0.2 W/mK. The temperature boundary conditions can be described as a constant temperature at the top, $T_C = 5$ °C, and bottom, $T_H = 35$ °C, and adiabatic at the side walls as is illustrated in Figure 2-2(c). This geometry and boundary condition with the working fluid of water, $Pr = 7$, provides a Rayleigh number, $Ra = 5.3 \times 10^7$ calculated based on the mean temperature of the hot and cold boundaries, $(T_H + T_C)/2$.

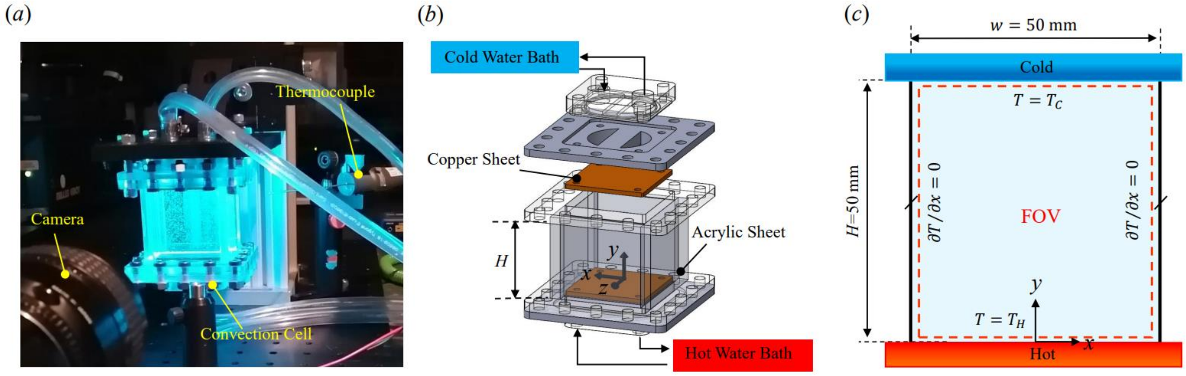

Figure 2-2. (a) An image of the experimental setup showing the convection cell. (b) A rendering of the convection cell showing its components. (c) Schematic of the convection cell showing the boundary conditions and convection cell dimensions.

It is important to monitor the temperature of the side wall of the convection cell to record the temperature variation to examine if the heat transfer through it is negligible as is defined for the RBC boundary condition. While relatively thick acrylic walls with a low heat transfer coefficient were used to minimize the heat transfer through vertical walls, the temperature was monitored using a thermocouple connected to the outer side of one of the vertical walls of the enclosure. The maximum temperature change from the start of the convection was measured to be 1.2 ℃ which was much smaller than the temperature difference of the RBC flow which was equal to 30 ℃.

To ensure that the temperature of the hot and cold heat sources remained constant during the experiment, heat exchangers were connected to thermal baths (PolyScience, Preston Industries, Inc.) with a temperature stability of 0.01 ℃ to control the horizontal surface temperatures. The heat exchangers featured a copper plate to improve the uniformity of the heat transfer surface. The support bases were made using an SLA 3D printer (Form3, Formlabs Inc.) and printing material, a liquid photopolymer, with a low thermal conduction coefficient of 0.15 W/mK. To ensure that the heat source and sink used in this experiment generated a continuous distribution of temperature, an IR camera (FLIR A35, FLIR Systems Inc.) was used to visualize the temperature distribution on the copper surface while the heat exchanger was connected to the water bath. This was a preliminary experiment to examine the performance of the designed and fabricated heat exchanger to see if the temperature distribution was constant on the surface of the copper sheet as was intended. This test was done while the heat exchanger was connected to the hot water bath and the copper sheet was in contact with air not the main RBC enclosure which had the working fluid of water. During the experiment, the flow rate of the water bath was maximized (much higher than the velocity scale of the RBC flow) to maintain the temperature consistency of the surface of the heat exchanger.

The temperature of the outlet of the heat exchanger was monitored using a thermocouple and had a temperature difference lower than $0.5\ ℃$ showing a negligible temperature loss. Figure 2-3(a) shows the dimensionless temperature distribution on the copper surface. The temperature profile along the two axes of $x/h = 0$ and $z/h = 0$ are also shown in FIG.3(b). From both of these figures are shown in Figure 2-3, it can be seen that temperature distribution on the surface of the solid boundary was relatively uniform with a maximum deviation from the mean value of the temperature of the surface found to be $\sim 4.5\ \%$.

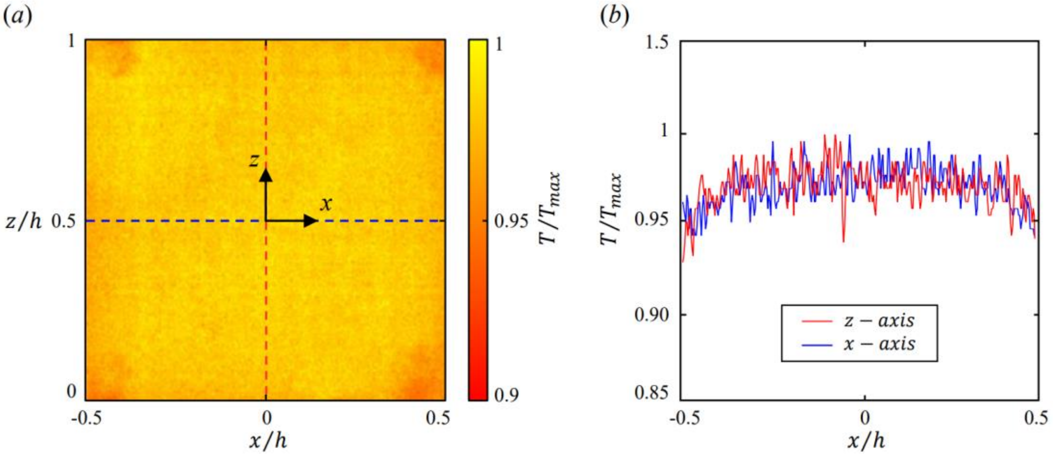

Figure 2-3. (a) Temperature map of the surface of the solid horizontal boundary of the heat exchanger of the convection cell captured by an IR camera. (b) The temperature profile of the solid boundary along two lines of $x/h = 0$ and $z/h = 0$.

In order to detect the flow rolling structures, a combinatorial vortex detection algorithm was employed. This algorithm was developed by Bussiére et al. [33] for use on PIV data. Two different vortex detection criteria using a maximum vorticity method [34] and streamline method were employed [35] in this combinatorial algorithm. The streamline method works based on the winding angle criterion $\alpha_w \geq 2\pi$, in which the winding angle is defined as $\alpha_w = \sum_{i=1}^{N-1} \angle\,(P_{i-1}, P_i\,, P_{i+1})$, see Figure 2-5, where $\angle$ denotes the angle between two discretized lines of the streamline defined based on the three successive points of P_{i-1}, P_i, and P_{i+1} [35]. Although this combinatorial vortex detection algorithm is computationally expensive in comparison to other common methods such as Q-criterion, it is more robust since it is a geometrical method [34]. This is required especially in this case in which a velocity field with multi-scale and dense rolling structures is going to be examined. The process of detection of the rolling structures for an example data set is shown in Figure 2-4. The dimensionless vorticity field, $\overline{\omega} t_f$, of the mean flow is shown in Figure 2-4(a). Here, the vorticity is defined as $\equiv \nabla \times V$, where V represents the velocity vector field.

From the vorticity field, regions with high vorticity are detected. These regions are identified as regions of interest (ROI) shown in Figure 2-4(b). Erroneous regions, which are also highlighted in this figure, identify locations with high vorticity. However, these do not represent a flow rolling structure but rather regions of high shear. These erroneous regions were eliminated by applying the streamline method. By fitting an ellipse to the detected regions as shown in Figure 2-4(c), the number and geometry properties of the rolling structures can be defined. For a flow field with higher vortex density such as the one in Figure 2-4(d), it is more challenging to detect true rolling structures due to the numerous numbers of erroneous regions in the ROI field (Figure 2-4(e)). However, by applying the streamline method the erroneous regions are eliminated and most of the true rolling structures are detected as is shown in Figure 2-4(f).

An LSC is identified based on the rolling structures of the flow, though there is not a quantified criterion to define the size of a rolling structure to be known as an LSC [19]. Qualitatively, the size of a rolling structure should be dominant in the convection cell to be known as an LSC [19]. Conventionally in a cubical enclosure, it is known that only a single LSC could be developed [19]. Hence, the half-size of the convection cell could be defined as a threshold to identify the LSC. This has been defined based on the dimensionless area of the rolling structures, $A^* = A/h^2$ where A is the area of each rolling structure enclosed by the fitted ellipse. Based on this, rolling structures with the size of $A^* < 0.5$, and $A^* > 0.5$ are named small-scale rolling (SSR) and LSC respectively.

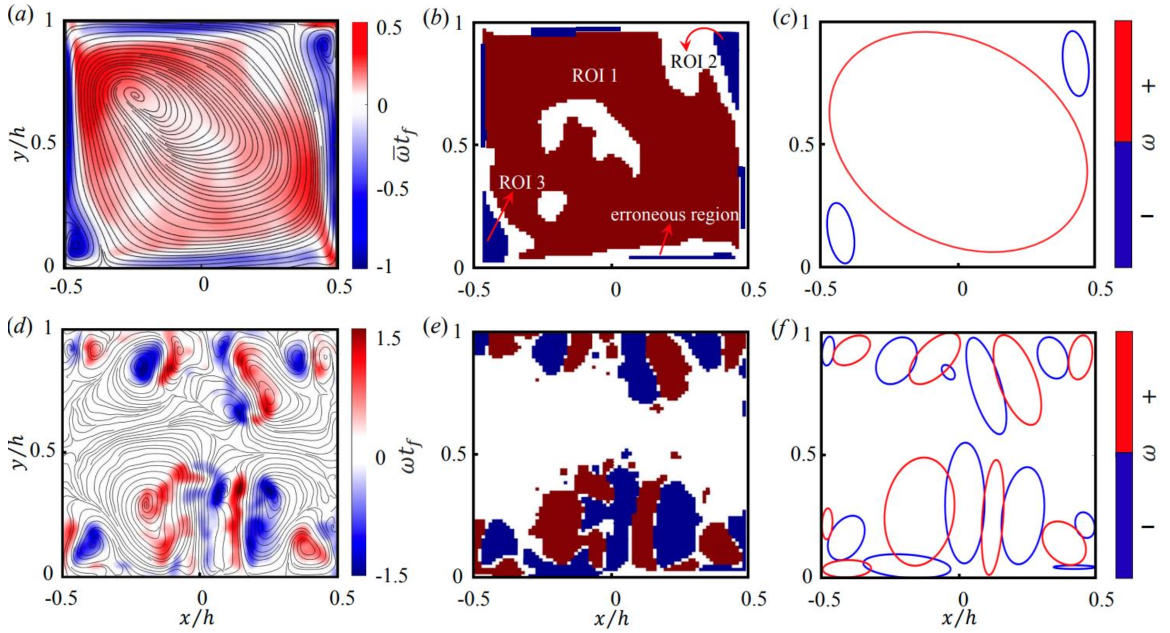

Figure 2-4. (a)-(c) The process for detecting flow rolling structures of the mean flow of the developed RBC flow showing the mean wind at the center and two small corner rolling structures. (a) Mean vorticity field. (b) Regions of interest. (c) Ellipses showing the detected rolling structures of the mean flow. For the developed flow, (d)-(f) shows the flow rolling structure detection process of an instantaneous flow field with high number of rolling structures. (d) Instantaneous vorticity field after a short time after the start of convection, $t/t_f = 8$. (e) Regions of interest. (f) Ellipses showing the detected rolling structures of the instantaneous flow. Red and blue colours show the CCW and CW rolling structures respectively.

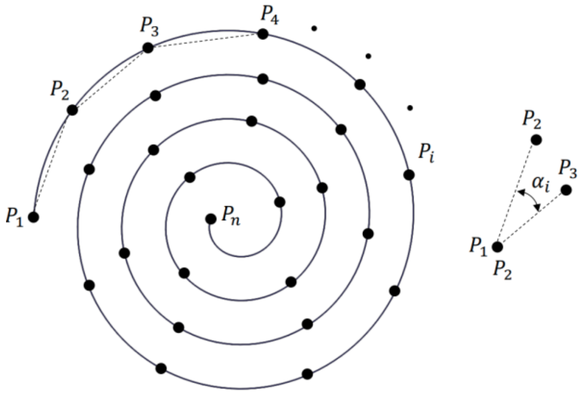

Figure 2-5. Schematic of the streamline of a vortex segmented by n number of points α_i which is used to define the winding angle shows the angle between two lines of $P_{i-1} - P_i$ and $P_i - P_{i+1}$.

2.2 Experimental condition

Many studies have shown that there are multiple states occurring in RBC flow with different conditions [11]. The transformation between the states may occur due to different reasons. Developing the flow and flow reversal and cessation are the most frequent phenomena observed leading to the formation of different states of the RBC flow [36]. Flow reversal in RBC flow refers to the frequent change in the direction of the LSC or the mean wind [38]. While the physics behind this phenomenon is still a question in the context of RBC flow, the formation of the corner rolling flow structures and their interaction with the LSC is known as one of the main reasons for this phenomenon [23].

In this chapter, experiments were conducted for a chosen three different temporal states of the RBC while the Rayleigh and Prandtl numbers remained constant. Experiments were conducted time-resolved and during $\Delta t/tf = 315$, where t_f is the free-falling time defined as $t_f \equiv H/\sqrt{g\alpha\Delta TH}$, to reach the statistically steady state which has been examined and shown in Figure

2-6. The first state, S1 is selected from the start of convection from $\Delta t/tf = 0$ to $\Delta t/tf = 315$. The second state, S2 and third states, S3 are from $t/t_f = 1260$ to $t/t_f = 1575$ and $t/t_f = 2520$ to $t/t_f = 2835$, respectively both with a $\Delta t/tf = 315$ period which the flow is at a pseudo-steady state. It is worth noting that for both S2 and S3, the LSC is well formed and steady. While both S2 and S3 are developed states, they have different rotation directions of the mean wind due to the flow reversal of the RBC [37, 38]. During S2, the mean LSC is clockwise (CW) and during S3 it is counter-clockwise (CCW).

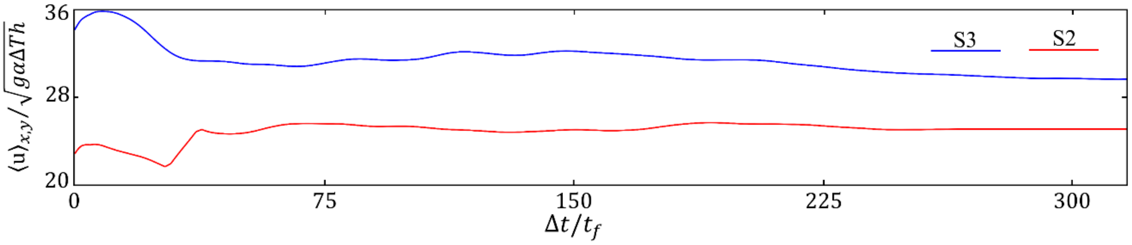

Figure 2-6. Shows the statistical convergence of the spatial average velocity magnitude of S2 (red) and S3 (blue) during the period of the examination.

Although, it is interesting to take a look at the effect of controlling conditions, here it is preferred to investigate different states at the same condition which forms and evolve temporally. This preference and focus on the different states is because of the interest of the previous works on the different states and temporal evolution which has led to new understanding of the RBC flow [18-20]. To explore different states of the RBC flow a very long time examination of the flow is required and some factors such as computational cost and storage of the raw data are the main limitations, limiting the experimental studies when the whole field measurement is required. Hence, in many works it can be seen that the investigated physics is limited in time or the number of cases with different controlling conditions. Here, to overcome these limitations the most important states of the flow have been selected to investigate the properties of the flow rolling structures and their effect on the momentum transfer. The first state S1 is important since it shows the start of the convection and usually it is missed in previous investigations and there is a gap in understanding of the flow properties. This was investigated qualitatively by [8] in the past. Hence, it is interesting to quantify the qualitative explanation about the start of the convection. The other point about S1 is that since the flow is underdeveloped, the formation of the LSC is not expected. Hence, the flow structure was expected to be quite different from the developed flow in which LSC exists. Hence, it represents the underdeveloped transient state of RBC flow. Investigating this state helps to see the correlation between the flow rolling structures and the momentum transfer in the transient state of the RBC flow.

The second state is the developed flow, e.g. S2, in which LSC is developed and steady. The other state, S3 with the different rotation direction also has been chosen to investigate due to two main reason: First, to see if the result of the S2, i.e. the correlation between rolling structures and momentum transfer, is repeatable, and second, to investigate the flow rolling structure properties when flow reversal occurs. The mean vorticity field of the asymptotic state of S3 obtained from the described experiment condition is shown in Figure 2-4(a). As can be seen in this figure, a single LSC with two small rolling structures at the two corners of the cell is characteristic of the developed turbulent RBC flow in a cubical enclosure which has been reported earlier [25, 39, 40].

To increase the probability of the formation of an uncondensed flow state, a relatively high-temperature difference, $\Delta T = 30\ ^{\circ}\mathrm{C}$ was selected for the experiment. For a high-temperature difference, the RBC flow is in non-Oberbeck-Boussinesq (NOB) condition. In this condition, the effect of temperature difference on fluid transfer properties such as viscosity and density are significant [24]. The variation of the parameters such as falling-time, t_f and falling-velocity, V_f

along with the variation of Prandtl and Rayleigh numbers with the temperature of the top and bottom boundaries is highlighted in TABLE I. Here, the variation of the highlighted properties could be compared to their values at the mean temperature, where $(T_H + T_C)/2.$ While in OB RBC the variation of the parameters such as Rayleigh and Prandtl number at the temperature of the hot and cold boundaries is almost equal to the one at the mean temperature, here it can be seen that Rayleigh number varies by an order of magnitude by moving from the hot boundary to the cold boundary at the top of the convection cell. This variation also could be found significant for other parameters such as Prandtl number and falling-time and falling-velocity. For this study in which the temperature of the hot boundary is equal to $T_H = 35℃$ and temperature of the cold boundary is equal to $T_H = 5℃$, all properties can be seen in Table 2-1. Although all the properties are a function of temperature, the thermal expansion coefficient has a significant variation and has the most effect on the variation of the Rayleigh number which contains the physics of the buoyancy driven Rayleigh-Bénard convection flow. Furthermore, the effect of the kinematic viscosity is significant due to its high sensitivity to the temperature variation and its influence on both Rayleigh and Prandtl numbers.

Table 2-1. Variation of the flow properties of the RBC flow according to the temperature of the hot and cold boundaries in comparison to the mean temperature.

T	$T_H = 35$ ℃	$T_C = 5$ ℃	$\bar{T} = 20$ ℃
t_f	0.816	3.367	0.906
V_f	0.061	0.015	0.055
Pr	4.66	11.11	6.99
Ra	8.9×10^7	2.7×10^6	5.3×10^7
ρ $(\mathrm{Kg/m^3})$	994.1	999.9	998.2
$a \times 10^{-4}$(℃$^{-1}$)	2.5	0.15	2.1
μ (mPa. s)	0.7	1.5	1.0
$\nu \times 10^{-6}(\mathrm{m^2}/s)$	0.7	1.5	1.0
$\kappa \times 10^{-6}(\mathrm{m^2}/s)$	0.15	0.13	0.14

The importance of identifying the NOB condition in theoretical and numerical studies is that the governing equations under the OB assumption is not valid and more sophisticated equations should be considered to resolve the physics of RBC flow under the NOB condition. Hence, we have reported the condition of the current experiment to highlight the NOB condition of the current work. In this work, the NOB condition is due to the high temperature difference between the hot and cold boundaries which results in a temperature distribution of the fluid flow in that range. As a result, the properties that are relevant to the controlling parameters of the Rayleigh-Bénard convection i.e. Rayleigh number and Prandtl number are varying both temporally and spatially in the RBC flow under the NOB condition. The properties that are affecting these two parameters are density, ρ, thermal expansion coefficient, a, dynamic viscosity, μ, and kinematic viscosity, ν, and thermal diffusivity, κ, since Rayleigh number is defined as $Ra \equiv ag\Delta TH^3/\nu\kappa$ and Prandtl number as $Pr \equiv \nu/\kappa$. As is highlighted in TABLE I, the variation of these properties with temperature can influence the Rayleigh and Prandtl number significantly while in the OB condition since the temperature variation is relatively small, usually $\Delta T < 1$ ℃, the Rayleigh and Prandtl number is both temporally and spatially constant.

Identifying when a system transitions from the OB to the NOB regime, particularly under high temperature differences between boundaries, can be challenging. To address this, Gray and Giorgini [41] developed a method for validating the OB approximation for both air and water. Figure 2-7, based on the work of Horn and Shishkina [30] and utilizing Gray and Giorgini's criteria [41], illustrates the temperature range within which the OB approximation is valid for RBC in water. The diagram includes a star marker representing the three temporal states, which demonstrate the NOB conditions observed. For the current study, with an enclosure height of 50 mm and a temperature difference of 30 °C, as shown in Figure 2-7, it is evident that the flow is within the NOB condition.

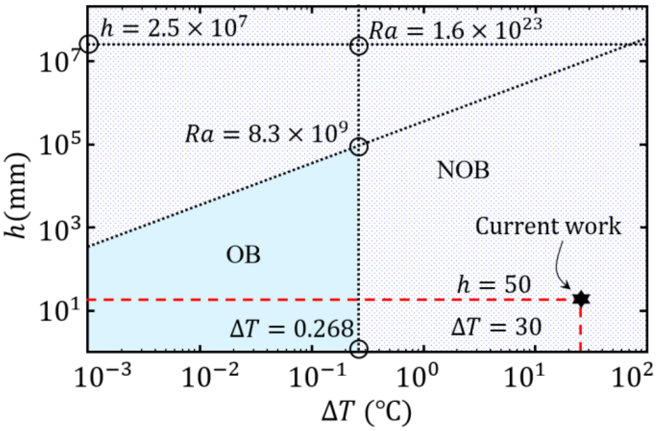

Figure 2-7. The diagram shows the height of the enclosure, h, versus the temperature difference, ΔT to classify the Oberbeck-Boussinesq (OB) from non-Oberbeck-Boussinesq (NOB) condition in Rayleigh-Bénard flow. The asterisk indicates the current work. This diagram is after Horn and Shishkina [30].

2.3 Results and discussion

To investigate the flow properties of the investigated RBC flow and compare it with the flow properties of OB RBC and previous NOB RBC flows, the normalized mean velocity magnitude of the two states of S2 and S3 are plotted in Figure 2-8(a) and (b|) where $\langle u \rangle_t$ indicates temporal mean velocity magnitude normalized by the free-falling velocity $V_f = \sqrt{\alpha g \Delta T h}$, where α, is the thermal expansion coefficient, g is the gravitational acceleration, ΔT is the temperature difference between the bottom and top boundaries, and h is the height of the convection cell. As can be seen, for S2 the LSC is clockwise in Figure 2-8(a), while for S3 it is counter clockwise in Figure 2-8(b). The two corner rolling structures which are one of the usual characteristics of an RBC flow in convection cells with an aspect ratio close to unity can be observed for both states of S2 and S3. From this figure, some characteristics of the flow structure of NOB RBC can be observed. For instance, it can be seen that for both states, the stagnation region is shifted from the center of the convection cell to a corner of the convection cell. The direction of this shift is proportional to the direction of the LSC. Hence, for S2 it shifted from the center to the top-right, and for S3 it shifted to the top-left of the convection cell. Furthermore, the vertical and horizontal asymmetry in the velocity distribution can be seen. However, to have a better understanding of the characteristic asymmetries in the velocity distribution, an examination of the horizontal and vertical velocity components is necessary.

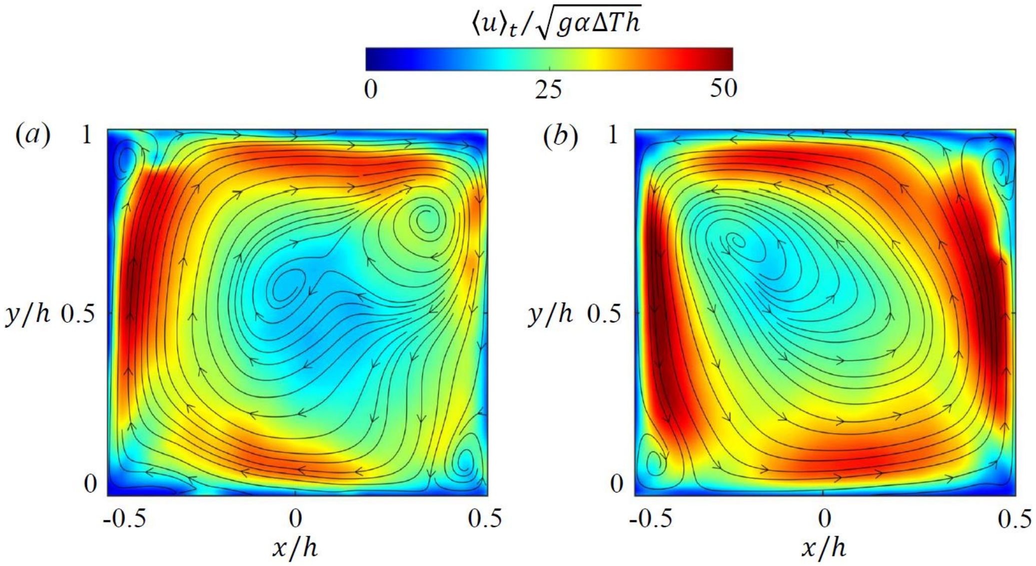

Figure 2-8. The velocity magnitude map of the two states of (a) S2 and (b) S3.

For this purpose, the normalized mean horizontal velocity, $\langle u_x \rangle_t / \sqrt{g\alpha\Delta TH}$ along the vertical axis of the convection cell at the center, $x/h = 0$ has been plotted in Figure 2-9(a). As can be seen in this figure, the velocity profiles of S2 and S3 are quite similar both in variation along the vertical direction and in the magnitude of the velocity. For both of these states, a shift in the velocity profile could be observed, as a result, it can be seen that the zero velocity where the direction of the horizontal velocity is changing is occurring at $y/h > 0.5$ which is a known characteristic of NOB RBC. However, it could be seen that the velocity variation near the wall is very similar near both hot and cold boundaries. The results of the vertical velocity, $\langle u_y \rangle_t / \sqrt{g\alpha\Delta TH}$ along the horizontal axis of the convection cell at $y/h = 0$ shown in Figure 2-9(b) indicates the flow generated due to the rise and fall of the thermal plumes deriving the LSC. It can be seen that the horizontal velocity profile looks similar for both states. It is worth noting that the standard deviation of both horizontal and vertical velocity profiles are shown as well in Figure 2-9. Looking into that it can be seen that for both states the standard deviation is significant. This also could be inferred from the instantaneous velocity profiles along the y-axis and x-axis shown in Figure 2-9(c) and (d), respectively. In these two figures, along with the velocity profile of S2 and S3, the velocity profiles of S1 are plotted as well. It can be seen that in comparison to S2 and S3, for velocity profiles of S1 there is no evidence of formation of LSC. It worth noting that since the first state of the flow, S1 is indicates the start of the convection, it is statistically unsteady, hence, there is not a meaningful mean flow field for this state to be compared with the mean properties of the two other states. To be able to compare all three states, the probability density function, PDF of the normalized horizontal and vertical velocities has been investigated.

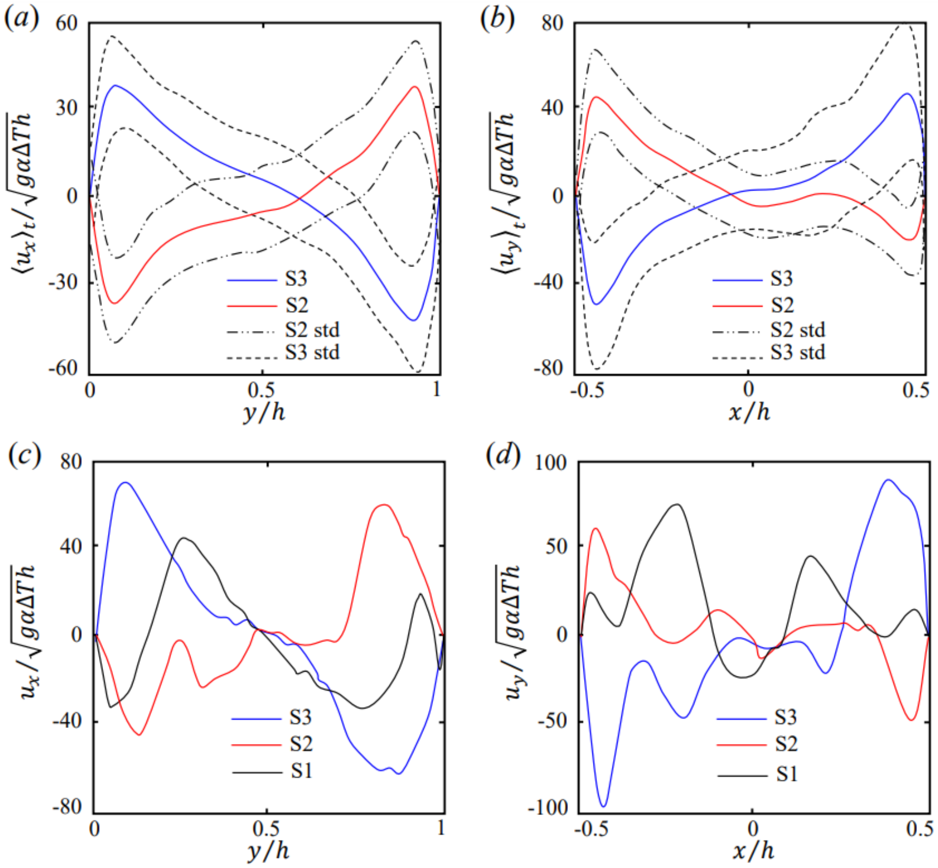

Figure 2-9. (a) Normalized mean horizontal velocity, $\langle u_x \rangle_t/\sqrt{g\alpha\Delta TH}$ along the vertical axis of the convection cell at the center, $x/h = 0$. (b) Normalized mean vertical velocity, $\langle u_y \rangle_t/\sqrt{g\alpha\Delta TH}$ along the horizontal axis of the convection cell at $y/h = 0$. (c) instantaneous normalized horizontal velocity, $u_x/\sqrt{g\alpha\Delta TH}$ along $x/h = 0$ axis. (d) Instantaneous normalized vertical velocity, $u_y/\sqrt{g\alpha\Delta TH}$along $x/h = 0$ axis.

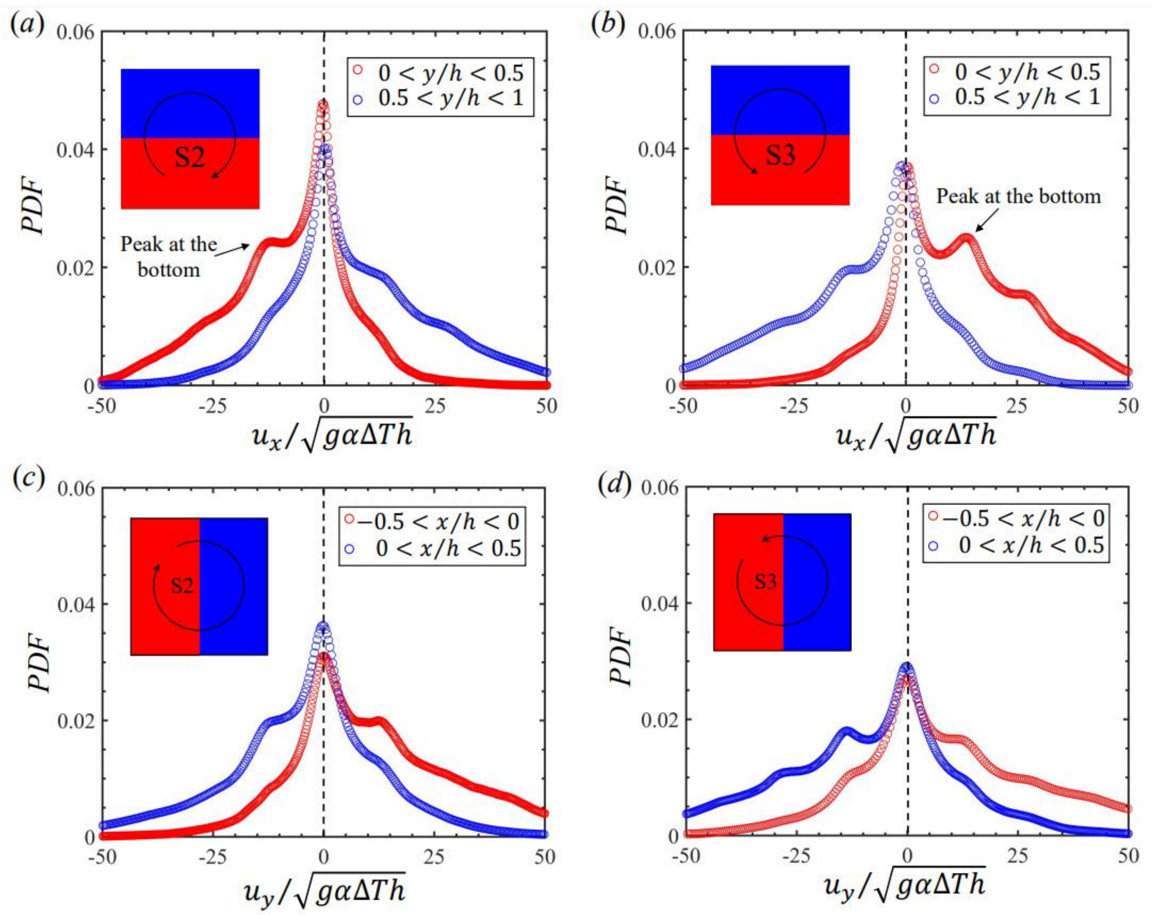

Figure 2-10. The probability density function (PDF) of (a) and (b) normalized horizontal velocity, $u_x/\sqrt{g\alpha\Delta TH}$ of S2 and S3 and (c) and (d) normalized vertical velocity $u_y/\sqrt{g\alpha\Delta TH}$ of S2 and S3. The schematics at the top left side of the plots indicate the direction of LSC. In (a) and (b) the red colour shows the region near the bottom (hot) wall and the blue colour shows the region near the top (cold) wall. In (c) and (d), the red colour shows the region where thermal plumes are rising and the blue colour shows the region where they are falling.

For the two developed states of S2 and S3, the probability density functions are plotted in Figure 2-10 and for the start of the convection, S1 it is plotted in FIG. 11. As can be seen in these two figures, for the horizontal velocity component, $u_x/\sqrt{g\alpha\Delta TH}$, the horizontal symmetricity of the horizontal velocity component regarding the $y/h = 0.5$ line has been investigated. This has been done by plotting the horizontal velocity at the first half of the convection cell from the hot wall to the mid-height, $0 < y/h < 0.5$ versus the second half from the mid-height to the cold wall of the convection cell, $0.5 < y/h < 1$. Similarly, to investigate the vertical symmetricity of the vertical velocity component, $u_y/\sqrt{g\alpha\Delta TH}$regarding the $x/h = 0$ line, the probability density function of the vertical velocity has been compared for the first half of the convection cell, $-0.5 < x/h < 0$ with the second half, $0 < x/h < 0.5$.

As can be seen in Figure 2-10(a) and (b), the horizontal component of the velocity of both halves of the convection cell has a peak at $u_x/\sqrt{g\alpha\Delta TH} = 0$ which is due to the nonslip boundary conditions, the pure vertical jets due to rise/fall of the thermal plumes, and the stagnation regions form by rolling structures. The second dominant mode that could be observed for S2 and S3 is occurring at $u_x/\sqrt{g\alpha\Delta TH} \approx -15$ for S2 and $u_x/\sqrt{g\alpha\Delta TH} \approx 15$ for S3. As is highlighted in Figure 2-10(a) and (b), this peak is attributed to the higher velocity near the hot wall which is a characteristic of NOB RBC highlighted by [25, 26]. Despite the horizontal velocity component, the vertical velocity component distribution of S2 and S3 is shown in Figure 2-10(c) and (d) are similar. For both S2 and S3, the vertical velocity component is dominant by the jet stream forms due to the rise and fall of the thermal plumes. However, the existence of the vertical velocity in the opposite direction of the rise and fall of the thermal plumes could be distinguished as a NOB characteristic in comparison to RBC flow.

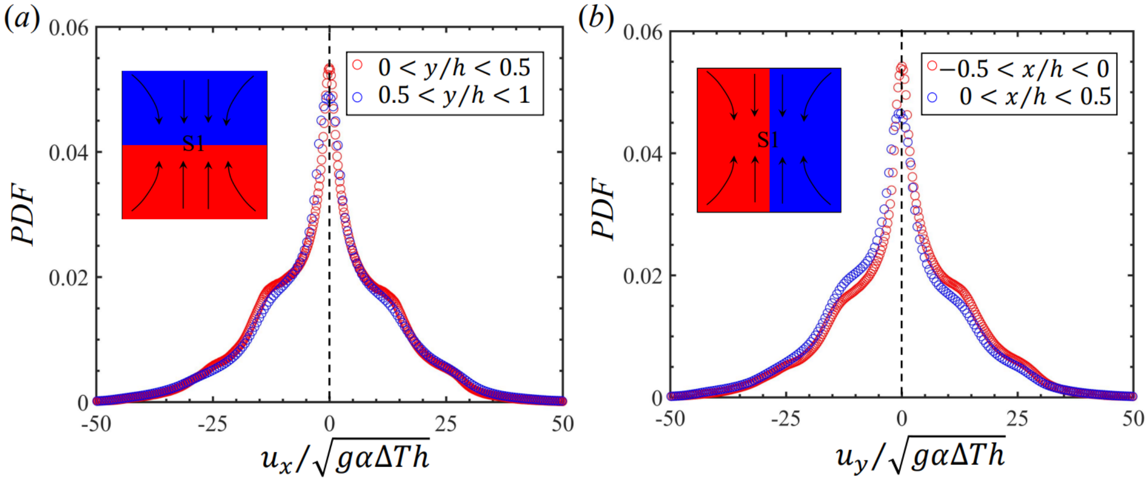

Figure 2-11. The probability density function (PDF) of (a) normalized horizontal velocity, $u_x/\sqrt{g\alpha\Delta TH}$ and (b) normalized vertical velocity, $u_y/\sqrt{g\alpha\Delta TH}$ of S1.

For the start of the convection regime, S1, as can be seen in Figure 2-11(a), the horizontal velocity component near both hot and cold walls have a similar distribution which is symmetric about the zero velocity. The same similarity and summitry can also be observed for the vertical velocity shown in Figure 2-11(b). The symmetry in both horizontal and vertical velocities indicates that the flow is dominant by the thermal plumes while LSC is still not formed and the thermal plumes are not disrupted by the stream of the LSC. The similarity in the distribution of the horizontal and vertical velocities near hot and cold walls and near the right and left sides of the convection cells indicates that the properties of the thermal plumes that are generated by the hot and cold walls are similar at the beginning of the convection while the flow is still not developed. Since there is no quantitative data on the start of the convection of RBC flow, it is challenging to draw a conclusion on the significant difference between this regime in NOB RBC in comparison to the OB RBC. However, in NOB RBC, the thermal plumes have higher energy due to the high-temperature difference and, therefore more persistence in comparison to the OB RBC flow. Hence, some asymmetries could be expected from the velocity distribution of OB RBC at the start of the convection.

To visualize the evolution of the rolling structures during each state of S1, S2, and S3 and compare the rolling structures of each state the criterion of the positive second invariant of the velocity gradient tensor $L_{i,j} = \partial_j V_i$, known as Q-critarion is analyzed. The visualized flow rolling structures based on iso-surfaces of Q-critarion are depicted in Figure 2-12. In this figure, iso-surfaces are coloured based on the rotation direction of the vortices, i.e. red and blue iso-surfaces show the CCW and CW vortices respectively. Figure 2-12(a), (d), (g) show the isometric view of the evolution of the iso-surfaces of Q-critarion $>$ 0.1 during $\Delta t/tf = 0 - 315$ for S1, S2, and S3, respectively. The same iso-surfaces from the front view, $\Delta t/tf = 0$ are shown in Figure 2-12(b), (e), (h) and from the back view $\Delta t/tf = 315$ in Figure 2-12(c), (f), (i).

The rise and fall of the thermal plumes can be seen after the start of convection, Figure 2-12(a) and (b). From these figures, it can be seen that rolling structures develop after the start of convection while the size of the CW and CCW rolling structures are almost the same. This also can be seen from Figure 2-12(c) at the end of the S1. The development of rolling structures of the same size could be referred to as the formation of thermal plumes not being disrupted by the main stream of the LSC since it has not been developed yet at the start of the convection. For S2 and S3, in comparison to S1, from Figure 2-12(d)-(i), it can be seen that for S2 CW rolling structure are dominant while for S3 CCW rolling structure are dominant. The dominant rolling structure at each state of S2 and S3 indicates the development of the LSC at that specific state.

The temporal evolution of the vorticity field for all three states of S1, S2, and S3 can be seen in Figure 2-13(a) (multimedia available online), Figure 2-13(b) (multimedia available online), and

Figure 2-13(c) (multimedia available online). For S2 and S3, a large-scale circulating structure can be observed at the center which is CW for S2 and CCW for S3. For both of these states, multiple small-scale rolling structures can be seen. This flow structure, i.e. existence of an LSC at the center and small-scale rolling structures surrounding it, resembles the mean flow structure of the developed RBC flow shown in FIG. 8. For S1, however, the flow field contains several CW and CCW small-scale rolling structures implying a significant contradiction in the flow structure of this state with the developed states of S2 and S3. These observations of the flow structure evolution of RBC are consistent with the qualitative report of Xi et al. [8] of turbulent RBC flow development.

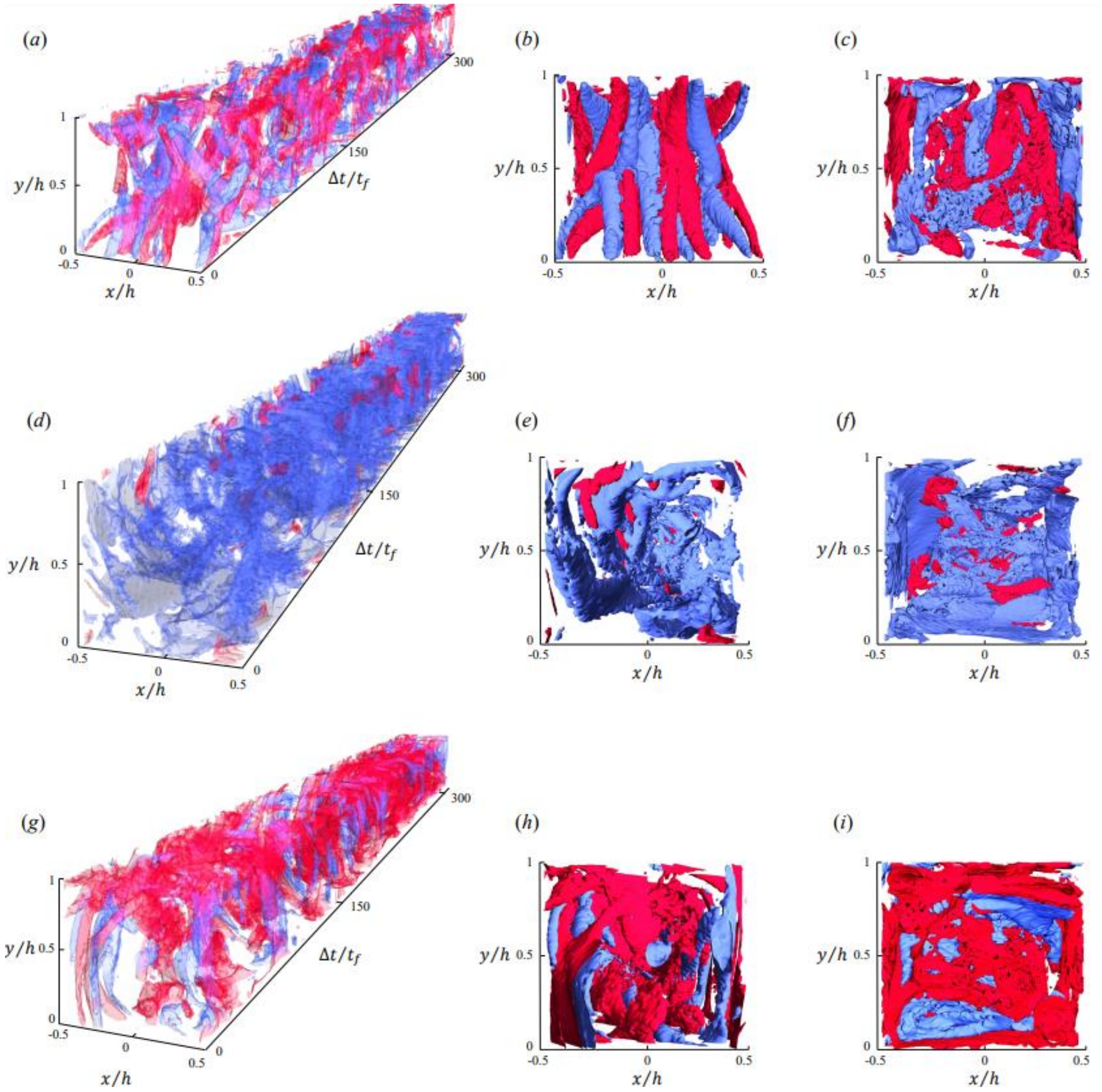

Figure 2-12. Isometric, front, and back view of the time-reconstructed Q-criterion > 0.1 iso-surfaces of (a)-(c) S1, (d)-(f) S2, and (g)-(i) S3 during $\Delta t/tf = 0 - 315$. Red and blue iso-surfaces represent the CCW and CW rolling structures. (a), (d), and (g) show the isometric view. (b), (e), and (h) show the front view, and (c), (f), and (i) show the back view of this 3D map.

Although the vorticity field and the 3D map of the evolution of the Q-critarion provide insight into the development of the flow rolling structures, a quantitative analysis is necessary to characterize the properties of the rolling structures at each state. To have a quantitative understanding of the scale of the rolling structures of S1 and compare them with two other states, S2 and S3, the normalized size distribution of the rolling structures is shown in FIG.12 based on the normalized area of the rolling structures, A^*. As can be seen in Figure 2-14(a), for S1, the size distribution of CW and CCW rolling structures are similar, implying the existence of vortex pairs due to the formation of thermal plumes. Examples of these vortex pairs can be seen in Figure 2-13(a) (multimedia available online), Figure 2-13(b) (multimedia available online), and Figure 2-13(c) (multimedia available online), showing the evolution of the vorticity field. The formation of the vortex pairs in S1 shows the direct role of the thermal plumes on the flow structure after the start of convection. However, in the developed state, the formation of vortex pairs can be observed rarely, which is due to the disruption of the thermal plumes by the main LSC flow. From Figure 2-14(a), it can also be seen that the peak of the distribution is occurring at $A^* \approx 0.05$ and small-scale rolling structures are significantly dominant in this state.

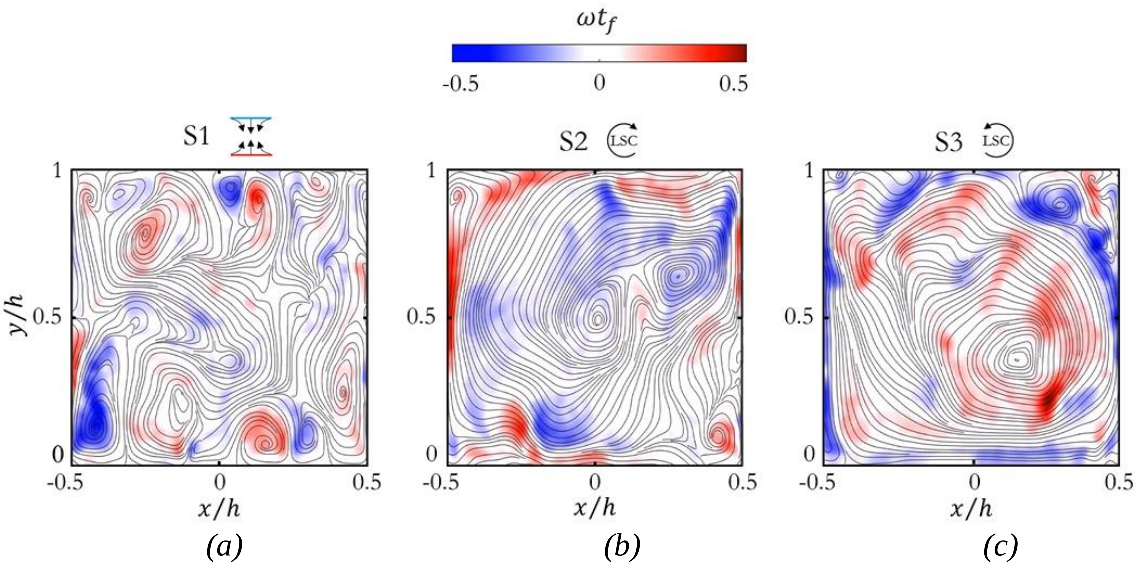

Figure 2-13. Instantaneous vorticity field of the three states of (a) S1 (Multimedia available online), (b) S2 (Multimedia available online), and (c) S3 (Multimedia available online). The temporal evolution of the vorticity field can be seen in the multimedia.

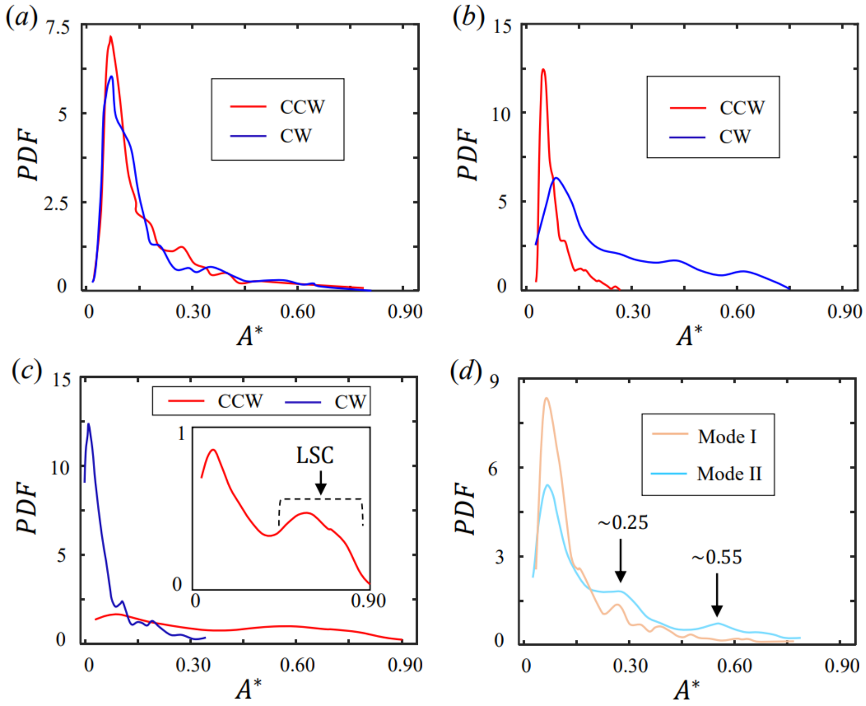

Figure 2-14. Normalized size distribution of the CW and CCW flow rolling structures during (a) S1, (b) S2, (c) S3, (d) two different modes of S1.

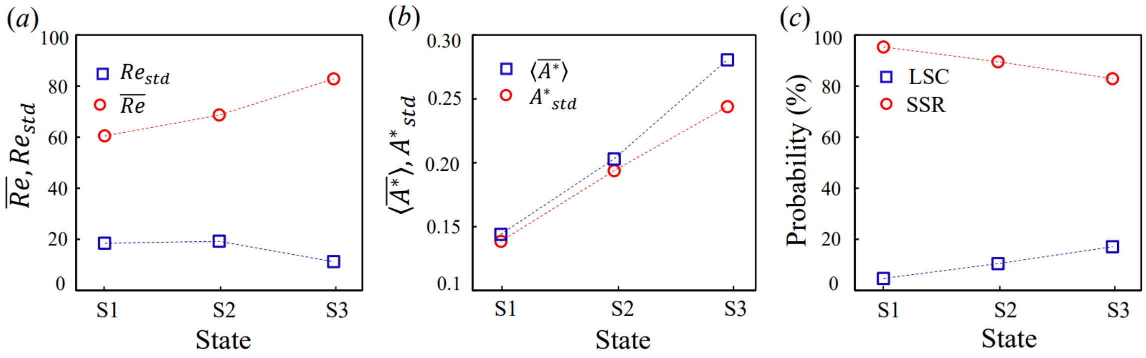

Figure 2-15. (a) Variation of time average Reynolds number, $\overline{Re}$ and its standard deviation, R_{estd} versus the three states. (b) Variation of the temporal and spatial average of the rolling structure size, $\langle\overline{A^*}\rangle$ and its standard deviation, A^*_{std} versus the three states. (c) Variation of the normalized number of the large-scale circulating structure (LSC) and the small-scale rolling structure (SSR) versus the three states of S1, S2, and S3.

The normalized size distributions of the rolling structures of S2 and S3 are shown in Figure 2-14(b) and Figure 2-14(c), respectively. For S2, it can be seen that in comparison to S1, the CW rolling structures are shifted from small rolling structures to larger ones. However, CCW rolling structures are shifted to the smaller scale rolling structures and no LSC is present since $A^* < 0.3$. For S3, the same scenario occurs, but in the reverse direction. CCW rolling structures have a bimodal distribution characterizing the formation of the LSC (Figure 2-14(c)). The CW rolling structures distribution is also similar to the CCW rolling structures of S2 all in the small-scale range $A^* < 0.5$. By investigating the evolution of kinetic energy-based Reynolds number [20] of S1, $Re \equiv H\overline{\langle V^2 \rangle}/\nu$, where $\langle\cdot\rangle$ denotes the spatial average, as is shown in Figure 2-16, it can be observed that the flow is divided in two different modes with high variation (Mode 1) and low variation (Mode 2) based on a threshold of the squared coefficient of variance of Reynolds number, $SCV \equiv \sum_{i=1}^{N}(Re_i - \overline{Re})^2/(N-1)\overline{Re}^2 = 10\ \%$ where Re is the temporal average Reynolds number and N is the number of instances. The variation of SCV is depicted in Figure 2-17 highlighting the 10 % threshold. As can be seen in this figure, the kinetic energy-based Reynolds number variation decreases over time which highlights the regime after the start of the convection. Though, the 10 % threshold is a common criterion to define a statistically low variation dividing this regime, S1 into two modes. The normalized size distribution of the rolling structures of these two modes, Figure 2-14(d) indicates a shift from the peak at $A^* \approx 0.05$ in Mode 1 to larger rolling structures at $A^* \approx 0.25$ and $A^* \approx 0.55$ in Mode 2 showing a growth in the size of the rolling structures stepping forward in time. This growth in the size of the rolling structure after the start of the convection indicates the first steps in the formation of the larger rolling structure developing the LSC.

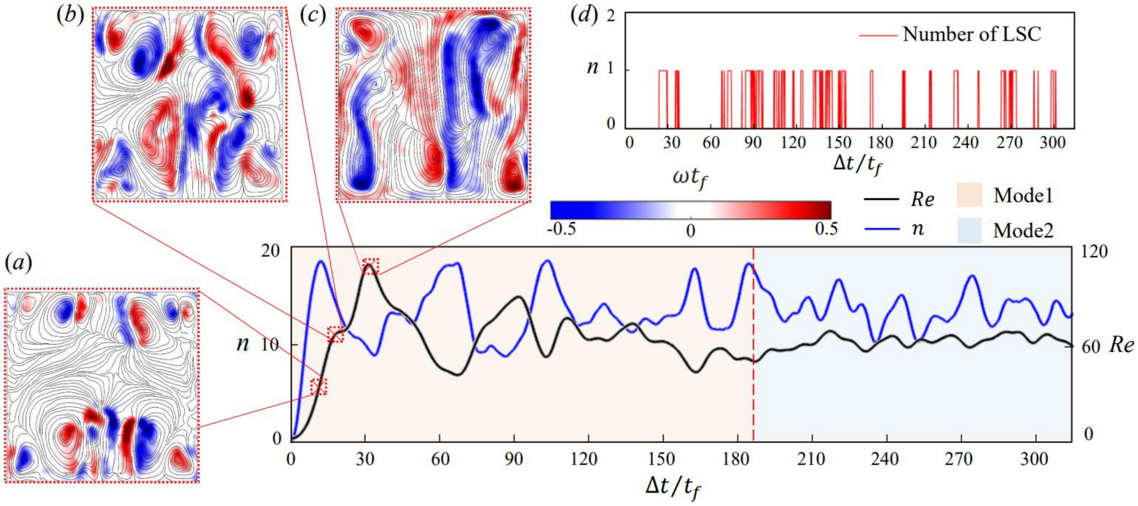

Figure 2-16. A plot of the Reynolds number (black line), Re, and the number of the rolling structures (blue line), n, versus the dimensionless time interval, $\Delta t/t_f$, after the start of convection, S1. The dashed red line at $\Delta t/t_f = 190$ divides the plot into two modes with high variation (light red region), Mode 1 and low variation (light blue region), Mode 2 based on the threshold of the squared coefficient of variance of Reynolds number, $V = 10\ \%$. Contours show the vorticity field at (a) $\Delta t/t_f \approx 8$ (b) $\Delta t/t_f \approx 16$ (c) $\Delta t/t_f \approx 31$. (d) Plot of the variation of the number of the LSC during the first state, S1.

For all three states, the temporal average Reynolds number, $\overline{Re}$ and temporal and spatial average of the rolling structures size, $\langle\overline{A^*}\rangle$ and their standard deviation, Re_{std} and A^*_{std} are shown in Figure 2-15(a) and (b). As can be seen, moving to higher states leads to an increase in Reynolds number, $\overline{Re}$ which also occurs with the increase in the size of the rolling structures, $\langle\overline{A^*}\rangle$. The deviation of the Reynolds number, Re_{std} is lower for higher states while it is higher for the size of the rolling structures, A^*_{std} due to the growth of the rolling structures in one direction and shrink in the other direction. Figure 2-15(c) also indicates the growth in the number of the LSC and the decrease in the number of the small-scale rolling structures by moving from S1 to S3. As can be seen in this figure, the probability of the formation of the large-scale flow rolling structure is almost zero which is consistent with the observation of the size distribution of the rolling structures shown in Figure 2-14(a).

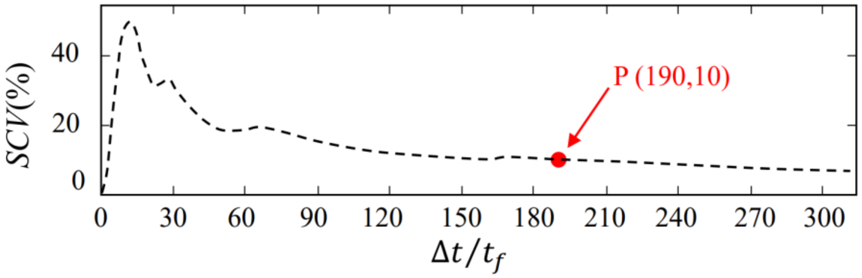

Figure 2-17. Temporal variation of the squared coefficient of variance of Reynolds number SCV of the first state, S1. Highlighted point at $\mathrm{P}(190{,}10)$ indicates the point in which the SCV reach to $10\ \%$.

To investigate the correlation between the number of rolling structures and the momentum transfer, the temporal evolution of kinetic energy-based Reynolds number is calculated as suggested by [20]. In that work it was shown that the variation of this Reynolds number has a direct correlation with the heat transfer, hence it can highlight the effect of the number of rolling structures on the overall energy transferred to the system. Variation of the number of rolling structures, n, and the Reynolds number, Re during S1 is plotted in Figure 2-16. In this figure it can be seen that from the start of convection, both the Reynolds number and the number of the rolling structures start rising and reach a local maximum value. This initial period sees the rise and fall of the primary thermal plumes that develop into the primary rolling structures of the flow as is shown in Figure 2-16(a) by the vorticity field at $\Delta t/t_f \approx 8$. The first peak of the Reynolds number and the number of the rolling structures occurs in the vicinity of $\Delta t/t_f = 16$. From the vorticity field at this time, depicted in Figure 2-16(b), it can be seen that the first maximum peak is when the hot and cold thermal plumes first collide. Beyond this time, after the first peak, in the vicinity of $\Delta t/t_f = 31$ the Reynolds number and the number of the rolling structures reach their maximum and minimum value respectively during the whole S1. The vorticity field for this can be seen in Figure 2-16(c), showing a smaller number of rolling structures in comparison to the very beginning of the start of convection, $\Delta t/t_f < 31$.

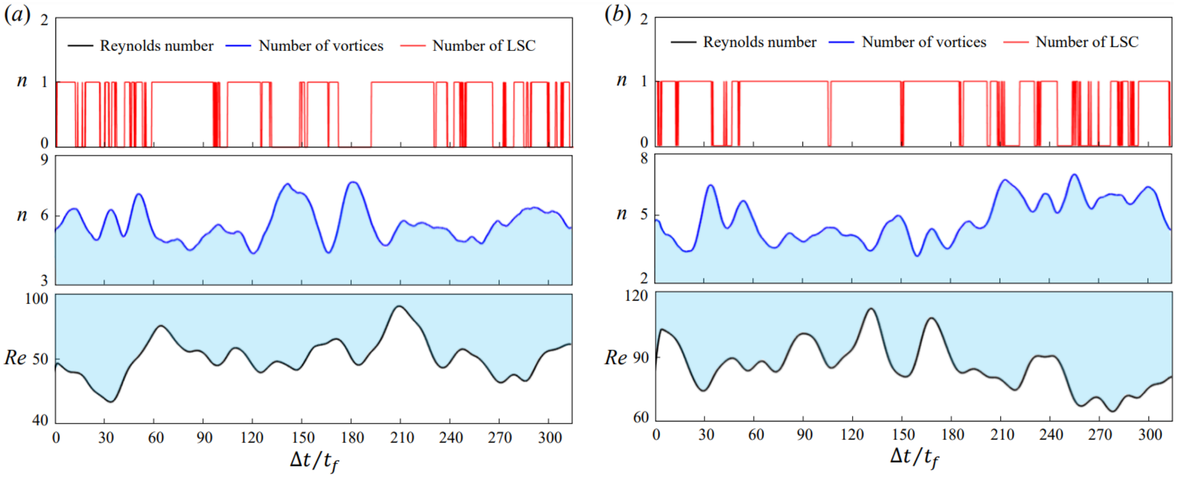

Figure 2-18. Plot of the variation of the number of LSC, number of rolling structures, and Reynolds number, for (a) S2 and (b) S3. The areas with light blue colour in $n - \Delta t/t_f$ and $Re - \Delta t/t_f$ are highlighted for better visualization of these two plots.

From Figure 2-16(d) which is a binary plot showing the formation of LSC during S1 it can be seen that the formation of LSC or a rolling structure larger than the half area of the convection cell occurs rarely, with the probability of $P = 17$ %. Here, the probability, P is defined as the total life time of the LSC to the total time of the experiment. In the vicinity of $\Delta t/t_f = 31$ in Figure 2-16(d) the formation of LSC can be observed, however, for this state, the mean size of the LSC is found to be $A^*_{std} = 0.56$, close to the defined threshold for detecting an LSC. In Figure 2-16(c) it can also be seen that although larger rolling structures are formed compared to the beginning, $\Delta t/t_f < 31$ the flow structure at this instant is quite different from the LSC formed at the center of the enclosure in S2 or S3.

Table 2-2. Correlation, cross-correlation function, and de- lay time of the cross-correlation of the two signal of kinetic energy-based Reynolds number and number of the rolling structures for the investigated regimes of S1, S2, and S3.

	S1 Mode1	S1 Mode2	S2	S3
$P(\%)$	17	17	45	77
$\lvert C_\rho \rvert$	0.48	0.43	0.31	0.44
$\lvert C_\tau \rvert$	0.96	0.95	0.90	0.91
τ	0	0	0	0

By comparing the signals of the Reynolds number and the number of rolling structures in Figure 2-16, an inverse correlation between these two signals can be observed. This is more observable for Mode 1 where the variation in these two signals is more significant. To identify the connection between the signals of Reynolds number and the rolling structures number, the correlation coefficient of these two signals is calculated and it is found to be $C_\rho = 0.48$ for Mode1 and $C_\rho = 0.43$ for Mode2 indicating the strength of the inverse correlation between Re and n signals. The maximum value for normalized cross-correlation, C_τ of these two signals as is shown in Figure 2-19(a) and (b) is also equal to $C_\tau = 0.96$ and $C_\tau = 0.95$ for Mode1 and Mode2, respectively. The delay time for both modes of S1 was found to be $\tau \approx 0$ showing zero delay between the correlation of the signals of Reynolds number and number of the rolling structures.

In previous works that the effect of the number of the LSC on the momentum and heat transfer of RBC was indicated, the enclosure had an aspect ratio $\Gamma < 1$, which leads to the formation of multiple LSC's in a time instant [20]. However, in the current case, the flow is developing in an enclosure with unit aspect ratio and based on the defined threshold and previous qualitative definition of the LSC [2], the formation of only one LSC is possible at each time instant. Figure 2-18(a) and (b) show the binary plots of the formation of LSC during S2 and S3 respectively. In comparison to S1, it can be seen that the probability of the formation of LSC during S2 and S3 is significantly higher and equal to $P = 45\ \%$ and $P = 77\ \%$ respectively. However, the plot does not provide any information on its effect on the momentum transfer evolution represented by Reynolds number, Re depicted in Figure 2-18. For these two states the evolution of the total number of the rolling structures, n instead of only LSC is plotted and shown in Figure 2-18. Similar to S1, a general inverse correlation can be observed between the two signals of Re and n. The correlation coefficient, C_ρ of these two signals is equal $C_\rho = 0.31$ and $C_\rho = 0.44$ for S2 and S3 respectively. Similar to S1, as is shown in Figure 2-19(c) and (d), the delay time for this correlation is equal to $\tau \approx 0$, obtained from the optimum cross-correlation of $C_\tau = -0.90$ and $C_\tau = -0.91$ for S2 and S3, respectively.

The probability of the formation of the LSC or a rolling structure larger than the half-area of the convection cell is summarized in Table 2-2 for the start of the convection, S1 (including both modes) and for the developed states of S2 and S3. Comparing all three states, it can be seen that the temporal development of the flow leads to an increase in the probability of the formation of LSC, however, in the developed regimes such as S2 and S3 in the case of NOB RBC and high Prandtl number, the formation of LSC is interrupted by high energy thermal plumes which leads to the formation of small-scale, flow rolling structures. Looking into the correlation between the total number of rolling structures and the Reynolds number which is summarized in Table 2-2, a moderate inverse correlation could be observed for all the states from the beginning of the convection to the developed states of S2 and S3. It can be seen that the inverse correlation is stronger for the S1 in which small-scale rolling structures are dominant. However, for the two other states, the correlation stays in the same order highlighting the formation and role of small-scale rolling structures in momentum transfer.

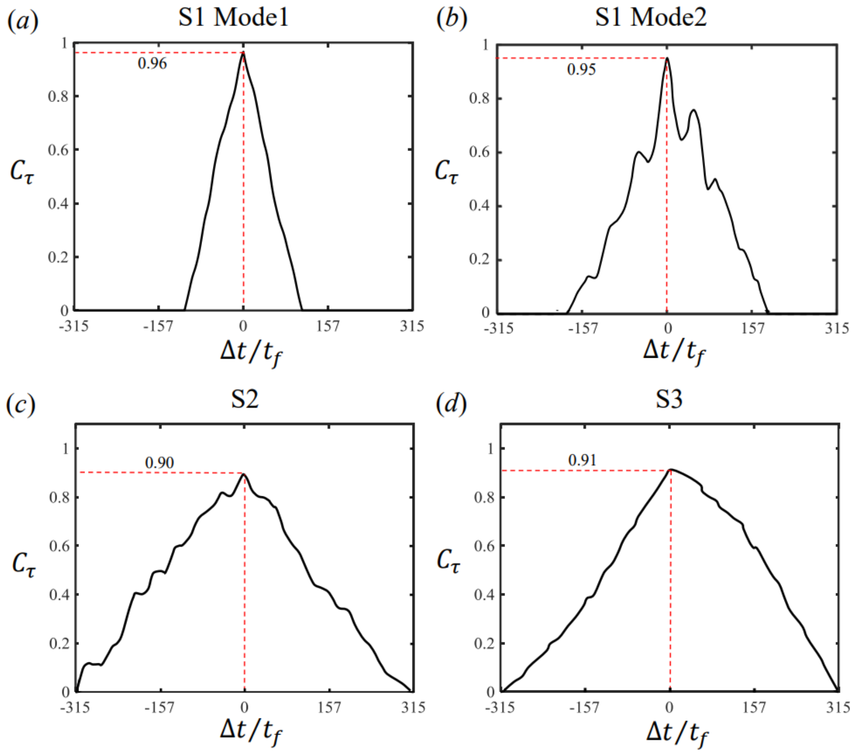

Figure 2-19. Cross-correlation function between the signal of the kinetic energy-based Reynolds number and the number of the rolling structures for states of (a) S1 Mode1, (b) S1 Mode2, (c) S2, and (d) S3.

2.4 Conclusion

An experimental study on the formation of flow rolling structures in a turbulent non-Oberbeck-Boussinesq (NOB) Rayleigh-Bénard convection (RBC) with $Pr = 7$, and $Ra = 5.3 \times 10^7$ and an aspect ratio of $\Gamma = 1$ was reported. The first goal of this work was to evaluate the formation of the flow rolling structures after the start of convection and compare them with the rolling structures formed during the flow states after the establishment of the coherent LSC. It was identified that in contrast to developed states, the probability of the formation of the large-scale rolling structures is quite low, less than $17\ \%$ and only $4.7\ \%$ of the rolling structures are large-scale during S1. It was also found that both CW and CCW rolling structures have the same size distribution and vortex-pair formation was a frequent phenomenon in this state. For the two other states, in which LSC is a dominant flow structure with the formation probability of $45\ \%$ and $77\ \%$, it was shown that a large number of rolling structures are small scale, $89.5\ \%$ and $82.9\ \%$ was still present. The second goal of this work was to identify the connection between the number of rolling structures with the kinetic energy-based Reynolds number. By considering the total number of rolling structures, an inverse correlation was found between the total number of the rolling structures and the kinetic-based Reynolds number for all the three investigated states showing the role of small-scale rolling structures in momentum transfer in turbulent Rayleigh-Bénard convection with relatively high Prandtl number. The effect of the small-scale rolling structures on the momentum transfer provides a new insight into the role of these structures in turbulent RBC specifically, in the conditions where the small-scale rolling structures are dominant, such as high temperature difference and high Prandtl numbers. Further investigations on the influence of small-scale rolling structures can lead to the development of new methods in heat transfer enhancement and flow control.

References

[1] A. Bejan, Convection Heat Transfer (*John Wiley & Sons*, 2013).

[2] G. Ahlers, S. Grossmann, and D. Lohse, Heat transfer and large-scale dynamics in turbulent Rayleigh-Bénard convection, *Reviews of Modern Physics* 81, 503 (2009).

[3] T. Meuel, M. Coudert, P. Fischer, C.-H. Bruneau, and H. Kellay, Effects of rotation on temperature fluctuations in turbulent thermal convection on a hemisphere, *Scientific Reports* 8, 1 (2018).

[4] M. Krishnan, V. M. Ugaz, and M. A. Burns, PCR in a Rayleigh-Bénard convection cell, *Science* 298, 793 (2002).

[5] D. Khodakov, J. Li, J. X. Zhang, and D. Y. Zhang, Highly multiplexed rapid DNA detection with single-nucleotide specificity via convective PCR in a portable device, *Nature Biomedical Engineering* 5, 702 (2021).

[6] O. Shishkina, Rayleigh-Bénard convection: The container shape matters, *Physical Review Fluids* 6, 090502(2021).

[7] G. Ahlers, E. Bodenschatz, R. Hartmann, X. He, D. Lohse, P. Reiter, R. J. Stevens, R. Verzicco, M. Wedi, S. Weiss, et al., Aspect ratio dependence of heat transfer in a cylindrical Rayleigh-Bénard cell, *Physical Review Letters* 128, 084501 (2022).

[8] H. D. Xi, S. Lam, and K. Q. Xia, From laminar plumes to organized flows: the onset of large-scale circulation in turbulent thermal convection, *Journal of Fluid Mechanics* 503, 47 (2004).

[9] R. Krishnamurti and L. N. Howard, Large-scale flow generation in turbulent convection, *Proceedings of the National Academy of Sciences* 78, 1981 (1981).

[10] J.-Q. Zhong and G. Ahlers, Heat transport and the large- scale circulation in rotating turbulent Rayleigh-Bénard convection, *Journal of Fluid Mechanics* 665, 300 (2010).

[11] H.-D. Xi and K.-Q. Xia, Flow mode transitions in turbulent thermal convection, *Physics of Fluids* 20, 055104 (2008).

[12] R. Hartmann, K. L. Chong, R. J. Stevens, R. Verzicco, and D. Lohse, Heat transport enhancement in confined Rayleigh-Bénard convection feels the shape of the container, *Epl* 135, 10.1209/0295-5075/ac19ed (2021).

[13] G. Ahlers, S. Grossmann, and D. Lohse, Heat transfer and large-scale dynamics in turbulent Rayleigh-Bénard convection, *Reviews of modern physics* 81, 503 (2009).

[14] D. Funfschilling, E. Brown, A. Nikolaenko, and G. Ahlers, Heat transport by turbulent Rayleigh-Bénard convection in cylindrical samples with aspect ratio one and larger, *Journal of Fluid Mechanics* 536, 145 (2005).

[15] A. Nikolaenko, E. Brown, D. Funfschilling, and G. Ahlers, Heat transport by turbulent Rayleigh-Bénard convection in cylindrical cells with aspect ratio one and less, *Journal of Fluid Mechanics* 523, 251 (2005).

[16] C. Sun, L.-Y. Ren, H. Song, and K.-Q. Xia, Heat transport by turbulent Rayleigh-Bénard convection in 1 m diameter cylindrical cells of widely varying aspect ratio, *Journal of Fluid Mechanics* 542, 165 (2005).

[17] S. Weiss and G. Ahlers, Effect of tilting on turbulent convection: cylindrical samples with aspect ratio, *Journal of Fluid Mechanics* 715, 314 (2013).

[18] E. P. Van Der Poel, R. J. Stevens, and D. Lohse, Connecting flow structures and heat flux in turbulent Rayleigh- Bénard convection, *Physical Review E* 84, 1 (2011).

[19] E. P. van der Poel, R. J. Stevens, K. Sugiyama, and D. Lohse, Flow states in two-dimensional Rayleigh- Bénard convection as a function of aspect ratio and Rayleigh number, *Physics of Fluids* 24, 085104 (2012), 1206.3823.

[20] L. Zwirner, A. Tilgner, and O. Shishkina, Elliptical instability and multiple-roll flow modes of the large-scale circulation in confined turbulent Rayleigh-Bénard convection, *Physical Review Letters* 125, 54502 (2020).

[21] L. Zwirner and O. Shishkina, Confined inclined thermal convection in low-Prandtl number fluids, *Journal of Fluid Mechanics* 850, 984 (2018).

[22] H. Xia, M. Shats, and G. Falkovich, Spectrally condensed turbulence in thin layers, *Physics of Fluids* 21 (2009).

[23] X. Chen, D. P. Wang, and H. D. Xi, Reduced flow reversals in turbulent convection in the absence of corner vortices, *Journal of Fluid Mechanics* 891, 10.1017/jfm.2020.202 (2020).

[24] Z.-H. Wan, Q. Wang, B. Wang, S.-N. Xia, Q. Zhou, and D.-J. Sun, On non-Oberbeck-Boussinesq effects in Rayleigh-Bénard convection of air for large temperature differences, *Journal of Fluid Mechanics* 889, A10 (2020).

[25] V. Valori, G. Elsinga, M. Rohde, M. Tummers, J. Westerweel, and T. Van Der Hagen, Experimental velocity study of non-Boussinesq Rayleigh-Bénard convection, *Physical Review E* 95, 53113 (2017).

[26] G. Ahlers, E. Brown, F. F. Araujo, D. Funfschilling, S. Grossmann, and D. Lohse, Non-Oberbeck–Boussinesq effects in strongly turbulent Rayleigh–Bénard convection, *Journal of Fluid Mechanics* 569, 409 (2006).

[27] A. D. Demou and D. G. Grigoriadis, Direct numerical simulations of Rayleigh–Bénard convection in water with non-Oberbeck–Boussinesq effects, *Journal of Fluid Mechanics* 881, 1073 (2019).

[28] S. Kashanj and D. S. Nobes, Temperature field of non-Oberbeck–Boussinesq Rayleigh–Bénard convection in a low aspect ratio cell, *Physics of Fluids* 36 (2024).

[29] S. Horn, O. Shishkina, and C. Wagner, On non-Oberbeck–Boussinesq effects in three-dimensional Rayleigh–Bénard convection in glycerol, *Journal of Fluid Mechanics* 724, 175 (2013).

[30] S. Horn and O. Shishkina, Rotating non-Oberbeck–Boussinesq Rayleigh–Bénard convection convection in water, *Physics of Fluids* 26 (2014).

[31] V. Valori, G. Elsinga, M. Rohde, M. Tummers, J. Westerweel, and T. van der Hagen, Experimental velocity study of non-Oberbeck–Boussinesq Rayleigh–Bénard convection, *Physical Review E* 95, 053113 (2017).

[32] V. Valori, G. E. Elsinga, M. Rohde, J. Westerweel, and T. H. van Der Hagen, Particle image velocimetry measurements of a thermally convective supercritical fluid, *Experiments in Fluids* 60, 1 (2019).

[33] M. Bussiére, G. M. Bessa, C. R. Koch, and D. S. Nobes, Application of a combinatorial vortex detection algorithm on 2 component 2 dimensional particle image velocimetry data to characterize the wake of an oscillating wing, *Fluids* 9, 53 (2024).

[34] M. Jiang, R. Machiraju, and D. Thompson, Detection and visualization of, *The visualization handbook* 295 (2005).

[35] I. A. Sadarjoen and F. H. Post, Detection, quantification, and tracking of vortices using streamline geometry, *Computers & Graphics* 24, 333 (2000).

[36] E. Brown and G. Ahlers, Rotations and cessations of the large-scale circulation in turbulent non-Oberbeck–Boussinesq Rayleigh– Bénard convection, *Journal of Fluid Mechanics* 568, 351 (2006).

[37] F. F. Araujo, S. Grossmann, and D. Lohse, Wind reversals in turbulent Rayleigh-Bénard convection, *Physical Review Letters* 95, 084502 (2005).

[38] K. Sugiyama, R. Ni, R. J. Stevens, T. S. Chan, S. Q. Zhou, H. D. Xi, C. Sun, S. Grossmann, K. Q. Xia, and D. Lohse, Flow reversals in thermally driven turbulence, *Physical Review Letters* 105, 1 (2010).

[39] K. Q. Xia, C. Sun, and S. Q. Zhou, Particle image velocimetry measurement of the velocity field in turbulent thermal convection, *Physical Review E* 68, 1 (2003).

[40] K. Sugiyama, E. Calzavarini, S. Grossmann, and D. Lohse, Flow organization in two-dimensional non-Oberbeck-Boussinesq Rayleigh-Bénard convection in water, *Journal of Fluid Mechanics* 637, 105 (2009).

[41] Gray, D.D. and Giorgini, A., 1976. The validity of the Boussinesq approximation for liquids and gases. *International Journal of Heat and Mass Transfer*, *19*(5), pp.545-551.

Chapter 3: Effect of convection cell confinement on the properties of the large-scale circulating structures in Rayleigh-Bénard convection

The influence of lateral confinement of the convection cell on the stability of the LSC of RBC flow is investigated in this chapter. 2D PIV and 3D scanning PIV were applied to measure spatio-temporal characteristics of the LSC within the confined cell. The influence of the lateral confinement on the elliptical instability is also investigated to examine the influence of confinement on suppressing this instability. Experiments were conducted for a convection cell with aspect ratio of $\Gamma = 1/10$ and Rayleigh numbers of $Ra = 2.3 \times 10^7$, 5.6×10^7, and 8.8×10^7 using a working fluid of water.

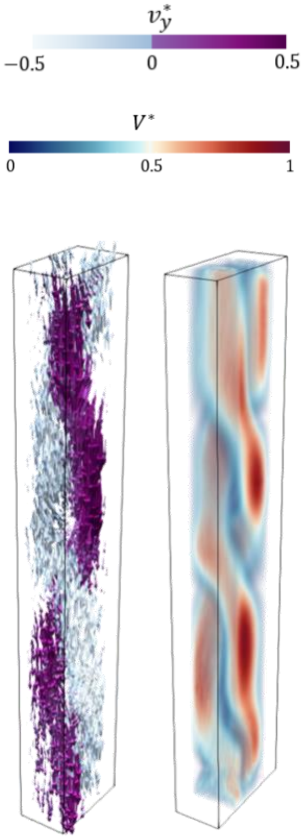

Graphical abstract for Chapter 3

3.1 Introduction

Rayleigh-Bénard convection (RBC) is a thermal driven flow in a geometry heated from below and cooled from above [1]. As a model system, RBC captures the essence of buoyancy-driven flows, where temperature gradients induce complex flow patterns representing a wide range of natural phenomena, including atmospheric circulation, ocean currents, and the Earth's mantle convection, as well as industrial processes like chemical reactors [2]. Rayleigh number, $Ra \equiv ag\Delta TH^3/\nu\kappa$, Prandtl number, $Pr \equiv \nu/\kappa$, and the geometry of the convection cell are the controlling parameters of RBC flow [3]. Large-scale circulation (LSC) is known as one of the most important characteristics of the RBC due to its high impact in heat and momentum transfer [2].

LSC was introduced for the first time by [4] via experimental visualization of the flow structure. Importance of the LSC was highlighted by the recent studies showing the influence of the number of LSC on the heat and momentum transfer [5], [6], [7]. Generally, for a relatively low Prandtl fluid e.g. gaseous flow with $Pr{\sim}0.1$, there is an inverse correlation between the number of LSCs and the heat and momentum transfer [5], [6], [7]. However, for higher Prandtl numbers e.g. water with $Pr{\sim}5$, this correlation is not strong [2], [8]. Our recent work has shown that in a cubical convection cell with $Pr = 7$ and $Ra = 5.3 \times 10^7$ in a cubical convection cell, the inverse correlation exists between the total number of the rolling structures and the momentum transfer.

The shape of the convection cell specially the aspect ratio of the convection cell has been shown that have significant effect on the dynamics of the LSC [3]. Among the shape properties, lateral confinement in two directions has been found to have significant influence on the LSC characteristics [9]. Hence, the impact of lateral confinement on the heat and mass transfer has been the focus of interest in the recent studies revealing sophisticated dynamics of LSC [7]. In a cubic convection cell with the height of H, and the width and depth of W, lateral confinement in two-directions means a low aspect ratio convection cell, $\Gamma < 1$, where aspect ratio is $\Gamma = W/H$. The focus of these studies was on the flow modes based on the number of the LSC formed on top of each other, the duration of each mode, and the heat transport associated to each mode [7]. Based on these studies, it can be concluded that decreasing the aspect ratio of the convection cell i.e., two-directional lateral confinement, can lead to formation of modes with a greater number of LSCs [7], [10].

In a recent study, Zwiner et al. [7] within a convection cell with the aspect ratio of $\Gamma = 1/5$, $Pr = 0.1$, and $Ra = 10^6$ both twisting and sloshing states were observed temporally evolving during $\Delta t/t_f = 350$ forming sloshing regimes with up to 4 LSCs. They proposed that the formation of multiple LSCs is driven by an elliptical instability, which disrupts the single LSC, leading to the emergence of several LSCs stacking vertically. Their work was groundbreaking, as it involved the first detailed investigation of the formation and evolution of LSCs in low-aspect-ratio convection cells using 3D direct numerical simulations (DNS). This approach enabled the clear distinction between twisting and sloshing regimes, while also proposing a dynamic mechanism for the formation of multiple stacked rolls within the convection cell. The effect of the two-directional lateral confinement has been focusing of many recent studies conducting numerical simulation [10], [10]. However, there only few experimental studies focusing on the LSC dynamics in a confined convection cell [11] and there is not any experimental observation of 3D flow structure of the lateral confined RBC flow.

In this letter, we explore the flow structure of RBC within a cubical convection cell confined severely in two-direction with the aspect ratio of $\Gamma = 1/10$ and Prandtl number of $Pr = 6.3$ i.e. working fluid of water. To see the effect of Rayleigh number, experiments were carried out for three Rayleigh numbers of $Ra = 2.3 \times 10^7$, 5.6×10^7, and 8.8×10^7. The elliptical instability also has been investigated to examine the proposal of Zwiner et al. [7] associating the sloshing regime to the existence of the elliptical instability. The experimental observations of the spatiotemporal characteristics of the LSC within confined convection cell was captured by times resolved 2D particle image velocimetry (PIV) for a relatively long time of $\Delta t = 1300$ from the start of the convection and the developed flow has been captured in 3D using a scanning PIV approach.

3.2 Experimental approach

The convection cell of this work had a square cross-section with the width and depth, $W = 5$ mm, and height, $H = 50$ mm making a convection enclosure with the aspect ratio of $\Gamma = 1/10$. The boundary condition was set to temperature constant at the top, T_C and bottom, T_H and the Rayleigh number were set by changing the temperature difference, $\Delta T = T_H - T_C$. Sidewalls were in adiabatic condition, $\partial T/\partial x = \partial T/\partial y = 0$. Although there are numerous studies using 2D particle image velocimetry (PIV) to investigate the flow properties of RBC, the 3D investigations are very limited. [12] showed the possibility of the 3D investigation of RBC using time-resolved 3D particle tracking velocimetry (PTV). [13] also used the 3D tomographic PIV for the first time to study the physics of the RBC flow within a cylindrical convection cell with the aspect ratio of $\Gamma = 1/2$ and $Ra = 10^8$ and $Pr = 5.3$. Using proper orthogonal decomposition (POD) they identified evolution of the different flow modes including sloshing and twisting. We used a 3D scanning PIV approach for this study. The low aspect ratio and the small size of the convection cell makes the 3D measurement of the flow challenging using multiple cameras and measuring the whole flow field. Here we used a single camera and scanned the whole flow domain by a laser sheet allowing us to calculate the out of plane velocity component and reconstruct the 3D flow field. The details of this approach can be seen in the Movie1 in the supplementary materials. Using the scanning approach in a previous work we measured the temperature field of the convection cell which can be seen in [14].

3.3 Properties of different flow modes

In the context of RBC flow with Rayleigh numbers in the range $10^7 < Ra < 10^8$, we typically expect unsteady, turbulent flow regimes [15], [16]. These regimes are often characterized by chaotic fluctuations in both the velocity and temperature fields [16]. However, in this study, the convection cell's aspect ratio, $\Gamma = 1/10$, introduces significant lateral confinement, which modifies the flow dynamics compared to unconfined or higher aspect ratio systems. This lateral confinement restricts horizontal motion, compressing the LSC that would typically span the width of the cell [17]. In Figure 3-1(a), to (b) the evolution of the vertical, $\langle u_z^2 \rangle_{x,z}/u_f^2$ and horizontal velocity, $\langle u_x^2 \rangle_{x,z}/u_f^2$ components for $Ra = 2.3 \times 10^7$, 5.6×10^7, and 8.8×10^7clearly demonstrates the transition between different flow regimes over time. Here, $\langle \cdot \rangle_s$ denotes the spatial average along the arbitrary direction i.e. s while u_f indicates the free-falling velocity, $u_f = \sqrt{\alpha g \Delta T h}$. Initially, there is a rapid increase in the vertical velocity component, indicating the formation of strong vertical plumes as buoyancy forces dominate. This peak is followed by a gradual stabilization, where the flow transitions to a steadier regime. For higher Rayleigh numbers, the horizontal velocity remains largely suppressed due to lateral confinement, while the vertical velocity continues to dominate, reflecting the system's tendency to form vertically aligned structures. The timing of the peak and subsequent stabilization, is driven by the interaction between buoyancy forces and viscous damping. The confinement effectively suppresses lateral turbulence, allowing for a more regular, quasi-steady to persist beyond the initial transition. The dominant vertical motion of the flow is consistent with the previous observations in [18] where formation of single strong thermal plumes was reported.

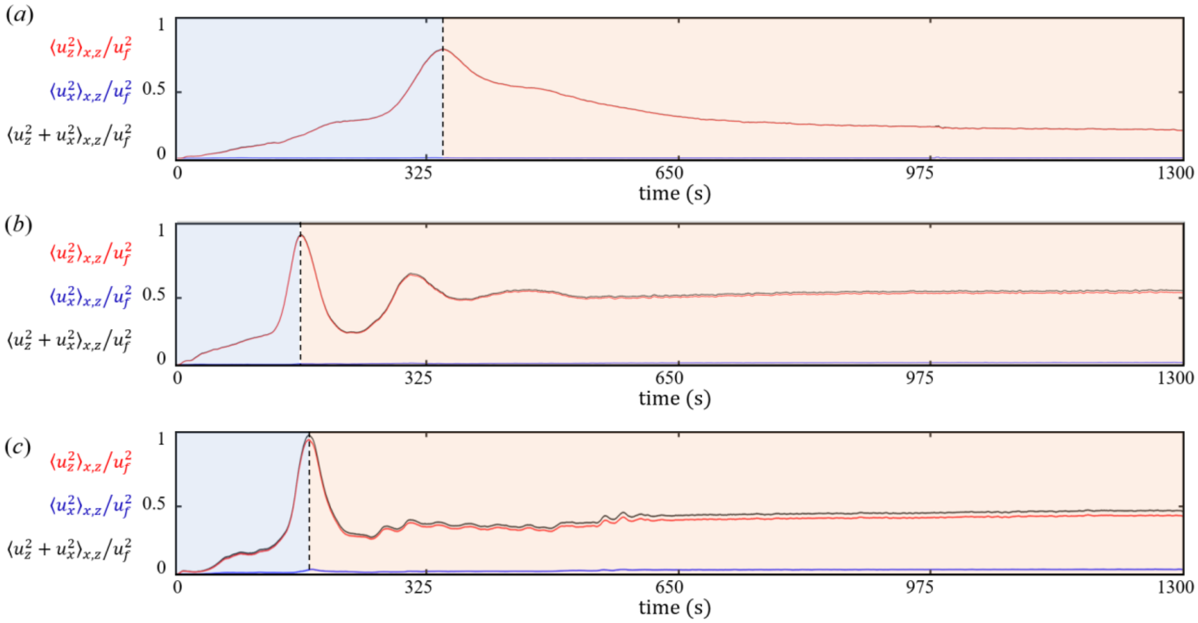

Figure 3-1. Evolution of three velocity components normalized by the free-fall velocity, i.e., vertical velocity $\langle u_z^2\rangle_{x,z}/u_f^2$, horizontal velocity, $\langle u_x^2\rangle_{x,z}/u_f^2$, and velocity magnitude $\langle u_z^2+u_x^2\rangle_{x,z}/u_f^2$ over period of $t = 1300$ s. Rayleigh number is varying from (a) $Ra = 2.3\times10^7$, (b) 5.6×10^7, and (c) 8.8×10^7. Movie 3 in the supplementary material indicates the temporal development this plot along with the 2D temporal evolution of the velocity and relevant properties for the three investigated Rayleigh number.

The autocorrelation function of the vertical velocity, $C(\tau)$ which is listed in Table 3-1, shows that for all the three Rayleigh numbers, flow reach to a quasi-steady state after around $\tau\sim650$ s considering an autocorrelation criterion of $C(\tau) = 10^{-1}$. During the quasi-steady state for each Rayleigh number the coefficient of variation of both horizontal and vertical velocity is listed in Table 1, as $\sigma_{u_x}/\langle u_x\rangle_{x,z,t}$ and $\sigma_{u_z}/\langle u_z\rangle_{x,z,t}$, where σ_u is the standard deviation of the velocity and $\langle u\rangle_{s,t}$ is the spatiotemporal mean of the velocity. As can be seen, the coefficient of variation for all the three Rayleigh numbers is very low, i.e. $\sigma_{u_x}/\langle u_x\rangle_{x,z,t} \ll 1$ and $\sigma_{u_z}/\langle u_z\rangle_{x,z,t} \ll 1$, indicating small variation in both horizontal and vertical velocity. It is worth noting that although for $Ra1$ the velocity fluctuations are lower than the two other Rayleigh numbers, it takes more time $\tau > 725$ s for this state to reach to the quasi-steady state. Although the velocity fluctuations are very small, looking to the study of the temperature field of the same phenomena with the same controlling parameters, i.e. Rayleigh number, Prandtl number, and aspect ratio of the convection cell, it can be seen that flow is driven by the constant generation of the thermal plumes which is the source to the temperature and flow fluctuations [18].

The 3D flow structure for the quasi-steady state of each Rayleigh number is reconstructed and shown in Figure 3-2. In this figure, the velocity vectors and magnitude for Rayleigh numbers increasing from left to right demonstrate a progression in the complexity of the LSC structures in the Rayleigh-Bénard convection cell. At lower Rayleigh numbers i.e. Figure 3-2(a), the flow is dominated by a single LSC with minimal twisting, indicating a relatively stable and coherent flow regime. As the Rayleigh number increases, we observe a gradual introduction of twisting within the LSC, with multiple twists up to a double-twist mode in the highest Rayleigh number case, i.e. $Ra3$ indicating more complex, vertically elongated structures. The increase in the number of twists with Rayleigh number can be attributed to the intensifying buoyancy forces by higher temperature gradient, which drive stronger thermal plumes which was confirmed earlier in [18]. As the Rayleigh number increases, the turbulent kinetic energy in the system grows, resulting in the destabilization of the flow structure. This leads to the formation of more complex and vertically elongated twisting regimes, where the flow patterns exhibit stronger vertical alignment due to the lateral confinement of the convection cell. At higher Rayleigh numbers, the increasing shear and thermal gradients amplify the vertical velocity components, promoting the development of these twist-dominated structures.

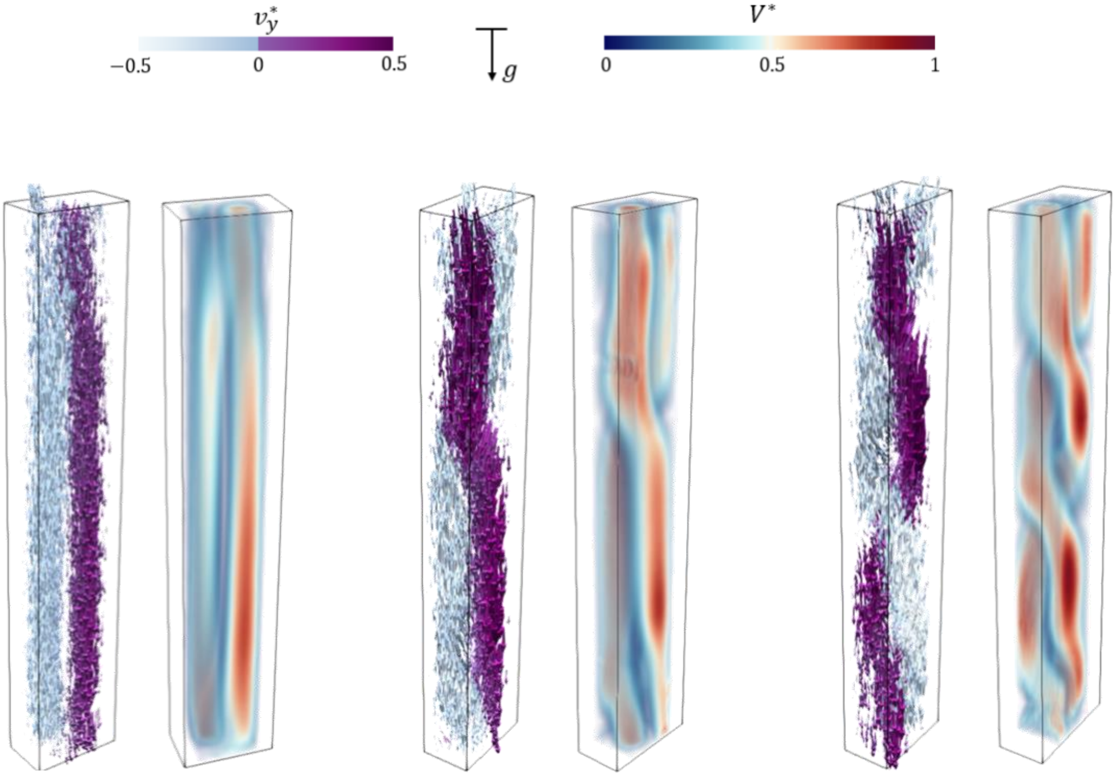

(a) (b) (c)

Figure 3-2. Velocity vectors and velocity magnitude of the mean velocity during the quasi-steady state for (a) $Ra = 2.3 \times 10^7$, (b) 5.6×10^7, and (c) 8.8×10^7. The in-depth variation of the flow properties is depicted for more information in Movie 2 in the supplementary materials.

The competition between buoyancy forces and viscous damping typically results in strong, turbulent plumes rising from the heated base and descending from the cooled top. In this laterally confined setup, the formation of lateral plumes is suppressed, promoting the development of vertical structures (see Figure 3-1), which exhibit regular, though complex, twist-like features (see Figure 3-2). This suppression of lateral instability likely explains the system's more stable, quasi-steady-state behavior post-transition, despite the high Rayleigh numbers that would otherwise lead to fully unsteady, turbulent convection as described theoretically and numerically by [9]. The lateral confinement effectively introduces order to these high-Rayleigh number flows, allowing for the persistence of steady and structured twisting regimes.

3.4 Twisted regime and restriction of elliptical instability

In Figure 3-3, we observe the vertical profiles of both horizontal and vertical velocity components, as well as the enstrophy distribution, for increasing Rayleigh numbers. The red curves represent the horizontal velocity component $\left\langle u_x^2 + u_y^2 \right\rangle_x / u_f^2$, the black curves represent the vertical velocity component $\langle u_z^2 \rangle_x / u_f^2$, and the blue curves represent the enstrophy $\left\langle \omega_x^2 + \omega_y^2 \right\rangle_x / \omega_f^2$, which is a measure of vorticity magnitude, indicating the intensity of rotational motion within the flow. At the lowest Rayleigh number, Figure 3-3(a) both the horizontal (red) and vertical (black) velocity profiles are predominantly concentrated near the top and bottom of the convection cell. The vertical velocity shows a clear dominance, with higher magnitude compared to the horizontal component. This is typical of a low Rayleigh number regime where convection is still relatively weak, and the flow is largely vertical, driven by the buoyant forces acting on the fluid. The enstrophy (blue curve) is minimal, reflecting the low level of rotational motion.

Table 3-1. Flow properties for the three investigated Rayleigh numbers of $a1 = 2.3 \times 10^{7}$, $Ra2 = 5.6 \times 10^{7}$, and $Ra3 = 8.8 \times 10^{7}$.

	$Ra1$	$Ra2$	$Ra3$
$C(\tau)$	10^{-1}	10^{-1}	10^{-1}
$\tau(\mathrm{s})$	725	662	643
$\sigma_{u_x}/\langle u_x\rangle_{x,z}$	10^{-6}	10^{-4}	10^{-3}
$\sigma_{u_z}/\langle u_z\rangle_{x,z}$	10^{-4}	10^{-3}	10^{-2}
$\langle Re\rangle_t$	161	326	305
$\left\langle \omega_x^2 + \omega_y^2\right\rangle_t/\omega_f^2$	0.32	0.41	0.46
σ	0.54	0.64	0.68
σ_d	0.40	0.40	0.40

As the Rayleigh number increases, the horizontal velocity component begins to increase significantly, with the profile showing deviations from the cell boundaries. The vertical velocity component, while still dominant, also exhibits more structure, suggesting the development of vertical plumes and enhanced convective rolls. The enstrophy profile also increases, indicating the formation of more intense rotational motion as the twisted regime develops. This is characteristic of the transition from a single roll to multiple roll flow structure. However, as described by [7], the roll can be defined separated indicating the sloshing regime when $\left\langle u_x^2 + u_y^2\right\rangle_x/u_f^2 = \langle u_z^2\rangle_x/u_f^2$. As can be seen in Figure 3-3(a) and (b) the values of horizontal and vertical velocity approach each other, yet they are far from equal indicating the twisting mode instead of a sloshing one. Furthermore, the increase in the horizontal velocity (red curve) by increasing the Rayleigh number, indicates the presence of multiple twisting modes within the flow, consistent with the earlier observation of multiple LSC twists in the velocity vector plots. The vertical velocity (black curve) similarly shows increased complexity, with relatively strong peaks. The enstrophy (blue curve) increases, with more oscillations and higher values throughout the cell, indicating the development of strong vorticity and rotational motion as the mean values are listed in Table 3-1. This is expected as higher Rayleigh numbers drive more intense thermal plume convection, leading to the twist of coherent structures i.e. LSC.

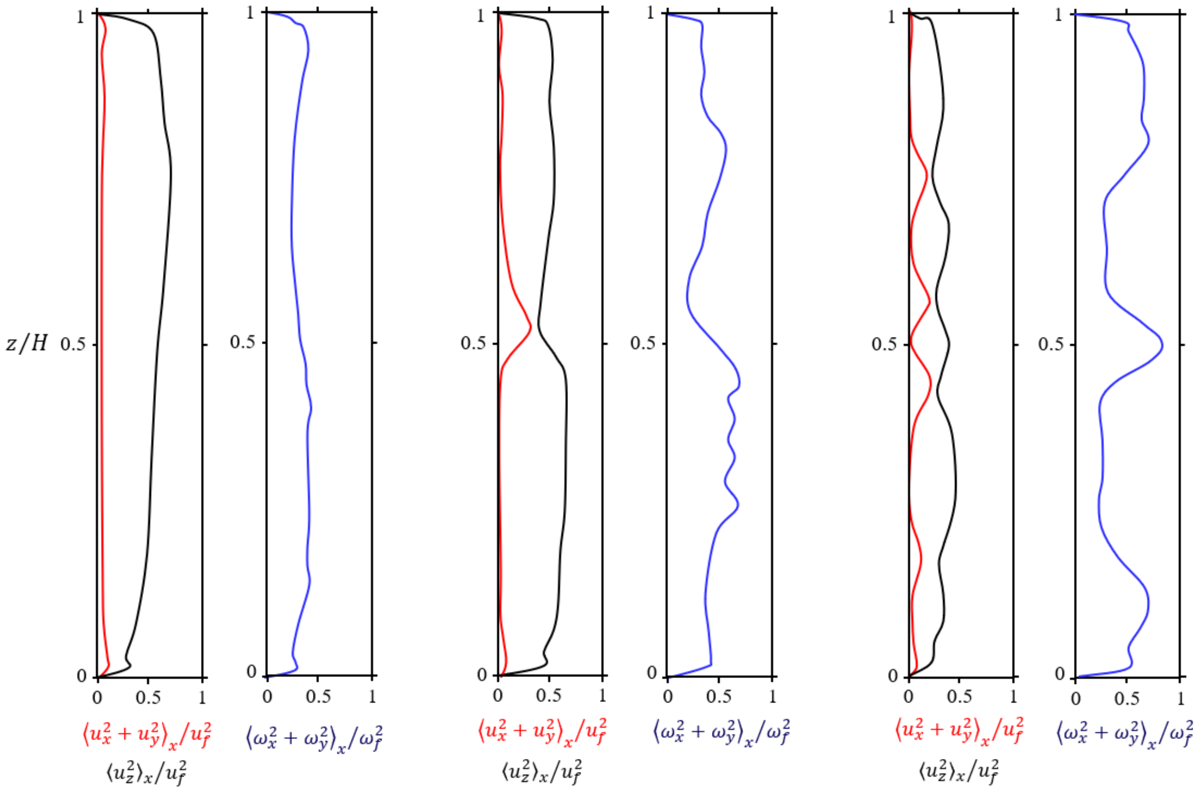

(a) (b) (c)

Figure 3-3. For three Rayleigh numbers of (a) $Ra = 2.3 \times 10^7$, (b) 5.6×10^7, and (c) 8.8×10^7, this figure is showing the horizontal velocity magnitude, $\langle u_x^2 + u_y^2\rangle_x/u_f^2$, in comparison with the vertical velocity $\langle u_z^2\rangle_x/u_f^2$. $\langle \omega_x^2 + \omega_y^2\rangle_x/\omega_f^2$ is also showing the enstrophy profile all along the vertical axis spatially averaged along the horizontal plane i.e. $x - y$.

Formation of the steady LSC within the laterally confined convection cell suggests that the elliptical insatiability that is responsible for the sloshing regime and formation of separated vertically stacked rolling structure is damped by the severe confinement. The comparison of the growth rate i.e. $\sigma \sim \varepsilon\omega/2H$ where ε represents the ellipticity of the flow rolling structure, with the damping rate i.e. $\sigma_d \sim \nu/H^2$ demonstrate the suppression of the elliptical instability [19]. As is listed in Table 1, for all the three Rayleigh numbers, it can be seen that the growth rate and the damping rate are at the same order. However, elliptical instability will occur when $\sigma \gg \sigma_d$ [7]

3.5 Conclusion

This chapter provided a comprehensive experimental analysis of Rayleigh-Bénard convection in a laterally confined cell with an aspect ratio of $\Gamma = 1/10$, across Rayleigh numbers ranging from $Ra = 2.3 \times 10^7$, 5.6×10^7, and 8.8×10^7. The results highlight how lateral confinement strongly influences the flow behavior, particularly by damping the typical elliptical instabilities that would otherwise break up the large-scale circulation (LSC) into multiple sloshing modes in an unconfined or moderately confined system. Instead, the confinement promotes the formation of a prolonged twisting regime, where the flow remains vertically dominant with limited lateral motion. At lower Rayleigh numbers, the flow is primarily vertical with a single LSC. As the Rayleigh number increases, the flow preserves the single LSC, but with the number of twists in the LSC increasing as buoyancy forces become stronger. This gradual increase in twists is driven by the amplification of turbulent plumes and vertical shear, constrained by the lateral boundaries. The suppression of lateral instability and sloshing allows the flow to evolve into a more structured, yet highly dynamic, state where twisting dominates. The velocity profiles and enstrophy further demonstrate the increased rotational motion of the flow at higher Rayleigh numbers. These findings emphasize the critical role of geometric confinement in shaping the large-scale circulation topology within the Rayleigh-Bénard convection. By preventing the onset of sloshing and facilitating the emergence of a prolonged twisting regime, suggesting the formation of unsteady turbulent regimes in much higher Rayleigh numbers. Besides the many controlling applications that this physics represents, this physics is important since it also suggest formation of ultimate regime in much higher Rayleigh numbers comparison with the RBC flow in regular enclosures.

References

[1] B. Adrian, CONVECTION HEAT TRANSFER. John Wiley and Sons, Inc, 2013.

[2] G. Ahlers, S. Grossmann, and D. Lohse, “Heat transfer and large scale dynamics in turbulent Rayleigh-Bénard convection,” Rev Mod Phys, vol. 81, no. 2, pp. 503–537, 2009, doi: 10.1103/RevModPhys.81.503.

[3] O. Shishkina, “Rayleigh-Bénard convection: The container shape matters,” Phys Rev Fluids, vol. 6, no. 9, Sep. 2021, doi: 10.1103/PhysRevFluids.6.090502.

[4] R. Krishnamurti and L. N. Howard, “Large-scale flow generation in turbulent convection,” Proceedings of the National Academy of Sciences, vol. 78, no. 4, pp. 1981–1985, Apr. 1981, doi: 10.1073/PNAS.78.4.1981.

[5] E. P. Van Der Poel, R. J. A. M. Stevens, and D. Lohse, “Connecting flow structures and heat flux in turbulent Rayleigh- Bénard convection,” Phys Rev E Stat Nonlin Soft Matter Phys, vol. 84, no. 4, pp. 1–4, 2011, doi: 10.1103/PhysRevE.84.045303.

[6] E. P. van der Poel, R. J. A. M. Stevens, K. Sugiyama, and D. Lohse, “Flow states in two-dimensional Rayleigh-Bénard convection as a function of aspect-ratio and Rayleigh number,” Physics of Fluids, vol. 24, no. 8, p. 085104, Aug. 2012, doi: 10.1063/1.4744988.

[7] L. Zwirner, A. Tilgner, and O. Shishkina, “Elliptical Instability and Multiple-Roll Flow Modes of the Large-Scale Circulation in Confined Turbulent Rayleigh-Bénard Convection,” Phys Rev Lett, vol. 125, no. 5, Jul. 2020, doi: 10.1103/PhysRevLett.125.054502.

[8] H. D. Xi and K. Q. Xia, “Flow mode transitions in turbulent thermal convection,” Physics of Fluids, vol. 20, no. 5, 2008, doi: 10.1063/1.2920444.

[9] G. Ahlers et al., “Aspect Ratio Dependence of Heat Transfer in a Cylindrical Rayleigh-Bénard Cell,” Phys Rev Lett, vol. 128, no. 8, p. 84501, 2022, doi: 10.1103/PhysRevLett.128.084501.

[10] R. Hartmann, R. Verzicco, L. Klein Kranenbarg, D. Lohse, and R. J. A. M. Stevens, “Multiple heat transport maxima in confined-rotating Rayleigh-Bénard convection,” J Fluid Mech, vol. 939, pp. 1–27, 2022, doi: 10.1017/jfm.2021.1031.

[11] Y. C. Xie, G. Y. Ding, and K. Q. Xia, “Flow Topology Transition via Global Bifurcation in Thermally Driven Turbulence,” Phys Rev Lett, vol. 120, no. 21, May 2018, doi: 10.1103/PhysRevLett.120.214501.

[12] D. Schanz, J. Bosbach, D. Schanz, P. Godbersen, and A. Schröder, “Dynamics of Coherent Structures in Turbulent Rayleigh-Bénard Convection by Lagrangian Particle Tracking of Long-Lived Helium Filled Soap Bubbles,” 2022. [Online]. Available: https://www.researchgate.net/publication/366066650

[13] G. Paolillo, C. S. Greco, T. Astarita, and G. Cardone, “Experimental determination of the 3-D characteristic modes of turbulent Rayleigh-Bénard convection in a cylinder,” J Fluid Mech, vol. 922, 2021, doi: 10.1017/jfm.2021.554.

[14] S. Kashanj and D. S. Nobes, “Application of 4D two-colour LIF to explore the temperature field of laterally confined turbulent Rayleigh–Bénard convection,” Exp Fluids, vol. 64, no. 3, Mar. 2023, doi: 10.1007/s00348-023-03589-9.

[15] R. E. Ecke and O. Shishkina, “Annual Review of Fluid Mechanics Turbulent Rotating Rayleigh-Bénard Convection,” 2022, doi: 10.1146/annurev-fluid-120720.

[16] E. Bodenschatz, W. Pesch, and G. Ahlers, “Recent developments in Rayleigh-Benard convection,” Annu. Rev. Fluid Mech, vol. 32, pp. 709–778, 2000, Accessed: Jan. 03, 2022. [Online]. Available: www.annualreviews.org

[17] Q. Wang, R. Verzicco, D. Lohse, and O. Shishkina, “Multiple States in Turbulent Large-Aspect-Ratio Thermal Convection: What Determines the Number of Convection Rolls?,” Phys Rev Lett, vol. 125, no. 7, Aug. 2020, doi: 10.1103/PhysRevLett.125.074501.

[18] S. Kashanj and D. S. Nobes, “Temperature field of non-Oberbeck-Boussinesq Rayleigh-Bénard convection in a low aspect ratio cell,” Physics of Fluids, vol. 36, no. 4, Apr. 2024, doi: 10.1063/5.0197275.

[19] R. R. Kerswell, “ELLIPTICAL INSTABILITY,” 2001. [Online]. Available: www.annualreviews.org

Chapter 4: Temperature field and its oscillations in confined Rayleigh-Bénard convection

The spatio-temporal characteristics of the temperature field within a laterally confined convection cell of RBC with the aspect ratio of $\Gamma = 1/10$ is investigated in this chapter. Time-resolved 2D temperature field is visualized and measured using two-colour two-dye PLIF.[*]

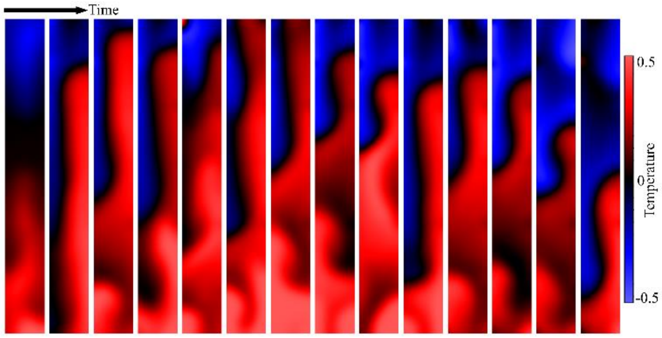

Graphical abstract for Chapter 4

---

[*] This chapter is published as: Sina Kashanj, and David S. Nobes. "Temperature field of non-Oberbeck-Boussinesq Rayleigh-Bénard convection in a low aspect ratio cell", *Physics of Fluids*, 2024; 36 (4): 047110.

4.1 Introduction

Rayleigh-Bénard convection (RBC) is a natural convection that occurs in a fluid layer confined by two horizontal boundaries, heating at the bottom and cooling at the top which leads to a vertical temperature gradient across these two boundaries [2]. RBC plays a crucial role in a range of scientific fields, including geophysics, atmospheric sciences, and astrophysics [1]. Practical applications of this phenomenon include the development of energy-efficient cooling systems and the optimization of thermal processes in industries such as metallurgy and materials processing [1]. RBC also can be employed in bioengineering for DNA polymerase chain reaction (PCR) purpose [20]. PCR is a widely used method for amplifying specific DNA sequences, but it requires precise temperature control to ensure that the DNA is amplified efficiently and accurately [21]. RBC has been used to develop new PCR techniques that rely on natural convection to achieve the necessary temperature control [21]. To design the geometry and heating profiles of these devices, knowledge of the temporal and spatial temperature distribution is necessary [21]. Hence, there are many attempts to understand the temporal and spatial variation of temperature of RBC at different conditions of RBC at different conditions [22], [23], [24].

Controlling parameters of RBC are defined as the Rayleigh number, $Ra \equiv \alpha g \Delta T h^3/\nu\kappa$, Prandtl number, $Pr \equiv \nu/\kappa$, and aspect ratio of the enclosure, $\Gamma \equiv w/h$, where α is the thermal expansion coefficient, w and h are the width and height of the enclosure respectively, g is gravitational acceleration, ν is kinematic viscosity, κ is thermal diffusivity of the fluid, and $\Delta T = T_H - T_C$ is the temperature difference between the hot, T_H, and cold, T_C, horizontal boundaries [25]. RBC is characterized by the formation of hot and cold thermally-driven plumes rising and falling, respectively [26]. The resulting motion of thermal plumes forms unsteady vortical structures [4], [27]. Development of the vortical structures leads to the formation of unsteady large-scale circulating (LSC) structures which is another characteristic of RBC [4].

In RBC, convection initiates temporally by the rise and fall of the hot and cold thermal plumes [28] as is shown in the schematic in Figure 4-1(a). The development of the RBC flow involves interaction between the thermal plumes, and the convection cell boundaries. This development of the thermal plumes leads to the formation of a mean flow or the LSC [28] shown in Figure 4-1(b). Thermal plumes develop from the hot and cold boundaries and as a coherent flow structures they have a different velocity from the mean flow [29], [30]. Experimental analysis of the turbulent RBC in a cubical enclosure with the working fluid of water and Rayleigh number of $Ra = 3.8 \times 10^{9}$ and $Ra = 3.5 \times 10^{10}$ has been shown to have a high turbulent production close to the thermal boundaries of the enclosure [31]. The region has been highlighted as region “A” for both hot and cold boundaries in Figure 4-1(c). This region is highlighted as a high Reynolds stress region can be demonstrated as a region where all the thermal plumes rise and detach from the thermal boundaries. The detachment and rise of the thermal plumes form a jet flow toward the opposite thermal boundary [31] which is shown in Figure 4-1(c). The impact of the jet into the thermal boundary leads to kinetic energy dissipation along with the formation of corner rolls [32] shown in Figure 4-1(b). The impact region can be visualized by the high turbulent kinetic energy which is highlighted as region “B” in Figure 4-1(c).

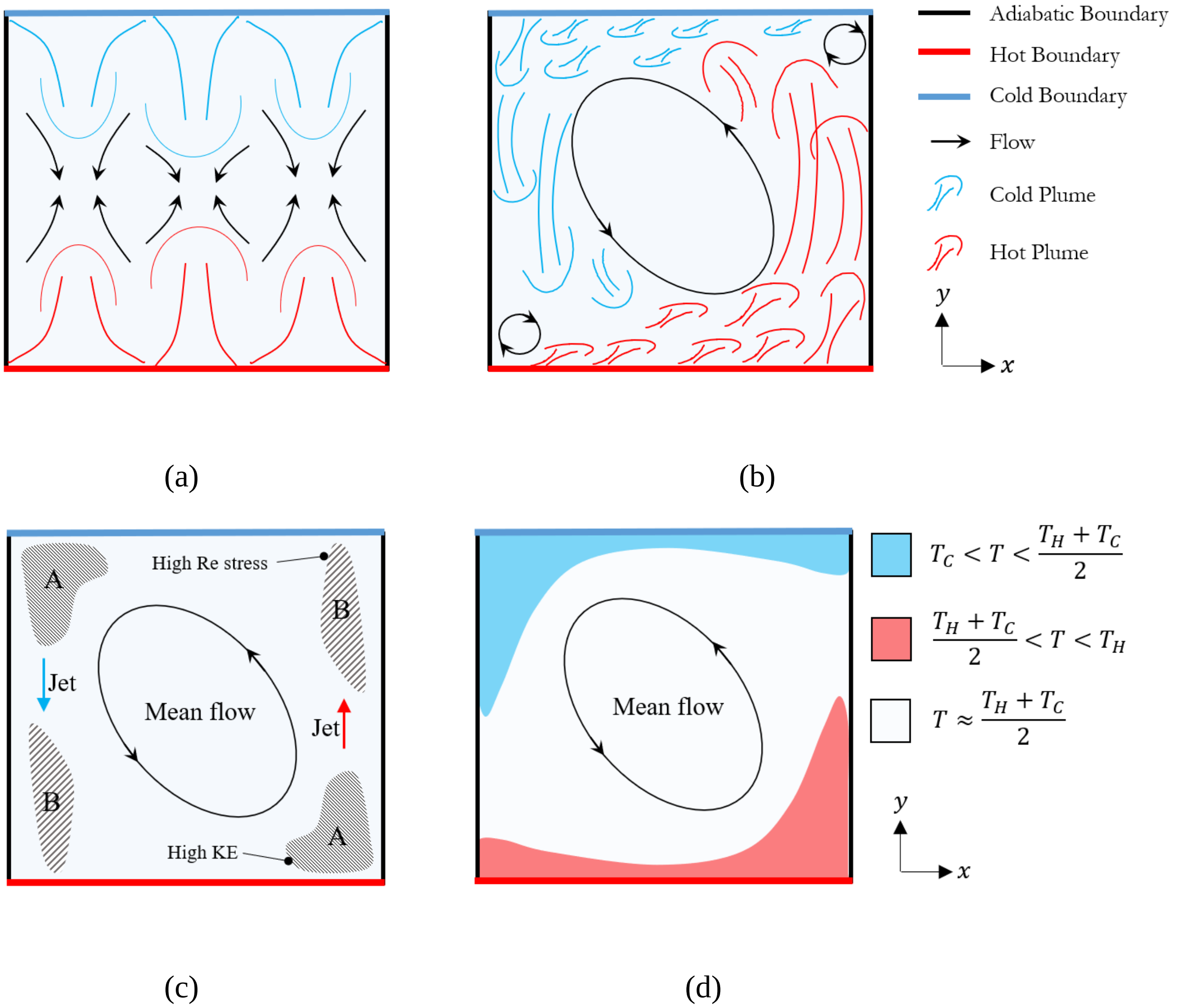

(a) (b)

(c) (d)

Figure 4-1. Schematic of the beginning of the convection and developed flow in RBC. (a) shows the start of the convection, (b) developed flow and formation of LSC, (c) Mean flow and highlighted high Reynolds stress and kinetic energy regions, (d) Mean flow and temperature map.

The schematic of the mean temperature field corresponding to the flow organization in a cubical enclosure is shown in Figure 4-1(d). It is known that the temperature at the center of the enclosure is equal to the mean temperature of the hot and cold boundaries, $(T_H + T_C)/2$ [23]. Above and below the hot and cold thermal boundary layers, the temperature stands close to the center temperature, $(T_H + T_C)/2$ [33], [34]. As can be seen in Figure 4-1(d), the region with high temperature stretch along the jets in vertical direction which is associated with the high kinetic energy region where the thermal plumes detach and form the thermal jets [35]. This flow organization and temperature field can be attributed to the RBC with low Prandtl numbers (i.e. air) and moderate to high Rayleigh number $10^6 < Ra < 10^{10}$ in an enclosure with unit aspect ratio, $\Gamma = 1$ [35].

One condition that can affect the flow organization and temperature field and thermal properties of RBC is changing the aspect ratio of the enclosure to lower values, $\Gamma < 1$, i.e., confining the convection cell in both width and depth directions [6]. The influence of slendering the enclosure on RBC properties has been a focus of interest recently [36], [37], [38]. By numerical simulation of RBC in a cubical enclosure within the Rayleigh number of $10^7 \leq Ra \leq 10^9$ and Prandtl number of $Pr = 4.3$ and of $Pr = 0.7$, [5], [6] investigated the flow organization of slender RBC with the aspect ratio of $0.4 \leq \Gamma \leq 1.25$. They showed that by increasing the aspect ratio of the enclosure, multiple LSCs may form in which the number of structures vary temporally. They also showed that heat transport reduces by increasing the number of LSCs. While the effect of the number of the LSCs on heat transport was found to be negligible or very low in some of the experimental works [8], [39], using DNS within Rayleigh number of $Ra = 5 \times 10^5$ and Prandtl number of $Pr = 0.1$, and aspect ratio of $\Gamma = 0.2$, Zwinner et al. [7] identified two regimes of sloshing and twisting and found an inverse correlation between the number of LSCs in sloshing regime with both heat and momentum transfer. They also attributed the formation of multiple LSCs to the elliptical instability.

The influence of slendering the convection cell on heat transfer was investigated using DNS with a Rayleigh number of $Ra = 10^9$ [40]. It was found that by decreasing the aspect ratio from 1 to 0.2, the heat transfer stays almost the same. However, decreasing it to lower values leads to an increase in heat transfer maximizing at around $\Gamma = 0.07$. Decreasing the aspect ratio to a lower value than $\Gamma = 0.07$ leads to a sudden and sharp decrease in the heat transfer. A similar investigation was performed by Huang et al. [41], but in this case the geometry confinement was applied only in one direction. The results show an increase in the heat transfer mainly for an aspect ratio $\Gamma \leq 0.25$. Similar to the results of previous work, Chong and Xia [42] showed that the heat transfer reach to a maximum value at a specific aspect ratio, then decrease. This maximum value of heat transfer occurred at a lower aspect ratio for higher Rayleigh numbers. This maxima in heat transfer via slendering the RBC enclosure was also investigated by Hartmann et al. [43] using DNS and investigating the temperature and velocity fields. They showed that decreasing the aspect ratio led to heat transfer enhancement while the confinement of the enclosure may lead to stabilization of the temperature and velocity field.

The Oberbeck-Boussinesq (OB) approximation is a simplifying assumption made in the study of natural convection, specifically in RBC [44]. Within the OB approximation, the density of the fluid is assumed as constant except where it is affecting the buoyancy term in the equation of motion [45]. As a result of this assumption, the density dependent fluid properties such as thermal diffusivity and kinematic viscosity are constant [45]. This allows for a simpler mathematical description of the fluid motion. Following in equation(1) and equation(2), the Navier-Stokes and the energy equations are shown within OB assumption for RBC flow. In these equations, x_i is the dimensionless Cartesian location, where $i = 1, 2$ representing the x and y positions in the 2D space where y is the vertical direction along the gravitational acceleration, P is the dimensionless pressure, δ_{i2} is the chronical delta, u_i is the dimensionless velocity of the fluid flow and t^* and $T^*$are the dimensionless time and temperature, respectively.

$$\frac{\partial u_i}{\partial t^*} + \frac{\partial u_i u_j}{\partial x_j} = \frac{\partial P}{\partial x_i} + \frac{Pr}{\sqrt{Ra}} \frac{\partial^2 u_i}{\partial x_j \partial x_j} + PrT^* \delta_{i2} \tag{1}$$

$$\frac{\partial T^*}{\partial t^*}+\frac{\partial u_j T^*}{\partial x_j}=\frac{1}{\sqrt{Ra}}\frac{\partial^2 T^*}{\partial x_j \partial x_j} \tag{2}$$

The non-Oberbeck-Boussinesq (NOB) condition in RBC arises when the temperature difference between the top and bottom boundaries, ΔT becomes large enough that the fluid density can no longer be considered constant as discussed by Wan et al. [45]. In such cases, the density variations can no longer be neglected in the momentum equation, and the assumption of constant fluid density must be abandoned. The fluid properties such as the thermal diffusivity, thermal expansion coefficient, and the kinematic viscosity cannot be assumed constant and since the temperature is unsteady, they become a function of space and time which results in a more complex set of equations. In this case, the Navier-Stokes and the energy equations can be described as equation(3) and equation(4), respectively [46]. In these equations, ρ^*, μ^*, C_p^*, and $\kappa^*$are representing the dimensionless density, dynamic viscosity, specific heat, and thermal conductivity. In the Navier-Stokes equation, Fr represents the Froude number which is defined as $Fr = V_f/\sqrt{gh}$ in which V_f is the falling velocity representing the velocity scale in RBC flow.

$$\frac{\partial u_i}{\partial t^*}+\frac{\partial u_i u_j}{\partial x_j}=-\frac{1}{\rho^*}\frac{\partial P}{\partial x_i}+\frac{1}{\rho^*}\frac{Pr}{\sqrt{Ra}}\frac{\partial}{\partial x_j}\left(\mu^*(\frac{\partial u_i}{\partial x_j}+\frac{\partial u_j}{\partial x_i})\right)+\frac{1}{Fr^2}\delta_{i2} \tag{3}$$

$$\frac{\partial T^*}{\partial t^*}+\frac{\partial u_j T^*}{\partial x_j}=\frac{1}{\rho^* C_p^*}\frac{1}{\sqrt{Ra}}\frac{\partial}{\partial x_j}\left(\kappa^*\frac{T^*}{\partial x_j}\right) \tag{4}$$

The effects of the NOB condition can be significant. For instance, the onset of convection can occur at different critical Rayleigh numbers than in the OB regime [46]. The flow patterns and heat transfer rates also can be quite different from those observed in the OB regime [46]. In many of the situations, NOB can provide a better explanation of the physics due to the large temperature differences [47]. These situations can be found in geophysical settings such as the Earth's mantle, and in industrial and engineering applications such as PCR devices [47].

Experimental and analytical investigations on the effect of NOB condition on RBC flow with a working fluid of water showed that the effect of NOB on the global properties such as Reynolds and Nusselt is not significant [44]. However, it was found that the NOB condition leads to an asymmetric thermal boundary layer thickness between the top and bottom boundaries compared to the symmetrical thermal boundary layer within the OB approximation. An asymmetry was also reported between the top and bottom viscous boundary layer thickness of RBC flow with a working fluid of water within the NOB regime [48], [49], [50]. This asymmetry was attributed to the temperature dependency of the kinematic viscosity of the fluid [51].

The effect of the NOB condition on the flow structure of the RBC flow is another important matter due to the role of the flow structures in heat and momentum transfer. The few studies which focused on this effect showed that the main effect of the NOB condition is mainly on the horizontal component of the velocity close to the top and bottom boundaries [52]. This also can be inferred from the asymmetry in the viscous boundary layer thickness [53]. Another effect of the NOB condition on the flow structure of RBC was observed for RBC flow in a cubical enclosure in which is known for the formation of diagonal symmetric corner rolling structures [52]. It was found that while in RBC within the OB approximation the center of the enclosure is a stagnation region however, within the NOB condition the velocity is not zero in this region. It is also found that in a NOB RBC with a working fluid of water by increasing the temperature difference between the top and bottom boundary, from $20\ ℃$ to $60\ ℃$, the asymmetry between the top and bottom temperature distribution increases [46].

Belkadi et al., 2020 has highlighted that experimental investigation of the temperature field of RBC flow is a difficult matter. There are several temperature measurement methods that are usually employed in studying the temperature and thermal properties of the phenomena such as RBC. Thermometers, thermocouples, resistance temperature detectors (RTDs), and thermistors are some of the most commonly used methods [54]. One disadvantage that all these methods share is the limit in spatial resolution as the measurements are to limited to a small number of points within the fluid domain.

Optical temperature measurement methods have become increasingly popular for non-invasive and high-resolution temperature measurement of fluid flows [55]. Planar laser-induced fluorescence (PLIF), liquid crystal thermometry (LCT), and phosphorescent thermometry are the most common methods in measuring the temperature of the fluid flows [56], [57], [58], [59]. PLIF, involves the use of lasers to excite certain molecules within the fluid, which then emit fluorescence that is dependent on their temperature [59]. This can provide high-resolution temperature maps of the fluid [59]. PLIF is also a non-invasive method that does not require any contact with the fluid, making it ideal for use in applications where nonintrusive measurement is essential [60]. While PLIF does require the use of specialized equipment and can be challenging to implement, these advantages make it a valuable tool for fluid temperature measurements in a variety of applications such as studying the RBC [61].

There have been several attempts to apply PLIF and other optical measurement techniques such as LCT for measuring the temperature of RBC [62]. However, they have been used in few works to conduct experiments to study the physics of RBC [63]. LCT was applied along with PIV to measure the temperature field of RBC in a rectangular channel with working fluid of water by Moller et al. [52] and Kaufer and Cierpka [53]. LCT also has been used to investigate the temperature variation of turbulent superstructures of RBC in an enclosure with high aspect ratio [58]. Using 4D LIF, Kashanj and Nobes [14] captured the temperature and its temporal evolution in a low aspect ratio enclosure. Although, these techniques are more popular in studying RBC, there also limitations due to the cost and time of the massive data storage and processing [14].

While there are many studies on RBC flow, the effect of the non-Oberbeck-Boussinesq condition has been investigated by few. The influence of the lateral confinement of the convection cell also has been a focus of interest recently due its major effect on the RBC flow properties. Yet, to the best knowledge of the authors, the influence of lateral confinement on NOB RBC flow has not been investigated. In this chapter we will investigate temperature development, its spatial distribution and oscillation in an RBC flow at the NOB condition while the convection cell has a low aspect ratio of $\Gamma = 0.1$. This is investigated for three Rayleigh numbers of $Ra = 5.3 \times 10^7, 7.6 \times 10^7$, and 9.5×10^7 with the associated the temperature differences of $\Delta T = 30\ ℃$, $35\ ℃$, and $40\ ℃$ with the Prandtl number of $Pr \approx 6$. Investigations have been done experimentally by applying time-resolved two-colour two-dye PLIF for measuring the 2D temperature field from the beginning of the convection for 2400 seconds. The first aim of this chapter is to investigate the effect of severe lateral confinement of the convection cell of NOB RBC on suppressing the temperature oscillations. Then, to identify the origin of the temperature oscillations the physics of oscillations has been compared with the one in OB RBC in the common aspect ratio enclosures, $\Gamma \approx 1$. Furthermore, since the temperature of the whole field is measured, the spatial variation of the temperature oscillation has been investigated to see its behavior by moving away from the thermal boundaries. At the end, the influence of the lateral confinement on the vertical symmetry of the temperature field is investigated to see if severe lateral confinement preserves the vertical symmetry of the temperature field that is known for OB RBC flow or it leads to an increase in the asymmetry of the temperature field.

4.2 Methodology

A schematic of the RBC enclosure with highlighted boundary conditions can be seen in Figure 4-2(a). The enclosure had a square cross-section with the width and depth, w of $5\ \mathrm{mm}$, and height, h of $50\ \mathrm{mm}$ making a convection enclosure with the aspect ratio of $\Gamma = 0.1$. Bottom and top boundaries of the enclosure were connected to two heat exchangers with a surface made of copper sheet for high conductivity. Both heat exchangers were connected to thermal baths to provide a constant temperature boundary condition at the bottom and top of the cell. The temperature of the water recirculating in the heat exchangers were controlled with the precision of $0.01\ ℃$. The temperature is distributed evenly over the surface of the horizontal boundaries. The continuity of the temperature distribution on the surface of the heat exchangers has been examined using an IR camera (FLIR A35, FLIR Systems Inc.). The results of the temperature distribution can be seen in reference [14], which shows the mean variation of the temperature lower than $4\ \%$. To provide optical accessibility and an adiabatic boundary condition on the sidewalls, they were fabricated using a relatively thick, $6.35\ \mathrm{mm}$ acrylic sheet with low thermal conductivity of $0.15\ \mathrm{W/mK}$. Each heat exchanger of the convection cell was connected to a water bath. While the flowrate of the pumps of the water baths were set to be the same, the experiments started by circulating the hot and cold water in the heat exchangers at the same time. It is worth noting that both heat exchangers were connected to the water baths with the same length of tubing to ensure the circulation starts at the same time.

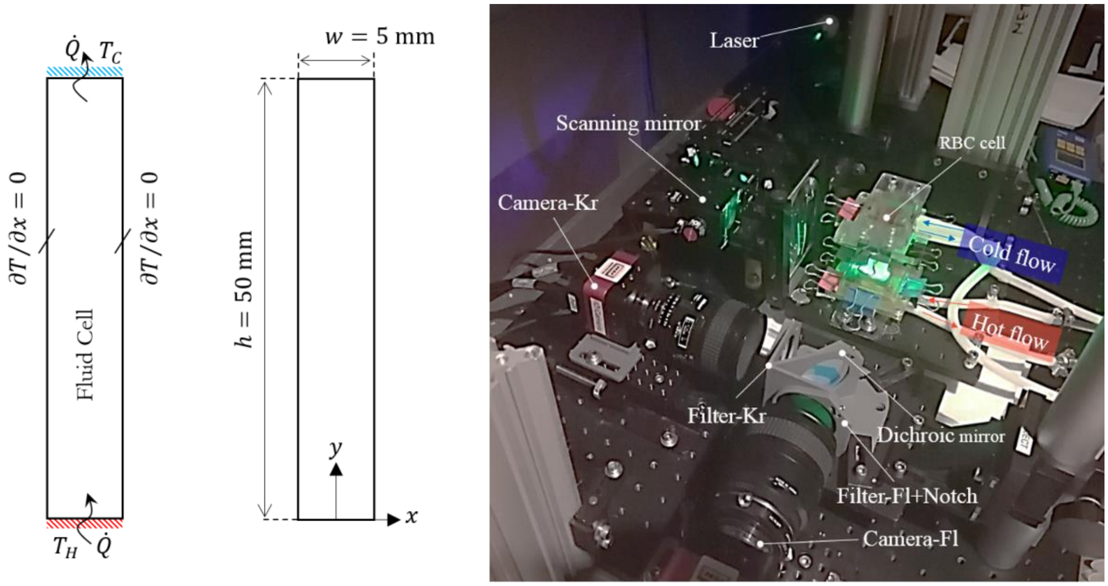

(a) (b)

Figure 4-2. (a) Schematic of the convection cell of RBC with boundary conditions. (b) The RBC flow cell and optical measurement system.

Different fluorescent dyes sensitive to the temperature could be used for conducting thermometry of in different liquids. Rhodamine B and Rhodamine 110 are the most common pair of the fluorescent dyes that have been used for thermometry [66]. However, due to the low temperature sensitivity of this pair of dyes which is around 2 %/℃ there are new studies investigating different dyes to enhance the temperature sensitivity [66]. The main key in enhancing the temperature sensitivity in a ratiometric approach is employing two dyes with opposite temperature sensitivity [62]. Fluorescein-Rhodamin B, Fluorescein-Kiton red, Fluorescein-Sulforhodamine 640, Fluorescein-Sulforhodamine 101 are some of the pair of the dyes used for different applications, yet all to enhance the temperature sensitivity of the ratiometric approach [61], [62], [67], [68]. Among these pairs it is found that Fluorescein-Kiton red could provide the highest temperature sensitivity. Furthermore, the solubility of these two dyes in water make them a perfect fluorescent dyes to perform two-colour two-dye PLIF for the current work in which water is used as the working fluid. Hence, in this work this pair of fluorescent dye has been used for thermometry of the RBC flow.

The calibration graph of the Fluorescein and Kiton red and along to the ratiometric calibration graph is shown in Figure 4-3(a) and (b), respectively. From individual temperature calibration in Figure 4-3(a), it can be seen that the temperature sensitivity of the Fluorescein is equal to $+1.3\ \%/℃$ and the temperature sensitivity of Kiton red is equal to $-1.9\ \%/℃$. The overall ratiometric temperature sensitivity for the temperature in the range of is also equal to $\sim 7.3\ \%/℃$. One main concern regarding performing PLIF for a long time which is the purpose of this work, is the photo-bleaching effect. The temperature calibration was performed during ~ 2 hr which is almost 3 times longer than the experiments reported in the current work with the same laser and intensity. Yet, any change in the temperature sensitivity of the fluorescent dyes was not observed.

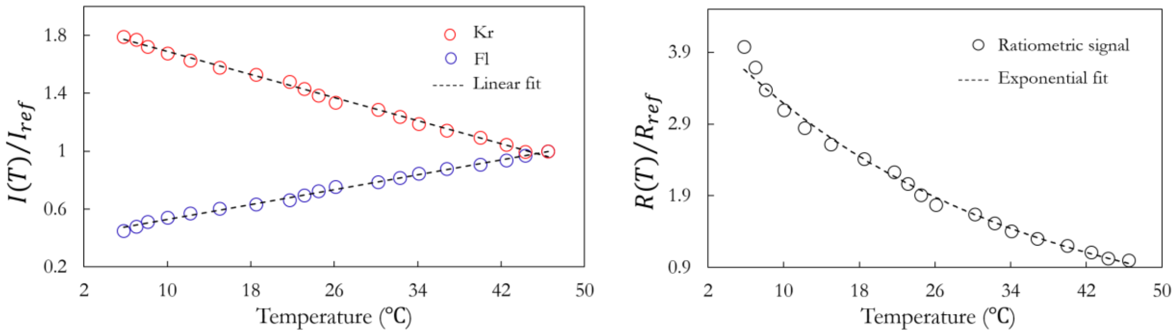

(a) (b)

Figure 4-3. (a) Normalized calibration of the Fluorescein and Kiton red each fitted with a linear function. (b) The ratiometric calibration graph of the ratiometric Fluorescein-Kiton red fitted with an exponential function.

The experimental setup made and integrated for this work including the RBC convection cell and the optical measurement apparatus can be seen in Figure 4-2(b). The schematic of the optical measurement system used to apply PLIF is illustrated in Figure 4-4. As can be seen in Figure 4-2(b) and Figure 4-4, a scanning mirrors were used (SM in Figure 4-4), for generating a highly uniform intensity laser sheet. For the experiments, a two-dye two-colour PLIF technique were employed which required two cameras (Flare 12M125, IO Industries Inc.) and a set of optical filters. The fluorescent dyes used in this work were Fluorescein and Kiton red. A notch filter (#86-130, Edmund Optics Inc.) with a central wavelength (CWL) of 532 nm and full width at half maximum (FWHM) of 17 nm along with a band pass filter (#86-992, Edmund Optics Inc.) with a central wavelength (CWL) of 525 nm and FWHM of 50 nm were used to collect the signal of Fluorescein dye signal. These two filters are depicted in Figure 4-4 as F1 for bandpass and F2 for notch filter. To collect the signal from the Kiton red dye a band pass filter (#84-118, Edmund Optics Inc.) with CWL of 607 nm and FWHM of 36 nm were employed which is indicated as F3 in Figure 4-4. A 532 nm Continuous-wave (CW) laser with the beam thickness equal to 120 μm within the full width at half maximum (FWHM) criterion was used to excite the fluorescent dyes. A dichroic mirror, DM, were employed to separate the low frequency and high frequency signal of the emitted light from the fluid flow and send each signal to a specific camera. Furthermore, two double convex lenses, L1 and L2 in Figure 4-2(b) were used to control the thickness of the laser beam. Another double convex lens, L3 was also used to collimate the laser sheet. The processing of the fluorescent signals was done using commercial software (Davis 10.0.5, LaVision GmbH) to apply PLIF for thermometry. More details on the processing scheme and calibration process of the applied PLIF can be found in reference [14].

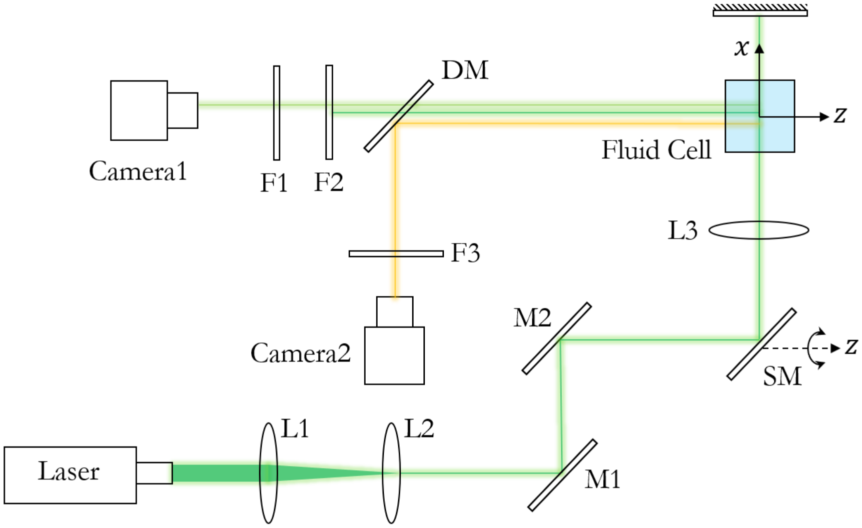

Figure 4-4. Schematic of the optical measurement system used for applying two-colour PLIF.

Using the working fluid of water, experiments were conducted in three different temperature conditions with a high temperature difference in the range of $30\ ℃ \leq \Delta T \leq 40\ ℃$, between the top and bottom boundaries. This led to three different cases with the details shown in Table 4-1. For the NOB condition with a high temperature difference, it is difficult to define a constant Rayleigh number and Prandtl number due to the high temperature variation of the flow field. In OB condition the average temperature, $\bar{T} = (T_H + T_C)/2$ is used as a reference to define dimensionless numbers. For the NOB, using the same definition could be misleading since the fluid properties can change significantly. In Table 4-1, the Rayleigh and Prandtl numbers variation due to the temperature dependency of the fluid properties such as kinematic viscosity, thermal expansion coefficient, and thermal diffusivity is shown. For the three studied cases, here in this table, Ra and Pr are referred to the Rayleigh and Prandtl numbers based on the mean temperature, $\bar{T}$ while $(\cdot)'_{max}$ and $(\cdot)'_{min}$ are denoting the ratio of the parameters at respectively, the highest, T_H, and lowest, T_C temperatures with respect to the value of that parameter at the mean temperature,

$\bar{T}$, e.g., $Ra'_{max} = Ra(T = T_H)/Ra(T = \bar{T})$. Figure 4-5(a) and (b) also show the variation of the Rayleigh and Prandtl numbers corresponding to the T_H, T_C, and $\bar{T}$. From this figure, it can be seen that the Rayleigh number in the case of $Ra3$, has the highest deviation since it has the highest temperature difference (see Table 4-1). For this case, the Rayleigh number at T_C increases comparing to the Rayleigh number at T_H by two orders of magnitude from 3.6×10^6 to 2.2×10^8 which is significant considering the physics of the RBC at these two regimes. For the Prandtl number of the same case, $Ra3$, it can be seen that it decreases from 11.111 to 4.667 by moving from T_C to T_H with a high deviation comparing to its value at the mean temperature, $\bar{T}$.

Table 4-1. Properties of the three different examined RBC cases.

Case	$Ra1$	$Ra2$	$Ra3$
T_H(°C)	35	40	45
T_C(°C)	5	5	5
Ra	5.3×10^7	7.6×10^7	9.5×10^7
Ra'_{max}	1.678	2.384	2.363
Ra'_{min}	0.051	0.041	0.038
Pr	6.993	6.250	6.164
Pr'_{max}	4.667	0.636	0.636
Pr'_{min}	11.111	1.778	1.802
$t_f(\Delta T)$ (s)	0.91	0.79	0.71

One of the important characteristics of the turbulent RBC is the temporal variation of the flow states. Hence, the time in which the flow is investigated has a crucial role in revealing the physics of this phenomena. However, capturing the whole field properties during the long-time experiments by optical measurement techniques or numerical simulations by DNS can be challenging due to the massive amount of data. In this work, experiments were conducted for each case during 2,400 seconds from the start of the convection with the data acquisition frequency of 25 Hz. As a result, a total amount of 360,000 images were captured and processed to visualize the temperature field and its temporal evolution. The free-falling time, $t_f \equiv h/\sqrt{\alpha g \Delta T h}$ in which each case was investigated can be seen in Figure 4-5(c). Deviation of the free-falling time, t_f within these temperature differences is significant for all the cases. Hence, in this chapter the real time instead of the dimensionless time were used when temporal unit matters. The free-fall time according to the mean temperature, $\Delta T = (T_H + T_C)/2$ is also highlighted in Table 4-1 for the reference.

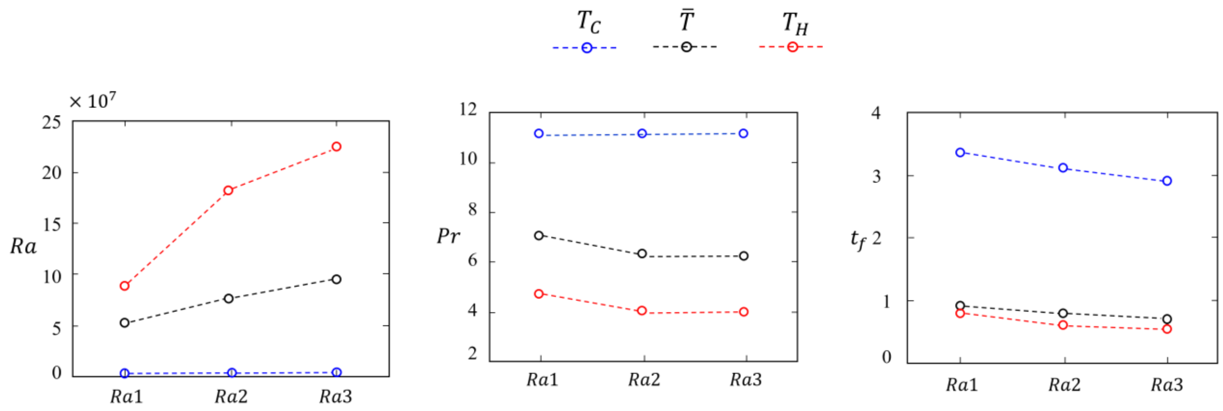

(a) (b) (c)

Figure 4-5. Variation of the (a) Rayleigh number, Ra, (b) Prandtl number, Pr, and (c) falling time, t_f within the three examined cases; $Ra1$, $Ra2$, and $Ra3$. This has been plotted for the parameters at the maximum temperature, T_H, minimum temperature, T_c, and the mean temperature, $\bar{T}$.

While it is known that a high temperature difference between the hot and cold boundaries can lead to NOB conditions, it is crucial to define a criterion to identify the NOB condition from OB one. Gray and Giorgini [69] derived a new method to validate the OB approximation for both air and water. The diagram in Figure 4-6 is plotted after Horn and Shishkina [49] and used the method of Gray and Giorgini [69] and shows the valid range for OB RBC flow with a working fluid of water. The rectangular points in diagram of Figure 4-6 show the three cases of the experiment highlighting the NOB condition. As can be seen in Figure 4-6, with the length scale of the enclosure used for the experiments of the current work of $h = 50$ mm and the temperature differences of $\Delta T = 30$ °C, 35 °C, and 40 °C the condition of the current RBC flow is well beyond the OB approximation.

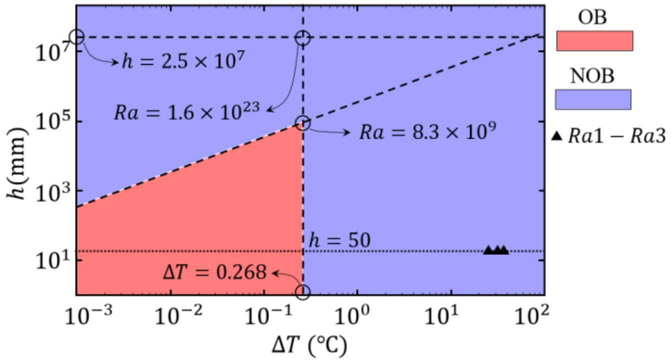

Figure 4-6. Height to temperature difference diagram indicating the validity range for OB assumption after Horn and Shishkina [49]. The red and blue colours indicate valid OB and NOB regions, respectively. The triangles are showing the three different cases that have been investigated in this chapter.

4.3 Results and Discussion

A temperature map associated to the start of convection showing the rise and fall of the hot and cold thermal plumes is depicted in Figure 4-7. The parameters are non-dimensionalized as $T^* = (T - \bar{T})/\Delta T$, $x^* = x/w$, and $y^* = y/w$. At first glance, there are two important features which distinguish the formation of the thermal plumes with the conventional knowledge of RBC flow. First, for all three cases, it can be seen that only one thermal plume is formed for both top and bottom boundaries. Secondly, all the thermal plumes have a conical shape with a sharp tip. However, the typical shape of a thermal plume is a mushroom shape with a wide tip reported earlier in many studies [28]. One may raise the point that this could be due to the low temperature sensitivity of the experimental method. However, the typical mushroom shape of the thermal plumes has been previously visualized and reported using the same experimental approach [14].

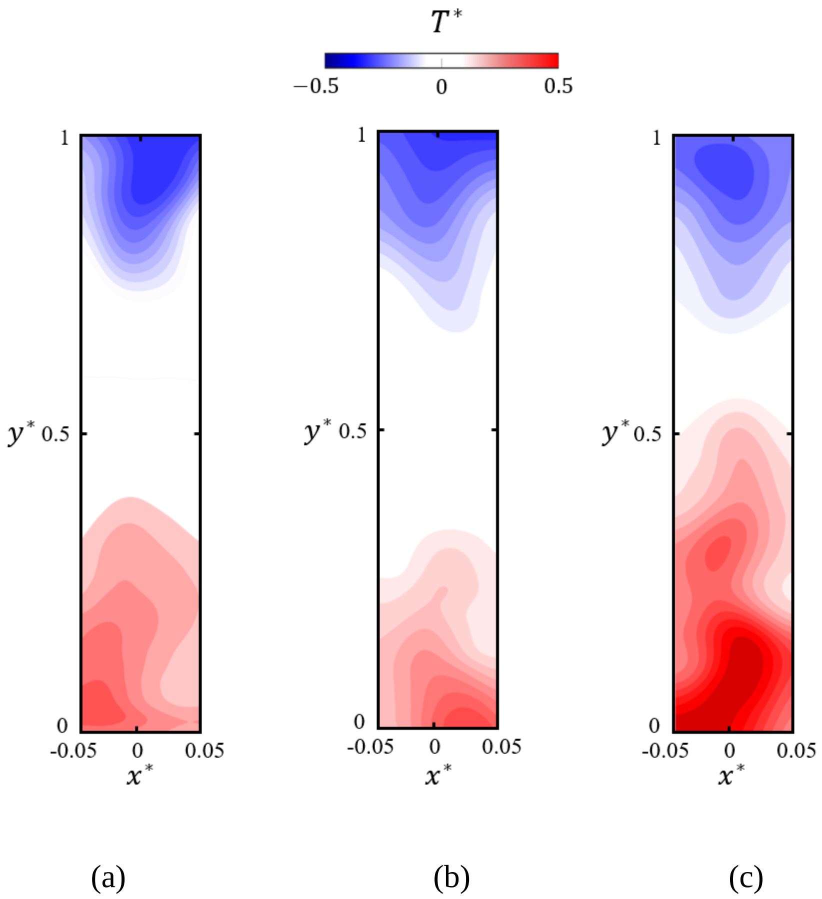

Figure 4-7. Instantaneous temperature map of RBC at the beginning of the convection at $t \approx 8$ s for (a) $Ra1$, (b) $Ra2$, (c) $Ra3$. The aspect ratio of the temperature field has been adjusted for a better visualization.

To have a better understanding of the temperature profile of the formed thermal plumes the variation of the temperature along the x-axis at two vertical locations of $y^* = 0.125$ and $y^* = 0.875$ is plotted in Figure 4-8. The temperature profile close to the cold boundary, $y^* = 0.875$ is almost consistent for all three cases since the temperature of the top boundary for all the cases is set to the same temperature of, $T_C = 5$ °C. However, it can be seen in Figure 4-8(b) that by moving from $Ra1$ to $Ra3$ and increasing the temperature of the hot boundary, the peak of the temperature increases. For all cases and temperature, the profile shows a single peak which confirms the formation of a single thermal plume from both hot and cold boundaries. It is important to note here that in Figure 4-8, the temperature is non-dimensionalized as $T^* = T - \bar{T}/\Delta T$ is based on the maximum, $T_H = 45$ °C and minimum, $T_C = 5$ °C temperatures.

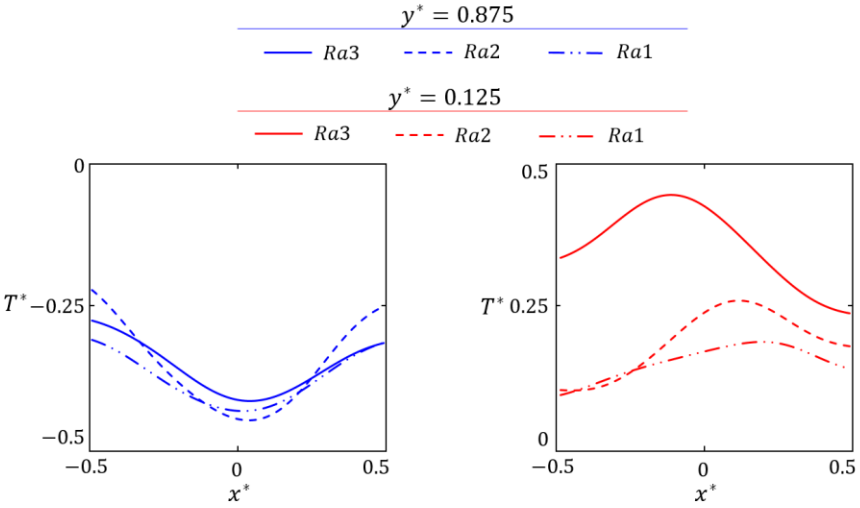

(a) (b)

Figure 4-8. Temperature variation along the x-axis at two vertical location of (a) $y^* = 0.875$ and (b) $y^* = 0.125$ lines for the three cases of $Ra1$, $Ra2$, and $Ra3$. Temperature is non-dimensionalized as $T^* = T - \bar{T}/\Delta T$ is based on the maximum, $T_H = 45$ °C and minimum, $T_C = 5$ °C temperatures.

In this experimental investigation of RBC with a low aspect ratio, the primary objective was to explore the impact of slenderness of the convection cell on the evolution of the temperature distribution over an extended period of 2400 s, which exceeds the typical duration found in existing literature, particularly in the context of NOB flows [58]. As is shown in Figure 4-9, the evolution of the horizontally mean temperature at the bottom, $\langle T^* \rangle_{x^*, y^* \approx 0}$, at the top, $\langle T^* \rangle_{x^*, y^* \approx 1}$, and the spatial mean temperature, $\langle T^* \rangle_{x^*, y^*}$ is plotted for the three different cases of $Ra1$, $Ra2$, and $Ra3$ each representing varying levels of temperature within the convection cell. Here, temperature is non-dimensionalized as $T^* = T - \bar{T}/\Delta T$ based on the maximum, T_H and minimum, T_C temperature of each case, $Ra1$ to $Ra3$. As a result, the mean temperature, $T = \bar{T}$ of each case is at $T^* = 0$. The near wall temperatures are also measured at $y^* = 0.975$ for the cold wall and $y^* = 0.025$ for the hot wall which is represented as $y^* \approx 1$ and $y^* \approx 0$, respectively.

From Figure 4-9, it can be observed that for all the cases the convection starts by a rise and fall of the temperature in vicinity of the bottom, $y^* \approx 0$ and top, $y^* \approx 1$ boundaries, respectively. This is due to the formation of the primary plumes as discussed in Figure 4-7 and Figure 4-8. For $Ra1$, the mean temperature decreases below the mean value, $\langle T^* \rangle_{x^*,y^*} \approx 0$, while for the two other cases, $Ra2$ and $Ra3$, mean temperature develops to the mean value $\langle T^* \rangle_{x^*,y^*} \approx 0$. For $Ra1$, all three temperature, $\langle T^* \rangle_{x^*,y^* \approx 0}$, $\langle T^* \rangle_{x^*,y^* \approx 1}$, and $\langle T^* \rangle_{x^*,y^*}$ indicates a steady state after ~ 2000 s. For two other Rayleigh numbers, i.e. $Ra2$ and $Ra3$, it can be seen that temperature does not reach a steady state and it is unsteady even during 2400 s of the experiment. This unsteadiness is more significant for higher temperature difference case of $Ra3$. This unsteadiness of the temperature and flow field can also be observed in the result of the DNS of OB RBC of a low aspect ratio, $\Gamma = 0.08$ enclosures in which for a very high Rayleigh number of $Ra = 7 \times 10^9$ the flow did not reach to steady state even after 3200 s [43].

It is worth noting that as can be seen in Figure 7(b), at the beginning the near hot and cold walls temperature increases and decreases, respectively. During this time interval the spatial mean temperature increases as well. However, at about $t \approx 5$ s, the spatial mean temperature increases even more than the temperature near the hot wall. The increase in the spatial temperature is due to the significant effect of the primary thermal plume and increase in the temperature of the whole domain. While after a while the temperature of the near hot wall decreases due to the detachment of the primary hot thermal plume, the spatial mean temperature is higher than the temperature near the wall due to the high energy of the thermal plumes dominating the temperature of the whole field. This also can be seen occurring significantly after $t \approx 2000$ s, in which a very harmonic temperature of the near hot wall can be observed which is an evidence of thermal plume detachment and decrease in the temperature of the near wall, while due to the generation of the thermal plumes the average temperature of the whole field is increasing.

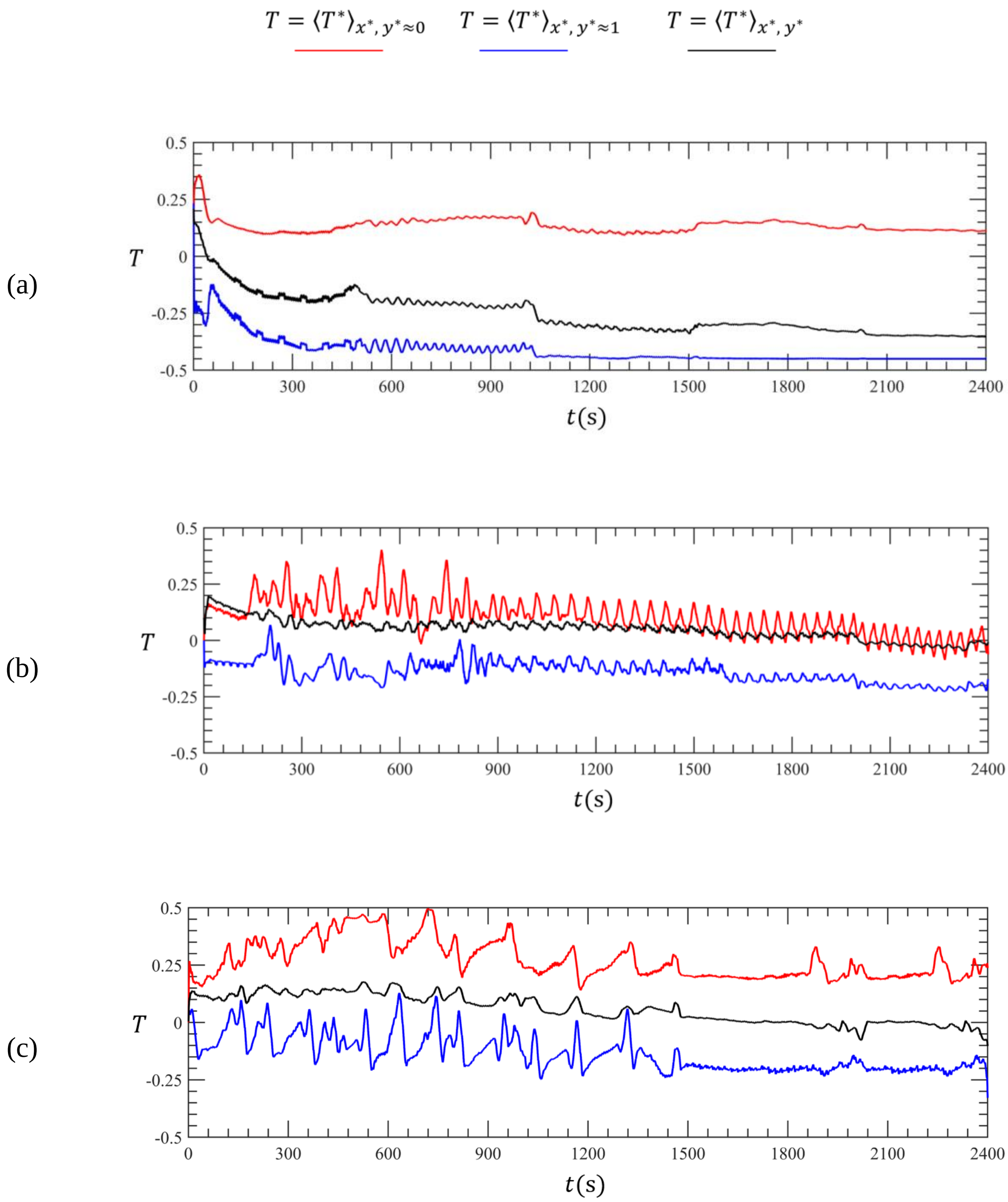

Figure 4-9. Temporal evolution of the temperature for (a) $Ra1$, (b) $Ra2$, (c) $Ra3$. Plots show the horizontal mean temperature at the bottom boundary, $\langle T^* \rangle_{x^*, y^* \approx 0}$, top boundary, $\langle T^* \rangle_{x^*, y^* \approx 1}$, and the spatial mean temperature, $\langle T^* \rangle_{x^*, y^*}$.

While Figure 4-9, provides information about the temperatures' temporal evolution near the thermal boundaries and the whole field mean temperature, to examine the temperature organization in the flow field, spatial analysis of the temperature field from the start of the convection developing to 2400 s is necessary. The spatio-temporal map of the temperature along the y-axis and x-axis is shown in Figure 4-10 for $Ra1$. For each time instance, the map in Figure 4-10(a) represents the temporal evolution of the horizontal mean temperature, $\langle T^* \rangle_x$ along the vertical direction, y^*. For each time instance, the map in Figure 4-10(b) represents the temporal evolution of the vertical mean temperature, $\langle T^* \rangle_y$ along the width of the convection cell, x^*. Similar maps for $Ra2$ and $Ra3$ are shown in Figure 4-11 and **Error! Reference source not found.**, respectively. Similar to Figure 4-9, the evolution of the temperature can be seen in these figures. At the very beginning of the convection, the rise and fall of the thermal plumes along the high temperature variation can be observed. Later, with the development of the flow, it can be seen that for $Ra1$ the mean temperature decreases which can be observed in both the horizontal and vertical temperature variations in Figure 4-10(a), and (b) respectively. It can be seen that the flow is becoming more stabilized with lower temperature fluctuations. Investigation of the mean value fluctuation shows that in this case, $Ra1$, the temperature at the top and bottom boundaries along the spatial mean temperature achieve a lower variation as can be seen in Figure 4-10(a), and (b) after $t \approx 2000$ s.

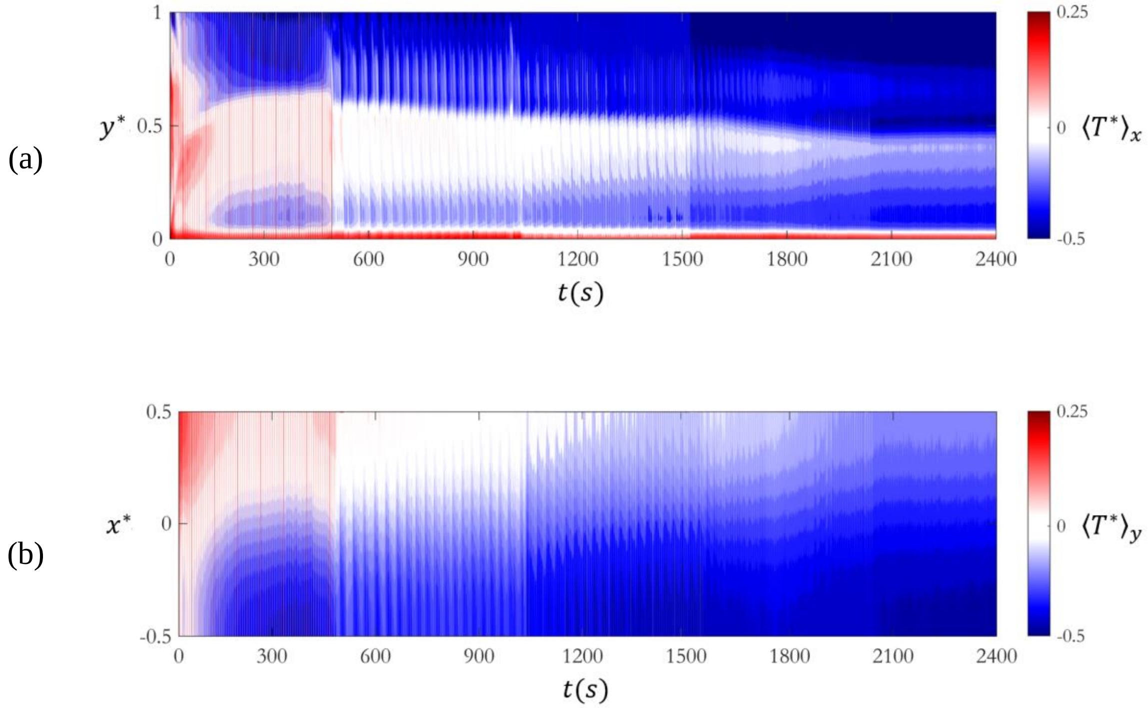

Figure 4-10. Spatio-temporal map of the temperature evolution for $Ra1$. (a) Shows the evolution of temperature in vertical direction, y-axis. (b) Shows the evolution of temperature along x-axis. For better visualization of the temperature map, the colour bar shows the dimensionless temperature, T^* variation from -0.5 to 0.25.

For $Ra2$ in Figure 4-11(a), (b), it can be seen that the temperature variation reaches a harmonic state with a periodic variation of the temperature field at the boundaries along with the mean value. This can be observed both from the temperature variation along the vertical and horizontal direction shown in Figure 4-11(a), (b), respectively. In comparison to the $Ra1$, it can be seen that although the temperature field appears to approach a steady state, the mean value is decreasing constantly during the experiment which also can be seen in Figure 4-9(b). For $Ra3$, also this cooling effect can be seen in both the spatio-temporal map of the temperature in Figure 4-12(a), (b) and also in the temperature evolution of the bottom and top boundaries along the mean temperature variation in Figure 4-9(c). This cooling is due to sudden heating after the start of the convection which leads to an increase in the temperature difference between the top boundary, and the mean flow. For $Ra1$, the temperature difference between the hot boundary and the mean temperature is the same as the cold boundary and the mean temperature, $T_H - \bar{T} = \bar{T} - T_C = 15$ °C, yet this sudden heating and a long-time cooling can also be observed for this case before the steady state, since the temperature of the cold boundary is $T_C = 5$ °C and it is in the vicinity of the minimum density criterion of the working fluid, water.

Observing the spatio-temporal map of the vertical mean temperature, $\langle T^* \rangle_y$ for three Rayleigh numbers, Figure 4-10(b), Figure 4-11(b), and Figure 4-12(b), it is evident that at the very beginning of the convection, $t < 50\ s$, the temperature of the right hand side of the convection cell i.e. $x^* > 0$ is higher than the mean temperature due to the preliminary development of the thermal plumes. Then by developing the flow, for $Ra1$ after $t \approx 450$ the whole mean temperature field is lower than the mean value, $\langle T^* \rangle_y = 0$ which can be seen by the white to blue colour in the temperature map in Figure 4-10(b). This is the similar cooling effect discussed earlier for vertical variation of the temperature. Same as $Ra1$, this cooling effect can be observed for $Ra2$ and $Ra3$. However, due to increasing the temperature difference and consequently Rayleigh number, the appearance and dominance of vertical mean temperature lower than the vertical mean temperature, $\langle T^* \rangle_y < 0$ delays to much more compared to $Ra1$. As a result, for $Ra2$, Figure 4-11(b), at $t = 2400\ s$, it can be seen that for $x^* > 0$ the vertical mean temperature is higher than the mean value, $\langle T^* \rangle_y > 0$ and for $x^* < 0$, it is lower than the mean value, $\langle T^* \rangle_y < 0$.

The oscillation of the temperature field can be also seen in the spatio-temporal maps for all the three Rayleigh numbers indicated in Figure 4-10, Figure 4-11, and Figure 4-12 in both vertical and horizontal mean temperature maps, $\langle T^* \rangle_y$ and $\langle T^* \rangle_x$, respectively. For $Ra1$, the amplitude of these oscillations reduces significantly after $t \approx 1500\ s$ which can also be seen in Figure 4-9. For $Ra2$, the oscillations have a harmonic appearance, yet as can be seen in Figure 4-11 and Figure 4-9 the mean temperature value is decreasing not reaching to a steady state. This is more evident for the vertical mean temperature evolution, $\langle T^* \rangle_y$ shown in Figure 4-11(b). For $Ra3$, multiple states can be seen based on the oscillation of both horizontal and vertical mean temperature variations. The first state is from the start of the convection, $t = 0$ s to $t \approx 1460$ s identified by slow fluctuations compared to the second state from $t \approx 1460$ s to $t \approx 1870$ s which has a harmonic oscillation with a symmetrical horizontal mean temperature map $\langle T^* \rangle_x$ in which for $y^* < 0.5$ the horizontal mean temperature is lower than the mean value, $\langle T^* \rangle_x < 0$, while for $y^* > 0.5$ the horizontal mean temperature is higher than the mean value, $\langle T^* \rangle_x > 0$. During this time interval, it can be seen that the vertical mean temperature is almost equal to the mean value, $\langle T^* \rangle_x \approx 0$ along the whole x-axis, $-0.5 \leq x^* \leq 0.5$. For the third state, which can be identified for $t > 1870$ s, it can be seen that the vertical symmetry is disrupted affecting the temperature oscillations. The details regarding the temperature oscillations are extended and quantified in the follow section.

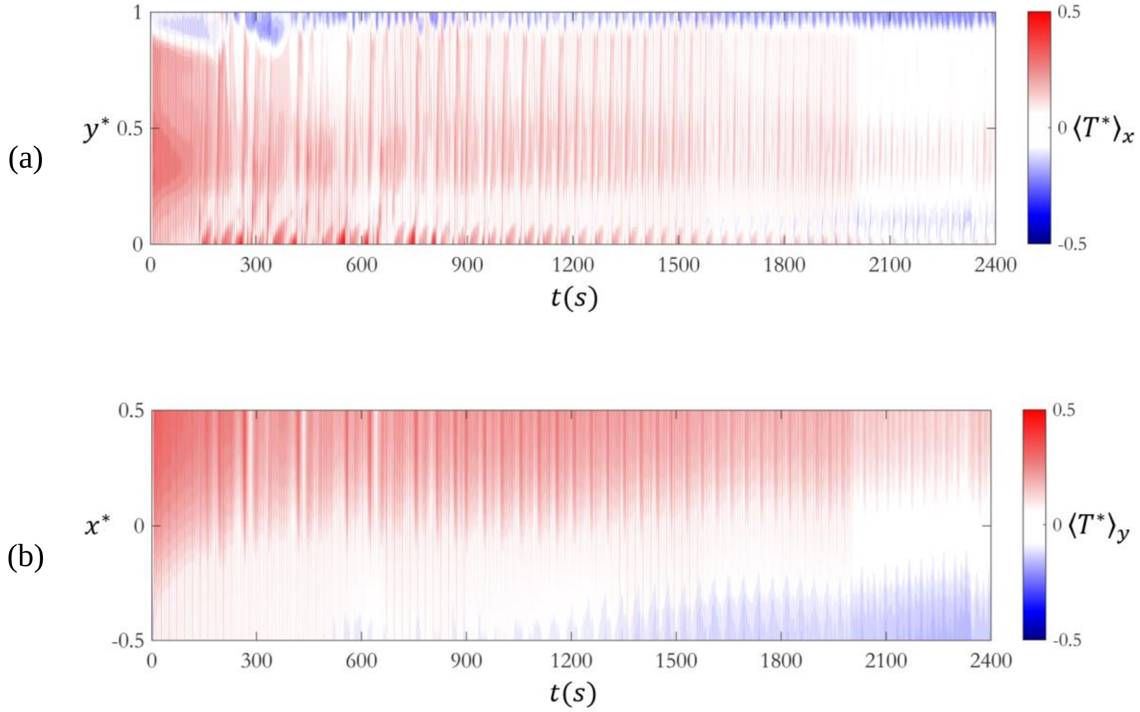

Figure 4-11. Spatio-temporal map of the temperature evolution for $Ra2$. (a) Shows the evolution of temperature in vertical direction, y-axis. (b) Shows the evolution of temperature along x-axis.

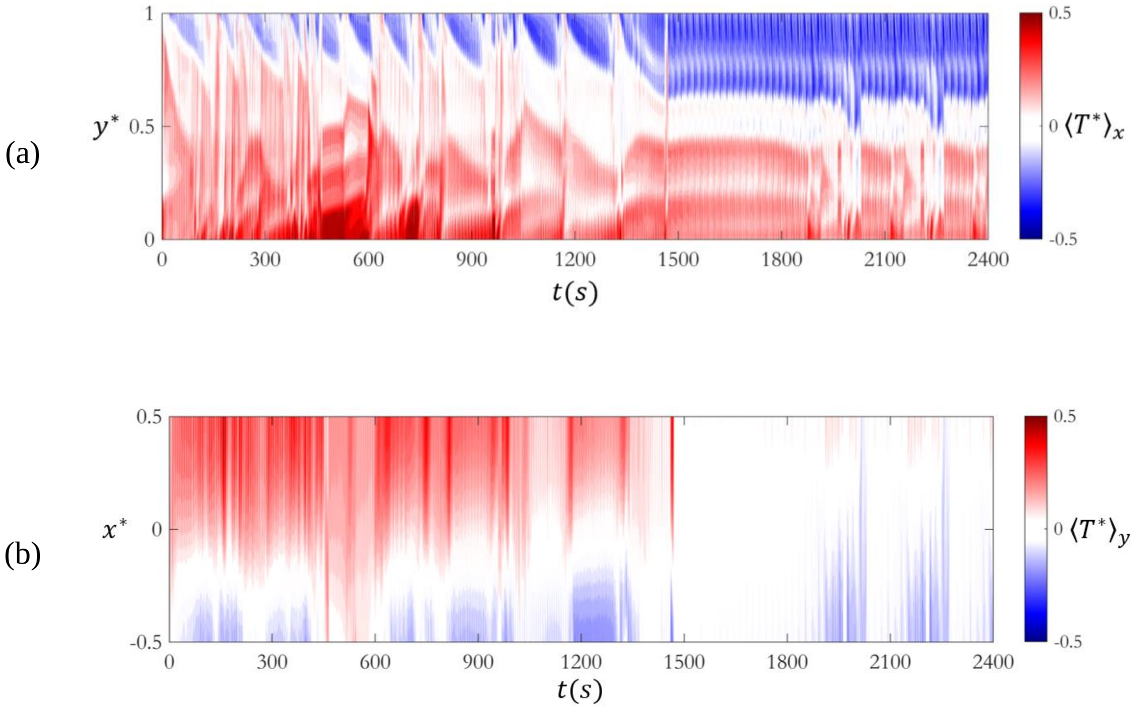

Figure 4-12. Spatio-temporal map of the temperature evolution for $Ra3$. (a) Shows the evolution of temperature in vertical direction, y-axis. (b) Shows the evolution of temperature along x-axis.

Understanding the underlying mechanisms behind temperature oscillations in RBC flow has been a subject of extensive research, with various hypotheses proposed in prior investigations. Some studies have suggested that these oscillations stem from the periodic and alternating emission and impingement of thermal plumes [70]. Conversely, other research has proposed an alternative explanation, emphasizing the role of the formation of sloshing and torsional regimes of LSC, in which thermal plumes are believed to emerge randomly and continuously [71]. The aspect ratio of the container and NOB condition can affect the temperature fluctuations. Figure 4-13 shows the variation of the power spectra of the horizontally mean temperature, $\langle T \rangle_x$ oscillations for three different vertical locations of the convection cell, $y^* \approx 0, 1$ and $y^* = 0.5$ for three Rayleigh numbers, $Ra1$, $Ra2$, and $Ra3$. Upon examination of Figure 4-13(a)-(c), it is evident that for $Ra1$, the peak frequency of the oscillations for all the three vertical locations is found to be in the same order. As is shown in Table 4-2, the oscillation frequency for all the vertical locations, i.e., $f_{y^*\approx 0}, f_{y^*=0.5}$, and $f_{y^*\approx 1}$ is varying from 0.022 Hz to 0.028 Hz. Prior experiments measured the peaks found in the power spectra near the frequency of ~ 0.028 Hz [71], [72] which is very close to the range of the prominent peak frequency of $Ra1$ regardless of the vertical location.

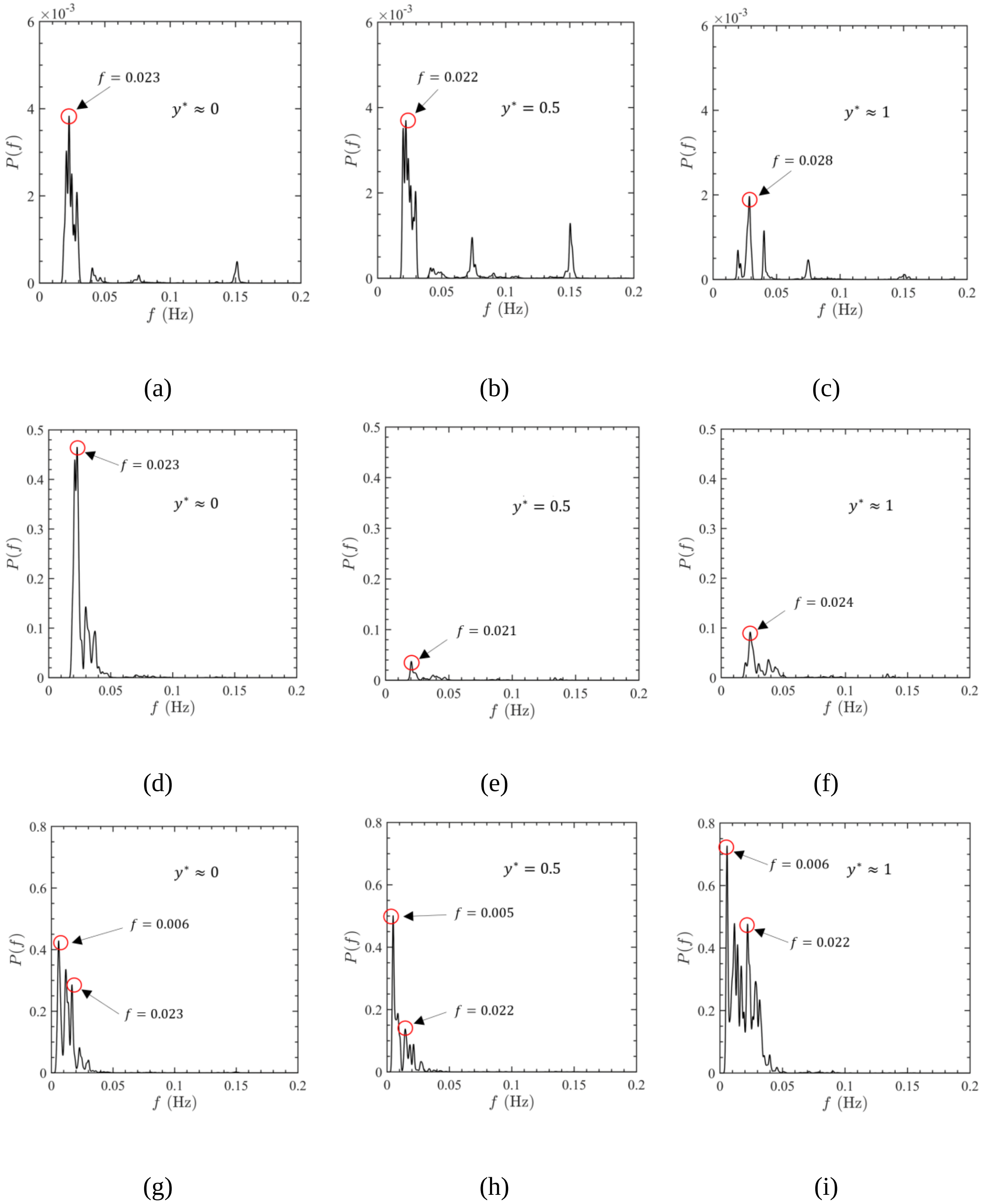

Figure 4-13. Power spectra of the horizontal mean temperature, $\langle T\rangle_x$ oscillation at three different vertical locations of bottom, top, and middle, $y^* \approx 0, 1, y^* =$ of the convection cell for three different Rayleigh numbers of (a)-(c) $Ra1$, (d)-(f) $Ra2$, and (g)-(i) $Ra3$.

The results for $Ra2$ which is shown in Figure 4-13(d)-(f) indicates that the frequency is almost constant for the three vertical locations. As can be observed from Table 4-2 the frequency corresponds to the peak of the power spectra for $Ra2$ varies from 0.021 Hz to 0.024 Hz, which similar to $Ra1$ is in the range of the frequency reported earlier for OB RBC flow. However, by increasing the temperature difference and moving to $Ra3$, it can be seen in Figure 4-13(g)-(i) that the temperature oscillation is quite different compared to the two other Rayleigh numbers, $Ra1$ and $Ra2$. The results show that multiple peaks exist within the frequency range of 0.005 Hz to 0.05 Hz, which reveals a more complex and dynamic nature of the flow in $Ra3$ compared to the $Ra1$ and $Ra2$. Unlike strictly periodic signals, flow is characterized by complex thermal fluctuations, resulting in a non-periodic temperature variation. These closely spaced frequency components represent various dynamic processes and thermal interactions within the system. The frequency corresponds to the peak of the power spectra for different vertical locations (see Table 4-2) for $Ra3$ varies from 0.005 Hz to 0.006 Hz which indicates slower fluctuations compared to the two other Rayleigh numbers and the temperature fluctuations of OB RBC. However, in the wide range of frequency oscillations, the frequency of 0.022 Hz to 0.023 Hz is one of the prominent values that exist for the two other Rayleigh numbers. For all the three Rayleigh numbers from Figure 4-13 and Table 4-2 it can be concluded that the frequency of the oscillations for both hot and cold boundaries are almost the same.

Table 4-2. Frequency of the horizontally mean temperature oscillation.

Vertical location	$Ra1$	$Ra2$	$Ra3$
$f_{y^*\approx 0}$ (Hz)	0.023	0.023	0.006
$f_{y^*=0.5}$ (Hz)	0.022	0.021	0.005
$f_{y^*\approx 1}$ (Hz)	0.028	0.024	0.006
$P\left(C_{T_{y_1^*}T_{y_2^*}}\right)$ (%)	46.8	55.4	52.6
$\rho_{T_{y_1^*}T_{y_2^*}}$ (%)	41.3	51.4	44.7
$\Delta\tau\ (s)$	21.9	20.4	16.2

Upon examination of Figure 4-13(a)-(c), it is evident that for $Ra1$, the power spectra of oscillations at the middle of the convection cell, $y^* = 0.5$ is as strong as the power spectra of oscillations at the bottom, $y^* \approx 0$. When a hot (cold) plume impinges to the cold (hot) boundary, it induces a thermal influence close to the boundary layer, affecting the temperature oscillation in that region. Similarly, when two thermal plumes impinge each other, a similar effect occurs even with a higher value for the power spectra in comparison to the impingement of the thermal plume to the boundary due to the aggregated kinetic energy of both plumes. This impact of the thermal plumes can lead to a higher temperature fluctuation compared to the scenario in which thermal plumes impinge one of the horizontal boundaries. Figure 4-14(a) shows an instantaneous temperature field of $Ra1$. In this figure, the zoomed view of the center of the convection cell indicates the boundary between hot and cold flow stream is a region where the impact of the hot and cold plumes occurs.

For two other Rayleigh numbers, $Ra2$ and $Ra3$, the power spectra can be seen in Figure 4-13(d)-(f) and Figure 4-13(g)-(i), respectively. For $Ra2$, it can be seen that the power spectra of the bottom and top boundaries, $y^* \approx 0$ and $y^* \approx 1$ are almost one order of magnitude larger than the one at the middle of the convection cell, $y^* = 0.5$. An instantaneous temperature field of $Ra2$ is shown in Figure 4-14(b), it can be seen that the temperature field is different compared to the one for $Ra1$ shown in Figure 4-14(a) and the cold and hot stream reach each other close to the thermal boundaries. For $Ra3$, however, as can be observed in Figure 4-14(c) the instantaneous temperature field is notably different and complex compared to the two other Rayleigh numbers inferring the formation of more rolling structures in the flow field compared to $Ra1$ and $Ra2$. Figure 4-13(g)-(i) shows that the power spectra of the oscillation for all the three vertical locations are in the same order. However more analysis in the vertical direction is required due to the complex temperature field containing multiple hot and cold streams.

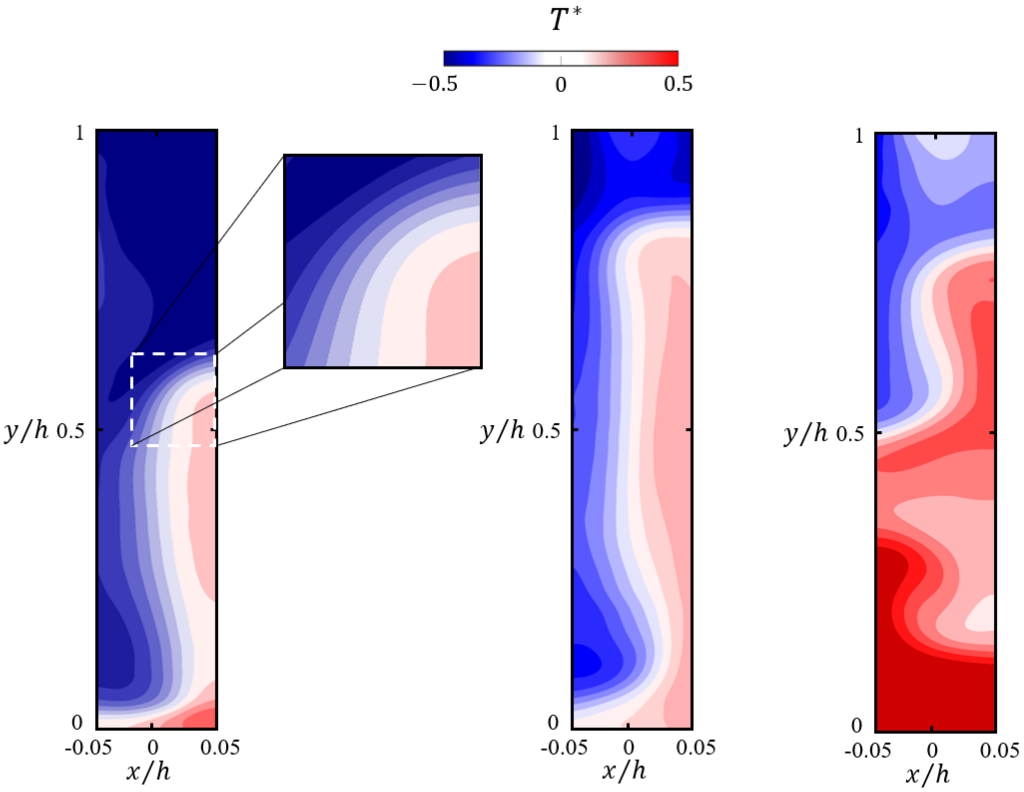

(a) (b) (c)

Figure 4-14. Instantaneous temperature fields for three different Rayleigh numbers of (a) $Ra1$, (b) $Ra2$, and (c) $Ra3$. The aspect ratio of the temperature field has been adjusted for a better visualization.

Reviewing the regions close to the thermal boundaries in Figure 4-14(a)-(c), it can be seen that the temperature varies horizontally along the x-axis, which infers the possibility of a variable temperature oscillation in this direction. This could be due to the impact of a thermal plume to a part of the thermal boundary, detachment of a thermal plume from a thermal boundary, asymmetric growth of a thermal plume, and the impact of an LSC on the thermal boundary.

Figure 4-15 shows the spatial variation of the peak of the power spectra and correspondent frequency along the x-axis for three vertical locations of $y^* \approx 0$, $y^* = 0.5$, and $y^* \approx 1$ at the three different Rayleigh numbers of $Ra1$, $Ra2$, and $Ra3$. By comparing the overall power spectra variation of the three Rayleigh numbers in Figure 4-15(a)-(c) it can be seen that by increasing the temperature difference between the hot and cold plates the temperature oscillation increases almost by an order of magnitude. Analyzing Figure 4-15(a), it becomes evident that the temperature oscillation's maximum power spectra of $Ra1$ occurs on the left-hand side of the convection cell, and this power gradually diminishes as one moves towards the right side of the convection cell. This trend holds true for all three vertical locations of bottom, top, and middle of the convection cell. The fact that temperature oscillations are more pronounced on the left side indicates that this is where thermal plumes are more actively interacting with the thermal boundaries or plumes with a different temperature, i.e., cold plume with hot plume. Conversely, on the right side of the convection cell, where the temperature oscillations are weaker, it suggests that thermal plumes are impinging or interacting less with the boundary (cold plate). This could be due to a decrease in the upward motion of fluid in that region or a weaker interaction between the plumes and the cold plate.

From Figure 4-15(a) a jump in the power spectra can also be observed at the bottom, $y^* \approx 0$, and middle, $y^* = 0.5$ of the convection cell at around $x^* \approx 0.4$, in which from Figure 4-14(a) it can be seen that this is the horizontal location where the hot and cold stream are in contact with each other. For $Ra2$, in Figure 4-15(b), the peak of the power spectrum occurs around the center of the convection cell, $x^* \approx 0.4$ where from Figure 4-14(a), it can be seen that it corresponds to the region where hot and cold streams meet. However, as can be seen in Figure 4-15(c) the power spectra variation for $Ra3$ is different when compared to $Ra1$ and $Ra2$ where there are multiple increases and decreases in the power spectra which is due to the complicated temperature field as shown in Figure 4-14(c). The variation of the power spectra variation along the x-axis in Figure 4-15(a)-(c) also indicates a lack of small-scale fluctuations. This observation suggests that the predominant temperature variations within the system are characterized by large-scale spatial patterns. This outcome is consistent with our initial observations made at the beginning of convection in Figure 4-7, during which, only the rise and fall of a single thermal plume were observed.

By examination of the frequency of temperature oscillations corresponding to the peak of the power spectra for $Ra1$ and $Ra2$, in Figure 4-15(d) and (e), it can be seen that the frequency of temperature oscillations remains almost consistent along the x-axis, with values ranging from 0.02 Hz to 0.03 Hz, irrespective of the vertical position within the fluid layer. However, for $Ra3$, the frequency dropped to approximately 0.006 Hz. These observations are consistent with the results in Figure 4-13 for mean temperature, $\langle T \rangle_x$ oscillations. However, at the top boundary of $Ra3$, the frequency increased to ~ 0.02 Hz by moving along the x-axis to $x = 0.5$, resembling the typical frequency values observed for $Ra1$ and $Ra2$. These observations suggest the sensitivity of the NOB RBC system to the temperature difference, particularly at $Ra3$, where a distinct behavior was observed, especially at the top boundary, implying alterations in convective patterns and energy transfer mechanisms.

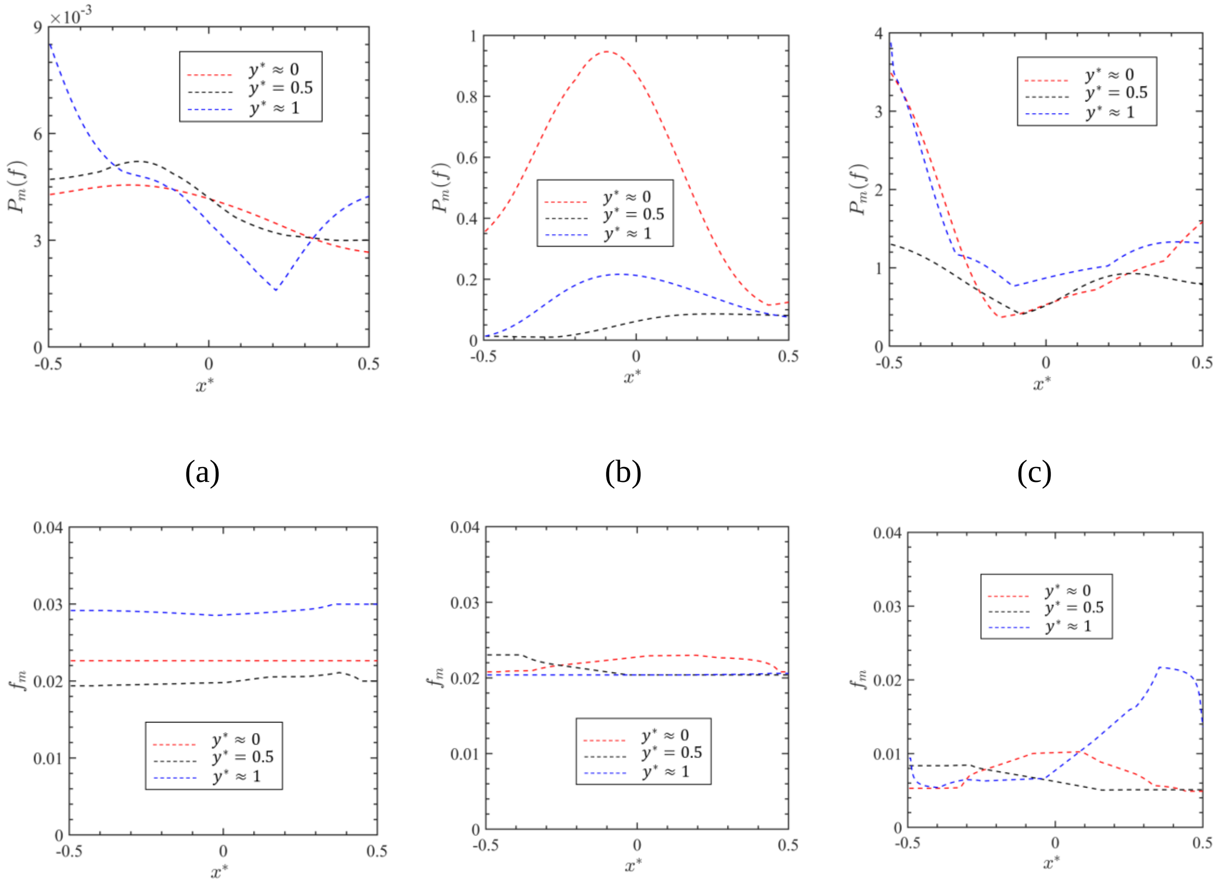

(a) (b) (c)

(d) (e) (f)

Figure 4-15. (a)-(c) Variation of the peak of the power spectra along the x-axis at three different vertical direction of bottom, top, and middle, $y^* \approx 0{,}1, y^* = 0.5$ of the convection cell for three different Rayleigh numbers of (a) $Ra1$, (b) $Ra2$, and (d) $Ra3$. (d)-(f) Corresponding frequency of the peak of the power spectra along the x-axis at the same vertical direction of bottom, top, and middle, $y^* \approx 0{,}1, y^* = 0.5$ for (d) $Ra1$, (e) $Ra2$, and (f) $Ra3$. In (a)-(c) the y-axis of each plot is adjusted for better visualization of the variation of frequency of each Rayleigh number.

Figure 4-16 illustrates the variation of the peak of power spectra of the horizontally averaged temperature, $\langle T \rangle_x$ oscillation along the y-axis, providing an examination of how temperature oscillations' strength and characteristic frequencies change in the vertical direction within the system. The result for $Ra1$ in Figure 4-16(a) shows multiple peaks from the mid-height, $y^* = 0.5$ of the convection cell to the hot boundary at $y^* \approx 0$. The fact that stronger temperature oscillations are observed at the mid-height of the convection cell suggests a level of symmetry in the convection cell structure. In a typical RBC, there is a symmetric pattern of rising warm fluid and descending cool fluid. The presence of stronger oscillations at the mid-height indicates that this region is also an active location for interaction of thermal plumes.

The result for $Ra2$ in Figure 4-16(b) shows that for this Rayleigh number, the oscillation of the temperature is stronger close to the boundaries, both hot and cold, while it dissipates along the vertical direction in the middle of the cell. The fact that the power spectra reaches its maximum value close to the boundary layers (both hot and cold) indicates that this is where temperature oscillations are most pronounced. In RBC, the boundary layers are regions where thermal plumes detach from the plates and rise (in the case of the hot plate) or descend (in the case of the cold plate). The maxima in the power spectra suggest that these regions play a crucial role in the generation and amplification of temperature oscillations. The result for $Ra3$ in Figure 4-16(c) shows multiple peaks along the y-axis. The observation of low and fluctuating power spectra along the vertical direction away from the boundary layers implies that the intensity of temperature oscillations diminishes as the location of interest moves into the interior of the convection cell. This is consistent with the expected behavior in RBC, where the thermal plumes become less dominant and the flow becomes less turbulent as one moves away from the boundary layers. The fluctuations in the power spectra along the vertical direction suggest that there is ongoing interaction and mixing between rising and descending thermal plumes within the interior of the convection cell. These fluctuations are linked to the convective rolls and cells that characterize the flow structure within the convection cell's interior.

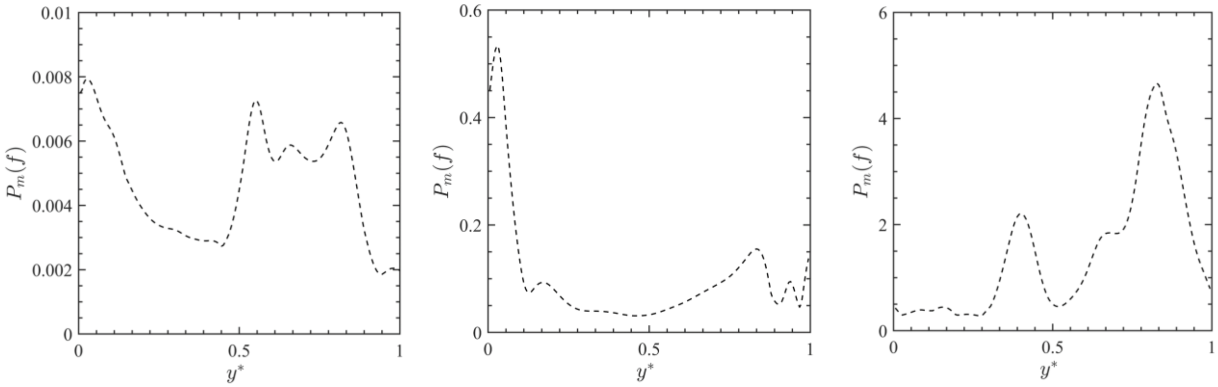

(a) (b) (c)

Figure 4-16. Variation of the peak of the power spectra of horizontally mean temperature, $\langle T \rangle_x$ oscillation along the y-axis for three different Rayleigh numbers of (a) $Ra1$, (c) $Ra2$, and (e) $Ra3$. The y-axis of each plot is adjusted for better visualization of the variation of the power spectra due to the significant difference of its value in different Rayleigh numbers.

Figure 4-17 shows the variation of the frequency corresponding to the peak of power spectra of horizontally mean temperature, $\langle T \rangle_x$ oscillation along the y-axis. Similar to the horizontal variation, here it can be seen that for $Ra1$ and $Ra2$, the frequency is in the range of 0.02 Hz to 0.03 Hz with a small increase in the vicinity of both thermal boundaries. However, for $Ra3$, it can be seen that the peak close to the bottom boundary is relatively significant with an overall frequency lower by an order of magnitude in comparison to the $Ra1$ and $Ra2$.

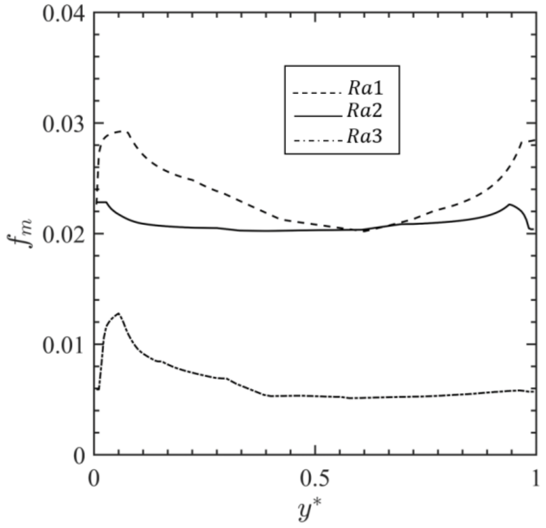

Figure 4-17. Variation of the correspondent frequency to the peak of the power spectra of horizontally mean temperature, $\langle T \rangle_x$ oscillation along the y-axis for Rayleigh numbers of $Ra1$, $Ra2$, and $Ra3$.

Temperature oscillations could be attributed to a recurring release of thermal plumes from the thermal boundary layers. A key feature here is the interplay between hot and cold plumes, i.e., a process where the detachment of one is triggered by the arrival of the other. This sets in motion a rhythmic alternation, with hot and cold plumes forming consecutively from the bottom and top plates. Notably, the timing of these emissions aligns with half of the oscillation period, as described in [70]. To examine this in this study, the correlation between the temperatures measured in the vicinity of the thermal boundaries is investigated. This has been investigated from the cross-correlation function of the temperature in the vicinity of the hot and cold boundaries, $T_{y_1^*}$ and $T_{y_2^*}$, as:

$$C_{T_{y_1^*},T_{y_2^*}}(\tau) = \langle \big[T_{y_1^*}(t+\tau) - \langle T_{y_1^*} \rangle\big][T_{y_2^*}(t) - \langle T_{y_1^*} \rangle]\rangle \big/ \sigma_{T_{y_1^*}} \sigma_{T_{y_2^*}} \tag{5}$$

In this equation, $\sigma_{T_{y_1^*}}$ and $\sigma_{T_{y_2^*}}$ are representing the corresponding standard deviations of $T_{y_1^*}$ and $T_{y_2^*}$, respectively. Figure 4-18 shows the cross-correlation function of the measured temperatures, $C_{T_{y_1^*},T_{y_2^*}}$ for $Ra1$, $Ra2$, and $Ra3$. The auto-correlation is also plotted in this figure as a reference. An alternative generation of the thermal plumes can be inferred in the case if a strong negative cross-correlation is found between the signal of the temperature close to thermal boundaries is found with a delay time equal to half of the oscillation period. This indicates that the formation of thermal plume from hot (cold) thermal boundary is triggered by the formation of the plume from the cold (hot) the thermal boundary [71].

Analysis of the cross-correlation function between temperature fluctuations at the bottom and top boundaries of the convection cell (the black line in Figure 4-18) reveals a positive correlation, with peak values, $P\left(C_{T_{y_1^*}T_{y_2^*}}\right)$, detailed in Table 4-2, measuring at $46.8\ \%$ for $Ra1$, $55.4\ \%$ for $Ra2$, and 52.6% for $Ra3$, indicating of relatively medium to weak association. Also, these correlation functions display a lack of sharp, singular peaks, with multiple peaks occurring at higher delay times in close proximity to the primary correlation peak. Furthermore, the correlation coefficients, $\rho_{T_{y_1^*}T_{y_2^*}}$, which are listed in Table 4-2, reflects a moderate to weak similarity in temperature oscillations between the hot and cold boundaries. The delay times, $\Delta\tau$, for $Ra1$ and $Ra2$, measured at 21.9 s and 20.4 s, respectively which aligns closely with the half oscillation period of ~ 20 s. This suggests a periodic and alternate emission pattern of thermal plumes, in harmony with the fundamental characteristics of RBC flow [70]. However, since the cross-correlation is positive, it can be inferred that the thermal plume from one thermal boundary (hot or cold) is not triggered by the emission of the thermal plume from the other thermal boundary. This positive cross-correlation with the half of the oscillation period actually demonstrates the direct effect of the one thermal plume (hot or cold) in increasing/decreasing of the thermal boundary layer where it impinges. This can be due to the high energy of the thermal plumes since the temperature difference is high compared to OB RBC and thermal plumes are single-large scale compared to the conventional aspect ratio enclosures. For $Ra3$, the delay time is notably different, 16.2 s, equivalent to $\sim 16\%$ of the corresponding temperature oscillation period. This variance from the half oscillation period implies a departure from the typical alternate and formation of thermal plumes, indicating a shift in the underlying dynamics of the convection system at higher Rayleigh numbers which is consistent with the experimental observation and temperature field discussed in Figure 4-14(c).

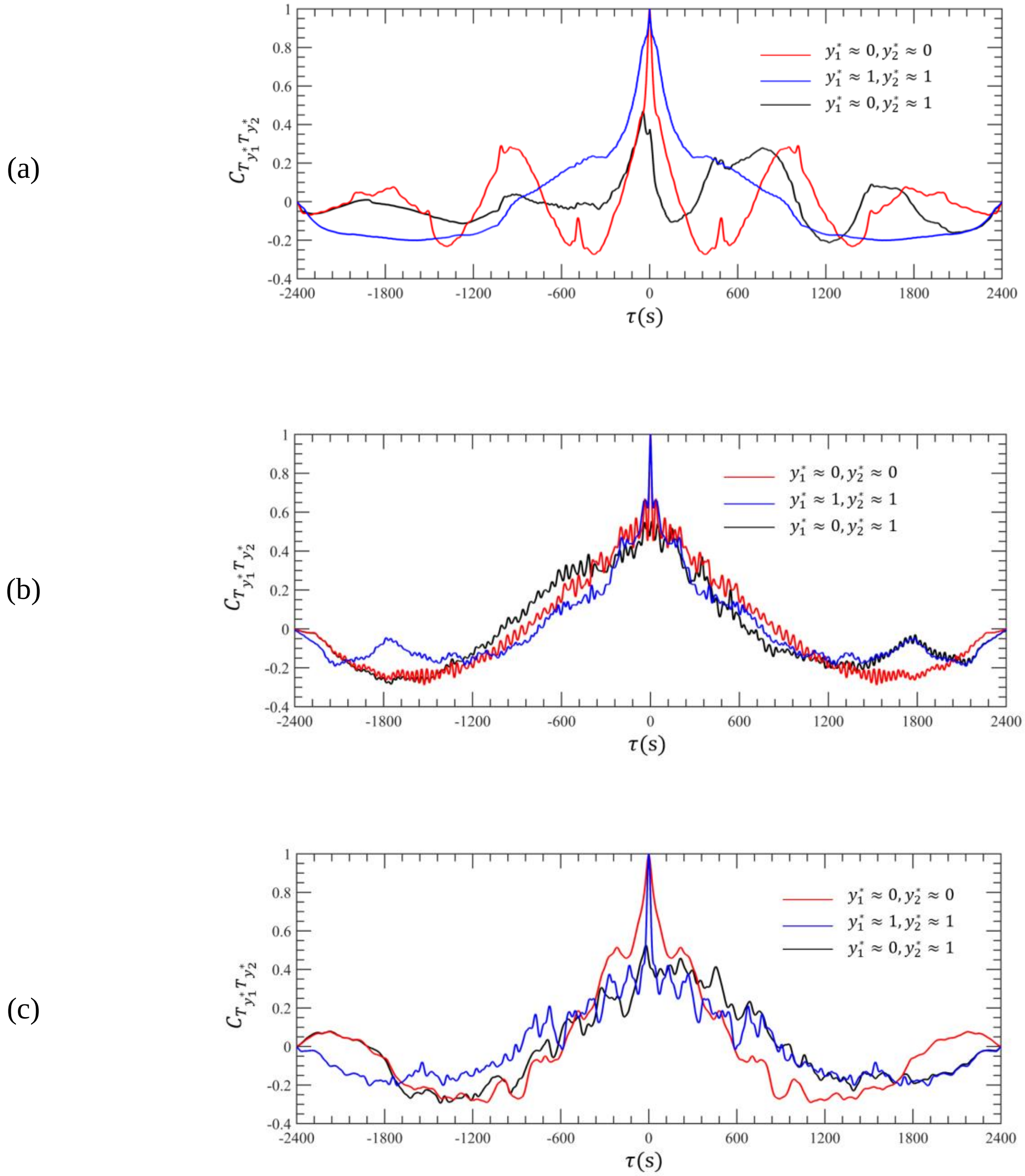

Figure 4-18. Temperature cross-correlation between the horizontally mean temperatures, $\langle T \rangle_x$ between hot and cold boundaries and their auto-correlations for three different Rayleigh numbers of (a) $Ra1$, (b) $Ra2$, and (c) $Ra3$. The black line is indicating the cross-correlation function between the temperature of the hot and cold boundary, red and blue lines are showing the auto-correlations just for comparison the auto-correlation function with the cross-correlation function.

Within the Oberbeck-Boussinesq condition, a normal distribution is anticipated for the probability density function of the temperature distribution due to the vertical symmetry between the hot and cold boundaries [73]. However, it is known that this temperature distribution deviates due to the NOB effect (Sugiyama et al., 2009). Hence it is interesting to see how does slendering the enclosure influence this asymmetry in the temperature distribution of NOB RBC. For this purpose, the probability density function (PDF) of the dimensionless temperature, $(T - \mu_T)/\sigma_T$ over both time and space is computed and shown in Figure 4-19 for three different Rayleigh numbers of $Ra1$, $Ra2$, and $Ra3$. Here, μ_T represents the spatial-temporal mean of the temperature, $\langle T \rangle_{x,y,t}$ and σ_T is showing its standard deviation.

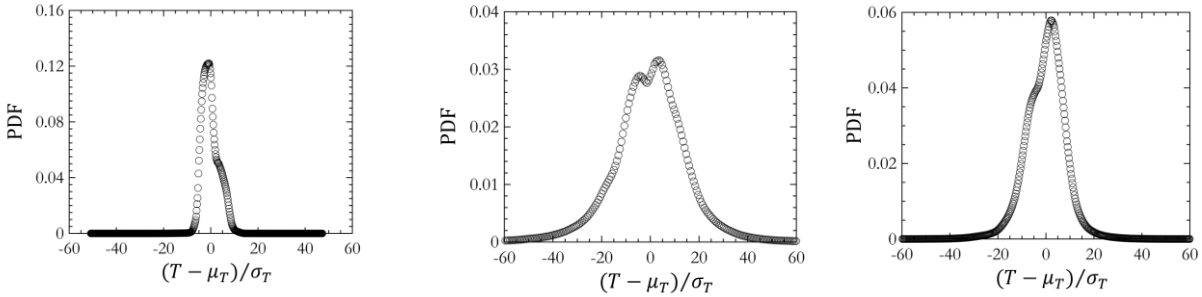

(a) (b) (c)

Figure 4-19. Probability Density Functions (PDF) of the normalized temperature distributions for different Rayleigh numbers of (a) $Ra1$, (b) $Ra2$, (c) $Ra3$.

For $Ra1$, the PDF exhibits a noticeable leftward skew with a bimodal distribution, indicating a propensity for temperatures to be lower than the mean temperature. However, for $Ra2$ and $Ra3$, there is a marginal rightward skew, suggesting temperatures that are slightly higher than the mean temperature. The skewness observed in this study, which deviates from the expected normal distribution, is more pronounced than what has been reported in prior numerical investigations [74]. This heightened skewness may be attributed to the unique conditions of the convection cell, particularly its high aspect ratio. The work of Hartmann et al. [38] can support the effect of lowering the aspect ratio on asymmetry of the temperature distribution. Their result of DNS within OB approximation showed that significant decrease in the aspect ratio of the convection cell such as $\Gamma = 0.1$ which is similar to current work leads to asymmetry in the vertical temperature profile. Hence, the high asymmetry in the temperature distribution in comparison to the NOB RBC in unit aspect ratios could be attributed to the influence of the aspect ratio.

The plot in Figure 4-20 depict skewness, $S_{T'} = \langle {T'}^3 \rangle_{x,y,t} / \langle {T'}^2 \rangle_{x,y,t}^{3/2}$ and flatness, $F_{T'} = \langle {T'}^4 \rangle_{x,y,t} / \langle {T'}^2 \rangle_{x,y,t}^{2}$ of temperature fluctuations as a function of Rayleigh numbers. This highlights the system's response to changing thermal conditions quantitively where T' denotes the deviation from mean, i.e., $T' = T - \mu_T$. As the Rayleigh number increases, indicating a more substantial temperature difference within the system, the skewness, $S_{T'}$ and flatness, $F_{T'}$ increases and decreases, respectively. Firstly, skewness, representing the asymmetry in the temperature distribution, rises with increasing Rayleigh numbers. This indicates a growing propensity for the distribution to deviate from normality, shifting towards higher-temperature anomalies. Secondly, flatness, which measures the sharpness of the distribution's peak, decreases as Rayleigh numbers increase. This reduction in flatness signifies a broader spread of temperature values, suggesting an increased likelihood of extreme temperature fluctuations. These trends collectively reflect the system's heightened sensitivity to temperature gradients as Rayleigh numbers increase, resulting in temperature fluctuations that are both skewed and broader in range.

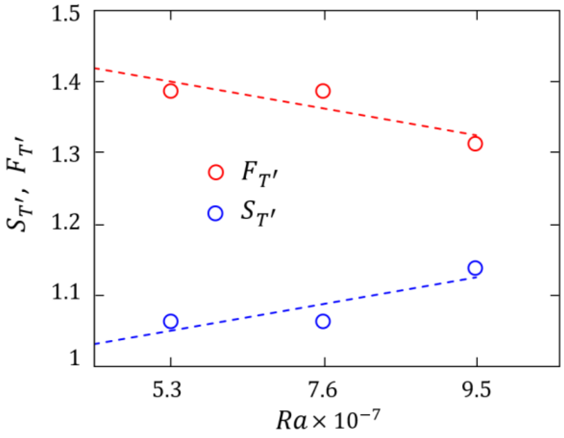

Figure 4-20. Plot of the temperature skewness, $S_{T'}$ and flatness, $F_{T'}$ versus Rayleigh number.

In RBC flow, the temperature distribution is symmetrical with respect to the center of the convection cell, hence the temperature at the center of the convection cell is equal to the mean temperature of the top and bottom boundaries. However, In NOB RBC, while the temperature distribution is asymmetric, there is a linear relation between the temperature of the center with the temperature difference, ΔT [46]. Variation of the mean temperature, $(T_H + T_C)/2$ and the half of the temperature difference, $\Delta T/2$ for the three Rayleigh numbers of $Ra1$, $Ra2$, and $Ra3$ is plotted in Figure 4-21 to examine the effect of the slendering the enclosure in NOB RBC on the centroid temperature of the convection cell. The temporal mean value of the temperature at the center of the convection cell, is compared with the mean temperature and half of the temperature difference in Figure 4-21. As can be seen in Figure 4-21, although there is a direct relation between the temperature difference, it is not linear and increases significantly by moving from $Ra2$ to $Ra3$. While for $Ra1$ and $Ra2$ the value of the temperature is close to half of the temperature difference as it approaches the mean temperature for $Ra3$. This observation of the temperature of the center of the convection cell is consistent with the PDF of the temperature distribution discussed earlier.

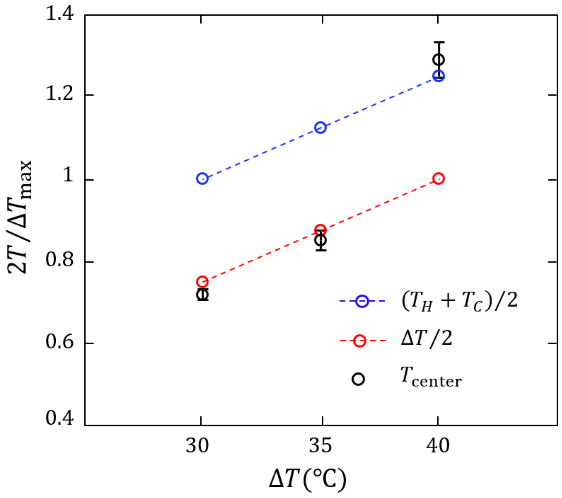

Figure 4-21. Variation of the center temperature for three cases of $Ra1$, $Ra2$, and $Ra3$. Error bar shows the standard deviation of temporal deviation.

Thermal dissipation rate, ε_T has a crucial role in heat transport processes explaining the thermal energy dissipation due to the effect of the fluid thermal diffusivity [75]. In a system such as RBC, it describes the global heat transport in the convection cell where the Nusselt number can be defined as $Nu = \varepsilon_T h^2/\kappa\Delta T^2$. The probability density function of the logarithmic normalized thermal dissipation for the three examined cases are shown in Figure 4-22, where the thermal dissipation rate is calculated as $\varepsilon_T = \kappa\sum(\partial T/\partial y)^2$. In Figure 4-22, μ_{ε_T} represents the temporal mean of the thermal dissipation rate and σ_{ε_T} is its standard deviation. Kolmogorov proposed the log-normal thermal energy dissipation rate [76], [77] while previous works clearly identify a non-log-normal distribution of the thermal dissipation rate with an extended tail to the left-hand side [76]. Here in Figure 4-22, similar behavior can be observed, with a sharper extended tail to the left-hand side of the distribution.

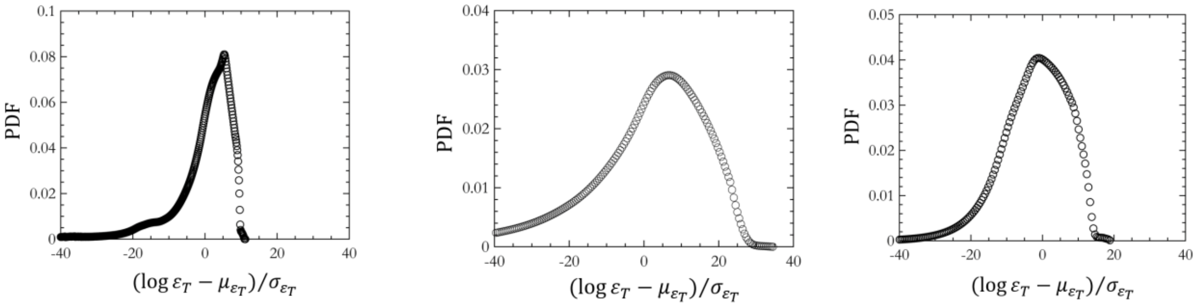

(a) (b) (c)

Figure 4-22. Probability Density Functions (PDF) of the normalized logarithm of the thermal dissipation distributions for different Rayleigh numbers of (a) $Ra1$, (b) $Ra2$, (c) $Ra3$.

4.4 Conclusion

The effect of lateral confinement of a convection cell along with the non-Oberbeck-Boussinesq condition (NOB) due to the high temperature difference of $\Delta T = 30$ ℃ to 40 ℃ was investigated in an RBC flow. The temperature field was visualized and measured by applying time-resolved two-colour two-dye planar laser-induced fluorescence during $2400\ s$ of the experiment from the start of convection and for three Rayleigh numbers of $Ra = 5.3 \times 10^7, 7.6 \times 10^7$, and 9.5×10^7. Rayleigh numbers were increased by increasing the temperature difference while the Prandtl number was $Pr \approx 6$. Visualization of the temperature field at the start of the convection showed that instead of multiple thermal plumes only a single plume is formed from both hot and cold boundaries. This was also inferred from the temperature oscillations close to the hot and cold boundaries during the development of the temperature field. It was also observed that the shape of the thermal plumes (both hot and cold) is not a common mushroom shape. Instead, they have a conical shape missing the top head. The shape and number of the thermal plumes were the same for all three Rayleigh numbers while increasing the temperature of the hot boundary in higher Rayleigh numbers led to the formation of a hot thermal plume with a higher temperature profile.

Examination of the development of the temperature in the vicinity of the thermal boundaries and whole field mean temperature showed that lateral confinement does not suppress the oscillations of the temperature. This was also evident by observing the spatio-temporal map of the evolution of the temperature field. It was also found that the amplitude of the oscillations generally increased by increasing the temperature difference between the top and bottom boundaries and moving to higher Rayleigh numbers since the hot thermal plumes have higher energy due to their higher temperature. By investigating the oscillation of the temperature field, it was found that the temperature oscillations are not strictly harmonic due to the wide range of frequencies in the vicinity of $f = 0.02$ Hz in which it became wider by increasing the temperature difference and moving to $Ra = 9.5 \times 10^7$. Investigation of the vertical variation of the power spectra of the oscillations showed that by increasing the temperature difference and consequently Rayleigh number, multiple rolling structures exist in the flow field along with a more complicated temperature field. The result of the temperature distribution and thermal dissipation revealed that slendering the enclosure does not suppress the vertical asymmetry of the temperature distribution known on NOB RBC, but it leads to an increase in the asymmetry of the temperature distribution. The probability density function of temperature distribution also showed a bimodal behavior in contrast to the Gaussian distribution of the temperature field in OB RBC. It was also found that the distribution of the thermal dissipation deviates from the log-normal thermal energy dissipation rate proposed by Kolmogorov.

References

[1] G. Ahlers, S. Grossmann, and D. Lohse, ‘Heat transfer and large scale dynamics in turbulent Rayleigh-Bénard convection’, Rev Mod Phys, vol. 81, no. 2, pp. 503–537, 2009, doi: 10.1103/RevModPhys.81.503.

[2] B. Adrian, CONVECTION HEAT TRANSFER. John Wiley and Sons, Inc, 2013.

[3] M. Krishnan, V. M. Ugaz, and M. A. Burns, ‘PCR in a Rayleigh-Bénard convection cell’, Science (1979), vol. 298, no. 5594, p. 793, Oct. 2002, doi: 10.1126/SCIENCE.298.5594.793/ASSET/9CB4B292-2B28-48C5-904A-F3E54DC8D228/ASSETS/GRAPHIC/SE4220979001.JPEG.

[4] D. Khodakov, J. Li, J. X. Zhang, and D. Y. Zhang, ‘Highly multiplexed rapid DNA detection with single-nucleotide specificity via convective PCR in a portable device’, Nature Biomedical Engineering 2021 5:7, vol. 5, no. 7, pp. 702–712, Jul. 2021, doi: 10.1038/s41551-021-00755-4.

[5] N. Fujisawa, S. Funatani, and N. Katoh, ‘Scanning liquid-crystal thermometry and stereo velocimetry for simultaneous three-dimensional measurement of temperature and velocity field in a turbulent Rayleigh-Bérnard convection’, Exp Fluids, vol. 38, no. 3, pp. 291–303, Mar. 2005, doi: 10.1007/s00348-004-0891-2.

[6] S. Zhou, C. Sun, and K. Xia, ‘Measured oscillations of the velocity and temperature fields in turbulent Rayleigh-Bénard convection in a rectangular cell’, pp. 28–30, 2007, doi: 10.1103/PhysRevE.76.036301.

[7] S. Ding, H. Li, W. Yan, and J. Zhong, ‘PHYSICAL REVIEW FLUIDS 4 , 023501 (2019) Temperature fluctuations relevant to thermal-plume dynamics in turbulent rotating Rayleigh-Bénard convection’, vol. 023501, pp. 1–11, 2019, doi: 10.1103/PhysRevFluids.4.023501.

[8] O. Shishkina, ‘Rayleigh-Bénard convection: The container shape matters’, Phys Rev Fluids, vol. 6, no. 9, p. 090502, Sep. 2021, doi: 10.1103/PHYSREVFLUIDS.6.090502/FIGURES/15/MEDIUM.

[9] E. P. Van Der Poel, R. Verzicco, S. Grossmann, and D. Lohse, ‘Plume emission statistics in turbulent Rayleigh–Bénard convection’, J Fluid Mech, vol. 772, pp. 5–15, Jun. 2015, doi: 10.1017/JFM.2015.176.

[10] R. Krishnamurti and L. N. Howard, ‘Large-scale flow generation in turbulent convection’, Proceedings of the National Academy of Sciences, vol. 78, no. 4, pp. 1981–1985, Apr. 1981, doi: 10.1073/PNAS.78.4.1981.

[11] X. L. Qiu and P. Tong, ‘Large-scale velocity structures in turbulent thermal convection’, Phys Rev E Stat Phys Plasmas Fluids Relat Interdiscip Topics, vol. 64, no. 3, p. 13, 2001, doi: 10.1103/PhysRevE.64.036304.

[12] H. D. Xi, S. Lam, and K. Q. Xia, ‘From laminar plumes to organized flows: the onset of large-scale circulation in turbulent thermal convection’, J Fluid Mech, vol. 503, no. 503, pp. 47–56, Mar. 2004, doi: 10.1017/S0022112004008079.

[13] S. Q. Zhou, Y. C. Xie, C. Sun, and K. Q. Xia, ‘Statistical characterization of thermal plumes in turbulent thermal convection’, Phys Rev Fluids, vol. 1, no. 5, p. 054301, Sep. 2016, doi: 10.1103/PHYSREVFLUIDS.1.054301/FIGURES/8/MEDIUM.

[14] Q. Zhou and K. Q. Xia, ‘Physical and geometrical properties of thermal plumes in turbulent Rayleigh–Bénard convection’, New J Phys, vol. 12, no. 7, p. 075006, Jul. 2010, doi: 10.1088/1367-2630/12/7/075006.

[15] K. Q. Xia, C. Sun, and S. Q. Zhou, ‘Particle image velocimetry measurement of the velocity field in turbulent thermal convection’, Phys Rev E Stat Phys Plasmas Fluids Relat Interdiscip Topics, vol. 68, no. 6, pp. 1–18, 2003, doi: 10.1103/PhysRevE.68.066303.

[16] X. Chen, D. P. Wang, and H. D. Xi, ‘Reduced flow reversals in turbulent convection in the absence of corner vortices’, J Fluid Mech, no. March, 2020, doi: 10.1017/jfm.2020.202.

[17] T. Käufer, P. P. Vieweg, J. Schumacher, and C. Cierpka, ‘Thermal boundary condition studies in large aspect ratio Rayleigh-B\’enard convection’, Feb. 2023, [Online]. Available: http://arxiv.org/abs/2302.13738

[18] J. Salort et al., ‘Thermal boundary layer near roughnesses in turbulent Rayleigh-Bénard convection: Flow structure and multistability’, Physics of Fluids, vol. 26, no. 1, Jan. 2014, doi: 10.1063/1.4862487.

[19] Q. Zhou, R. J. A. M. Stevens, K. Sugiyama, S. Grossmann, D. Lohse, and K. Q. Xia, ‘Prandtl–Blasius temperature and velocity boundary-layer profiles in turbulent Rayleigh–Bénard convection’, J Fluid Mech, vol. 664, pp. 297–312, Dec. 2010, doi: 10.1017/S0022112010003824.

[20] E. P. van der Poel, R. J. A. M. Stevens, K. Sugiyama, and D. Lohse, ‘Flow states in two-dimensional Rayleigh-Bénard convection as a function of aspect-ratio and Rayleigh number’, Physics of Fluids, vol. 24, no. 8, p. 085104, Aug. 2012, doi: 10.1063/1.4744988.

[21] X. He, E. Bodenschatz, and G. Ahlers, ‘Aspect ratio dependence of the ultimate-state transition in turbulent thermal convection’, Proc Natl Acad Sci U S A, vol. 117, no. 48, pp. 30022–30023, 2020, doi: 10.1073/pnas.2007399117.

[22] K. P. Iyer, J. D. Scheel, J. Schumacher, and K. R. Sreenivasan, ‘The dependence of heat transport law on aspect ratio is still unclear’, Proc Natl Acad Sci U S A, vol. 117, no. 48, p. 30024, 2020, doi: 10.1073/pnas.2007913117.

[23] R. Hartmann, K. L. Chong, R. J. A. M. Stevens, R. Verzicco, and D. Lohse, ‘Heat transport enhancement in confined Rayleigh-Bénard convection feels the shape of the container’, Epl, vol. 135, no. 2, 2021, doi: 10.1209/0295-5075/ac19ed.

[24] E. P. Van Der Poel, R. J. A. M. Stevens, and D. Lohse, ‘Connecting flow structures and heat flux in turbulent Rayleigh- Bénard convection’, Phys Rev E Stat Nonlin Soft Matter Phys, vol. 84, no. 4, pp. 1–4, 2011, doi: 10.1103/PhysRevE.84.045303.

[25] S. Weiss and G. Ahlers, ‘Effect of tilting on turbulent convection: Cylindrical samples with aspect ratio F = 0.50’, J Fluid Mech, vol. 715, pp. 314–334, Jan. 2013, doi: 10.1017/jfm.2012.520.

[26] H. D. Xi and K. Q. Xia, ‘Flow mode transitions in turbulent thermal convection’, Physics of Fluids, vol. 20, no. 5, 2008, doi: 10.1063/1.2920444.

[27] L. Zwirner, A. Tilgner, and O. Shishkina, ‘Elliptical Instability and Multiple-Roll Flow Modes of the Large-Scale Circulation in Confined Turbulent Rayleigh-Bénard Convection’, Phys Rev Lett, vol. 125, no. 5, Jul. 2020, doi: 10.1103/PhysRevLett.125.054502.

[28] K. L. Chong, S. Di Huang, M. Kaczorowski, and K. Q. Xia, ‘Condensation of Coherent Structures in Turbulent Flows’, Phys Rev Lett, vol. 115, no. 26, Dec. 2015, doi: 10.1103/PhysRevLett.115.264503.

[29] X. J. Huang, Y. P. Hu, and Y. R. Li, ‘Aspect ratio dependence of Rayleigh-Bénard convection of cold water near its maximum density in box-shaped containers’, Physics of Fluids, vol. 31, no. 7, Jul. 2019, doi: 10.1063/1.5097964.

[30] K. L. Chong and K. Q. Xia, ‘Exploring the severely confined regime in Rayleigh-Bénard convection’, J Fluid Mech, vol. 805, p. R4, Oct. 2016, doi: 10.1017/jfm.2016.578.

[31] R. Hartmann, R. Verzicco, L. Klein Kranenbarg, D. Lohse, and R. J. A. M. Stevens, ‘Multiple heat transport maxima in confined-rotating Rayleigh-Bénard convection’, J Fluid Mech, vol. 939, May 2022, doi: 10.1017/jfm.2021.1031.

[32] G. Ahlers, E. Brown, F. F. Araujo, D. Funfschilling, S. Grossmann, and D. Lohse, ‘Non-Oberbeck-Boussinesq effects in strongly turbulent Rayleigh-Bénard convection’, J Fluid Mech, vol. 569, pp. 409–445, 2006, doi: 10.1017/S0022112006002916.

[33] Z. H. Wan, Q. Wang, B. Wang, S. N. Xia, Q. Zhou, and D. J. Sun, ‘On non-Oberbeck-Boussinesq effects in Rayleigh-Bénard convection of air for large temperature differences’, J Fluid Mech, vol. 889, pp. A101–A1024, 2020, doi: 10.1017/jfm.2020.66.

[34] A. D. Demou and D. G. E. Grigoriadis, ‘Direct numerical simulations of Rayleigh–Bénard convection in water with non-Oberbeck–Boussinesq effects’, J Fluid Mech, vol. 881, pp. 1073–1096, Dec. 2019, doi: 10.1017/jfm.2019.787.

[35] Y. P. Hu, Y. R. Li, C. M. Wu, S. Z. Li, and M. H. Li, ‘Flow pattern and heat transfer in Rayleigh-Bénard convection of cold water near its density maximum in a rectangular cavity’, Int J Heat Mass Transf, vol. 107, pp. 1065–1075, Apr. 2017, doi: 10.1016/j.ijheatmasstransfer.2016.11.013.

[36] K. Sugiyama, E. Calzavarini, S. Grossmann, and D. Lohse, ‘Flow organization in two-dimensional non-Oberbeck-Boussinesq Rayleigh-Bénard convection in water’, J Fluid Mech, vol. 637, pp. 105–135, 2009, doi: 10.1017/S0022112009008027.

[37] S. Horn and O. Shishkina, ‘Rotating non-Oberbeck-Boussinesq Rayleigh-Bénard convection in water’, Physics of Fluids, vol. 26, no. 5, May 2014, doi: 10.1063/1.4878669.

[38] S. Horn, O. Shishkina, and C. Wagner, ‘On non-Oberbeck-Boussinesq effects in three-dimensional Rayleigh-Bénard convection in glycerol’, J Fluid Mech, vol. 724, pp. 175–202, Jun. 2013, doi: 10.1017/jfm.2013.151.

[39] K. Sugiyama, E. Calzavarini, S. Grossmann, and D. Lohse, ‘Flow organization in two-dimensional non-Oberbeck–Boussinesq Rayleigh–Bénard convection in water’, J Fluid Mech, vol. 637, pp. 105–135, Oct. 2009, doi: 10.1017/S0022112009008027.

[40] V. Valori, G. E. Elsinga, M. Rohde, J. Westerweel, and T. H. J. J. van der Hagen, ‘Particle image velocimetry measurements of a thermally convective supercritical fluid’, Exp Fluids, vol. 60, no. 9, pp. 1–14, 2019, doi: 10.1007/s00348-019-2789-z.

[41] H. Yik, V. Valori, and S. Weiss, ‘Turbulent Rayleigh-Bénard convection under strong non-Oberbeck-Boussinesq conditions’, Phys Rev Fluids, vol. 5, no. 10, Oct. 2020, doi: 10.1103/PhysRevFluids.5.103502.

[42] C. A. L. Y. and J. F. F. eds. Tropea, Springer Handbook of Experimental Fluid Mechanics. Berlin: Berlin: Springer, 2007.

[43] A. S. Nebuchinov, Y. A. Lozhkin, A. V. Bilsky, and D. M. Markovich, ‘Combination of PIV and PLIF methods to study convective heat transfer in an impinging jet’, Exp Therm Fluid Sci, vol. 80, pp. 139–146, 2017, doi: 10.1016/j.expthermflusci.2016.08.009.

[44] H. Hu, M. Koochesfahani, C. Lum, J. Coppeta, and C. Rogers, ‘Molecular tagging thermometry with adjustable temperature sensitivity’, Exp Fluids, vol. 40, no. 5, pp. 753–763, May 2006, doi: 10.1007/s00348-006-0112-2.

[45] D. Schiepel, D. Schmeling, and C. Wagner, ‘Simultaneous tomographic particle image velocimetry and thermometry of turbulent Rayleigh-Bénard convection’, Meas Sci Technol, vol. 32, no. 9, 2021, doi: 10.1088/1361-6501/abf095.

[46] S. Moller, C. Resagk, and C. Cierpka, ‘Long-time experimental investigation of turbulent superstructures in Rayleigh–Bénard convection by noninvasive simultaneous measurements of

temperature and velocity fields', Exp Fluids, vol. 62, no. 4, pp. 1–18, 2021, doi: 10.1007/s00348-020-03107-1.

[47] J. P. Crimaldi, 'Planar laser induced fluorescence in aqueous flows', Exp Fluids, vol. 44, no. 6, pp. 851–863, 2008, doi: 10.1007/s00348-008-0496-2.

[48] J. Sakakibara, K. Hishida, and M. Maeda, 'Measurements of thermally stratified pipe flow using image-processing techniques', Exp Fluids, vol. 16, no. 2, pp. 82–96, 1993, doi: 10.1007/BF00944910.

[49] M. B. Shafii, C. L. Lum, and M. M. Koochesfahani, 'In situ LIF temperature measurements in aqueous ammonium chloride solution during uni-directional solidification', in Experiments in Fluids, 2010, pp. 651–662. doi: 10.1007/s00348-009-0758-7.

[50] J. A. Sutton, B. T. Fisher, and J. W. Fleming, 'A laser-induced fluorescence measurement for aqueous fluid flows with improved temperature sensitivity', Exp Fluids, vol. 45, no. 5, pp. 869–881, 2008, doi: 10.1007/s00348-008-0506-4.

[51] H. Rochlitz and P. Scholz, 'Application of laser-induced fluorescence technique in a duct flow with one heated wall', Exp Fluids, vol. 59, no. 3, pp. 1–20, 2018, doi: 10.1007/s00348-018-2508-1.

[52] S. Moller, T. Käufer, A. Pandey, J. Schumacher, and C. Cierpka, 'Combined particle image velocimetry and thermometry of turbulent superstructures in thermal convection', J Fluid Mech, vol. 945, Aug. 2022, doi: 10.1017/jfm.2022.538.

[53] T. Käufer and C. Cierpka, 'Volumetric Lagrangian temperature and velocity measurements with thermochromic liquid crystals', Meas Sci Technol, vol. 35, no. 3, p. 035301, Mar. 2024, doi: 10.1088/1361-6501/ad16d1.

[54] S. Kashanj and D. S. Nobes, 'Application of 4D two-colour LIF to explore the temperature field of laterally confined turbulent Rayleigh–Bénard convection', Exp Fluids, vol. 64, no. 3, Mar. 2023, doi: 10.1007/s00348-023-03589-9.

[55] A. Eghtesad, M. A. Bijarchi, M. B. Shafii, and H. Afshin, 'A state-of-the-art review on laser-induced fluorescence (LIF) method with application in temperature measurement', Feb. 01, 2024, Elsevier Masson s.r.l. doi: 10.1016/j.ijthermalsci.2023.108686.

[56] W. Chaze, O. Caballina, G. Castanet, and F. Lemoine, ‘Spatially and temporally resolved measurements of the temperature inside droplets impinging on a hot solid surface’, Exp Fluids, vol. 58, no. 8, Aug. 2017, doi: 10.1007/s00348-017-2375-1.

[57] H. Ulrich, S. Sigl, M. Möhnle, E. Berrocal, and L. Zigan, ‘Droplet thermometry based on an optimized two dye two-color laser-induced fluorescence concept’, Front Phys, vol. 11, 2023, doi: 10.3389/fphy.2023.1235847.

[58] D. D. Gray and A. Giorcini, ‘THE VALIDITY OF THE BOUSSINESQ APPROXIMATION FOR LIQUIDS AND GASES’, Pergamon Press, 1976.

[59] E. Villermaux, ‘Memory-Induced Low Frequency Oscillations in Closed Convection Boxes’, 1995.

[60] H. D. Xi, S. Q. Zhou, Q. Zhou, T. S. Chan, and K. Q. Xia, ‘Origin of the temperature oscillation in turbulent thermal convection’, Phys Rev Lett, vol. 102, no. 4, Jan. 2009, doi: 10.1103/PhysRevLett.102.044503.

[61] Q. Zhou, H. D. Xi, S. Q. Zhou, C. Sun, and K. Q. Xia, ‘Oscillations of the large-scale circulation in turbulent Rayleigh-Bénard convection: The sloshing mode and its relationship with the torsional mode’, J Fluid Mech, vol. 630, pp. 367–390, 2009, doi: 10.1017/S0022112009006764.

[62] G. Ahlers, E. Brown, F. F. Araujo, D. Funfschilling, S. Grossmann, and D. Lohse, ‘Non-Oberbeck-Boussinesq effects in strongly turbulent Rayleigh-Bénard convection’, J Fluid Mech, vol. 569, pp. 409–445, 2006, doi: 10.1017/S0022112006002916.

[63] Y. Zhang et al., ‘Statistics of velocity and temperature fluctuations in two-dimensional Rayleigh-Bénard convection’, Phys Rev E, vol. 96, no. 2, Aug. 2017, doi: 10.1103/PhysRevE.96.023105.

[64] O. Shishkina and C. Wagner, ‘Analysis of thermal dissipation rates in turbulent Rayleigh-Bénard convection’, J Fluid Mech, vol. 546, pp. 51–60, Jan. 2006, doi: 10.1017/S0022112005007408.

[65] V. T. Vishnu, A. K. De, and P. K. Mishra, ‘Statistics of thermal plumes and dissipation rates in turbulent Rayleigh-Bénard convection in a cubic cell’, Int J Heat Mass Transf, vol. 182, Jan. 2022, doi: 10.1016/j.ijheatmasstransfer.2021.121995.

[66] H. Yang, Y. Wei, Z. Zhu, H. Dou, and Y. Qian, ‘Statistics of heat transfer in two-dimensional turbulent rayleigh-bénard convection at various prandtl number’, Entropy, vol. 20, no. 8, Aug. 2018, doi: 10.3390/e20080582.

Chapter 5: 2D vs 3D measurement of the temperature field and heat transfer in confined Rayleigh-Bénard convection

The time-resolved 3D temperature field of an RBC flow within a laterally confined convection cell is visualized and measured in this chapter. A high temperature sensitivity two-colour two-dye LIF system was developed along with a scanning system to apply 4D LIF for temperature measurement. The time-resolved 2D heat transfer coefficient is also estimated and compared with the one at the center of the convection cell.[*]

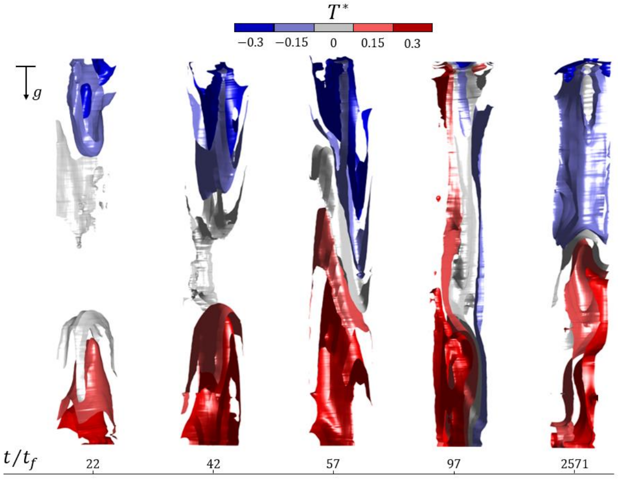

Graphical abstract for Chapter 5

---

[*] This chapter is published as: Sina Kashanj and David S. Nobes. “Application of 4D two-colour LIF to explore the temperature field of laterally confined turbulent Rayleigh–Bénard convection.” *Experiments in Fluids* 64.3 (2023): 46.

5.1 Introduction

Buoyancy-driven flow in an enclosure heated from below and cooled from above is known as Rayleigh-Bénard convection (RBC) [1]. Controlling parameters of RBC are defined as Rayleigh number, $Ra \equiv \alpha g \Delta T h^3 / \nu\kappa$, Prandtl number, $Pr \equiv \nu/\kappa$, and aspect ratio of the enclosure, $\Gamma \equiv w/h$, where α is the thermal expansion coefficient, w and h are the width and height of the convection cell respectively, g is gravitational acceleration, ν is kinematic viscosity, κ is thermal diffusivity of the fluid, and $\Delta T = T_H - T_C$ is the temperature difference between the hot, T_H, and cold, T_C, horizontal boundaries [2]. By exceeding the Rayleigh number from a critical value, convection initiates by the rise and fall of thermal plumes [3]. After this, development of the turbulent flow leads to the formation of unsteady circulation structures [4]. It is known that these circulating structures are driven by the formation of the thermal plumes [1].

RBC has been a focus of interest due to its many applications in engineering, studying the physics of the atmosphere, and in studying bifurcation and chaos [1]. Cubical and cylindrical enclosures are the most conventional shapes that have been used for studying RBC [2]. Among these two enclosures, both unit aspect ratio and high aspect ratio cells have been studied extensively [2]. However, recent investigations have found that the physics of heat and flow is quite different in lateral confined enclosures (low aspect ratio/vertically slender) [5]. Most of these studies are however, numerical works and are based on relevant experimental works that are limited to measurements of flow properties such as velocity and temperature at a limited number of points [6]. Although these experimental studies were insightful, whole field time-resolved measurements of flow properties are required to provide supporting evidence for the numerical studies.

The heat flux which is transferred by convection is defined as $Q = h_c A(T_w - T_\infty)$ in which h_c is the convection coefficient, A is the area of the solid boundary which is in contact with the fluid flow, T_w and T_∞ are the temperature of the solid boundary and fluid flow, respectively [7]. To measure the heat transfer and calculate the dimensionless heat transfer coefficient, Nusselt number, which is defined as $Nu = h_c l/\kappa$, where l is the characteristics length, measuring the temperature is necessary. Generally, in experimental works this is done by measuring the temporal variation of the temperature of the certain points of the domain, then the spatial averaged heat transfer can be calculated based on the number and distribution of the temperature sensors (thermocouple or thermistor) [7]. In RBC, similar procedure is usually taken to calculate the Nusselt number both for hot and cold boundaries [7].

To characterize and quantify the heat transport of RBC, two different theories have been proposed and investigated since 1954 [8]. The classical theory claims that the dimensionless heat transfer coefficient, the Nusselt number, Nu, of this system is only a function of Rayleigh number as $Nu \sim Ra^{1/3}$ [9], [10], [11]. However, the ultimate theory declares that heat transport of this system is also a function of the Prandtl number as $Nu \sim Pr^{1/2} Ra^{1/2}$ [11], [12], [13]. Many investigations have been untaken to unravel the physics of the heat transfer of an RBC and to explode the potential fit of either theory [14].

In experimental works on RBC, it can be seen that the measurement of flow properties such as temperature is usually limited to certain points in the domain [6]. Although whole field measurement of the temperature field was always a focus of interest [15], recently it can be seen that there are more attempts to apply whole field measurement techniques to measure the flow properties of the RBC [16], [17]. Theoretically, to calculate the Nusselt number solving the governing equations of the flow field is required [7]. In RBC by using the Oberbeck-Boussinesq approximation the Navier-Stokes equation is described as:

$$\partial_t u + u \cdot \nabla u + \nabla P = \nu \nabla^2 u + \alpha g T \hat{e}_y \tag{6}$$

in which u is the velocity of the fluid flow, P is the pressure, and $\hat{e}_y$ is the unit vector in vertical direction. The energy and continuity equations also can are defined as:

$$\partial_t T + u \cdot \nabla T = \kappa \nabla^2 T \tag{7}$$

$$\nabla \cdot u = 0 \tag{8}$$

As a result, in numerical studies of RBC, the calculation of the Nusselt number can be determined since the solution of above governing equations results in the calculation of the required velocity and temperature fields [7] In experimental studies, however, calculation of average Nusselt number is more usual due to the limited number of certain points on the boundary of the fluid domain due to the difficulties in the measurement of the velocity and temperature of the full spatial and temporal domain [6].

Other than heat transfer, knowledge of the temperature field and its evolution and dynamics of the evolving thermal plumes has also been a focus [8]. An example of this is the application RBC in the design of a new DNA polymerase chain reaction (PCR) which operates based on the circulation of flow in an enclosure with different temperature zones [18]. It is known that in confined RBC (confined only in one direction), 2D measurement and simulation can be used to capture the true physics [19]. However, the knowledge of the whole field in lateral confined RBC is necessary since generally the variation in the 3rd dimension is significant [5]. These points highlight the necessity to understand the time-resolve 3D data of the temperature of the whole domain of RBC to have a coherent understanding of the physics of this thermo-fluid system.

There are different techniques to measure the fluid temperature within an RBC such as thermocouples, liquid crystal [20], phosphorescent [21], and fluorescent thermography [22]. Planar laser-induced fluorescence (PLIF) is a non-intrusive fluorescent thermography technique that can be applied for temperature measurement of liquid or gaseous flow fields [23]. To increase the temperature sensitivity and reduce the effect of uncertainty sources such as the laser power fluctuation and local density gradient, two-colour PLIF has been developed [15]. Rhodamine B and Rhodamine 110 are a common pair of fluorescent dyes for two-colour PLIF in aqueous flow [24], [25]. However, due to the low temperature sensitivity of this pair of fluorescent dyes, there are several studies attempted to enhance the temperature sensitivity either by finding a new pair of fluorescent dyes or by changing the wavelength of the excitant source [26], [27], [28].

The experimental methodology for applying scanning 4D two-colour LIF on a laterally confined RBC is investigated in this chapter. The challenges and the solutions for achieving a relatively high temperature sensitivity is discussed. The evolution of the 3D temperature field from the onset of convection, $t = 0$ s to $t = 200$ s is captured using this method. From the temperature distribution near the horizontal boundaries, the whole field Nusselt number and its evolution is calculated for both hot and cold boundaries of RBC during the whole 200 seconds of the experiment. Results from the whole field measurement is also compared to the planar results to specify the role of 3^{rd} dimension in characterizing the physics of temperature distribution and heat transfer of the present RBC.

5.2 Two-colour PLIF

PLIF thermometry works based on the fluorescence light of some fluorescent materials [29]. Electrons of fluorescent molecules can be excited and move to a higher energy state by absorbing photons from a light course [29]. When this electron returns to the ground state, the fluorescence process occurs with the emission of a photon of light at a specific wavelength [29]. Usually the emitted signal of a fluorescent material has a longer wavelength than the excitant light [29].

The fluorescent intensity can be expressed as:

$$I_f = I_0 K \varepsilon L C \Phi \tag{9}$$

where K is a parameter representing the detection collection efficiency, depends mainly on optical apparatuses specification, I_0 is the incident laser intensity, C is the concentration of the fluorescent dye, ε is the absorption coefficient, L is the sampling length along the incident beam/sheet, and Φ is the photoluminescence quantum efficiency. For some molecules, the quantum efficiency Φ is temperature dependent. Based on that, by collecting the emitted signal of the fluorescent dye the temperature field can be quantified in a liquid/gas flow.

For one-colour PLIF, the emission from a single fluorescent dye, over a single spectral band can be used to measure the temperature field [30]. In this scenario, spatial and temporal variations of the laser intensity can affect the emitted signal of the fluorescent dye [15]. A good example of this is the formation of thermal plumes which is one of the characteristics of RBC [23]. Formation of thermal plumes in RBC leads to formation of different regions with variable temperature and concentration which influences the refractive index distribution of the whole field [23]. As an example, Figure 5-1 shows the calibrated fluorescence signal (one-colour) during the formation of hot plumes from a hot surface, excited by a laser sheet. As can be seen in this figure, the region at the top of the thermal plumes is quite smooth. But looking to the region filled with thermal plumes, some horizontal streaks can be observed which are due to beam steering as a results of refractive index variation in the flow field caused by the variation of the density of fluid by thermal plumes.

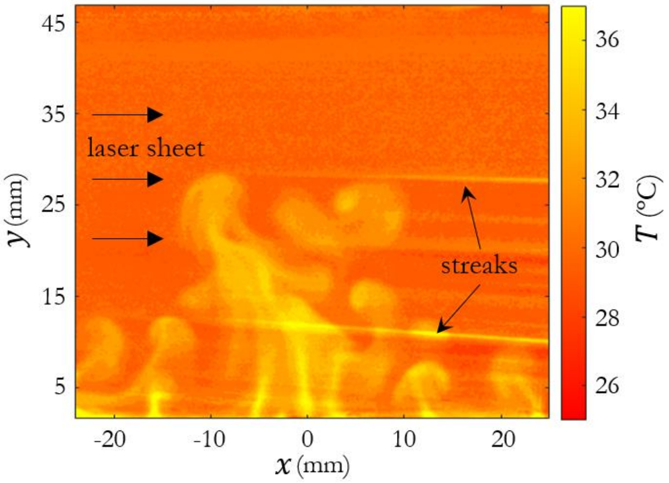

Figure 5-1. Signal of a temperature sensitive fluorescent dye (one-colour) showing the rise of the thermal plumes in an enclosure heated from below. Colour bar indicates the temperature range after applying the temperature calibration.

A common method to eliminate the effect of laser intensity variations is to use a ratiometric approach [31]. Applying a two colour two dye approach is the most common method to apply ratiometric PLIF. Using this approach, the temperature field will be calculated based on:

$$\frac{I_f(D1)}{I_f(D2)} = \frac{I_0 K \varepsilon(D1) L C(D1) \Phi(D1)}{I_0 K \varepsilon(D2) L C(D2) \Phi(D2)} \tag{10}$$

where $D1$ and $D2$ are representing the fluorescent signals of the first and second dyes. Assuming that same laser light with the same optical apparatus are used to collect the signal of both fluorescent dyes. Hence the temperature can be obtained considering fixed concentrations of a mixture of two fluorescent dyes, $C(D1)$ and $C(D2)$ the fluorescence intensity ratio R of the two dyes where $R = I_f(D1)/I_f(D2)$ can be defined as $R \equiv AF(T)$ [27]. In this definition, A is a constant representing the optical properties of the experimental setup, and $F(T)$ represents the overall temperature response function that is connected to the temperature dependence of the absorption coefficients, $\varepsilon(D1)$ and $\varepsilon(D2)$ and the quantum efficiencies of the two dyes, $\Phi(D1)$ and $\Phi(D2)$.

Rhodamine B (RhB) is a popular fluorescent dye that has been used for thermometry by one-colour PLIF [25]. The maximum temperature sensitivity that has been reported for this dye is around $-2\ \%\ /℃$ (Sakakibara et al. 1993). To apply two-colour two dye PLIF, Rhodamine 110 is the fluorescent dye that is commonly used with RhB [25]. Since this fluorescent dye is non-sensitive to temperature the overall temperature sensitivity of this pair of fluorescent dye stays the same as the one-colour RhB [15]. Table 5-1 shows studies that used this pair of fluorescent dyes to apply two-colour PLIF for thermometry. As can be seen, considering the different range of temperature and the wavelength of the laser, the maximum temperature sensitivity that has been obtained is similar to the one-colour PLIF reported by [15].

There have been several attempts to enhance the temperature sensitivity by finding new temperature sensitive fluorescent dyes, pairing different dyes, and changing the experimental conditions to apply two-colour PLIF [33]. The highest temperature sensitivity that has been found was reported by pairing Fluorescein, with positive temperature sensitivity, with Kiton red (Kr) and RhB, both with negative temperature sensitivity (see Table 5-1). Comparing the RhB with Kr, based on what has been reported by Sutton et al. (2008), Kr-Fl 27 has a higher temperature sensitivity than RhB-Fl 27. It is worth noting that there are two different types of Fluorescein dye have been applied for thermometry, Sodium Fluorescein (Fl) and Fluorescein 27 (Fl 27) with slightly different properties and temperature sensitivities [28].

Table 5-1. Fluorescent dye pairs and experimental specifications used to apply two-colour PLIF.

Dye	Excitation (nm)	Temperature range (℃)	Sensitivity (% /℃)	Reference
RhB-Rh110	488	15-40	1.7	Sakakibara and Adrian 1999
RhB-Rh110	532	20-65	1.7	Rochlitz and Scholz 2018
RhB-Rh110	532	15-85	2.0	Pérez et al. 2011
RhB-Rh110	532	30-88	1.2	Abdelghany et al. 2022
RhB-Rh110	488	20-40	2.0	Song and Nobes 2011
Fl 27-RhB	532	15-85	4.0	Perez et al. (2011)
Fl 27-RhB	532	20-60	5.0	Sutton et al. 2008
Fl-Kr	514	4-20	4.0	Shafii et al. 2010
Fl 27-Kr	532	20-60	6.0	Sutton et al. 2008

A list of experiments specifications of thermometry using Fl, Fl 27, and Kr is shown in Table 5-2. As can be seen, Fl emission signal is a function of laser wave length. The emitted signal of this dye has a positive temperature sensitivity when a 514 nm or 532 nm laser is used. However, it is negative and drastically lower when it is excited by a 488 nm laser light. For Kr, the temperature sensitivity is reported to be ~ $-1.5\ \%/\ ℃$ using 532 nm and 514 nm laser light.

Table 5-2 Fluorescent dyes and experimental specifications used to apply one-colour or two-colour PLIF.

Dye	Excitation (nm)	Temperature range (℃)	sensitivity (% /℃)	Reference
Fl	514	4-20	1.8	Shafii et al. 2010
Fl	514	20-60	2.4	Coppeta and Rogers 1998
Fl	488	20-60	0.16	Coppeta and Rogers 1998
Fl	488	24-46	0.30	Walker 1987
Fl 27	532	20-80	3.5	Sutton et al. 2008
Kr	514	4-20	1.5	Shafii et al. 2010
Kr	532	20-60	1.6	Sutton et al. 2008
Kr	514	20-60	1.5	Coppeta and Rogers 1998

Based on the literature, using Fl or Fl 27 with Kr can be used as two dyes for applying two-colour PLIF to achieve a high temperature sensitivity. However, since there is some lack of information regarding these three fluorescent dyes, such as the temperature sensitivity of Fl 27 when it is excited by a 488 nm laser, and it is different for each experimental setup, the temperature sensitivity of them was tested separately. This was carried out by calibrating the temperature versus the emitted light of each fluorescent mixture in the temperature range shown in Figure 5-2 using a dye calibration cell (LaVision GmbH) with a procedure similar to [15]). The properties of these three fluorescent dyes can be found in Table 5-3. As can be seen in Figure 5-2 (a), Fl and Fl 27 have a sensitivity of $+2.4$ % /℃ and $+2.2$ % /℃ respectively when they are excited by a 532 nm laser. When they are excited by a 488 nm source, the sensitivity of both of them was found to be as low as -0.3 % /℃.

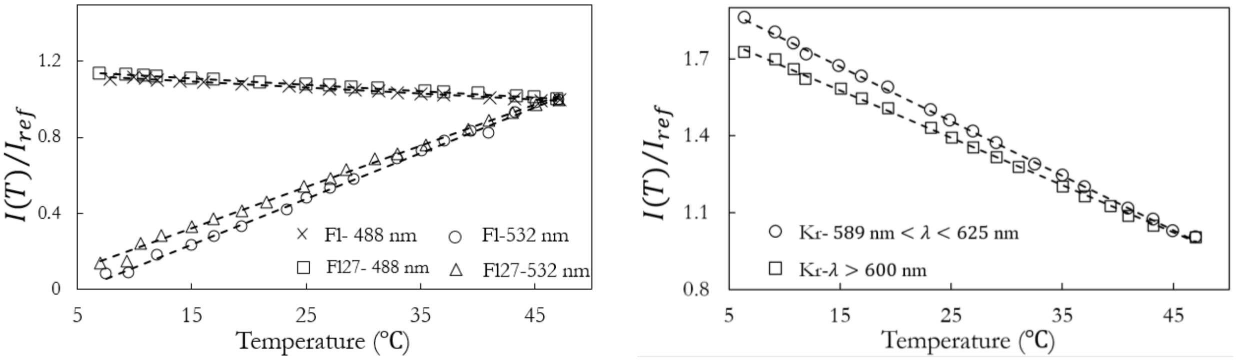

(a) (b)

Figure 5-2. (a) Temperature sensitivity of Fl and Fl 27, excited with 532 nm and 488 nm laser, (b) Temperature sensitivity of Kr, collected with $589\ \text{nm} < \lambda < 625\ \text{nm}$ band pass filter and with long pass, $\lambda > 600\ \text{nm}$ filter.

The emission spectrum of Kr at different temperatures given in [26] highlights that Kr has more sensitivity at the emission peak at 514 nm. Therefore, the temperature sensitivity of Kr signal when it is excited by a 532 nm laser is examined, once with a long pass filter with cut off wave length of 600 nm and once with a band pass filter capturing the signal of the peak of the emitted signal in the range of 589 nm to 625 nm. As can be seen in Figure 5-2(b), temperature sensitivity for the band pass and long pass filters is found to be $-2.1\ \%\ /℃$ and $-1.7\ \%\ /℃$ respectively, showing the advantage of the band pass filter.

Table 5-3 Properties of the fluorescent dyes used in two-colour LIF.

Fluorescent dye	Empirical formula	Molecular weight	λ_{abs} at peak (nm)	λ_{em} at peak (nm)
Sodium Fluorescein	$C_{20}H_{10}Na_2O_5$	376.27	586	490
Fluorescein 27	$C_{20}H_{10}Cl_2O_5$	401.20	504	529
Kiton red	$C_{27}H_{29}N_2NaO_7S_2$	580.65	565	514

To apply the two-colour PLIF in this study, an aqueous mixture of Sodium Fluorescein (Fl) and Kiton red (Kr) were used. The variation of the absorption and emission spectra of the dyes with the wavelength is illustrated in Figure 5-3, in addition to the location of the illumination laser at $\lambda = 532$ nm. A diagram depicting the fluorescent signals and optics is illustrated in Figure 5-4.

As can be seen in Figure 5-3, the laser light and absorption spectrum of Fl has a very small overlap which leads to a significant decrease in the emission signal of Fl [36] which leads to a decrease in signal to noise ratio, S/N of the Fl emitted light. To increase the intensity of the signal and prevent reduction in S/N ratio, the pH of this aqueous solution was increased to 11 by adding Sodium Hydroxide (NaOH) since the emission intensity of Fl has a direct relation with the pH of the aqueous solution [26]. As can be seen in Figure 5-3, the absorption spectrum of the Kr and emission spectrum of Fl have a considerable overlap. To prevent the absorption of the signal which is emitted by Fl, the concentration of both dyes was set to $10^{-7}\ \mathrm{mol/l}$ or $5.8 \times 10^{-5}\ \mathrm{g/l}$ for Kr and $3.8 \times 10^{-5}\ \mathrm{g/l}$ for Fl by accurately measurement the mass fraction of the dye powder in the mixture using a precision mass balance.

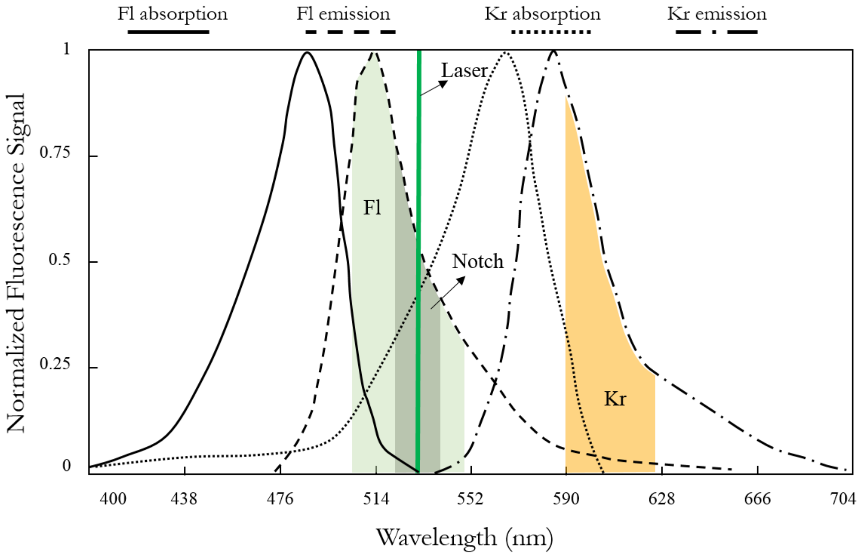

Figure 5-3. A plot of the absorption and emission signal variation with wavelength of Fl and Kr (after [27]). Different colours show the different filter wavelength range and the laser wavelength.

The Fl signal, which is marked in light green in Figure 5-3 and Figure 5-4, was collected using a band pass filter (#86-992, Edmund Optics Inc.) with a central wavelength (CWL) of 525 nm and full width at half maximum (FWHM) of 50 nm. The 532 nm laser light is also used to excite the Kr. To capture the Kr signal with maximum temperature sensitivity and to avoid receiving the Fl emitted signal, a band pass filter (#84-118, Edmund Optics Inc.) with CWL of 607 nm and FWHM of 36 nm was utilized, as shown in orange in Figure 5-3 and Figure 5-4. As can be seen in Figure 5-4, the emitted signal of the fluid domain can be divided into the three main signals of the Fl, Kr, and noise sources such as the laser light. A dichroic mirror with a cut-on wavelength of 567 nm (DMLP567L, ThorLabs Inc.) was used to divide the signals from the flow field to each camera. Using the dichroic mirror instead of a beam splitter was advantageous to maintain the whole energy of Fl emitted light. To avoid receiving the signal of the laser, shown in Figure 5-4, a notch filter (#86-130, Edmund Optics Inc.) with a central wavelength (CWL) of 532 nm and FWHM of 17 nm was utilized as shown in Figure 5-3.

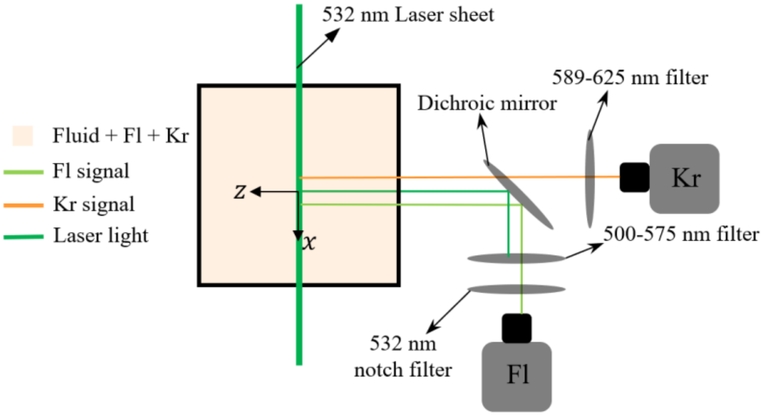

Figure 5-4. Two-colour PLIF signals and optics diagram.

Figure 5-5 shows the result of the intensity versus temperature calibration of the Fl-Kr mixture. The intensity-temperature calibration of the fluorescent dyes which leads to Figure 5-5(a) has been carried out using a dye calibration cell (LaVision GmbH) with the same conditions of the experiments, ranging from $5\ ℃ < T < 47\ ℃$. Fl has a positive temperature sensitivity of $\sim +$

$1.3\ \%/℃$ and Kr has a temperature sensitivity of $\sim -1.9\ \%/℃$. As can be seen, the temperature sensitivity of the signal of each dye is less comparing to their sensitivity when they were measured individually (as shown in Figure 5-2). One reason for this is increasing the pH of mixture for increasing the signal of Fl [31]. Figure 5-3 also highlight a notable overlap between the emission spectra of Kr and emission spectra of Fl which can lead to a decrease in temperature sensitivity of Kr. The ratiometric intensity-temperature graph, Figure 5-5 (b), indicates the temperature measurement with the overall temperature sensitivity of $\sim 7.3\ \%/℃$, which is a higher result compared to the literature shown in Table 5-1. Data points of the calibration graph of the two-colour method (Figure 5-5 (b)) was obtained by dividing individual data points of the linear calibration graphs of Kr and Fl (Figure 5-5 (a)). Dividing the linear, single-color calibration data for the two dyes leads to the non-linear ratiometric response shown in Figure 5-5 (b) of the two-color sensitivity with temperature. The general overall temperature sensitivity of $\sim 7.3\ \%/℃$ is calculated based on the mean linear slope of the graph in Figure 5-5(b) following the approach used by Sutton et al. (2008) and Shafii et al. (2010).

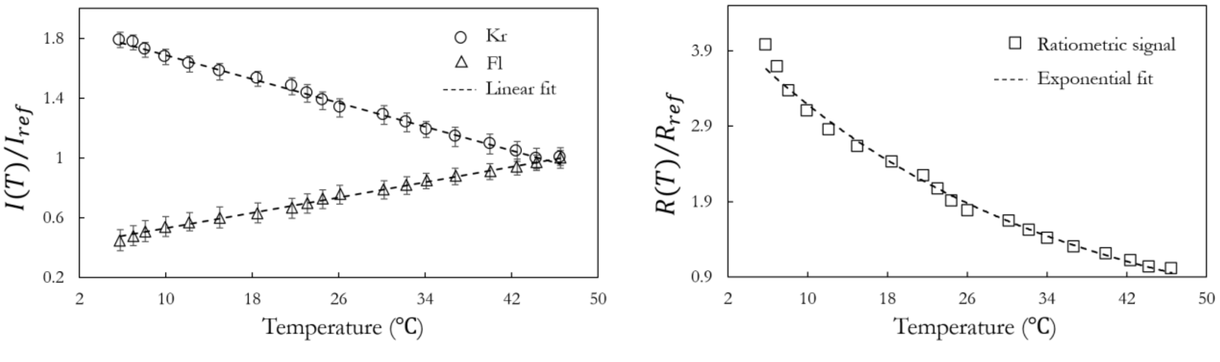

(a) (b)

Figure 5-5. Normalized intensity-temperature calibration graph. (a) One colour, Fl and Kr calibration, (b) Ratiometric intensity-temperature graph. Error bars in (a) indicates the standard deviation of the intensity of fluorescence signal in different depths.

Previous investigations [26] showed that a 532 nm laser can provide the highest temperature sensitivity in comparison to the lower excitation wavelengths such as 526 nm, 515 nm, 510 nm, and 488 nm when Fl 27 is used for Fluorescence thermometry. The results of temperature sensitivity of Fl27 indicated in Figure 5-2 (a) agrees with Pérez et al. results, and from the same figure it can be seen that Fl has the same temperature sensitivity variation as Fl 27 using 532 nm and 488 nm excitation wavelengths. As a result, it can be inferred that using 532 nm laser lead to maximum temperature sensitivity using Fl. For the experiments of this work, a diode pump laser with a maximum power of 2 W and wavelength of 532 nm was used to excite the fluorescent dyes.

A schematic of the optical measurement system implemented to apply 4D two-colour LIF is illustrated in Figure 5-6. Two scanning mirrors (GVS002, ThorLabs Inc.) were used first to make the laser sheet (scanning mirror-y) and then to scan the channel depth, z-direction (scanning mirror-z) with the laser sheet itself. As depicted in Figure 5-6, two double convex lenses were set in front of the laser beam to minimize the beam and respectively sheet thickness which led to FWHM of 120 μm. A double convex lens with a focal length of 80 mm also positioned in front of the scanning mirrors, collimates the laser sheet.

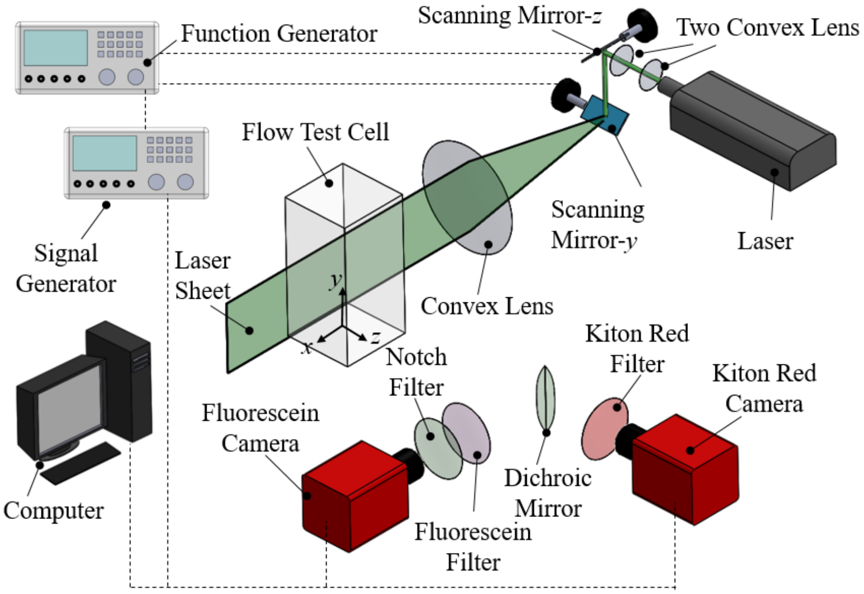

Figure 5-6. Schematic of the optical measurement system used to apply 4D two-colour LIF.

To collect signals of the fluorescent dyes, two 8-bit high-speed CMOS cameras (Flare 12M125, IO Industries Inc.) with a maximum frame rate of 220 fps and resolution of 2048 pixels × 2048 pixels were utilized. A two-channel function generator controlled the frequency and amplitude of the scanning mirrors. A signal generator was also utilized to synchronize the cameras and the two scanning mirrors. A timing plot of the signals generated to control the scanning mirrors and synchronize them with the cameras is illustrated in Figure 5-7. In this figure, Signal A is the waveform that scans the laser sheet in the depth of the test section. The waveform's initial voltage defines the initial position of the laser sheet in the *z*-direction obtained by the voltage-space calibration.

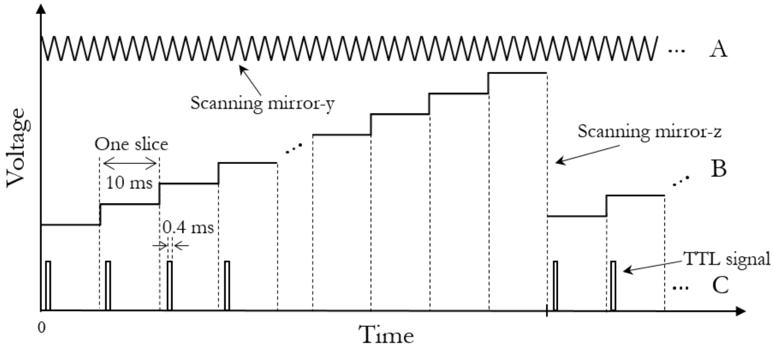

Figure 5-7. Schematic diagram of the three signals produced to synchronize the two scanning mirrors and the cameras.

To apply 4D LIF, 9 slices with a 0.5 mm spacing and 0.5 mm offset from the two vertical boundaries were used to scan the depth of the channel, z-direction. Signal B in Figure 5-7 is set to trigger the laser beam as it was scanned through the z-direction as is shown in Figure 5-6. The periodic-pulse, Signal C is a TTL signal generated to control the framerate of the cameras and synchronize them with the scanning mirrors. For each plane a single TTL signal was generated to capture a frame per plane. To freeze the motion of the thermal plumes and temperature variations, the frequency of the scan is set to be much higher than the time scale of the flow, free falling time defined as $t_f \equiv h/\sqrt{\alpha g \Delta T h}$. As a result, having a 9-slice planar temperature field stack allowed the generation of the 3D time-resolved temperature field.

For the PLIF application, a scanning laser beam to generate the laser sheet is advantageous comparing to generation of a static laser sheet by bulk optics such as cylindrical and Powell lenses [37]. Based on a numerical simulation [37], it was shown that to capture the flow features such as the thermal plumes and local temperature variations using a scanning system leads to a sharper image of those features. Using a scanning system also allows a relatively thin laser sheet to be used which avoids capturing the out of plane properties [37]. Figure 5-8(a) shows the intensity of both

Kr and Fl emission signal excited by the laser sheet at a constant temperature at $T = 25.4$ ℃. As can be seen for $y = 0$ line for both fluorescent dyes the signal distribution is uniform with the overall deviation of 0.2 %. For $x = 0$ line, as the light is absorbed by the fluorescent dye, decay in the emitted light is expected [38]. However, as can be seen in Figure 5-8(b) the overall deviation is equal to 1.5% minimizing the laser sheet correction requirement along the light sheet.

Temperature-intensity calibration was performed with the same laser sheet and optical system used to record the experiment images. This was performed separately for each plane, since the distance from the laser sheet to the collector sensor, in this case a CMOS camera affect the emitted light from the fluorescent dye [29]. Error bars in Figure 5-5(b) indicate the standard deviation in the intensity emitted from Kr and Fl from each plane for the images of temperature in the range of 5 ℃ $< T < 47$ ℃. Since a ratiometric approach has been employed in this work, it is necessary to match the field of view of each camera. For this purpose, each camera is set on a microstage having two degree of freedom in moving in x and $z -$direction. After the setting the field of view of each camera, calibration was performed using a target at 9 different planes by a commercial software (Davis 10.0.5, LaVision GmbH). The result of the camera calibration for each plane showed that the variation in magnification in the depth of the domain was as low as 0.5 % at the furthest distance from $z/w = -0.5$ to $z/w = 0.5$.

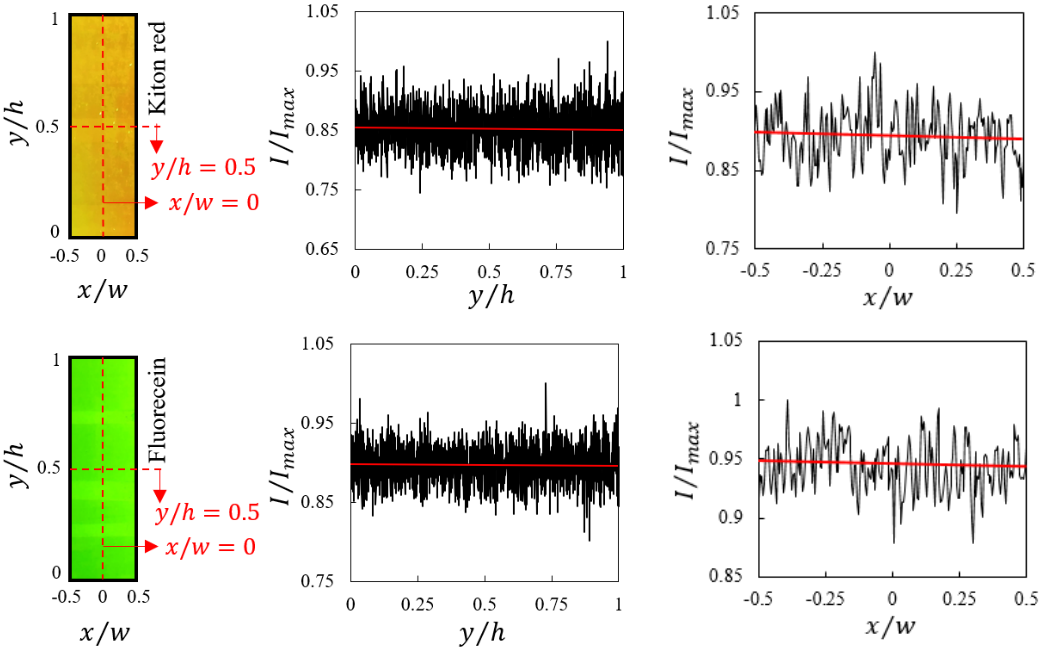

(a) (b)

Figure 5-8. (a) Variation of the emitted light of Kr (top) and Fl (bottom) along (a) $x/w = 0$ and (b) $y/h = 0$ lines.

A slender cell for the RBC with dimensions of $5\times5\times50$ mm^3 and aspect ratio, $\Gamma = w/h$, equal to 0.1, shown in Figure 5-9(c) was used for this experiment. The test section is made from an acrylic sheet with a thickness of 6.35 mm that has a low thermal conduction coefficient of $0.2\ \mathrm{W/mK}$. The temperature boundary conditions, shown in Figure 5-9(c), can be described as a constant temperature at the top, $T_H = 45$ °C and bottom, $T_C = 5$ °C and adiabatic at the side walls, $\partial T/\partial x = \partial T/\partial z = 0$. The field-of-view (FOV) of the imaging systems where the temperature investigations were carried out is also highlighted in Figure 5-9(c). A rendering of the physical set of the slender cell used for this experiment is shown in Figure 5-9(b). To ensure that the temperatures of the hot and cold heat sources remain constant during the tests, the heat exchangers were connected to thermal baths to control surface temperatures. End heat exchangers feature a copper plate to improve the uniformity of the heat transfer surface. The support bases are made using an SLA 3D printer (Form3, Formlabs Inc.) and printing material, a liquid photopolymer, with a low thermal conduction coefficient of $0.15\ \mathrm{W/mK}$. To ensure that temperature is distributed constantly on the surface of the copper plate, the temperature distribution was visualized by an IR camera (FLIR A35, FLIR Systems Inc.). The temperature distribution on the hot solid boundary is shown in Figure 5-9(a), showing a smooth constant distribution of the temperature for the whole domain.

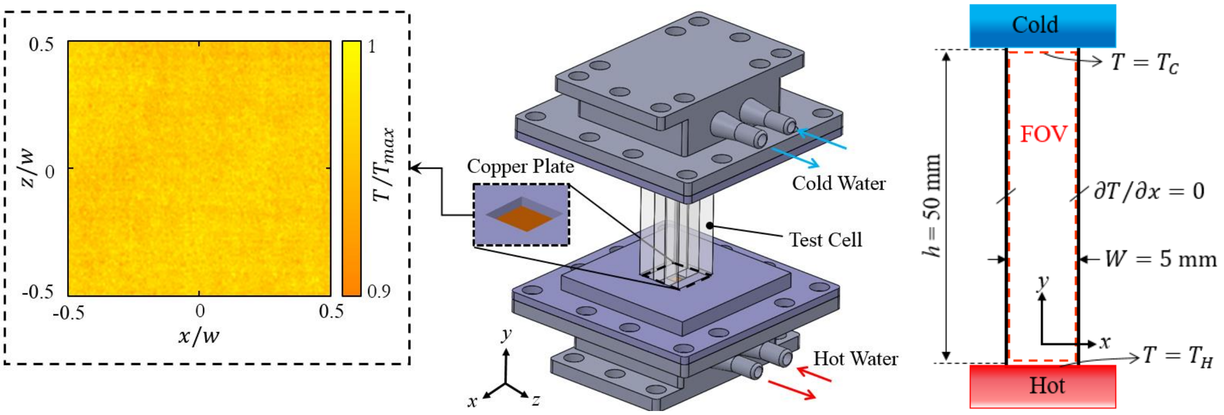

(a) (b) (c)

Figure 5-9. (a) Temperature distribution on the copper surface of the hot heat exchanger. (b) Rendering of the solid model of the slender rectangular RBC cell. (c) Schematic of the dimensions and boundary conditions of the RBC test cell.

5.3 Results and discussion

The instantaneous temperature field at four different time instances is shown in Figure 5-10. To examine and visualize the temperature field variations at the depth of the convection cell, the instantaneous temperature fields are shown in three different depths: at the center of cell where $z/w = 0$, close to the first vertical boundary, $z/w = -0.3$, and close to the second vertical boundary, $z/w = 0.3$. The instantaneous 3D reconstructed temperature fields are also shown in Figure 5-11 using temperature iso-surfaces. From the temperature fields at the first two time instances, $t/t_f = 22$ and $t/t_f = 42$, the number and shape of the hot and cold thermal plumes can be observed. In comparison to the thermal plumes that are formed in a unit aspect ratio enclosures such as those shown in Figure 5-1, and in (Xi et al.2004), it can be seen that only one thermal plume from each boundary is formed. It also can be observed that a conical shape is developed instead of the common observed mushroom shape. Although this has not been reported earlier, it was shown that in Hele-Shaw enclosures, which are severely confined only in one direction, the shape of the thermal plumes is different comparing to the mushroom shape plumes (Letelier et al. 2019; Liu et al. 2020). This implies the effect of the shape of the enclosure on properties of the thermal plumes.

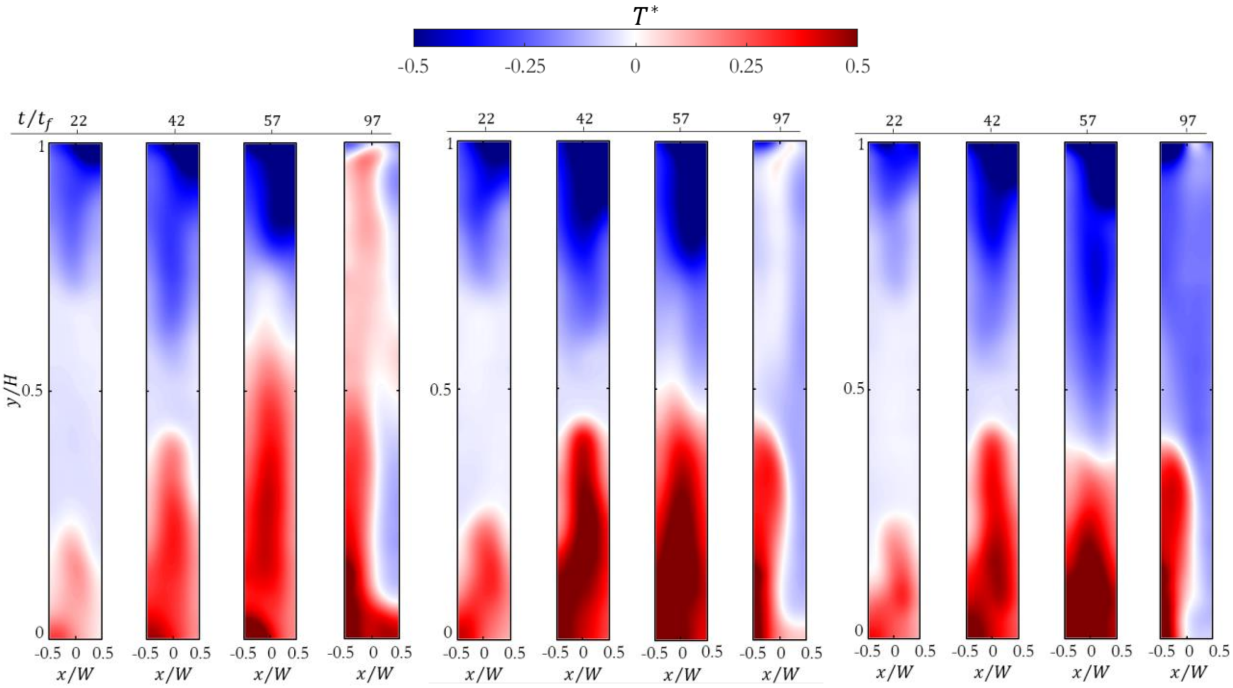

(a) (b) (c)

Figure 5-10. Instantaneous planar temperature fields at three different planes of (a) $z/w = -0.3$, (b) $z/w = 0$, and (c) $z/w = 0.3$.

For $t/t_f = 57$ in Figure 5-11, it can be seen that the two plumes do not collide and mix. Instead, they pass each other from a separate side of the enclosure. However, this cannot be inferred from the planar temperature field at $z/w = 0$ shown in Figure 5-10(b). However, by examining the planar temperature fields at the same time instance, $t/t_f = 57$, and at $z/w = -0.3$ (Figure 5-10(a)) and $z/w = 0.3$ (Figure 5-10(c)), it can be seen that at $z/w = -0.3$, the hot region, $T^* > 0$ is dominant and at $z/w = -0.3$ the cold region, $T^* < 0$ is dominant. At $t/t_f = 97$, from Figure 5-11, it can be seen that the cold and hot flow have reached the hot and cold boundary respectively. At this instant the temperature field is divided to two vertical regions implying the circulation of the flow from the bottom to the top and reverse. This has also been reported recently in [41] and [42] in which the flow properties of RBC in slender cells were investigated by applying DNS.

Similar to $t/t_f = 57$, the volumetric temperature field at $t/t_f = 97$ cannot be found by the temperature field at $z/w = 0$ unless the data of the other two planes is known. Although the time-resolved experiment was conducted for $\Delta t/t_f = 284$, to have insight into the heat transfer and temperature field after a long time, data was collected for other instances such as $t/t_f = 2571$ which is shown in Figure 5-11. As can be seen in this figure, the temperature field of the flow has been divided into two zones: a hot zone, $T^* > 0$ at the bottom and a cold zone $T^* < 0$ at the top of the fluid domain. This temperature field is consistent with the one has been reported recently in [41].

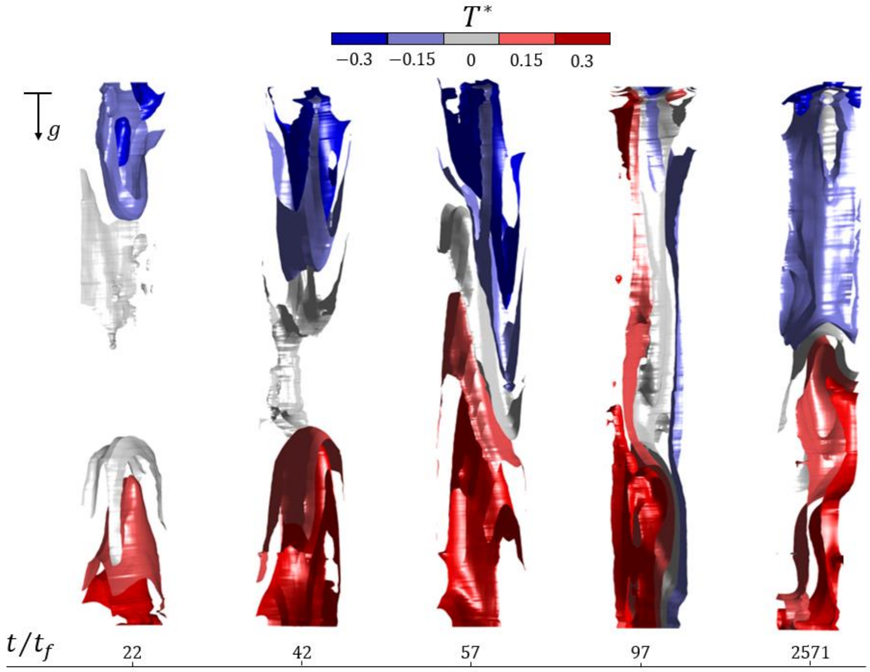

Figure 5-11. Evolution of the temperature iso-surfaces of $T^* = -0.3, -0.15, 0, 0.15, 0.3$ in the slender RBC for five different time instances.

To investigate and quantify the temperature evolution, the area of the temperature field, A is divided into two regions of hot, A_{hot} with threshold of $T^* > 0.025$, and cold, A_{cold} with the threshold of $T^* < 0.025$ where $T^* = 0$ is the initial temperature of the fluid domain. Using the same threshold, the volume of the temperature field, $\forall$ is divided to a hot region, $\forall_{\mathrm{hot}}$ and a cold region, $\forall_{\mathrm{cold}}$. The evolution of the hot and cold regions is examined both for 3D temperature field and the planar temperature fields at three planes discussed earlier in Figure 5-10. As is shown in Figure 5-12, for all the three planes, both hot and cold regions grow linearly and with the same rate after the onset of convection, $t/t_f = 0$ by rise and fall of the hot and cold thermal plumes. The time in which plumes meet for the very first time is a turning point in these plots. For $z/w = -0.3$, it can be seen that the hot region is significantly dominant during the whole time. For $z/w = 0.3$ however, the cold region is mainly dominant. For $z/w = 0$, it can be observed that although hot region is dominant, the cold region is higher than the cold region at $z/w = 0.3$ and lower than the cold region at $z/w = -0.3$. Similar moderate behavior for the hot region at $z/w = 0$ can be seen which shows the spatial temperature evolution moving from one side of the vertical boundary to the other, which is consistent with the visualization observed in Figure 5-10.

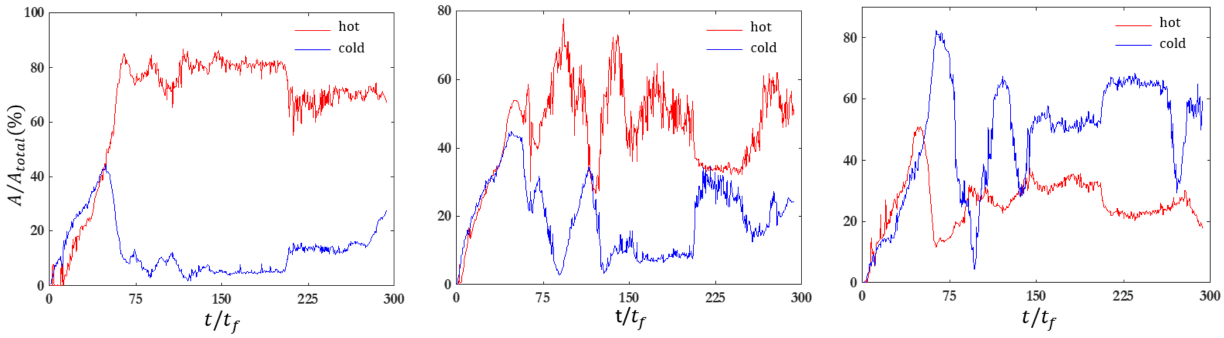

(a) (b) (c)

Figure 5-12. Temporal evolution of the hot and cold regions at three different planes of (a) $z/w = -0.3$ (b) $z/w = 0$ (c) $z/w = 0.3$.

The volumetric evolution of the hot and cold regions is shown in Figure 5-13 (a). As can be seen, the first $\Delta t/t_f = 57$ represents the same linear growth of both regions as the planar evolutions at the three different planes. After this time, the evolution of the both hot and cold regions resemble the behavior of hot and cold regions at $z/w = 0$ in Figure 5-12(b), however, the absolute values are different. From Figure 5-12 and Figure 5-13(a), for both planar and volumetric plots, an inverse correlation between the hot and cold variations can be observed. The absolute value of the anti-correlation coefficient, C_{hc} for all the planes has been calculated and plotted in Figure 5-13(b). As can be seen, the absolute value of the coefficient, C_{hc} for all the planes variates slightly around the mean value of $\sim 51\%$. This implies a moderate anti-correlation between the evolution of hot and cold region when the temperature field is investigated in 2D. For the volumetric measurement, however, as is shown in Figure 5-13(b), the absolute value of C_{hc} is equal to ~84% which shows a strong anti-correlation specially comparing to the 2D measurements.

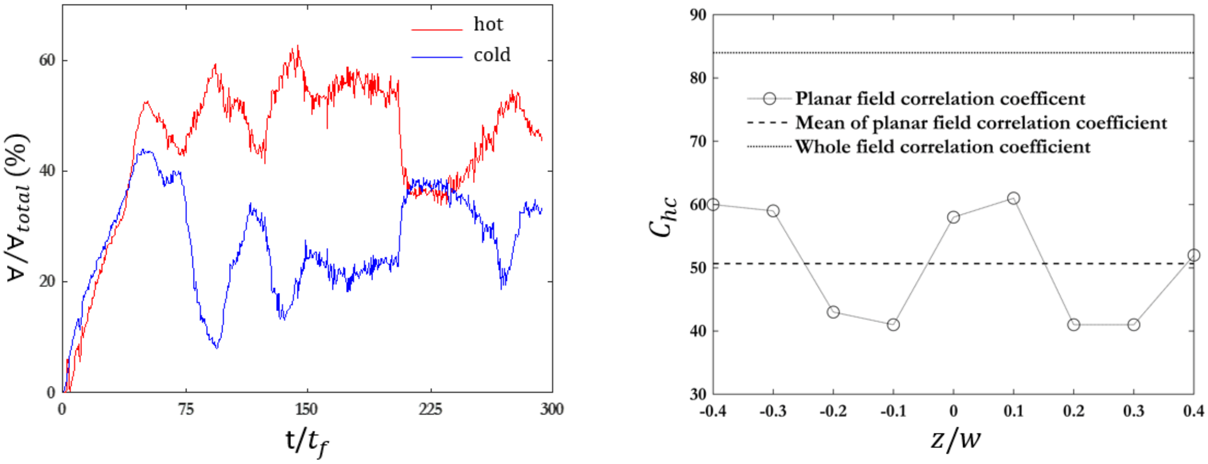

(a) (b)

Figure 5-13. (a) Temporal volumetric evolution of the hot and cold regions. (b) The absolute values of the correlation coefficient, C_{hc} of the two hot and cold regions for different planes and the volumetric measurement.

The instantaneous temperature fields in Figure 5-10 and Figure 5-11 showed that after the rise and fall of the hot and cold plumes, hot and cold flow develop at each side of the convection cell, z-direction. Since the instances of these two figures does not represent the physics of the whole experiment time interval, it is necessary to examine this temperature pattern for the whole time of $\Delta t/t_f = 284$. Accordingly, temporal evolution of spatial average of the temperature field, $\langle T^* \rangle$ on each plane ($x - y$ plane) is plotted in Figure 5-14. From this figure, temporal evolution of temperature along with its variation at different depths can be observed. To see more detail, temperature variations for each plane is also plotted in Figure 5-14(b). As can be seen in Figure 5-14(a) and (b), after development of the thermal plumes, temperature increases at $z/w < 0$ and it decreases at $z/w > 0$. Going further in time, at $t/t_f \approx 150$ temperature reach to a peak. This increase also affects the other side of the fluid domain though for $z/w > 0.2$ temperature is still lower than initial temperature, $\langle T^* \rangle = 0$. After this peak, the whole field temperature decreases leading to a symmetrical temperature distribution in depth of the cell at $t/t_f > 250$. It can be inferred that during the whole experiment, after the development of the primary plumes, temperature increases in one side of the fluid flow and it decreases in the other side, however, a certain boundary cannot be define due to the temperature swing.

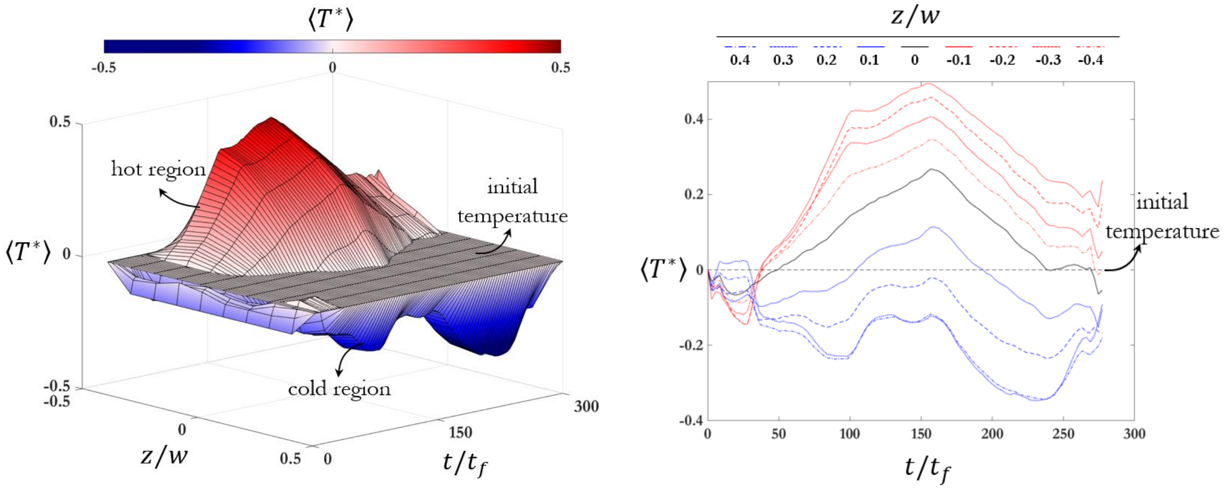

(a) (b)

Figure 5-14. (a) Evolution of the spatial average of the temperature field, $\langle T^* \rangle$ (b) $\langle T^* \rangle$ versus time on each plane.

The dimensionless heat transfer can be given by the Nusselt number, Nu as:

$$Nu = Qh/\kappa \Delta T \tag{11}$$

where Q is the heat flux normal to the hot and cold boundaries. Here, using the temperature distribution, Nusselt number is calculated directly based on vertical temperature gradient normal to the hot, $y^* = 0$, and cold, $y^* = 1$ boundaries as:

$$Nu = (\partial T^* / \partial y^*)_{y^*=0,1} \tag{12}$$

where $T^* = (T - T_0)/\Delta T$ is the dimensionless temperature based on the initial temperature, T_0. In this equation, y^* is also the vertical dimensionless length normal to the hot or cold boundaries. Using this equation on a structured grid the Nusselt number distribution on both hot and cold boundaries can be obtained as a function of time and space, $Nu(x, z, t)$ [7].

For four different time instances, the instantaneous dimensionless heat transfer, Nu on the hot and cold boundaries are shown in Figure 5-15. Reviewing this figure it can be seen that temporal and spatial variations, including in the z-direction, is significant. By moving in time from $t/t_f = 22$ to $t/t_f = 42$, it can be observed that the low heat transfer region grows with the growth of the hot and cold thermal plumes each on a different side of the enclosure (left and right). For $t/t_f = 57$, two regions with relatively high and low heat transfer can be seen which can be attributed to the cold and hot thermal plumes approaching to the hot and cold boundaries, respectively.

From Figure 5-15(a) at $t/t_f = 97$, it can be observed that the high heat transport region in the cold flow area and low heat transport in the hot area is consistent with the previous observations of the 3D temperature field. A similar observation for the cold boundary demonstrates the consistency between the heat transport and temperature field. For the first three time instances, it can be observed that the high and low heat transfer regions for hot and cold boundaries are opposite each other. This is due to the direct effect of the hot and cold thermal plumes affecting the cold and hot boundaries, respectively. However, at $t/t_f = 97$, this opposite behavior cannot be observed, which shows the development of the flow with a more complicated flow structure reducing the direct effect of the thermal plumes generated from the boundaries.

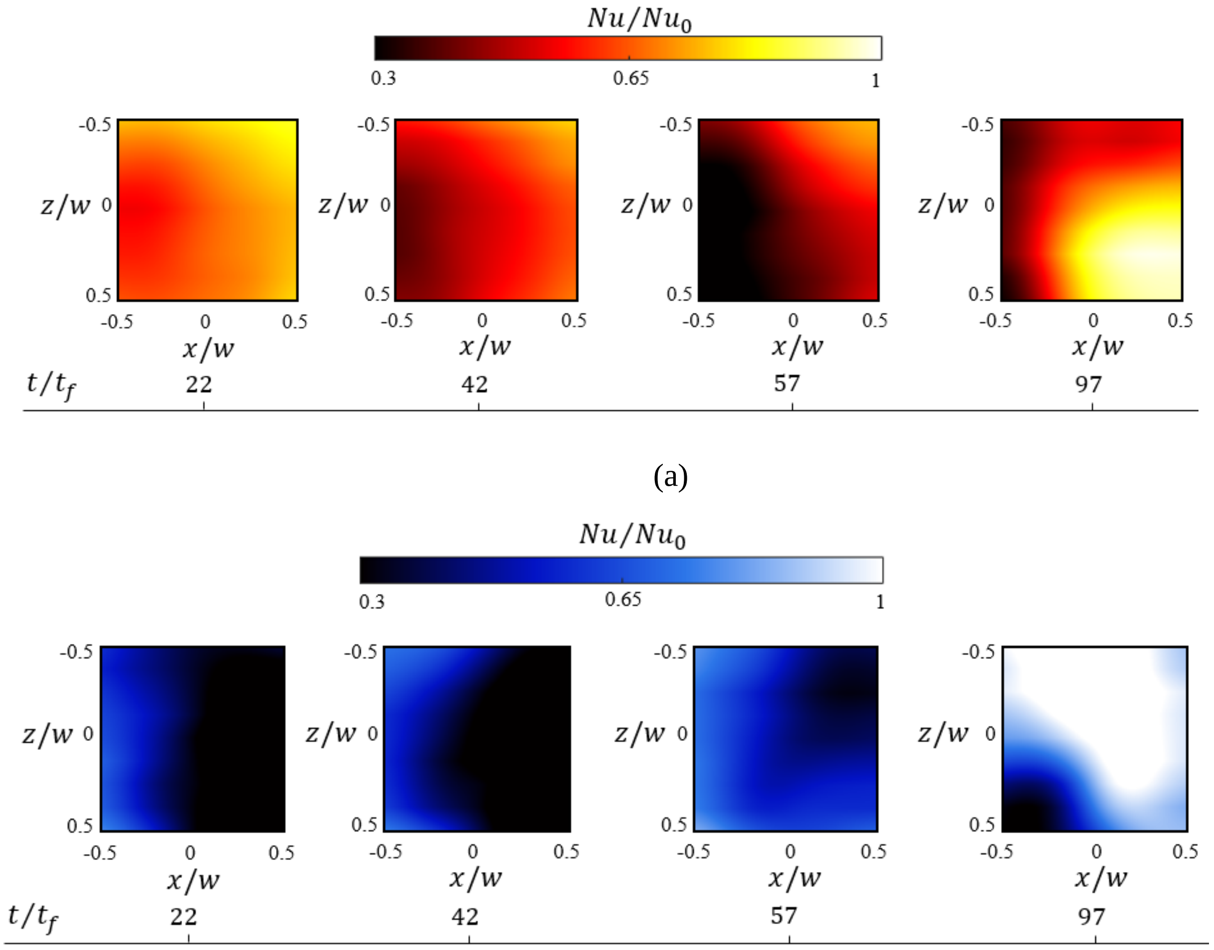

(b)

Figure 5-15. Dimensionless heat transfer, Nusselt number, Nu distribution on (a) hot boundary and (b) cold boundary for $t/t_f = 22, 42, 57, 97$.

The temporal evolution of the spatial averaged Nusselt number, $\langle Nu \rangle_{x,z}$ for both hot and cold boundaries are plotted in Fig. 16. After the onset of convection for both boundaries, heat transfer decreases and reaches a local minimum. By reaching the cold plume to the hot boundary and the hot plume to the cold boundary the heat transfer increases. Passing through time by reaching to the $t/t_f = 225$ as was shown in Figure 5-14, the temperature increases significantly, which leads to a notable decrease in the heat transfer of the cold boundary and an increase in the heat transfer of the hot boundary.

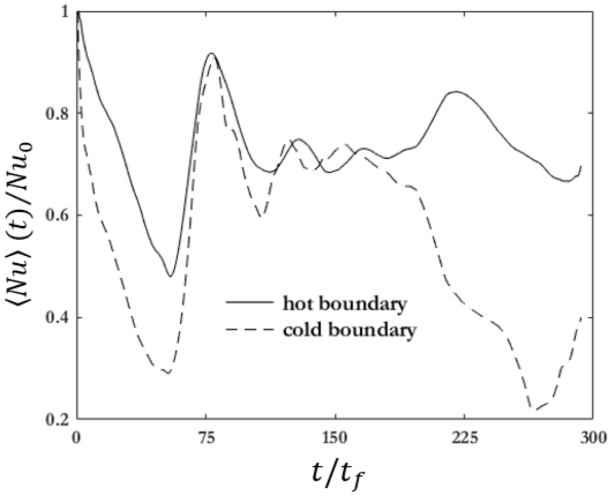

Figure 5-16. Evolution of spatial averaged Nusselt number for both hot and cold boundaries.

In Figure 5-17, the spatial averaged Nusselt number, $\langle Nu \rangle_{x,z}$ for both hot and cold boundaries is compared to the spatial averaged Nusselt number obtained from the planar temperature field at three location of $z/w = -0.3$, $z/w = 0$, and $z/w = 0$. For the beginning of the convection $t/t_f < 75$ all the values represent the same behavior. After that, for both boundaries, the averaged heat transport and its variations at $z/w = 0$ follow the same trend as the whole field averaged heat transfer, $\langle Nu \rangle_{x,z}$, yet there might be a considerable deviation (maximum $\sim 16\%$) between them. This indicates that in case of planar measurements only at the center of the flow field may provide information about the average heat transfer of the phenomena comparing to the other planes. It also implies that to have a coherent and true understanding of the heat transport evolutions, whole field measurement is necessary.

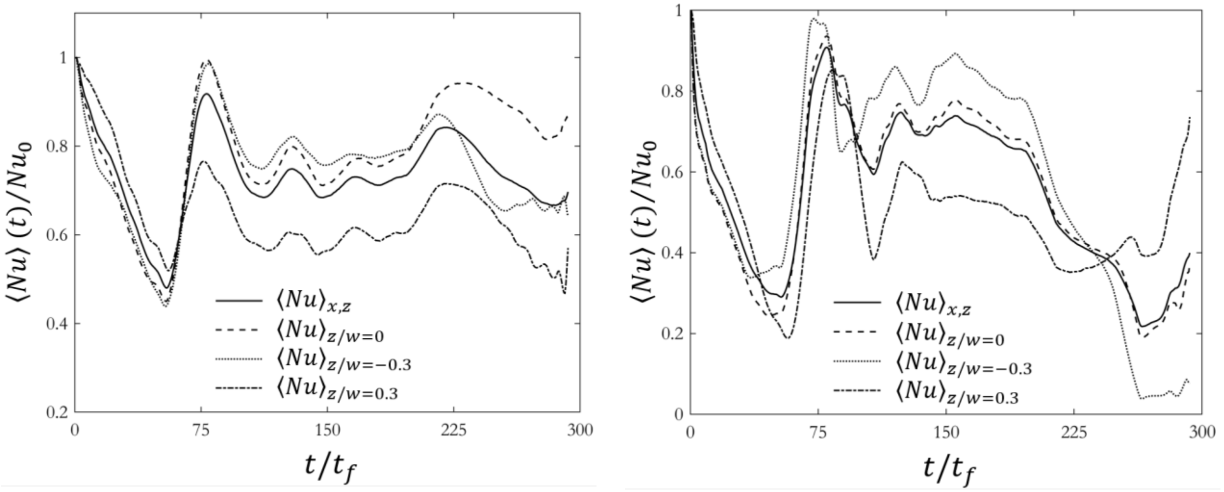

(a) (b)

Figure 5-17. Comparison of spatial averaged Nusselt number, $\langle Nu\rangle_{x,z}$ with $\langle Nu\rangle_{z=0}$, $\langle Nu\rangle_{z=-0.3}$, and $\langle Nu\rangle_{z=0.3}$ for (a) hot boundary and (b) cold boundary.

5.4 Conclusion

Application of 4D two-colour laser-induced fluorescence on a laterally confined Rayleigh-Bénard convection with Rayleigh number of $Ra = 9.9 \times 10^7$ and Prandtl number of $Pr = 6.1$ was investigated employing a scanning laser experimental setup. Two-colour and two dye ratiometric approach was utilized to apply laser-induced fluorescence thermometry. Two temperature sensitive fluorescent dyes, Fluorescein and Kiton red with opposite temperature sensitivity of $+1.3\ \%/℃$ and $-1.9\ \%/℃$ were used led to enhance the overall sensitivity to $7.3\ \%/℃$. Details of the experimental setup and optical system led to this high temperature sensitivity were also discussed. Using this method the whole field temperature of the Rayleigh-Bénard flow was measured during $\Delta t/t_f = 284$ from the onset of convection. From the volumetric temperature field, it was found that both hot and cold thermal plumes, after the onset of convection, develop a conical shape. During the development of these two primary thermal plumes for $0 < t/t_f < 75$ it was found that the spatial averaged Nusselt number followed the same trend for both planar and volumetric measurements regardless of the location of the measured 2D plane. However, with further development of the flow, only planar data at the center of the enclosure follow the behavior of the spatially averaged Nusselt number obtained from volumetric field. Nevertheless, deviation in the spatial averaged Nusselt number increases to $\sim 16\%$ even for the central plane. This shows that to evaluate the classic and ultimate theories, volumetric measurement is required for a coherent understanding of the physics. From the visualization of the time-resolved 3D temperature field and 2D distribution of the Nusselt number, it was also found that only by volumetric measurement, temporal and spatial variations of the temperature and heat transfer can be evaluated.

References

[1] G. Ahlers, S. Grossmann, and D. Lohse, “Heat transfer and large scale dynamics in turbulent Rayleigh-Bénard convection,” *Rev Mod Phys*, vol. 81, no. 2, pp. 503–537, 2009, doi: 10.1103/RevModPhys.81.503.

[2] O. Shishkina, “Rayleigh-Bénard convection: The container shape matters,” *Phys Rev Fluids*, vol. 6, no. 9, p. 090502, Sep. 2021, doi: 10.1103/PHYSREVFLUIDS.6.090502/FIGURES/15/MEDIUM.

[3] H. D. Xi, S. Lam, and K. Q. Xia, “From laminar plumes to organized flows: the onset of large-scale circulation in turbulent thermal convection,” *J Fluid Mech*, vol. 503, no. 503, pp. 47–56, Mar. 2004, doi: 10.1017/S0022112004008079.

[4] R. Krishnamurti and L. N. Howard, “Large-scale flow generation in turbulent convection,” *Proceedings of the National Academy of Sciences*, vol. 78, no. 4, pp. 1981–1985, Apr. 1981, doi: 10.1073/PNAS.78.4.1981.

[5] L. Zwirner, A. Tilgner, and O. Shishkina, “Elliptical Instability and Multiple-Roll Flow Modes of the Large-Scale Circulation in Confined Turbulent Rayleigh-Bénard Convection,” *Phys Rev Lett*, vol. 125, no. 5, p. 54502, 2020, doi: 10.1103/PhysRevLett.125.054502.

[6] R. E. Ecke and O. Shishkina, “Turbulent Rotating Rayleigh–Bénard Convection,” *https://doi.org/10.1146/annurev-fluid-120720-020446*, vol. 55, no. 1, Oct. 2022, doi: 10.1146/ANNUREV-FLUID-120720-020446.

[7] B. Adrian, *CONVECTION HEAT TRANSFER*. John Wiley and Sons, Inc, 2013.

[8] D. Lohse and K. Q. Xia, “Small-scale properties of turbulent rayleigh-benard convection,” *Annu Rev Fluid Mech*, vol. 42, pp. 335–364, 2010, doi: 10.1146/annurev.fluid.010908.165152.

[9] W. V. R. Malkus, “The heat transport and spectrum of thermal turbulence,” *Proc R Soc Lond A Math Phys Sci*, vol. 225, no. 1161, pp. 196–212, Aug. 1954, doi: 10.1098/RSPA.1954.0197.

[10] C. H. B. Priestley, “Convection From a Large Horizontal Surface,” *Australian Journal of Physics* , vol. 7, pp. 176–201, 1954, doi: https://doi.org/10.1071/PH540176.

[11] C. R. Doering, “Turning up the heat in turbulent thermal convection,” *Proc Natl Acad Sci U S A*, vol. 117, no. 18, pp. 9671–9673, 2020, doi: 10.1073/pnas.2004239117.

[12] R. H. Kraichnan, “Turbulent Thermal Convection at Arbitrary Prandtl Number,” *Citation: The Physics of Fluids*, vol. 5, p. 1374, 1962, doi: 10.1063/1.1706533.

[13] S. Grossmann and D. Lohse, “Multiple scaling in the ultimate regime of thermal convection,” *Phys. Fluids*, vol. 23, p. 45108, 2011, doi: 10.1063/1.3582362.

[14] C. R. Doering, “Thermal forcing and ‘classical’ and ‘ultimate’ regimes of Rayleigh–Bénard convection,” *J Fluid Mech*, vol. 868, pp. 1–4, Jun. 2019, doi: 10.1017/JFM.2019.118.

[15] J. Sakakibara and R. J. Adrian, “Whole field measurement of temperature in water using two-color laser induced fluorescence,” *Exp Fluids*, vol. 26, no. 1–2, pp. 7–15, 1999, doi: 10.1007/s003480050260.

[16] S. Moller, C. Resagk, and C. Cierpka, “Long-time experimental investigation of turbulent superstructures in Rayleigh–Bénard convection by noninvasive simultaneous measurements of temperature and velocity fields,” *Exp Fluids*, vol. 62, no. 4, pp. 1–18, 2021, doi: 10.1007/s00348-020-03107-1.

[17] D. Schiepel, D. Schmeling, and C. Wagner, “Simultaneous tomographic particle image velocimetry and thermometry of turbulent Rayleigh-Bénard convection,” *Meas Sci Technol*, vol. 32, no. 9, 2021, doi: 10.1088/1361-6501/abf095.

[18] D. Khodakov, J. Li, J. X. Zhang, and D. Y. Zhang, “Highly multiplexed rapid DNA detection with single-nucleotide specificity via convective PCR in a portable device,” *Nature Biomedical Engineering 2021 5:7*, vol. 5, no. 7, pp. 702–712, Jul. 2021, doi: 10.1038/s41551-021-00755-4.

[19] K. L. Chong and K. Q. Xia, “Exploring the severely confined regime in Rayleigh-Bénard convection,” *J Fluid Mech*, vol. 805, p. R4, 2016, doi: 10.1017/jfm.2016.578.

[20] N. Fujisawa, S. Funatani, and N. Katoh, “Scanning liquid-crystal thermometry and stereo velocimetry for simultaneous three-dimensional measurement of temperature and velocity field in a turbulent Rayleigh-Bérnard convection,” *Exp Fluids*, vol. 38, no. 3, pp. 291–303, 2005, doi: 10.1007/s00348-004-0891-2.

[21] H. Hu and M. M. Koochesfahani, “Molecular tagging velocimetry and thermometry and its application to the wake of a heated circular cylinder,” *Meas Sci Technol*, vol. 17, no. 6, pp. 1269–1281, 2006, doi: 10.1088/0957-0233/17/6/S06.

[22] J. Sakakibara, K. Hishida, and M. Maeda, “Measurements of thermally stratified pipe flow using image-processing techniques,” *Exp Fluids*, vol. 16, no. 2, pp. 82–96, 1993, doi: 10.1007/BF00944910.

[23] J. Sakakibara and R. J. Adrian, “Measurement of temperature field of a Rayleigh-Bénard convection using two-color laser-induced fluorescence,” *Exp Fluids*, vol. 37, pp. 331–340, 2004, doi: 10.1007/s00348-004-0821-3.

[24] X. Song and D. S. Nobes, “Experimental investigation of evaporation-induced convection in water using laser based measurement techniques,” *Exp Therm Fluid Sci*, vol. 35, no. 6, pp. 910–919, Sep. 2011, doi: 10.1016/j.expthermflusci.2011.01.010.

[25] H. J. Kim and K. D. Kihm, “Application of a two-color laser induced fluorescence (LIF) technique for temperature mapping,” *American Society of Mechanical Engineers, Heat Transfer Division, (Publication) HTD*, vol. 369, no. 7, pp. 335–341, 2001.

[26] C. E. Estrada-Pérez, Y. A. Hassan, and S. Tan, “Experimental characterization of temperature sensitive dyes for laser induced fluorescence thermometry,” *Review of Scientific Instruments*, vol. 82, no. 7, p. 74901, 2011, doi: 10.1063/1.3590929.

[27] M. B. Shafii, C. L. Lum, and M. M. Koochesfahani, “In situ LIF temperature measurements in aqueous ammonium chloride solution during uni-directional solidification,” in *Experiments in Fluids*, 2010, pp. 651–662. doi: 10.1007/s00348-009-0758-7.

[28] J. A. Sutton, B. T. Fisher, and J. W. Fleming, “A laser-induced fluorescence measurement for aqueous fluid flows with improved temperature sensitivity,” *Exp Fluids*, vol. 45, no. 5, pp. 869–881, 2008, doi: 10.1007/s00348-008-0506-4.

[29] D. A. Walker, “A fluorescence technique for measurement of concentration in mixing liquids,” *J Phys E*, vol. 20, no. 2, pp. 217–224, 1987, doi: 10.1088/0022-3735/20/2/019.

[30] T. Nakajima, M. Utsunomiya, and Y. Ikeda, “Simultaneous Measurement of Velocity and Temperature of Water Using LDV and Fluorescence Technique,” *Applications of Laser Techniques to Fluid Mechanics*, pp. 34–53, 1991, doi: 10.1007/978-3-642-61254-1_3.

[31] M. C. J. Coolen, R. N. Kieft, C. C. M. Rindt, and A. A. Van Steenhoven, “Application of 2-D LIF temperature measurements in water using a Nd : YAG laser,” Springer-Verlag, 1999.

[32] J. Sakakibara, K. Hishida, and M. Maeda, “Measurements of thermally stratified pipe flow using image-processing techniques,” *Exp Fluids*, vol. 16, no. 2, pp. 82–96, 1993, doi: 10.1007/BF00944910.

[33] J. P. Crimaldi, “Planar laser induced fluorescence in aqueous flows,” *Exp Fluids*, vol. 44, no. 6, pp. 851–863, 2008, doi: 10.1007/s00348-008-0496-2.

[34] H. Rochlitz and P. Scholz, “Application of laser-induced fluorescence technique in a duct flow with one heated wall,” *Exp Fluids*, vol. 59, no. 3, pp. 1–20, 2018, doi: 10.1007/s00348-018-2508-1.

[35] A. Abdelghany, K. Kuribayashi, and M. Tange, “Ratiometric laser-induced fluorescence for liquid-phase thermometry around boiling bubbles at extended temperatures above 70 °C,” *Exp Fluids*, vol. 63, no. 2, pp. 1–9, 2022, doi: 10.1007/s00348-022-03397-7.

[36] J. Coppeta and C. Rogers, “Dual emission laser induced fluorescence for direct planar scalar behavior measurements,” *Exp Fluids*, vol. 25, no. 1, pp. 1–15, 1998, doi: 10.1007/s003480050202.

[37] J. P. Crimaldi, “Planar laser induced fluorescence in aqueous flows,” *Exp Fluids*, vol. 44, no. 6, pp. 851–863, 2008, doi: 10.1007/s00348-008-0496-2.

[38] P. S. Karasso and M. G. Mungal, “PLIF measurements in aqueous flows using the Nd: YAG laser,” *Exp Fluids*, vol. 23, no. 5, pp. 382–387, 1997, doi: 10.1007/s003480050125.

[39] S. Liu *et al.*, “From Rayleigh-Bénard convection to porous-media convection: How porosity affects heat transfer and flow structure,” *J Fluid Mech*, vol. 895, 2020, doi: 10.1017/jfm.2020.309.

[40] J. A. Letelier, N. Mujica, and J. H. Ortega, “Perturbative corrections for the scaling of heat transport in a Hele-Shaw geometry and its application to geological vertical fractures,” *J Fluid Mech*, vol. 864, pp. 746–767, 2019, doi: 10.1017/jfm.2019.3.

[41] R. Hartmann, R. Verzicco, L. Klein Kranenbarg, D. Lohse, and R. J. A. M. Stevens, “Multiple heat transport maxima in confined-rotating Rayleigh-Bénard convection,” *J Fluid Mech*, vol. 939, pp. 1–27, 2022, doi: 10.1017/jfm.2021.1031.

[42] R. Hartmann, K. L. Chong, R. J. A. M. Stevens, R. Verzicco, and D. Lohse, “Heat transport enhancement in confined Rayleigh-Bénard convection feels the shape of the container,” *Epl*, vol. 135, no. 2, 2021, doi: 10.1209/0295-5075/ac19ed.

Chapter 6: Flow and temperature properties in Poiseuille-Rayleigh-Bénard convection

The temperature and velocity field of the PRBC flow with a Richardson number variation from $Ri = \infty$ to 2.2 is investigated in this chapter. A simultaneous velocity and temperature measurement system was developed by applying simultaneous PIV and PLIF. The heat transfer coefficient, Nusselt number, is also estimated based on two approaches using the temperature gradient and vertical convection.

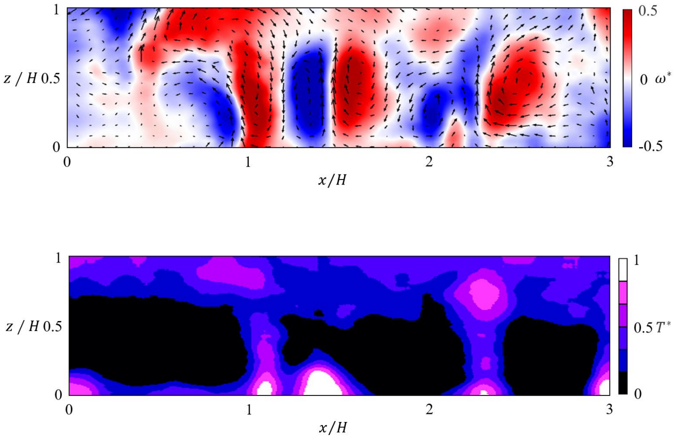

Graphical abstract for Chapter 6

6.1 Introduction

Poiseuille-Rayleigh-Bénard Convection (PRBC) is the flow inside a channel heated from below [1]. PRBC is a type of fluid convection system that combines two driving mechanisms of Rayleigh-Bénard convection (RBC) and Poiseuille flow [2]. RBC is a classic fluid dynamics system where a fluid is confined between two horizontal plates, heated from below and cooled from above [3]. In this system onset of convection occurs by a certain temperature difference threshold [4]. By the onset of convection, the flow develops by rise and fall of thermal plumes [5]. The development of the thermal plumes and their interaction with the boundaries of the convection cell leads to formation of flow rolling structures [6]. Large-scale circulation (LSC) is one of the most important characteristics of the RBC flow [5]. Recent studies have revealed that LSC can have a significant influence on heat and momentum transfer in RBC flow [7].

PRBC flow is basically similar to RBC flow in which a crossflow is also affecting the development of the thermal plumes and flow rolling structurers [1]. A schematic of the PRBC is shown in Figure 6-1. As can be seen the channel has a rectangle cross section and while the flow is driven vertically due to temperature and buoyancy difference it interacts by the horizontal Poiseuille flow. This leads to the development of the flow both temporally similar to RBC and spatially along the channel in x-direction [1]. In previous studies, it has been shown that for a very long channel i.e. $x \gg H$, the flow develops LSC similar to RBC flow [2]. The developed LSC in PRBC while makes a rotational flow in $y-z$ plane it also develops streamwise along the Poiseuille flow in x-direction [8].

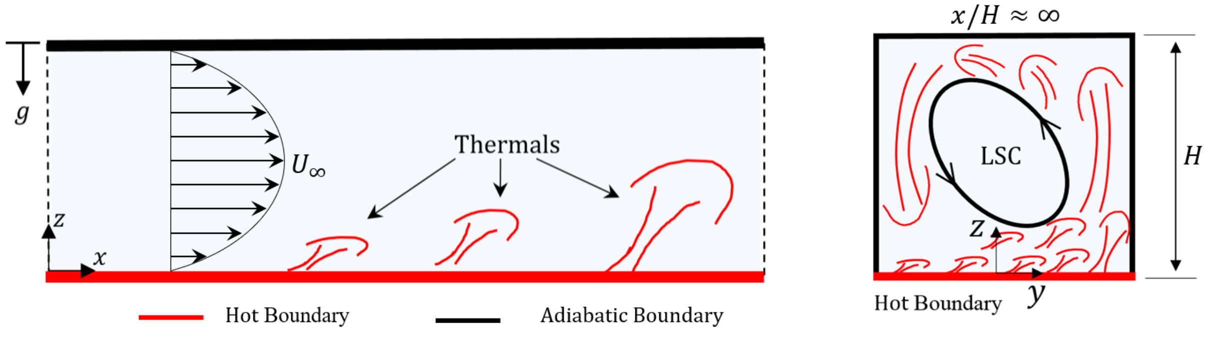

(a) (b)

Figure 6-1. Schematic of the Poiseuille-Rayleigh-Bénard convection flow in a channel. (a) Shows the side view of the channel and the flow develops along the channel in x-direction. (b) Indicates the cross-section of the developed flow for $x/H \approx \infty$ forming the large-scale circulation. The channel is heated from below with the constant temperature, T_H, while the side and top walls are in adiabatic condition. U_∞, also indicates the flow Poiseuille flow along x-direction.

The controlling parameters in PRBC flow are as Prandtl number, $Pr = \alpha/\nu$, Rayleigh number, $Ra \equiv \beta g \Delta T H^3/\nu\alpha$, and Reynolds number, $Re \equiv U_\infty H/2\nu$, in which α is the thermal diffusivity, ν is the momentum diffusivity (kinetic viscosity), β is the thermal expansion coefficient, g is the gravitational acceleration, $\Delta T = T_H - T_\infty$ is the temperature difference between the bottom wall (hot wall) temperature and the free stream temperature, T_∞. In the definitions of the controlling parameters, H also indicates the length scale which is the height of the channel as can be seen in Figure 6-1(b). In the definition of the Reynolds number, Re, U_∞ is the free stream velocity indicated in Figure 6-1(a) as well. It is worth noting that while in the definition of Rayleigh number, Ra, the length scale is the height of channel i.e. H, For Reynolds number, Re, the half-height of the channel i.e. $H/2$ is characterized as the length scale [8].

The flow inside a channel heated from below may experience different regimes of convection from natural convection to mixed and forced convection [9]. The criterion that can define the regime of the convection is Richardson number and it is defined as $Ri = Gr/Re^2 = /U_\infty^2 = Ra/Re^2Pr$ where Gr is the Grashof number, $Gr = \beta g \Delta T H^3/\nu^2$ [9]. This nondimensional number is basically driven from the relation between the buoyancy forces in z-direction i.e. $\beta g \Delta T H$ and inertial forces in x-direction i.e U_∞^2 [9]. Very high Richardson numbers, $Ri \gg 10$ indicates a natural convection regime. However, very low Richardson numbers, $Ri \ll 1$ shows a forced convection Regime [9]. The PRBC flow though is within the mixed convection regime i.e. $1 < Ri < 10$ in which both natural and forced convection are critical in heat transport of the system [10].

Incropera et. al [11], [12] extensively studied the PRBC flow characteristics decades ago both numerically and experimentally. According to their research, the flow develops multiple stages along the channel [13]. At the very beginning the streamwise flow interact with thermal plumes development of the flow along the channel forms the LSC [13]. Hence, at the very beginning the heat transfer decreases due to the increase in temperature and decrease in the temperature gradient between the bottom wall (hot wall) and the free stream [14]. However, by development of the flow and formation of flow rolling structures especially the LSC, heat transfer increases gradually [13]. The development of the thermal plumes and formation of LSCs within the PRBC flow has been visualized in [2] indicating consistent results with the previous studies of Incropera et. al [11] . Hence, it can be concluded that the LSC and as a result the heat transport maxima occurs in PRBC flow within an infinity length channel. However, in most of the engineering and industrial applications such as heat exchangers and radiators the length of the channel is limited to the order of the length scale of the flow i.e. H to one order of magnitude larger i.e. $10H$.

It is important to have unique definition for the heat transfer while studying the physics of a phenomena such as PRBC. The efficiency of convective heat transfer relative to pure conduction is quantified by the Nusselt number, Nu, which serves as a key parameter in evaluating the enhancement of heat transfer due to convection over conduction alone as is defined in equation 1 below:

$$Nu \equiv \frac{Q_{convection}}{Q_{condution}} = \frac{hH}{\kappa} \tag{1}$$

in which, h represents the convection coefficient and H, is the length scale of an ideal thermofluid system and κ is the conduction coefficient of the fluid [9]. Although this definition looks simple to identify, estimating the true heat transfer coefficient, h is very challenging making the Nusselt number calculation a sophisticated concept, yet critical in in the context of thermofluid science.

When investigating thermofluid systems, two primary boundary conditions are often assumed: constant wall temperature and constant heat flux at the boundary [15], [16]. In experimental studies, the constant heat flux condition is usually more practical and favorable [15], [16]. This condition is typically implemented using a heat source like an electrical heater that provides a steady rate of energy transfer [16]. The electrical power supplied to the heater can be calculated using the electrical current and the voltage [16]. As a result, the Nusselt number can be calculated based on the calculation of the convection coefficient, h, using the classical equation of $Q = hA\Delta T$, where A, is the section area of the solid boundary, the temperature difference, ΔT, is the temperature difference between the solid boundary, $T_s = T_H$ and the fluid flow, T_∞ [17], [18]. Then, temperatures i.e. T_s and T_∞ can be measured using temperature sensors e.g. thermistors and thermocouples [18].

In the estimation of the Nusselt number, several uncertainties arise, primarily from simplifying assumptions and measurement limitations. The first source of uncertainty is based on the assumption that the heat transfer to the fluid volume is constant. This is a simplification that neglects various losses, including electrical losses, system inefficiencies, and, most critically, heat transfer losses between the heat source and the fluid. As a result, the energy transfer to the fluid volume is often overestimated. The second major source of uncertainty is related to temperature measurements. As depicted in the Figure 6-2, temperature sensors can only measure temperature at specific points, leading to deviations between the measured temperature and the actual temperature distribution along the solid boundary. Additionally, temperature sensors are typically embedded within the solid layer, rather than being placed directly on the boundary surface, introducing another layer of discrepancy. This causes a difference between the actual boundary temperature T_{s-real} and the measured temperature $T_{s-measured}$, as indicated by the distance, Δz between the solid surface and the sensor location. This offset creates further uncertainty in accurately identifying the Nusselt number, as it relies on precise temperature differences to quantify heat transfer.

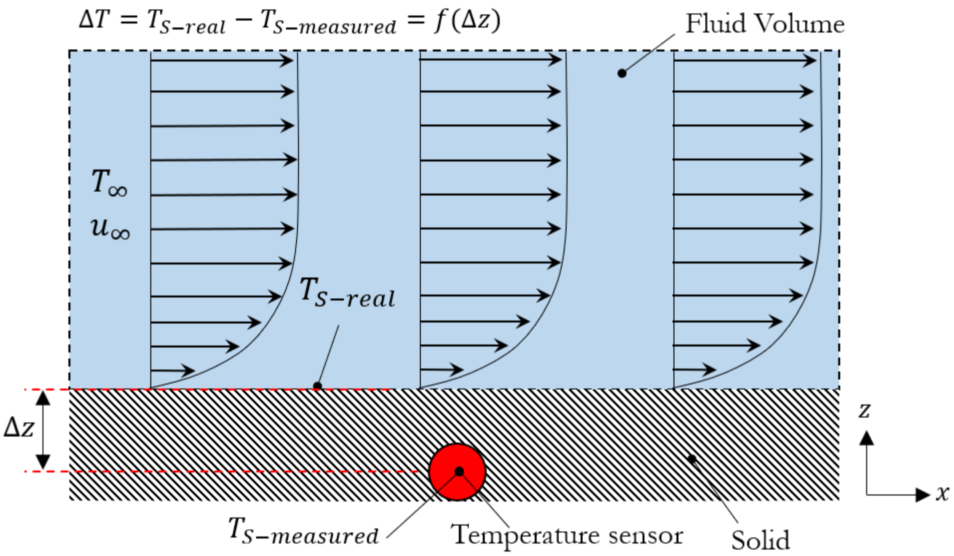

Figure 6-2. Schematic of temperature measurement uncertainty in a fluid, showing the discrepancy between the real surface temperature T_{s-real} and the measured temperature $T_{s-measured}$ due to the sensor's location within the solid layer and the resulting temperature deviation Δz.

In numerical simulations, the use of a constant temperature boundary condition at the solid-fluid interface is often preferred when studying heat transfer. This boundary condition offers greater control over the solution of the governing equations that capture the physics of thermofluid systems. By maintaining a constant temperature along the solid boundary, as shown in Figure 6-3, the temperature distribution within the fluid can be resolved. Furthermore, by this boundary condition the temperature variation within the fluid flow and near the boundary layer can be resolved making the focus of simulation only on the fluid part. This is important since focusing on both solid and fluid part is very demanding in the numerical simulations. Having the constant temperature boundary condition as is depicted in Figure 6-3, the Nusselt number can be driven as follow within the assumption of $Q_{convection} = Q_{conduction}$:

$$hA(T_s - T_\infty) = \kappa \Delta T / \Delta z \tag{2}$$

Considering that in this equation, ΔT is the vertical temperature variation and y can be normalized as $z^* = z/H$, the Nusselt number based on the definition in Equation 1 can be calculated as follow:

$$Nu = (\partial T^* / \partial z^*)_{z^*=0} \tag{3}$$

Therefore, for calculating the Nusselt number, calculation of the gradient of the temperature in vertical direction, see Figure 6-3, near the boundary is required, i.e. resolving the physics of thermal boundary layer. This is advantageous, because the final results provide the Nusselt number distribution for the whole desire geometry. This is necessary when studying the flow is in mind so spatiotemporal characteristics of the heat transfer can be investigated. However, in the context of experimental measurement by the methodology that explained earlier in Figure 6-2, only an average of the heat transfer coefficient, Nu can be estimated. Although, this calculation is valuable for estimating the performance of thermofluid system, studying the physics of the flow with this method is barely feasible since spatiotemporal characteristics of the flow and heat transport cannot be resolved.

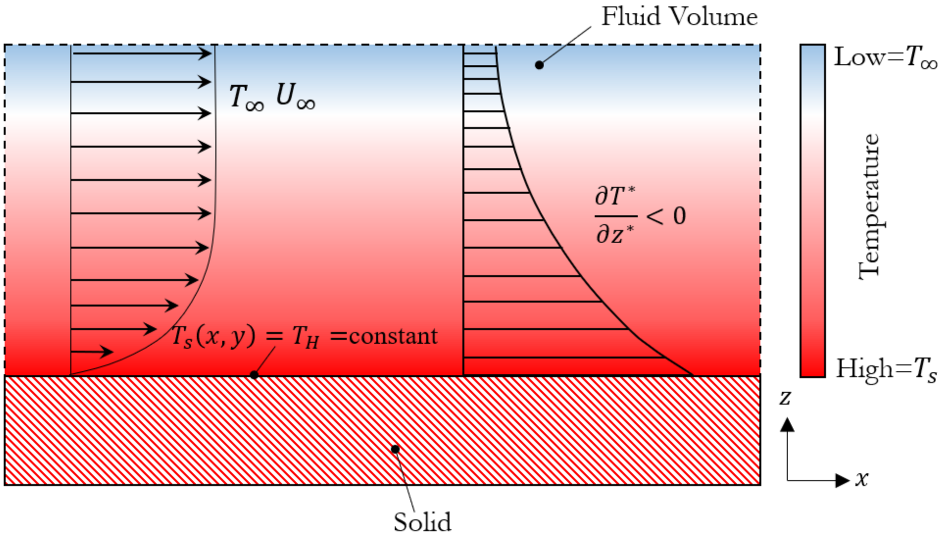

Figure 6-3. The schematic showing the temperature distribution near a solid boundary with constant temperature distribution of T_s, indicating the temperature gradient in vertical direction, y-axis, identifying the magnitude of the vertical heat transfer from the solid boundary to the fluid flow.

Measurement of the convective heat transfer coefficient is even more sophisticated and demanding when considering more complex physics such as mixed convection [19]. Here, both horizontal and vertical heat and mass transfer are controlling the physics of the flow [8]. In this condition, besides the temperature gradient, the vertical velocity also has a significant contribution to the heat transport [8]. Hence, the convective heat transfer coefficient can be calculated by considering the momentum equation with the Oberbeck-Boussinesq (OB) approximation [20]:

$$\partial u + u \cdot \nabla u + \nabla p = \nu \nabla^2 u + \beta g T e_z \tag{4}$$

That has terms for fluid velocity u, pressure p, kinematic viscosity ν, gravitational acceleration g, thermal expansion coefficient β, temperature T, and the unit vector in the z-direction e_z. The following equation indicates the energy equation as:

$$\partial_t \partial T + u \cdot \nabla T = \kappa \nabla^2 T \tag{5}$$

Hence the Nusselt number can be estimated as:

$$Nu = \frac{\langle u_z T \rangle_z - \alpha \partial z \langle T \rangle_z}{\alpha \Delta T / H} \tag{6}$$

It is important to note that in this definition of the Nusselt number, both the temperature near the solid boundary and the vertical velocity component, u_z, must be measured. While this requirement is not demanding in the context of numerical simulations—since the coupled momentum and energy equations, as shown in equations 4 and 5, are solved simultaneously—it presents challenges in experimental studies, as illustrated in Figure 6-2. Calculating the Nusselt number based on the definition in equation 6 is often not feasible in experiments due to the difficulty in obtaining precise measurements of both temperature gradients and vertical velocity. To achieve a reliable estimation, full-field measurements of both temperature and velocity are necessary.

With current advancements in thermofluid measurement techniques, optical methods, such as particle image velocimetry (PIV) and particle tracking velocimetry are the most popular methods for velocity measurement and they are well developed [21]. For temperature measurement of the fluid flow, there are several optical techniques e.g. laser-induced fluorescence (LIF) [22] thermometry, thermochromic liquid crystal (LCT) thermometry [23], and phosphorescent thermometry [24]. Molecular tagging velocimetry (MTV) and thermometry (MTV&T) is a combinatorial method works very good for simultaneous measurement of the velocity and temperature based on the molecular marking of different materials e.g. phosphorescent, make it a high-resolution seedless method for measuring both velocity and temperature [25], [26]. However, this method is very demanding since it requires very high-power lasers and sophisticated optical alignments [26]. Hence, to have a simultaneous measurement of the velocity and temperature field it is common to combine a velocimetry method with a thermometry method.

Combination of PIV and LIF is an ideal solution for this purpose due to high temperature sensitivity of LIF thermometry and ease of use of PIV. Looking into the previous works, Hishida and Sakakibara [27] applied a double camera PIV/PLIF approach to show the ability of this method for visualization of the temperature and the velocity field of different thermofluid phenomena such as thermal stratified flow, natural convection and flow of an impinging jet. They used a one-colour PLIF approach using negative temperature sensitive dye of Rhodamine B (RhB) and for seeding particles, they used 5 μm Polystyrene particles. Two cameras were set with stereo configuration in an ideal angle, one camera for capturing the PLIF signal and the other to capture the signal of the seeding particle. Following this work, there are many other studies applying same approach either one-colour or two-colour with the second fluorescent dye non-sensitive to the temperature to combine with either PIV or PTV for simultaneous thermometry and velocimetry [28], [29], [30]. Although, there are many works investigating and developing different methods for simultaneous velocity and temperature measurement, due to vast optical diagnostics systems for thermometry even in a limited technique of temperature PLIF, there is a gap in understanding different configuration, each may be suitable for different conditions depending on the thermofluid phenomena and experimental limitations and approach.

This work investigates the heat transfer and flow dynamics in Poiseuille-Rayleigh-Bénard Convection by determining the Nusselt number using simultaneous measurements of temperature and velocity fields. A combined planar laser-induced fluorescence and particle image velocimetry system was developed to simultaneously measure the temperature field and the velocity field. This methodology enables the spatiotemporal analysis of both heat and momentum transfer in a mixed convection regime, allowing for a detailed examination of the interaction between thermal plumes and the imposed Poiseuille flow.

6.2 Fluid Test Rig

Based on the properties of the PRBC flow a fluid test rig has been designed and fabricated. A rendering of the fluid test rig is depicted in Figure 6-4(a). This fluid test rig is designed to provide the test condition for both continuous and oscillatory flow. As can be seen in Figure 6-4(a), an actuator which is a cylindrical piston drives the flow inside the flow test rig. The actuator is controlled by a traverse which has been driven by a high precision low noise motor (ClearPath-SD, Teknik, Inc.).

The test section shown in Figure 6-4(b) is a rectangular channel with a cross-section with the height of $H = 10$ mm and width of $W = 55$ mm and length of $L = 150$ mm. The test section is made from an acrylic sheet with a thickness of 6.35 mm that has a low thermal conduction coefficient of $0.2\ \mathrm{W/mK}$. This test section has been designed to have maximum possible optical access, hence both side walls and the top wall of the test section is made from acrylic sheet. The bottom of the test section is featured by a heat exchanger with a relatively thin copper sheet transferring the heat from a channel underneath to the test section containing the working fluid, which is water in this case.

This heat exchanger is connected to a water bath to control the temperature and provide the temperature constant boundary condition at the bottom wall of the test section. The heat exchanger and the support bases of the test section are made using an SLA 3D printer (Form3, Formlabs Inc.) and printing material, a liquid photopolymer, with a low thermal conduction coefficient of

$0.15\ \mathrm{W/mK}$. Other than the actuator and the traverse, most of the fluid test rig components were made using the same 3D printing method and material. Fabrication of the fluid test rig using the SLA 3D printing for this study was very advantageous since many sophisticated components such as the honeycomb for flow straightening and vanes of the bend channel could be fabricated with minimum cost and time. The field of view for measuring the velocity and temperature is depicted in Figure 6-4(c). The field of view, FOV is located in $x - z$ plane as is shown in Figure 6-4(c). This field of view is located at the center of the heated channel with the length of $\Delta x = 30$ mm and height of $\Delta z = 10$ mm capturing the whole vertical field.

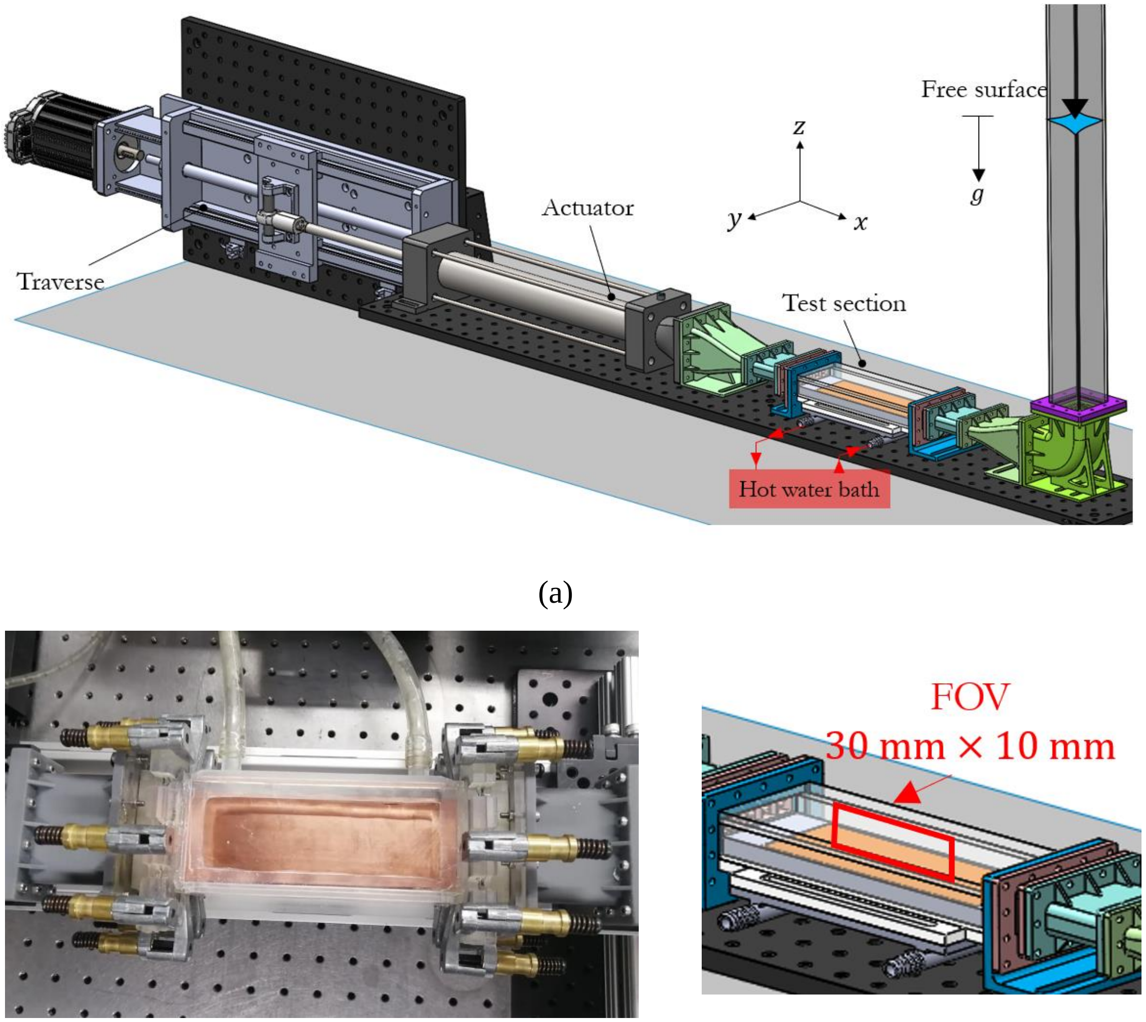

(a)

(b) (c)

Figure 6-4. (a) Model of the designed fluid test rig, (b) us the actual test section of the fluid test rig, and (c) indicates the field of view (FOV) used for this study.

6.3 Experiment Condition

Based on the design fluid test rig discussed earlier, flow insert the test section with a mean constant velocity i.e. U_∞ developing a Poiseuille flow within the test section. Hence, the Reynolds number is defined as $Re = U_\infty H/2\nu$ where $H/2$ is the half-height of the test section. In this study the Reynolds number is varying by variation of the velocity from $Re = 33$ to $Re = 200$ as has been listed in Table 6-1. With the constant temperature condition at the bottom of the test section (hot wall), T_H, the temperature difference within the Rayleigh number is defined as $\Delta T = T_H - T_\infty$ where T_∞ is the temperature of the free stream inserting to the test section. In this study, temperature of the bottom boundary is set to $T_H = 45$ °C. Based on the flow properties based on the mean temperature i.e. $\bar{T} = (T_H + T_\infty)/2$, the Rayleigh number is $Ra = 4.5 \times 10^5$ while the Prandtl number based on the mean temperature is equal to $Pr = 5$. Therefore, The Richardson number based on the parameters listed in Table 6-1 varies from $Ri{\sim}2$ to $Ri{\sim}80$. This range of Richardson number i.e. $2 < Ri < 80$ is within the classical criterion of mixed convection with some cases tends to the natural convection $10 < Ri$ and pure natural convection case $Ri = \infty$, where the Reynolds number is equal to $Re = 0$ indicating zero cross flow i.e. $U_\infty = 0$.

Based on what is described in Table 6-1, the experimental condition is for 6 different Richardson numbers within the mixed convection regime and one case purely natural convection regime. Figure 6-5 depicts these experimental conditions within the test section. For the purely natural convection case, it can be seen that while the flow is captured at the center of the test section, the test section has an infinite wall condition at the left and right side along x-direction. Hence, in comparison to the RBC flow which is limited from the side walls, here the natural mass transfer occurs along x-direction. For the other 6 conditions, flow is driven with constant velocity from right to left along x-axis.

Table 6-1. Flow properties of the PRBC investigated flow.

Ri	79.5	19.9	8.8	5	3.2	2.2	∞
Re	33	67	100	133	167	200	0
$Ra \times 10^{-5}$	4.5	4.5	4.5	4.5	4.5	4.5	4.5
Pr	5	5	5	5	5	5	5
$U_\infty \times 10^{-3}$ (m/s)	5	10	15	20	25	30	0
T_H (℃)	45	45	45	45	45	45	45
T_∞	25	25	25	25	25	25	25
$Ra(T_H) \times 10^{-5}$	9	9	9	9	9	9	9
$Ra(T_\infty) \times 10^{-4}$	2.2	2.2	2.2	2.2	2.2	2.2	2.2
$Pr(T_H)$	3.9	3.9	3.9	3.9	3.9	3.9	3.9
$Pr(T_\infty)$	6.2	6.2	6.2	6.2	6.2	6.2	6.2

Based on the experimental condition that has been listed in Table 6-1, the convection is within non-Oberbeck-Boussinesq (NOB) condition. The Boussinesq approximation assumes that fluid density variations are negligible except in the buoyancy term [31]. This approximation simplifies the equations of motion and is valid when temperature differences are small, usually $\Delta T < 1$ ℃, leading to only minor density variations [26]. Under Oberbeck-Boussinesq (OB) conditions, equations governing convection, such as RBC and PRBC, are simplified [32]. However, at higher temperatures i.e. $\Delta T > 1$ ℃, where the fluid experiences significant temperature differences, this assumption breaks down [33]. The NOB condition accounts for large temperature-induced density variations that affect both buoyancy and other fluid properties, such as viscosity, thermal conductivity, and specific heat. Under these conditions, the temperature dependence of the fluid's properties leads to more complex behavior, which may not be captured using the Boussinesq approximation [34].

In the context of this experimental work, the mention of NOB conditions is important primarily as a reference for readers and for future numerical and theoretical studies. While the experiments are conducted without directly accounting for NOB effects, it's crucial to acknowledge that simulations based on the Boussinesq approximation might not fully capture the physics observed under NOB conditions. In this work the temperature variation within the fluid flow is from T_H to T_∞. Considering this temperature variation, the Rayeligh number and Prandtl number associated to minimum temperature (T_∞) and maximum temperature (T_H) have been listed in Table 6-1. As can be seen the Prandtl number varies from $Pr(T_H) = 3.9$ to $Pr(T_\infty) = 6.2$. The variation of the Rayleigh number can be seen that is even higher from $Ra(T_H) = 9 \times 10^5$ to $Ra(T_\infty) = 2.2 \times 10^4$ which is an order of magnitude difference indicating the high impact of temperature on variation of the flow properties.

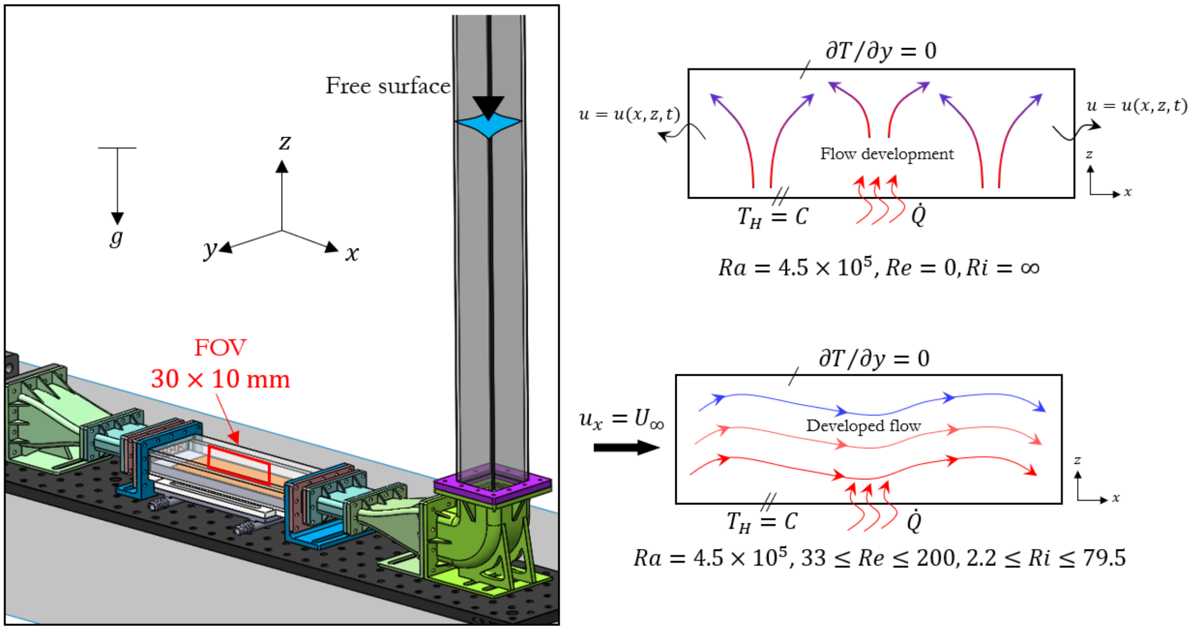

(a) (b)

Figure 6-5. For the field of view indicated in the model of the fluid test rig in (a), the experiment conditions are shown schematically in (b).

6.4 Optical Configuration

The basic physics behind PLIF involves exciting specific molecules or dyes within the fluid using a laser light, which induces these molecules to emit fluorescence at a different wavelength [35]. The emitted fluorescent signal intensity is sensitive to the temperature and calibrating the temperature sensitivity of the signal can be used for measurement [35]. The emitted light intensity is captured by a camera, and the intensity of this fluorescence is correlated to the scalar quantity being measured e.g., temperature [35]. The intensity of the emitted fluorescence, I_f, is given by the equation:

$$I_f = I_0 K \varepsilon X C \Phi \tag{7}$$

where I_0 is the intensity of the incident laser, K is the detection collection efficiency, ε epsilon is the absorption coefficient, X is the path length through which the laser interacts with the dye, and C is the concentration of the fluorescent dye. The term Φ, known as the photoluminescence quantum efficiency, can vary with temperature for certain dyes which defines the temperature sensitivity of that dye. As the laser excites the dye, the emitted fluorescent signal changes depending on temperature because Φ is temperature-dependent.

Table 6-2. Flow properties of the PRBC investigated flow.

Fluorescent dye	Empirical formula	Molecular weight (g/mol)	λ_{abs} at peak (nm)	λ_{em} at peak (nm)
Sodium Fluorescein	C20H10Na2O5	376.27	490	586
Rhodamine B	C28H31ClN2O3	479.02	546	567

Many temperature sensitive fluorescent dyes have been studied for thermometry application in PLIF [35]. Among these fluorescent dyes, Rhodamine B (RhB) is the most applied fluorescent dye for PLIF thermometry and it is well known even for two-colour PLIF when it combines with other fluorescent dyes [36]. In this study, Sodium Fluorescein (SFL) has been used as the temperature sensitive fluorescent dye. The specification of this fluorescent dye is listed in Table 6-2. The first reason for choosing this fluorescent dye is that different studies have shown that in certain conditions this fluorescent dye, SFL, may have higher temperature sensitivity in comparison with the other dyes [37], [38], [39]. The second reason is relevant to the application of PLIF simultaneous to the PIV. For applying PIV in this work, fluorescent based seeding particles with diameter of 3.2 µm was used and they are based on RhB. The specification of the coating material i.e. RhB has been listed in Table 6-2. To avoid noise from the seeding particles in the collected signal of SFL, it is necessary to have the emitted signal of the seeding particles and the temperature sensitive fluorescent dye at the two separate range of the spectrum.

Figure 6-6 illustrates the absorption and emission spectra of two fluorescent dyes, SFL and RhB, showing distinct emission bands for each dye. SFL emits in the green region (~514 nm), while RhB emits in the red region (~590 nm). This separation is crucial in ensuring minimal interference between their signals during simultaneous measurements. The SFL signal is collected with low noise, while the RhB emission results in a high signal-to-noise ratio (S/N) for velocity measurements. The minimal overlap between their emission spectra prevents any interference between the signals, allowing for precise and independent capture of both temperature and velocity fields. This clear spectral distinction enhances the accuracy and clarity of the experimental data, making these dyes well-suited for combined PIV and PLIF.

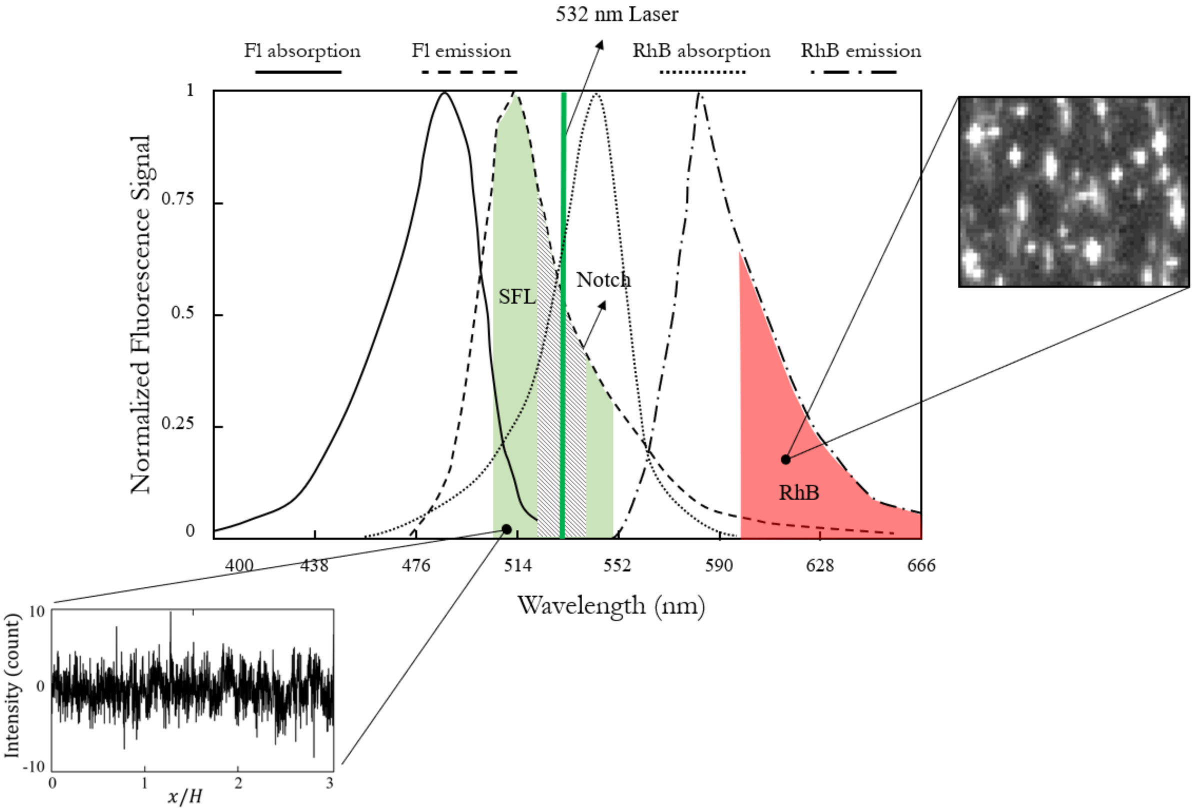

Figure 6-6. Absorption and emission spectra of Sodium Fluorescein and Rhodamine B, with the laser wavelength and optical filters used for applying simultaneous PLIF and PIV. A zoomed view of the image of the seeding particles is shown to highlight is relative high signal to noise ratio. The signal of the SFL along the x-axis is shown with the standard deviation of 2.1 counts is also shown at the left bottom to highlight the relatively low noise of the collected florescent signal.

6.5 Simultaneous configuration

The schematic of the optical measurement system used for applying the simultaneous PLIF and PIV is illustrated in Figure 6-7. As is depicted in this figure and in Figure 6-6, a 532 nm laser was used to illuminate SFL and RhB-coated seeding particles in the flow field. The combined emitted fluorescence signal is split using a dichroic mirror, which reflects wavelengths below 567 nm toward the LIF camera. The LIF system includes a band-pass filter (500 nm $< \lambda <$ 550 nm) for isolating the SFL signal with relatively maximum temperature sensitive spectrum of the SFL emitted signal. A notch filter also was used to block the laser light, ensuring minimum interfere with the collected SFL signal. The spectra for the PLIF system including the banned-pass filter and the notch filter is also shown in Figure 6-6. Wavelengths above 567 nm, including the RhB emission, are transmitted through the dichroic mirror to the PIV camera, which further isolates the signal using a long pass filter with $\lambda > 600$ nm which is also depicted in Figure 6-6.

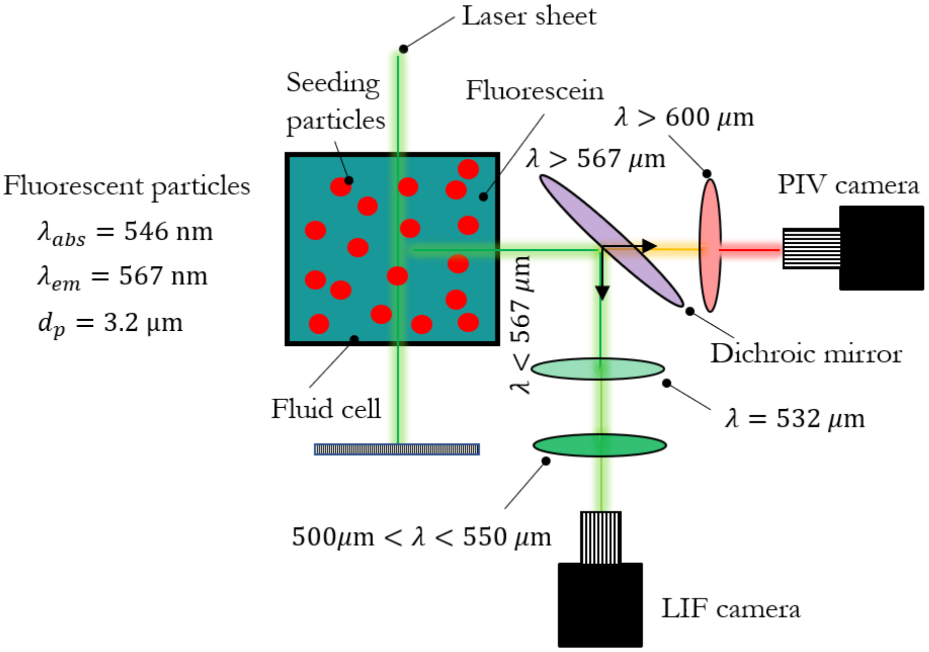

Figure 6-7. Schematic of the optical system for simultaneous PIV and PLIF measurements, illustrating the use of a laser sheet, dichroic mirror, filters, and two cameras to capture velocity and temperature fields independently.

An image of the actual experimental setup is shown in Figure 6-8 and Figure 6-9. These figures illustrate the optical system used for simultaneous PIV and PLIF measurements along to the fluid test rig. The setup is composed of three main components: the fluid test rig, the illumination/excitation unit, and the imaging unit. As can be seen in Figure 6-8 and Figure 6-9(a), the illumination unit features a continuous wave (CW) laser with a maximum power of 5 W. A laser power meter also was employed to monitor temporal fluctuations in the laser power during the experiment. A scanning mirror is used to generate the laser sheet, which is then collimated using a double convex lens shown in Figure 6-8. A front face mirror was used to reflect the collimated laser sheet vertically through the top wall of the test section illuminating the fluid mixture of SFL and RhB seeding particles. As can be seen in Figure 6-8 and Figure 6-9(b), the imaging unit consists of two cameras ((Flare 12M125, IO Industries Inc.) with a maximum frame rate of 220 fps and resolution of 2048 pixels × 2048 pixels. Each camera equipped with a 60 mm focal length lens. These cameras capture the velocity and temperature data separately as discussed in Figure 6-7. The optical path is managed using a custom-designed filter and dichroic mirror holder, which were fabricated via SLA 3D printing to ensure precise alignment. Within this configuration this setup enabled the capture of both velocity and temperature fields in the flow.

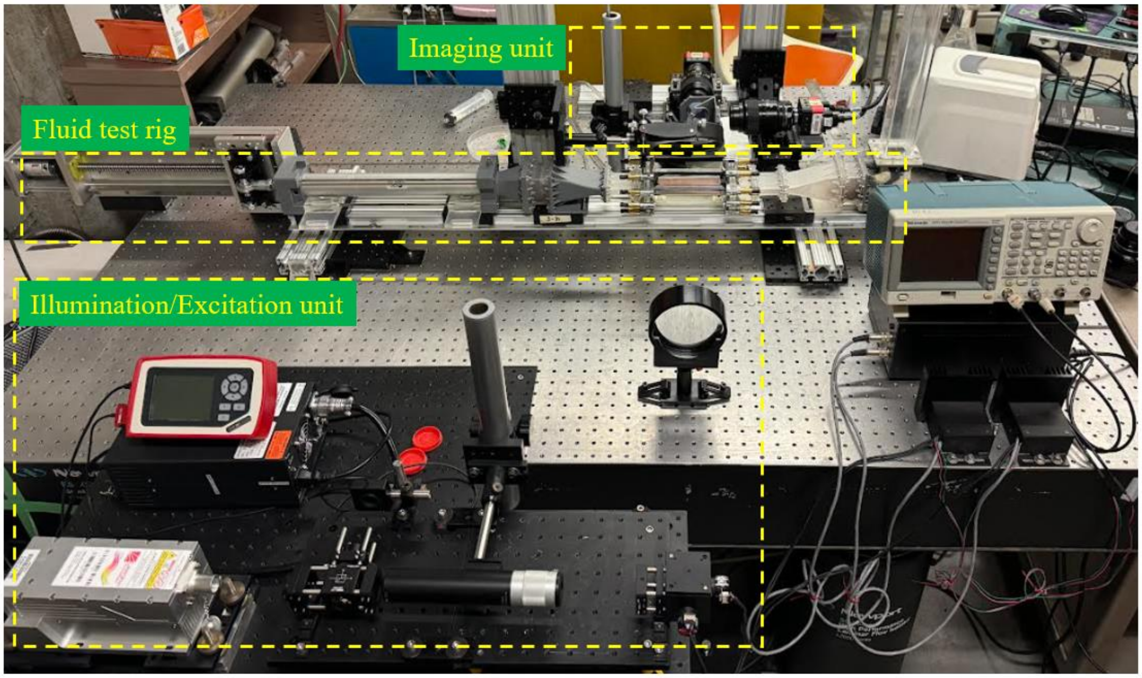

Figure 6-8. Image of the real experimental setup showing the fluid test rig, illumination/excitation unit and the imaging unit.

(a)

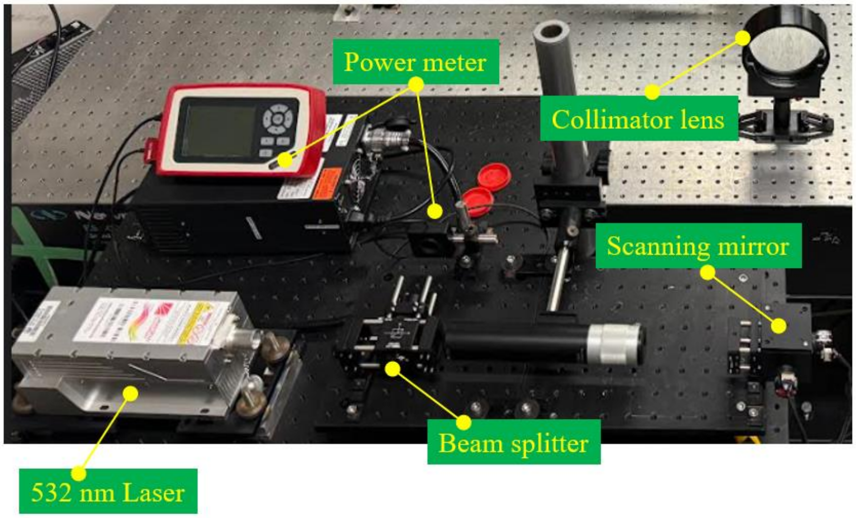

(b)

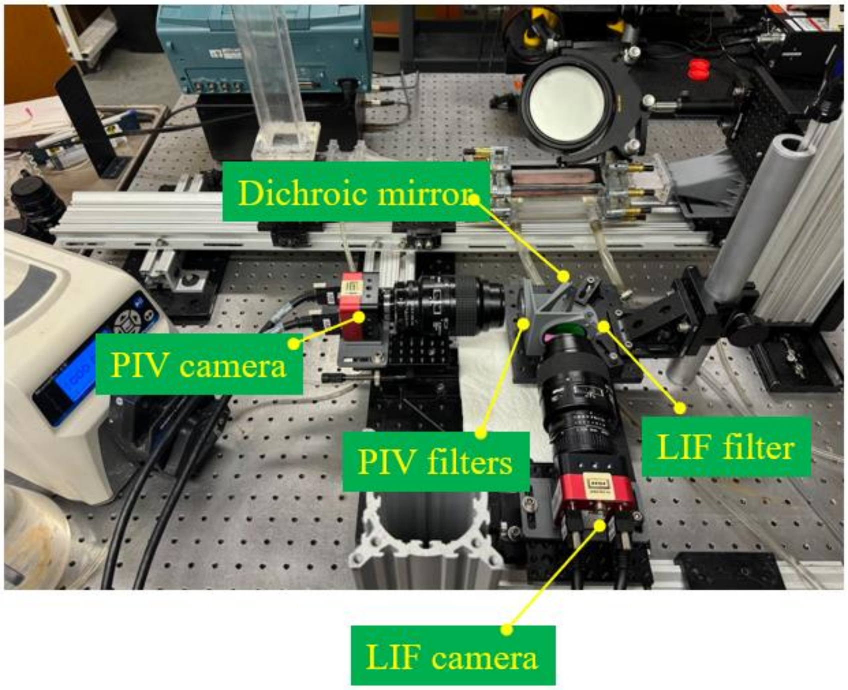

Figure 6-9. (a) The image of the components of the illumination/excitation unit. (b) The image of the components of the imaging unit.

6.6 Results and discussion

The case with Richardson number of $Ri = \infty$, i.e. Reynolds number is $Re = 0$, represents similarities with the RBC flow. However, there differences such as the side wall conditions and the cold boundary above in which here does not exist. Hence, it is interesting to look at this regime separately from the other cases of PRBC flow with the Richardson number being in the criteria of the mixed convection. Typically, the condition with $Ri = \infty$, is known as the natural convection, although development of the flow organizations such as LSC in RBC or condense rolling structures make the flow characteristics different from the usual natural convection phenomena with the constant vertical flow rising from the hot boundary.

The experiment for this scenario i.e. $Ri = \infty$, is conducted from the start of the convection for duration of $\Delta t = 400$ s. This relatively long-time experiment is necessary since in the flows similar to this case e.g. RBC flow, there are different modes and states with different flow organizations (see [40]). The evolution of the spatial mean temperature of the fluid flow at $Ri = \infty$, during the $\Delta t = 400$ s from the start of the convection, $t = 400$ s is shown in Figure 6-10(a). The spatial mean temperature $\langle T \rangle$ is the average of the temperature of the whole field in $x - z$ plane. As can be seen in this figure, at the very beginning, temperature increases suddenly. This sudden peak of temperature is, highlighted by P in the figure, is due to the rise of the thermal plumes from the bottom boundary. After that, the temperature rises gradually reaching to $\sim 0.7 T_H$ at $t \sim 218$ s. Moving forward in time, it can be seen that temperature reach to a quasi-steady state which is highlighted with a light-yellow box in Figure 6-10(a).

Despite the RBC, in which the boundary condition is featured to a cold boundary at top, here there is only a single heat source, as a result, the temperature of the fluid flow hypothetically must increases temporally reaching to the temperature of the heat source i.e. T_H. Hence, the temperature during the quasi-steady state highlighted in Figure 6-10(a) is might be increasing but with a very long time-scale which is beyond the measurement of this study. The evolution of the mean second moment of the velocity magnitude, $(\langle u_x^2\rangle + \langle u_z^2\rangle)/u_f^2$ is depicted in Figure 6-10(b). Here, u_f is the free-fall velocity defined as $u_f = \sqrt{ag\Delta TH}$. As can be seen in Figure 6-10(b), a trend similar to the temperature variation can be observed. At the very beginning of the start of the convection, a peak in the velocity simultaneous to the temperature is detectable depicted by P in Figure 6-10(b). Similar to the temperature, this peak in the velocity magnitude is associated by the rise of the hot thermal plumes inducing a significant vertical motion to the flow field. The fact of the strong vertical motion at the start of the convection can also be clearly understood by looking into the mean second moment of vertical velocity, $\langle u_z\rangle^2$ and the horizontal one $\langle u_x\rangle^2$ which is shown in Figure 6-11(a) and (b), respectively. As can be seen in these two figures, the peak in the velocity magnitude is due to the peak in the rise of the thermal plumes since the vertical velocity is significant while the horizontal velocity is almost negligible as is highlighted by a light-green box in Figure 6-11(b).

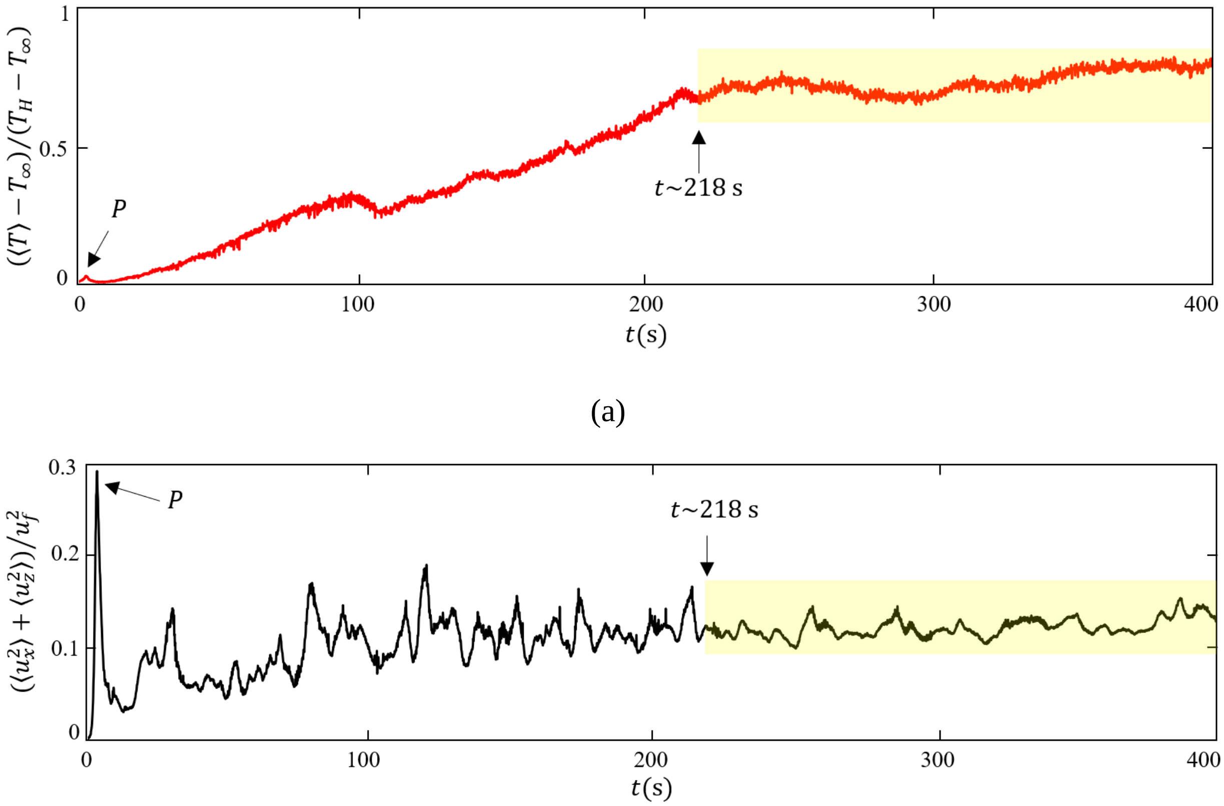

(a)

(b)

Figure 6-10. (a) Temporal evolution of the dimensionless mean temperature variation, $(\langle T\rangle - T_\infty)/(T_H - T_\infty)$, during $\Delta t = 400$ s of measurement of the flow with $Ri = \infty$ i.e. $Re = 0$ and $Ra = 4.5 \times 10^5$. (b) Temporal evolution of the dimensionless mean velocity magnitude, $(\langle u_x^2\rangle + \langle u_z^2\rangle)/u_f^2$ during $\Delta t = 400$ s of measurement of the flow with $Ri = \infty$ i.e. $Re = 0$ and $Ra = 4.5 \times 10^5$.

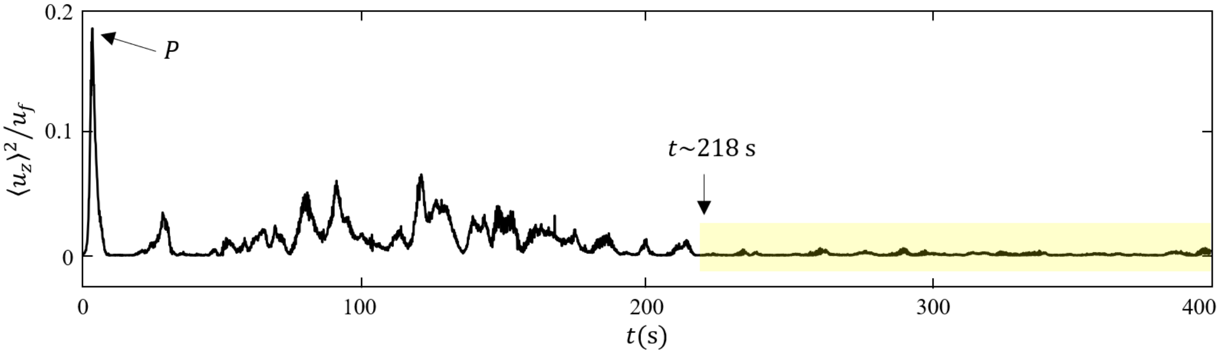

(a)

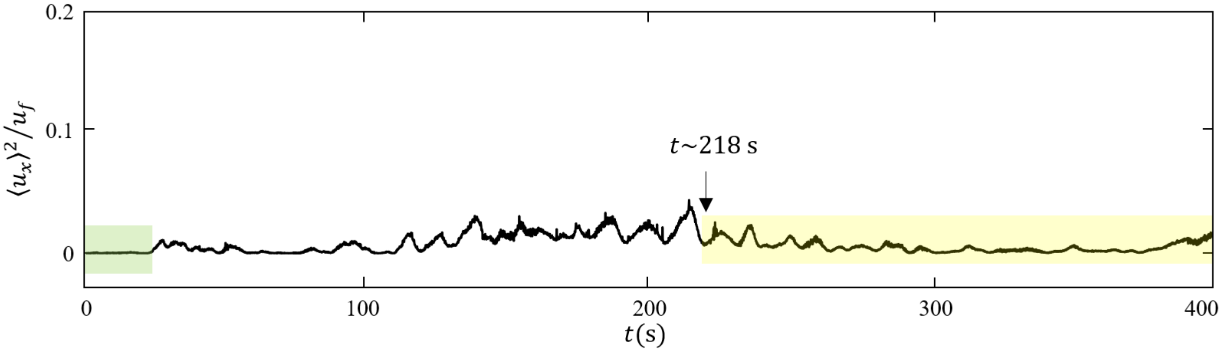

(b)

Figure 6-11. (a) Temporal evolution of the dimensionless second moment of velocity in z-direction, $\langle u_z \rangle^2/u_f$, during $\Delta t = 400$ s of measurement of the flow with $Ri = \infty$ i.e. $Re = 0$ and $Ra = 4.5 \times 10^5$. (b) Temporal evolution of the dimensionless second moment of velocity in x-direction, $\langle u_x \rangle^2/u_f$, during $\Delta t = 400$ s of measurement of the flow with $Ri = \infty$ i.e. $Re = 0$ and $Ra = 4.5 \times 10^5$.

After the start of convection, the trend in the velocity magnitude can be seen being similar to the temperature increase up to $t \sim 218$ s and then reach to a quasi-steady state. This same behavior in the heat and momentum transfer was also reported for RBC flow within OB condition by direct numerical simulation (DNS) by [41], [42]. The criterion of $t \sim 218$ s which has been highlighted in both Figure 6-10 and Figure 6-11 has been determined based on the variation of the second order mean vertical velocity i.e. $\langle u_z \rangle^2/u_f$. As can be seen in Figure 6-11(a), after $t \sim 218$,$\langle u_z \rangle^2/u_f$ stays close to zero. This can be either due to the symmetric vertical motion (symmetric upward and downward motion) resembling the thermal plumes motion within the fluid flow or due to the negligible vertical motion and development a horizontal motion state which can be expected based on the variation of the horizontal velocity. Hence, a closer look to these two modes can helps better understanding of the difference between these two states specially the second one after development of the flow.

To have a more detail understanding of the physics of flow at $Ri = \infty$, and realizing the distinction between the two states of the flow at this regime, probability density function (PDF) of both normalized horizontal velocity, u_x/u_f and vertical velocity u_z/u_f is depicted in Figure 6-12. For the first state, which is associated with rise of the thermal plumes, almost a symmetrical distribution can be observed for the horizontal velocity shown in Figure 6-12(a). However, for vertical velocity which is shown in Figure 6-12(c), a shift to into positive velocities can be seen in the peak while the negative velocities also have high values up to $u_z/u_f = -0.06$. This suggest the same behavior of the under develop flow in which thermal plumes rise and reach to the top boundary and develop horizontally further. In comparison to the first state, for the second state, from Figure 6-12(b) and (d), a bimodal behavior for the horizontal velocity can be observed. The horizontal PDF shows two peaks, one at the positive velocities at $u_x/u_f \sim 0.06$ and the other at $u_x/u_f \sim -0.06$. With the positive velocities being stronger, it can be inferred that the flow state has transformed from the developing mode to a circulating mode with a dominant motion to positive direction of the x-axis. The shift in the peak of the vertical velocity to the zero with a much smaller range of the vertical velocity also indicates a dominant flow motion to positive direction of the x-axis.

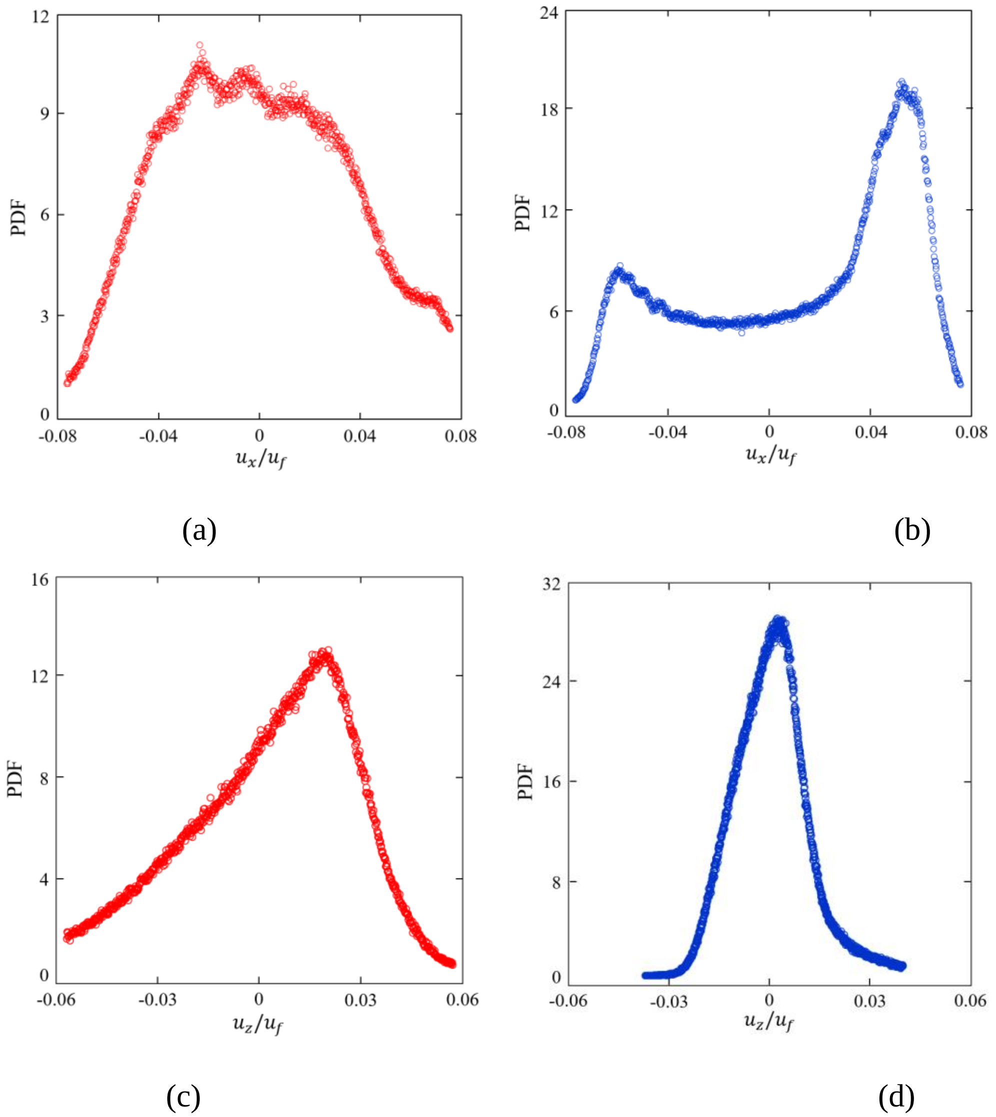

(a) (b)

(c) (d)

Figure 6-12. Probability density function (PDF) of the normalized streamwise, u_z/u_f and lateral, u_z/u_f velocities for the flow with $Ri = \infty$ i.e. $Re = 0$ and $Ra = 4.5 \times 10^5$. (a) and (b) indicates the PDF of the normalized streamwise velocity, u_x/u_f for the start of the convection from $t = 0$ s to $t = 218$ s and $t = 0$ s to $t = 400$ s, respectively. (c) and (d) indicates the PDF of the normalized vertical velocity, u_x/u_f for the start of the convection from $t = 0$ s to $t = 218$ s and $t = 0$ s to $t = 400$ s, respectively.

From instantaneous flow field and temperature field at these two states also the two different organization can be observed. Figure 6-13 and Figure 6-14 show the instantaneous velocity and temperature field at the first and second states, respectively. In Figure 6-13(a), the normalized instantaneous vorticity field, ω^* for $Ri = \infty$ at the time step of $t = 50$ s along with the velocity vectors indicates the flow rolling structures form by development of the thermal plumes. At the same time step in the same condition, Figure 6-13(b) indicates the normalized temperature field depicting vertically high temperature regions showing the formation of thermal plumes. For the second state, however, as can be seen in Figure 6-14(a) and (b), longitudinal flow along x-axis near the bottom wall and opposite to x-axis near the top wall can be observed. In this condition, the temperature field can be seen more uniform with high temperature regions near the bottom and top walls.

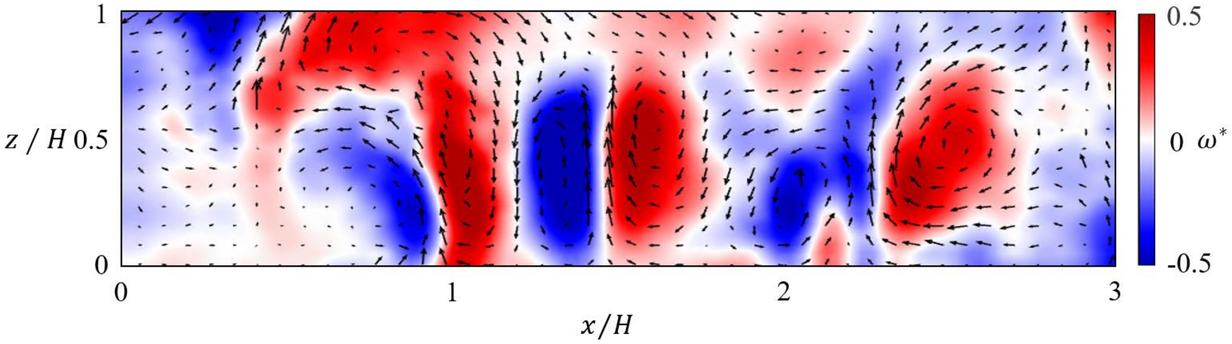

(a)

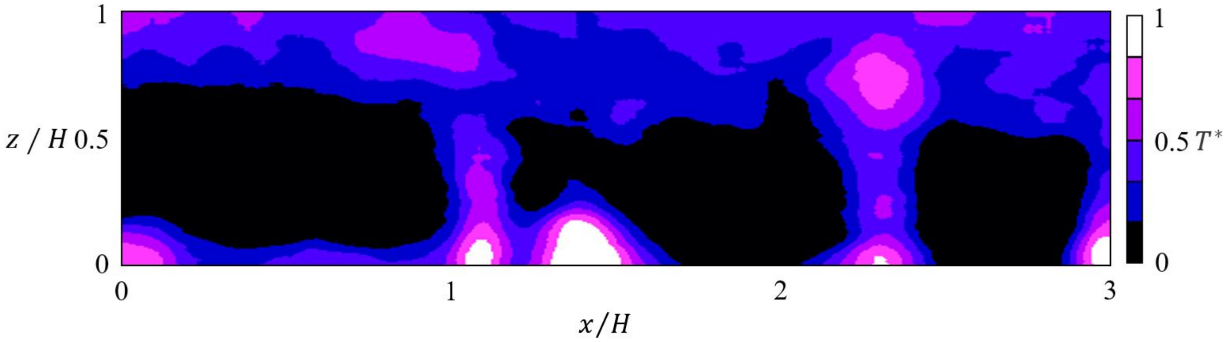

(b)

Figure 6-13. (a) The normalized instantaneous vorticity field, ω^* for $Ri = \infty$ at the time step of $t = 50$ s. (b) The normalized temperature field, T^* for $Ri = \infty$ at the time step of $t = 50$ s.

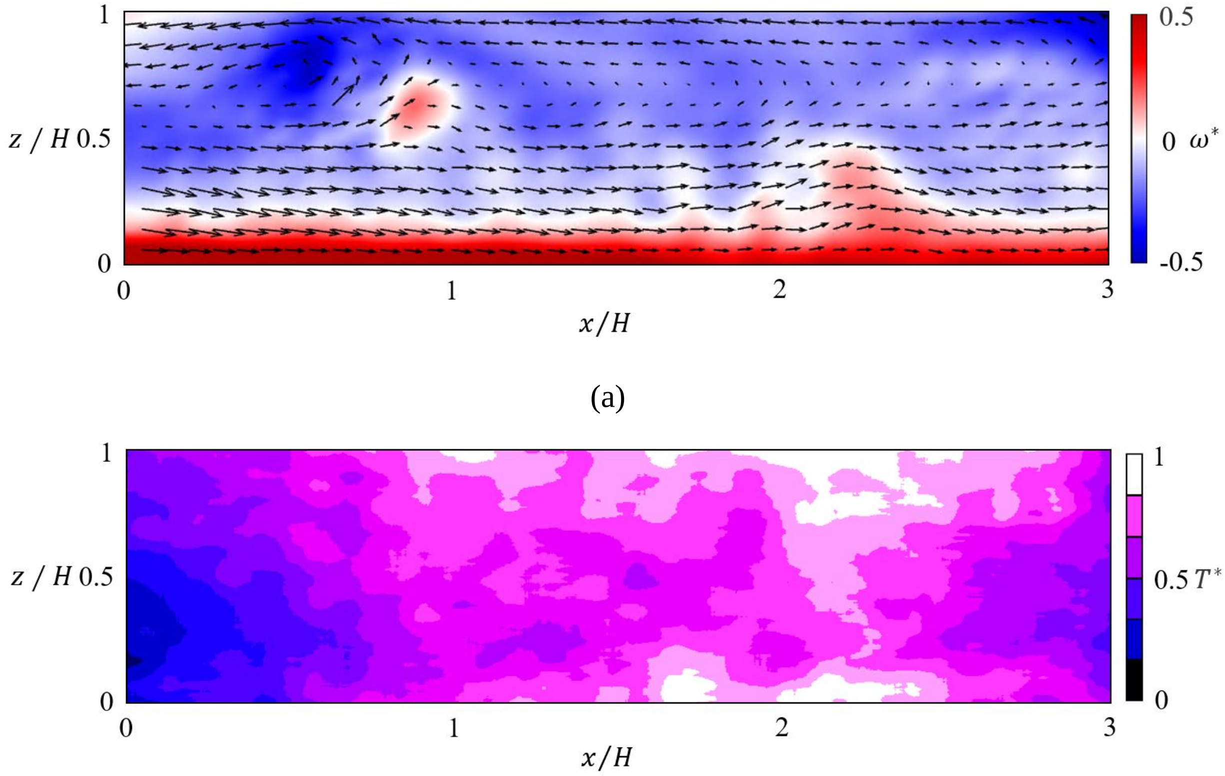

(a)

(b)

Figure 6-14. (a) The normalized instantaneous vorticity field, ω^* for $Ri = \infty$ at the time step of $t = 50$ s. (b) The normalized temperature field, T^* for $Ri = \infty$ at the time step of $t = 266$ s.

The two different terms of the heat transfer coeeficient i.e. the vertical temperature gradient ,$-\partial\langle T^*\rangle/\partial z^*$, and the vertical convection, $\langle u_z^* T^*\rangle$, have been investigated for $Ri = \infty$ case. The temporal evolution of the mean vertical temperature gradient during the $\Delta t = 400$ s, is shown in Figure 6-15(a). Each time step shows the vertical temperature gradient averaged horizontally i.e. x-direction. As can be seen in this figure, there is a sudden decrease at the very beginnig which is associated to the peak of the temperature occures by the rise of the thermal plumes. After that, it decreases constantly which is expected since the temperature of the fluid flow is increased through the time and less heat is transferred to the flow.

The vertical convection term, which is shown in Figure 6-15(b) highlights a high variation at the first state, $t < 218$ s while it decreases by moving to the second phase. Considering the total heat transfer coefficient evolution shown in Figure 6-15(c), it can be seen that vertical convection increases the overall heat transfer at the first state which is associated with high vertical current. However, at the second state in which the horizontal flow motion is dominant the overall heat transfer is controlled by the temperature gradient while the vertical convection fluctuations induce fluctuations in the overall heat transfer at this state. Hence, it can be concluded that while vertical convection influence both states in $Ri = \infty$, its effect is more significant at the first state in which flow is underdeveloped dominated by development of the thermal plumes.

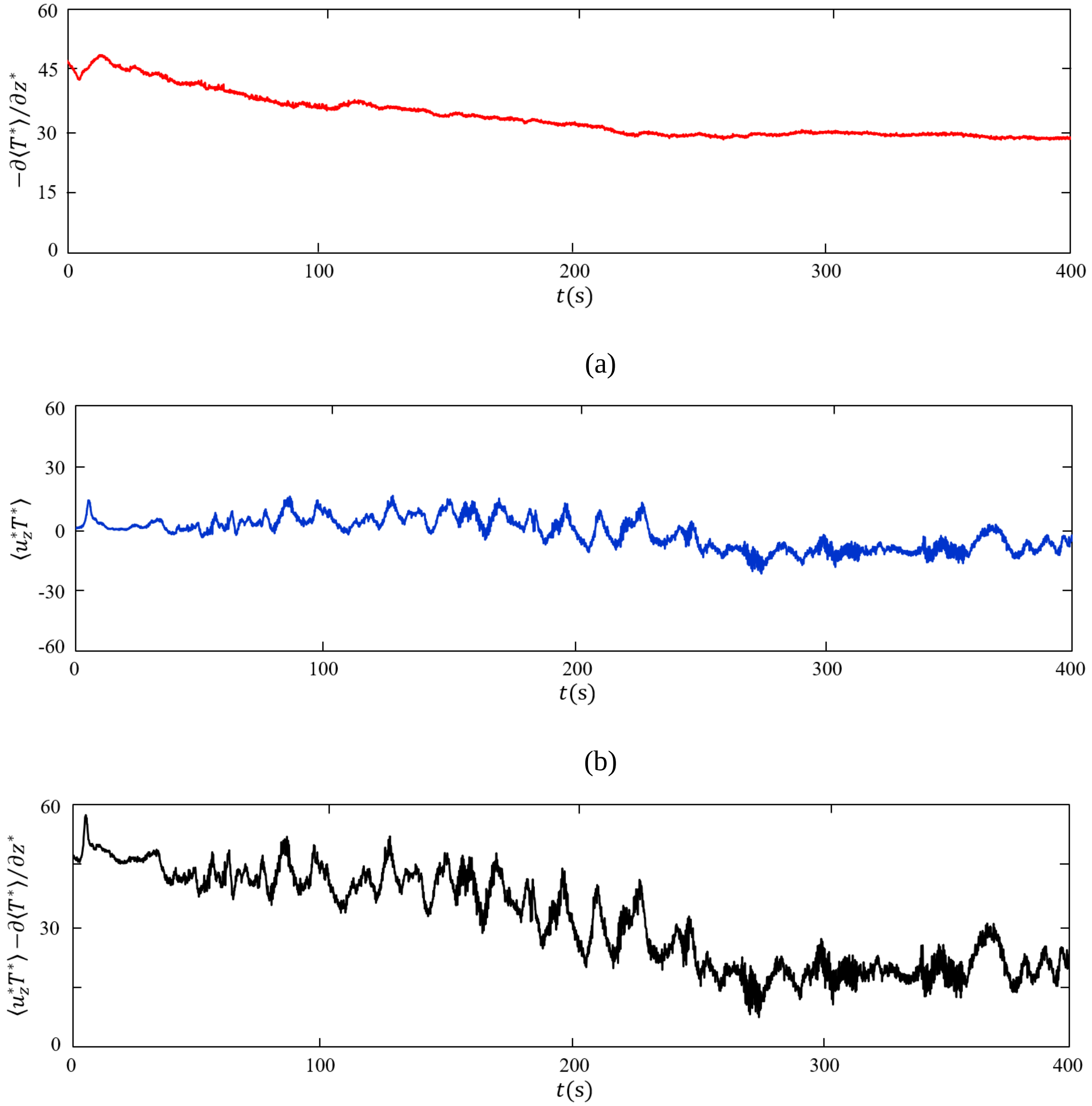

(a)

(b)

(c)

Figure 6-15. (a) Temporal evolution of the dimensionless vertical mean temperature gradient, $-\partial\langle T^*\rangle/\partial z^*$, during $\Delta t = 400$ s of measurement of the flow with $Ri = \infty$ i.e. $Re = 0$ and $Ra = 4.5 \times 10^5$. (b) Temporal evolution of the dimensionless vertical convection, $\langle u_z^* T^*\rangle$ during $\Delta t = 400$ s of measurement of the flow with $Ri = \infty$ i.e. $Re = 0$ and $Ra = 4.5 \times 10^5$. (c) Temporal evolution of Combination of temperature gradient and vertical convection, $\langle u_z^* T^*\rangle - \partial\langle T^*\rangle/\partial z^*$ within the same condition of (a) and (b).

Figure 6-16 presents the normalized temperature profiles measured along the vertical direction (z-axis) at the center of the test section, $x = 0$ for various Richardson numbers, Ri, as indicated in the legend of this figure. The profiles show how the ensemble-averaged temperature, normalized by the temperature difference between the hot plate, T_H and the ambient temperature T_∞, varies with height, z/H across the flow. As can be seen in this figure, the decrease in the Richardson number is asociated with an increase in the influence of shear compared to buoyancy as the temperature profiles show distinct changes in shape and distribution. For $Ri = \infty$ which represents the RBC flow rather than PRBC, the temperature profile shows a strong thermal gradient near the top and bottom boundaries, typical of buoyancy-dominated convection where heat is transferred primarily by vertical plumes. The high temperature at the top boundary in comparison with the lower heights also suggest the rise of the thermal plumes to the top boundary increasing the temperature near that area over time.

By inducing the Poiseuille flow and as the Richardson number decreases, e.g., $Ri = 79.5$ to $Ri = 2.2$, the thermal gradient flattens in the core region and shifts toward the upper part of the domain, indicating the increasing influence of shear flow from the imposed Poiseuille flow. At lower Ri values, the temperature profile is more uniformly distributed along the center, with the gradient concentrating near the top boundary, reflecting a transition toward shear-dominated heat transfer. This suggests that shear is disrupting the convective plumes, redistributing heat more effectively along the horizontal axis, leading to a more uniform temperature field. It is also worth noting that decreasing the Richardson number leads to decrease in the temprature field while the temperature of the hot boundary is the same for all cases. This is even more important when investigating the heat transfer in which temprature gradient near the hot boundary has significant effect. Considering this, a glance into Figure 6-16, it can be inferred that decrease in the Richardson number which in this experiment is associated with the increase in the induced Poiseuille flow velocity leads to an increase in the heat transfer.

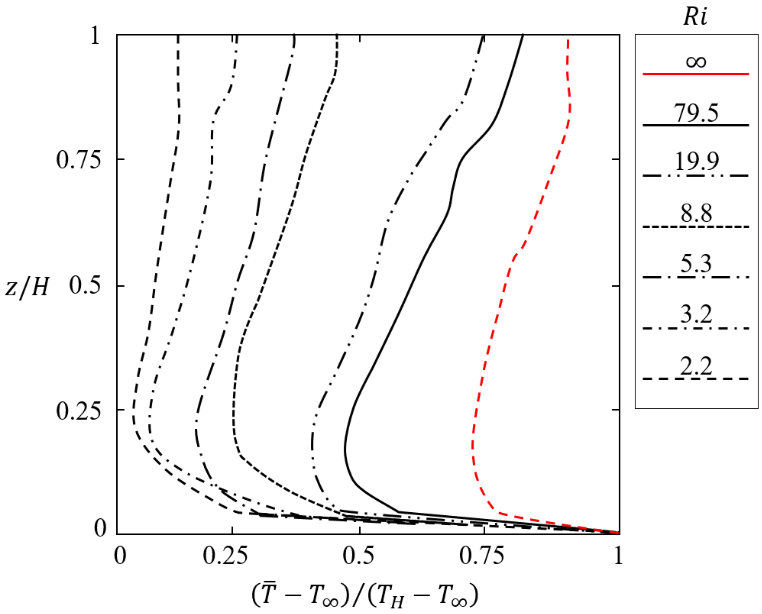

Figure 6-16. Temperature profile of the dimensionless mean temperature $(\overline{T}-T_\infty)/(T_H-T_\infty)$ along the vertical axis, z-direction at the center, $x/H=0$, for Richardson numbers, Ri, listed in the figure from $Ri=2.2$ to $Ri=\infty$.

For various Richardson numbers, Ri, the normalized streamwise velocity profiles, $\bar{u}_x/\langle\bar{u}_x\rangle$, measured along the vertical direction, z-axis at the center of the test section is depicted in Figure 6-17. These profiles represent the ensemble-averaged streamwise velocity at different heights, z/H providing insight into how the flow structure transitions from buoyancy-dominated at $Ri=\infty$ to shear-dominated regimes as the Richardson number decreases down to $Ri=2.2$. It should be noted that for $Ri=\infty$, the quasi-steady state of the flow is averaged over time, so the characteristics of that can be observed in the horizontal velocity profile is regardless of the first state in which the flow is underdeveloped and vertical motion of the thermal plumes are dominant. It is also worth noting that for each Richardson number, the ensemble horizontal velocity, is normalized by its mean value along the vertical axis, $\langle\bar{u}_x\rangle$, hence, the variation of the velocity along the vertical axis is the focus not the absolute values of the velocities.

As can be seen in Figure 6-17, for $Ri = \infty$, the horizontal velocity is developed in both directions, along and opposite to the x-axis with the negative flow being much sharper with a peak up to $\bar{u}_x/\langle\bar{u}_x\rangle = -2$ in comparison with the flow in x-direction. However, the positive flow has a thicker layer considering the $\bar{u}_x/\langle\bar{u}_x\rangle = 0$ occurring at around $z/H = 0.61$. This observation of the velocity profile aligns with the observations from the PDF of the horizontal velocity discussed in Figure 6-12. By inducing the Poiseuille flow, for the two high Richardson numbers of $Ri =$ 79.5 and 19.9, negative horizontal velocity still can be observed near the top boundary similar to what could be seen for $Ri = \infty$. However, the layer of the negative velocity near the top boundary decreases significantly by moving from $Ri = \infty$ to $Ri = 79.5$ and also it decreases slightly with decreasing the Richardson number from $Ri = 79.5$ to $Ri = 19.9$. This reduce in the layer of the negative horizontal velocity is also asocitaed with decrease in the peak of the velcoity. The negative horizontal velocity region is highlighted in Figure 6-17 with a light-yellow region.

Decreasing the Richardson number to lower values i.e. $Ri < 10$, it can be seen that the the influence of Poiseuille flow is very significant making the whole horizontal velocity profile positive suggesting the dominancy of the cross flow over the motion of the thermal plumes and the flow induced by them. Looking into the positive part of the horizontal velocity, decreasing the Richardson number leads to a more symmetric velocity profile resembling the Poiseuille flow. However, due to the influence of the thermal plumes it can be seen the horizontal velocity profile is still assymetric even for the lowest Richrdson number i.e. $Ri = 2.2$ forming the peak of the velocity at the bottom-half of the channel $z/H \sim 0.42$.

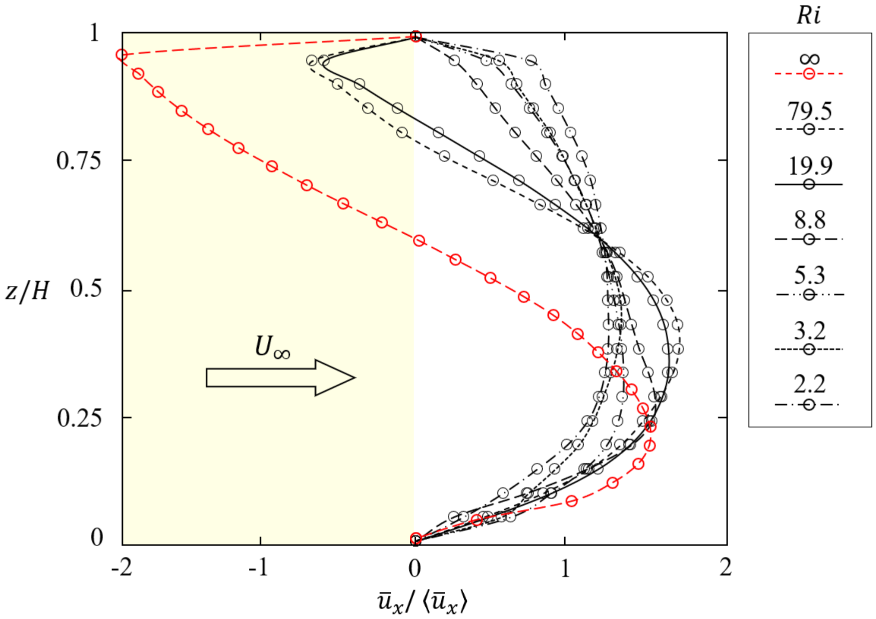

Figure 6-17. Velocity profile of the dimensionless mean horizontal velocity, $\bar{u}_x/\langle\bar{u}_x\rangle$ along the vertical axis, z-direction at the center, $x/H = 0$, for Richardson numbers, Ri, listed in the figure from $Ri = 2.2$ to $Ri = \infty$.

The characteristics of the temperature and the horizontal velocity profile shows three separate flow organization within the flow which can be classified by the Richardson number. The first distinguished regime is for $Ri = \infty$. The second is relevant to the $10 < Ri < 100$ and the third regime is limited to $1 < Ri < 10$. To see the characteristics of the heat transfer for each regime and also investigate the influence of the vertical temperature gradient and the vertical convection term in the heat transfer coefficient, these two terms and the combine effect of them has been investigated and illustrated in Figure 6-18. In this figure, red circles resemble the vertical temperature gradient for the Richardson numbers from $Ri = 2.2$ to $Ri = \infty$. The vertical temperature gradient term, $-\partial\langle\overline{T^*}\rangle/\partial z^*$ is the ensemble average of the spatial mean (in $x - z$ plane). The red rectangle indicates the same parameter for $Ri = \infty$ but only considering the ensemble of the developed flow i.e. $t < 218$ s. The red circle at $Ri = \infty$, however, is the average of the first state. It should be noted that the first state is not statistically convergent meaning this state is unsteady and the mean value does not resemble the true physics, yet, it is plotted along to the other cases as a reference for comparison. Similarly, the blue circles indicate the vertical convection term, $-\partial\langle\overline{T^*}\rangle/\partial z^*$ varying with Richardson number while blue rectangle is the same term for $Ri = \infty$ of the developed state. The combination of these two terms is also plotted in Figure 6-18 highlighted by black circles.

As can be seen in Figure 6-18, by increasing the Richardson number which is aligned with the increase in the free stream of the Poiseuille flow, the vertical temperature gradient increases. This increase from $Ri = \infty$ to $Ri = 79.5$ is significant in comparison with the second range of the Richardson number i.e. $Ri = 79.5$ to $Ri = 19.9$. The increase in the temperature gradient still occurs with a much slower rate at the third range of the Richardson number, $1 < Ri < 10$. Regarding the vertical convection term, it can be seen that the influence of this term is significant at the first two range of the Richardson number, $Ri = \infty$ and $1 < Ri < 10$. However, for the last range i.e. $1 < Ri < 10$, its influence in the overall heat transfer coefficient is negligible. This can be highlighted by comparing the combination of both terms with the temperature gradient, in which it can be seen that for $Ri = 8.8$ the difference between the overall coefficient and the temperature gradient is lower than 4%. This difference for the last three cases i.e. $Ri = 5$, 3.2, and 2.2 is lower than 1%.

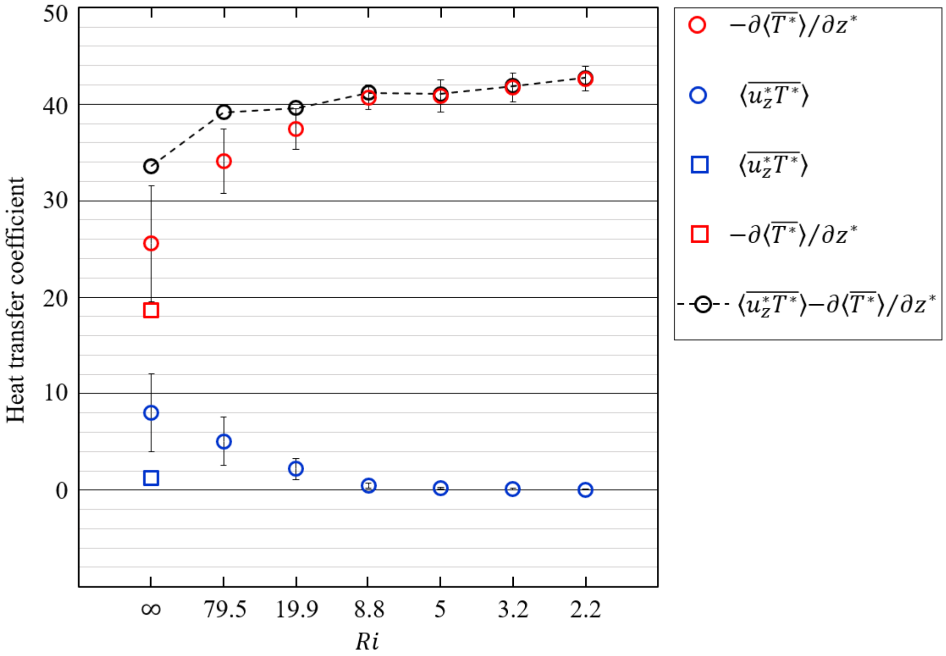

Figure 6-18. Mean heat transfer coefficient components of PRBC flow with the Richardson number from $Ri = 2.2$ to $Ri = \infty$. Red circles indicate the vertical temperature gradient term, while the blue circles show the vertical convection term. Red and Blue rectangles indicate the vertical temperature gradient term and vertical convection term, respectively for the $Ri = \infty$ when the flow is developed, $t > 218$ s. Error bars indicate the standard deviation.

6.7 Conclusion

The purpose of this study was to investigate heat transfer characteristics in Poiseuille-Rayleigh-Bénard Convection (PRBC) by determining the Nusselt number across a broad range of Richardson numbers, $Ri = 2.2$ to $Ri = \infty$ which covers both buoyancy-dominated and shear-dominated regimes. The methodology combined an experimental setup with a custom-designed fluid test rig. The fluid test rig consisted of a rectangular channel heated from below, with a controlled heat source providing constant boundary conditions. The rig was designed for maximum optical access, featuring transparent acrylic walls and a thin copper plate heat exchanger. Water was used as the working fluid. Simultaneous temperature and velocity measurements were achieved using a temperature laser-induced fluorescence (PLIF) and particle image velocimetry (PIV) system. Sodium fluorescein (SFL) was employed as the temperature-sensitive fluorescent dye, with Rhodamine B (RhB)-coated seeding particles for the PIV measurements. The spectral separation between the emission wavelengths of SFL and RhB ensured minimal interference between the PLIF and PIV signals, enabling simultaneous capture of both temperature and velocity fields. Three separate regimes were found based on the Richardson number. For $Ri = \infty$ it was found that flow develops in two states during the period that flow was captured, $\Delta t = 400$ s. The first state is associated by the development of the thermal plumes and the second state could be characterize by longitudinal motion of the flow along the x-axis near the bottom (hot) boundary and opposite to the x-axis near the adiabatic (top) boundary. For $Ri = 79.5$ and $Ri = 19.9$ it was found that the both vertical temperature gradient and the vertical convection term in heat transfer coefficient influence the heat transport significantly. However, for lower Richardson numbers down to $Ri = 2.2$, the effect of the vertical convection is negligible since the Poiseuille flow dominates the vertical motion of the thermal plumes.

References

[1] H. V. Mahaney, F. P. Incropera, and S. Ramadhyani, “Development of laminar mixed convection flow in a horizontal rectangular duct with uniform bottom heating,” *Numerical Heat Transfer*, vol. 12, no. 2, pp. 137–155, 1987, doi: 10.1080/10407788708913578.

[2] R. Taher, M. M. Ahmed, Z. Haddad, and C. Abid, “Poiseuille-Rayleigh-Bénard mixed convection flow in a channel: Heat transfer and fluid flow patterns,” *Int J Heat Mass Transf*, vol. 180, Dec. 2021, doi: 10.1016/j.ijheatmasstransfer.2021.121745.

[3] G. Ahlers, S. Grossmann, and D. Lohse, “Heat transfer and large scale dynamics in turbulent Rayleigh-Bénard convection,” *Rev Mod Phys*, vol. 81, no. 2, pp. 503–537, 2009, doi: 10.1103/RevModPhys.81.503.

[4] I. Catton, “Convection in a Closed Rectangular Region: The Onset of Motion,” *J Heat Transfer*, vol. 92, no. 1, pp. 186–188, Feb. 1970, doi: 10.1115/1.3449626.

[5] H. D. Xi, S. Lam, and K. Q. Xia, “From laminar plumes to organized flows: the onset of large-scale circulation in turbulent thermal convection,” *J Fluid Mech*, vol. 503, no. 503, pp. 47–56, Mar. 2004, doi: 10.1017/S0022112004008079.

[6] S. Kashanj and D. S. Nobes, “Experimental evidence of the correlation between the flow rolling structures and momentum transfer in Rayleigh–Bénard convection,” *Physics of Fluids*, vol. 36, no. 10, Oct. 2024, doi: 10.1063/5.0225406.

[7] L. Zwirner, A. Tilgner, and O. Shishkina, “Elliptical Instability and Multiple-Roll Flow Modes of the Large-Scale Circulation in Confined Turbulent Rayleigh-Bénard Convection,” *Phys Rev Lett*, vol. 125, no. 5, Jul. 2020, doi: 10.1103/PhysRevLett.125.054502.

[8] S. Pirozzoli, M. Bernardini, R. Verzicco, and P. Orlandi, “Mixed convection in turbulent channels with unstable stratification,” *J Fluid Mech*, vol. 821, pp. 482–516, Jun. 2017, doi: 10.1017/jfm.2017.216.

[9] B. Adrian, *CONVECTION HEAT TRANSFER*. John Wiley and Sons, Inc, 2013.

[10] J. R. Maughan and F. P. Incropera, “Experiments on mixed convection heat transfer for airflow in a horizontal and inclined channel,” 1987.

[11] F. P. Incropera, A. L. Knox, and J. R. Maughan, “mixed-convection flow and heat transfer in the entry region of a horizontal rectangular duct,”, Journal of Heat and Mass Transfer, 1987.

[12] J. R. Maughan and F. P. Incropera, “Experiments in Fluids Secondary flow in horizontal channels heated from below,” 1987.

[13] D. G. Osborne and F. P. Incropera, “Experimental study of mixed convection heat transfer for transitional and turbulent flow between horizontal, parallel plates,” 1985.

[14] D. G. Osborne and F. P. Incropera, “Laminar, mixed convection heat transfer for flow between horizontal parallel plates with asymmetric heating,” 1985.

[15] G. Zhou and Z. Feng, “Experimental investigations of heat transfer enhancement by plane and curved winglet type vortex generators with punched holes,” *International Journal of Thermal Sciences*, vol. 78, pp. 26–35, Apr. 2014, doi: 10.1016/j.ijthermalsci.2013.11.010.

[16] T. Y. Chen and H. T. Shu, “Flow structures and heat transfer characteristics in fan flows with and without delta-wing vortex generators,” *Exp Therm Fluid Sci*, vol. 28, no. 4, pp. 273–282, 2004, doi: 10.1016/S0894-1777(03)00107-9.

[17] U. Akdag and A. F. Ozguc, “Experimental investigation of heat transfer in oscillating annular flow,” *Int J Heat Mass Transf*, vol. 52, no. 11–12, pp. 2667–2672, 2009, doi: 10.1016/j.ijheatmasstransfer.2009.01.006.

[18] J. D. Patil and B. S. Gawali, “Experimental study of heat transfer characteristics in oscillating fluid flow in tube,” *Experimental Heat Transfer*, vol. 30, no. 4, pp. 328–340, 2017, doi: 10.1080/08916152.2016.1258018.

[19] M. Mommert, D. Schiepel, D. Schmeling, and C. Wagner, “Reversals of coherent structures in turbulent mixed convection,” *J Fluid Mech*, vol. 904, no. October, 2020, doi: 10.1017/jfm.2020.705.

[20] O. Shishkina, “Rayleigh-Bénard convection: The container shape matters,” *Phys Rev Fluids*, vol. 6, no. 9, Sep. 2021, doi: 10.1103/PhysRevFluids.6.090502.

[21] “Particle Image Velocimetry: A Practical Guide: Raffel, Markus, Willert, Christian E., Scarano, Fulvio, Kähler, Christian J., Wereley, Steve T., Kompenhans, Jürgen: 9783030098551:

Books - Amazon.ca." Accessed: Jun. 17, 2021. [Online]. Available: https://www.amazon.ca/Particle-Image-Velocimetry-Practical-Guide-dp-3030098559/dp/3030098559/ref=dp_ob_title_bk

[22] A. Eghtesad, M. A. Bijarchi, M. B. Shafii, and H. Afshin, "A state-of-the-art review on laser-induced fluorescence (LIF) method with application in temperature measurement," Feb. 01, 2024, *Elsevier Masson s.r.l.* doi: 10.1016/j.ijthermalsci.2023.108686.

[23] N. Fujisawa, S. Funatani, and N. Katoh, "Scanning liquid-crystal thermometry and stereo velocimetry for simultaneous three-dimensional measurement of temperature and velocity field in a turbulent Rayleigh-Bérnard convection," *Exp Fluids*, vol. 38, no. 3, pp. 291–303, Mar. 2005, doi: 10.1007/s00348-004-0891-2.

[24] T. Käufer and C. Cierpka, "Volumetric Lagrangian temperature and velocity measurements with thermochromic liquid crystals," *Meas Sci Technol*, vol. 35, no. 3, p. 035301, Mar. 2024, doi: 10.1088/1361-6501/ad16d1.

[25] M. Koochesfahani, R. Cohn, and C. Mackinnon, "Simultaneous whole-field measurements of velocity and concentration fields using a combination of MTV and LIF," 2000.

[26] B. Stier and M. M. Koochesfahani, "Molecular Tagging Velocimetry (MTV) measurements in gas phase flows," Springer-Verlag, 1999.

[27] K. Hishida and J. Sakakibara, "Combined planar laser-induced fluorescence-particle image velocimetry technique for velocity and temperature fields," in *Experiments in Fluids*, 2000. doi: 10.1007/s003480070015.

[28] A. S. Nebuchinov, Y. A. Lozhkin, A. V. Bilsky, and D. M. Markovich, "Combination of PIV and PLIF methods to study convective heat transfer in an impinging jet," *Exp Therm Fluid Sci*, vol. 80, pp. 139–146, 2017, doi: 10.1016/j.expthermflusci.2016.08.009.

[29] S. Grafsronningen and A. Jensen, "Simultaneous PIV/LIF measurements of a transitional buoyant plume above a horizontal cylinder," *Int J Heat Mass Transf*, vol. 55, no. 15–16, pp. 4195–4206, 2012, doi: 10.1016/j.ijheatmasstransfer.2012.03.060.

[30] S. Funatani, N. Fujisawa, and H. Ikeda, "Simultaneous measurement of temperature and velocity using two-colour LIF combined with PIV with a colour CCD camera and its application

to the turbulent buoyant plume," *Meas Sci Technol*, vol. 15, no. 5, pp. 983–990, 2004, doi: 10.1088/0957-0233/15/5/030.

[31] A. D. Demou and D. G. E. Grigoriadis, "Direct numerical simulations of Rayleigh–Bénard convection in water with non-Oberbeck–Boussinesq effects," *J Fluid Mech*, vol. 881, pp. 1073–1096, Dec. 2019, doi: 10.1017/jfm.2019.787.

[32] K. Sugiyama, E. Calzavarini, S. Grossmann, and D. Lohse, "Flow organization in two-dimensional non-Oberbeck–Boussinesq Rayleigh–Bénard convection in water," *J Fluid Mech*, vol. 637, pp. 105–135, Oct. 2009, doi: 10.1017/S0022112009008027.

[33] G. Ahlers, E. Brown, F. F. Araujo, D. Funfschilling, S. Grossmann, and D. Lohse, "Non-Oberbeck-Boussinesq effects in strongly turbulent Rayleigh-Bénard convection," *J Fluid Mech*, vol. 569, pp. 409–445, 2006, doi: 10.1017/S0022112006002916.

[34] H. Yik, V. Valori, and S. Weiss, "Turbulent Rayleigh-Bénard convection under strong non-Oberbeck-Boussinesq conditions," *Phys Rev Fluids*, vol. 5, no. 10, Oct. 2020, doi: 10.1103/PhysRevFluids.5.103502.

[35] J. Coppeta and C. Rogers, "Dual emission laser induced fluorescence for direct planar scalar behavior measurements," *Exp Fluids*, vol. 25, no. 1, pp. 1–15, 1998, doi: 10.1007/s003480050202.

[36] J. Sakakibara and R. J. Adrian, "Whole field measurement of temperature in water using two-color laser induced fluorescence," *Exp Fluids*, vol. 26, no. 1–2, pp. 7–15, 1999, doi: 10.1007/s003480050260.

[37] M. B. Shafii, C. L. Lum, and M. M. Koochesfahani, "In situ LIF temperature measurements in aqueous ammonium chloride solution during uni-directional solidification," in *Experiments in Fluids*, 2010, pp. 651–662. doi: 10.1007/s00348-009-0758-7.

[38] J. A. Sutton, B. T. Fisher, and J. W. Fleming, "A laser-induced fluorescence measurement for aqueous fluid flows with improved temperature sensitivity," *Exp Fluids*, vol. 45, no. 5, pp. 869–881, 2008, doi: 10.1007/s00348-008-0506-4.

[39] S. Kashanj and D. S. Nobes, “Application of 4D two-colour LIF to explore the temperature field of laterally confined turbulent Rayleigh–Bénard convection,” *Exp Fluids*, vol. 64, no. 3, Mar. 2023, doi: 10.1007/s00348-023-03589-9.

[40] Q. Wang, R. Verzicco, D. Lohse, and O. Shishkina, “Multiple States in Turbulent Large-Aspect-Ratio Thermal Convection: What Determines the Number of Convection Rolls?,” *Phys Rev Lett*, vol. 125, no. 7, Aug. 2020, doi: 10.1103/PhysRevLett.125.074501.

[41] E. P. Van Der Poel, R. J. A. M. Stevens, and D. Lohse, “Connecting flow structures and heat flux in turbulent Rayleigh- Bénard convection,” *Phys Rev E Stat Nonlin Soft Matter Phys*, vol. 84, no. 4, pp. 1–4, 2011, doi: 10.1103/PhysRevE.84.045303.

[42] E. P. van der Poel, R. J. A. M. Stevens, K. Sugiyama, and D. Lohse, “Flow states in two-dimensional Rayleigh-Bénard convection as a function of aspect-ratio and Rayleigh number,” *Physics of Fluids*, vol. 24, no. 8, p. 085104, Aug. 2012, doi: 10.1063/1.4744988.

Chapter 7: Inducing LSC in Poiseuille-Rayleigh-Bénard convection for heat transfer enhancement

This chapter looks into the hypothetical improvement of the heat transfer within PRBC flow with a limited length of heated channel. Using a custom design swirler, LSCs were induced passively through the PRBC flow. The temperature field near the boundary and consequently heat transfer was calculated by applying two-colour two dye PLIF for Richardson numbers of $Ri = 2.2, 3.2,$ and 5.

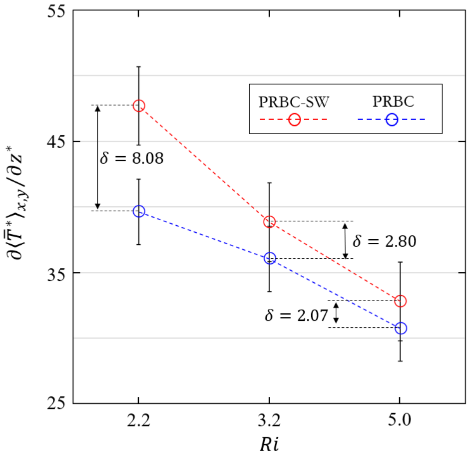

Graphical abstract for Chapter 7

7.1 Introduction

Heat transfer in fluid flows can occur in several regimes: natural, forced, and mixed convection [1]. In forced convection, where an external force like a pump or fan drives the flow, the movement of the fluid enhances heat transfer significantly [1]. Vortex generators, often used in channel-bounded forced convection, are popular tools for improving heat transfer, as they create eddies in the flow that disturb the thermal boundary layer [1]. Studies have shown that the use of vortex generators can lead to a heat transfer enhancement especially when optimized for shape and type [2]. However, these methods works for relatively high Reynolds numbers, usually $Re > 10000$ and they lose efficiency as Reynolds numbers decrease [3]. In mixed convection systems such as Poiseuille Rayleigh-Bénard convection (PRBC), where both forced and buoyancy-driven flows coexist vortex generators become less effective [4], [5]. In wall-bounded natural convection systems such as the Rayleigh-Bénard convection (RBC), application of vortex generators is not possible since the flow is only driven by buoyancy.

In RBC flow it is found that heat transfer is influenced significantly by flow rolling structures especially large-scale circulation (LSC) [6]. Hence, controlling the LSC could be a potential way to enhance the heat transfer both in wall-bounded natural and mixed convection systems such as RBC and PRBC flows. It was experimentally shown that in an RBC flow with unit aspect ratio in which the flow organization is usually dominated by a single LSC and two corner flow rolling structures, heat transfer can be improved by eliminating the corner rolling structures and dominating the flow by only the single LSC [7]. For PRBC flow, it was shown that LSC develops along the channel at very high lengths which leads to an increase in heat transfer [8]. In previous chapter, it was shown that LSC does not form in a limited channel length and flow is dominated by the thermal plumes and the flow structures induced by their interaction with the cross-flow.

This chapter explores the application of inducing LSC in PRBC flow to enhance heat transfer in mixed convection scenarios. By experimentally inducing large-scale circulations in PRBC and measuring the temperature field through two-color, two-dye laser-induced fluorescence (PLIF), the investigation aims to estimate the heat transfer coefficient i.e. Nusselt number. The goal is to evaluate how the introduction of LSC influences the overall heat transfer in the mixed convection regime.

7.2 Methodology

A schematic of the experimental fluid test rig is depicted in Figure 7-1(a). This fluid test rig was also used for investigating the PRBC flow in previous chapter. Hence, the properties of the fluid test rig is exactly the same as described in previous chapter. However, the measurement is conducted differently. As the real image of the test section can be seen in Figure 7-1(c), the field of view in this experiment is at the top of the test section shown in Figure 7-1(b). The field of view (FOV) is in $x - y$ plane, near the solid boundary at $z/H = 0$. The height of the measurement is also limited to the thickness of the laser sheet used for the illumination of the temperature sensitive fluorescent dyes, which is 250 µm within full width half-maximum (FWHM) criterion.

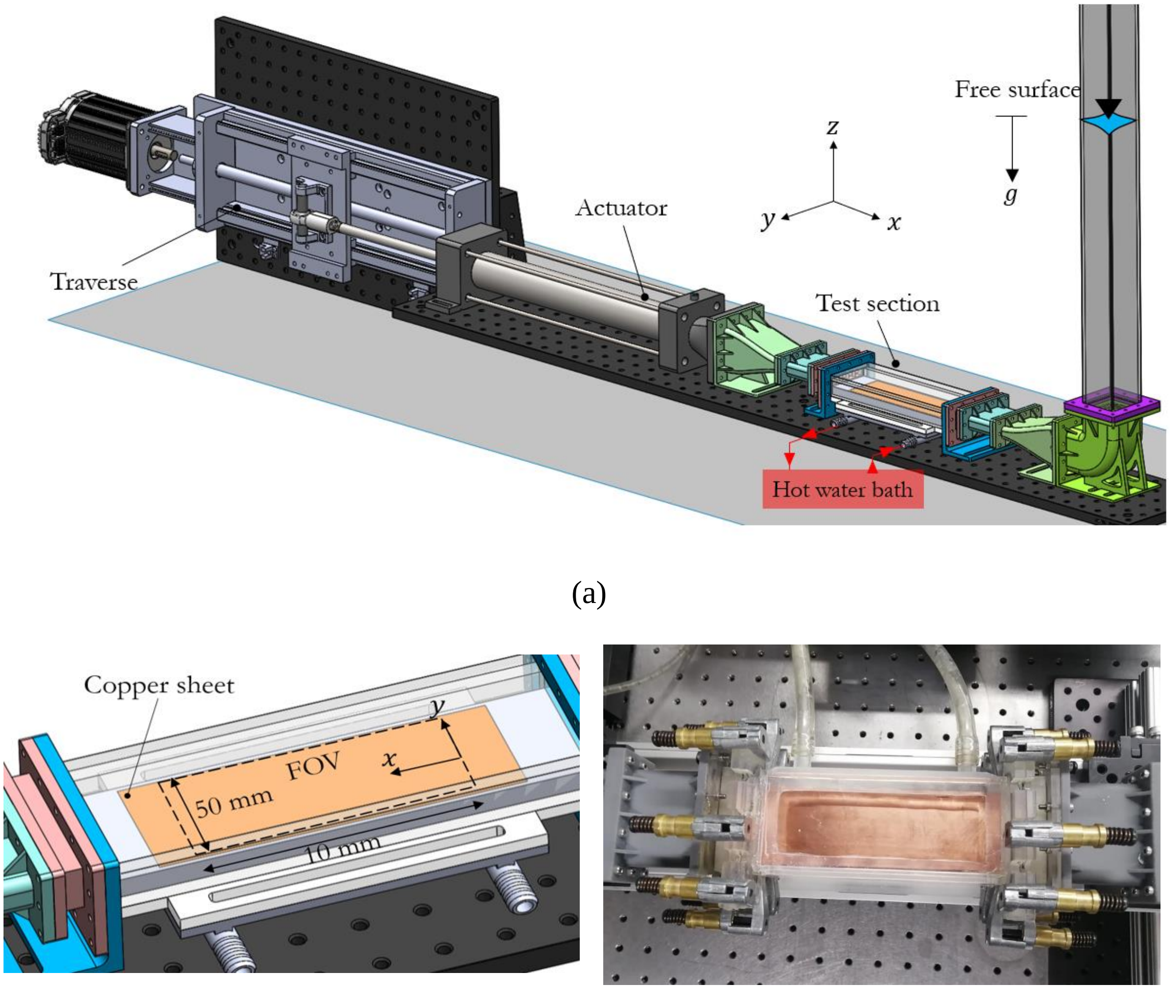

(a)

(b) (c)

Figure 7-1. (a) Rendering of the solid model of the fluid test rig designed and fabricated to generate the PRBC flow. (b) Depicts the test section properties and the field of view, FOV in $x - y$ plane; FOV. (c) The real image of the test section.

To induce large-scale circulating flow structures a swirler was designed. The model of the swirler is shown in Figure 7-2. This swirler features five swirling sections. The design is based on the size of the flow structures. Considering the observations and explanation of the LSC with maximum heat transfer, it can be concluded that the LSC should have a length scale equivalent to the length scale of the convection cell which here is $H = 10$ mm, to maximize the heat transfer.

Furthermore, the rolling structure should be non-elliptical to have the most stability considering the elliptical instability as a source of breakup of LSC in RBC flow. Considering these factors each swirling section has a dimension of 10 mm × 10 mm inducing five LSCs located horizontally side by side. Each swirler is featured by four vanes with a twist angle of 30°. It is important to note that the vane design is not optimized, hence only the geometric properties of the induced swirling flow is optimized to have a LSC with maxima heat transfer properties. The designed swirler is then fabricated using SLA 3D printing with precision of 10 μm which is necessary for fabrication of the swirler, which has twisted thin vanes with 1 mm thickness.

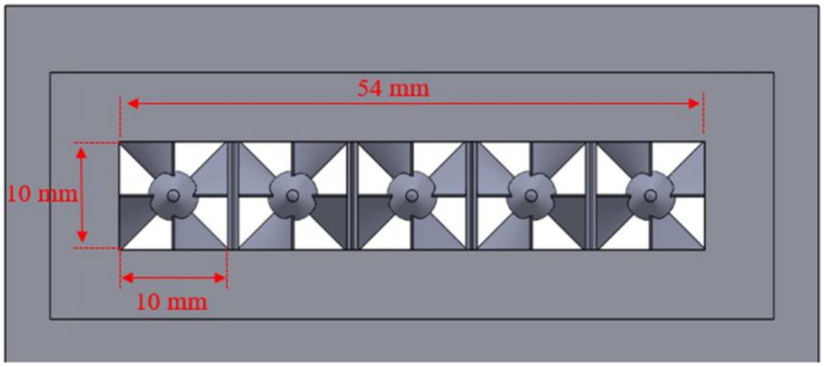

Figure 7-2. CAD model of the designed swirler for generating large-scale circulating structures.

To visualize and quantify the temperature field of the fluid flow near the solid boundary (hot wall) at the bottom of the test section, a two-colour two-dye laser induced fluorescence approach was employed. The details of the used method can be found in [9]. For this experiment, the optical configuration of the optical system is illustrated in Figure 7-3(a). In this configuration laser sheet is generated horizontally illuminating the field of view within the test section. A front face mirror is also located at the top of the test section to reflect the signals of each dye i.e. Fluorescein and Kiton red, to each camera. This configuration is also shown in Figure 7-3(b) and (c), indicating the reflection of the fluorescent signal to the cameras. The details of the filters and optics used in this setup can be found in [9].

The two-colour PLIF that has been applied in this work has a high temperature sensitivity of $\sim 7\%/℃$ which is advantageous for detecting the spatiotemporal evolution of the temperature field within the flow field. This is also important since the data of the temperature is used for calculation of the heat transfer coefficient i.e. Nusselt number. In Figure 7-4 the temperature field at the beginning of the convection when thermal plumes rise and impinge to the top wall of the test section is shown. This temperature field is captured near the top boundary, $z/H = 0.9$ and with no cross flow, i.e. $Ri = \infty$. As can be seen in this figure, the thermal plumes are distinct from the temperature field which indicates the high spatial resolution and high temperature sensitivity of the employed technique for temperature measurement.

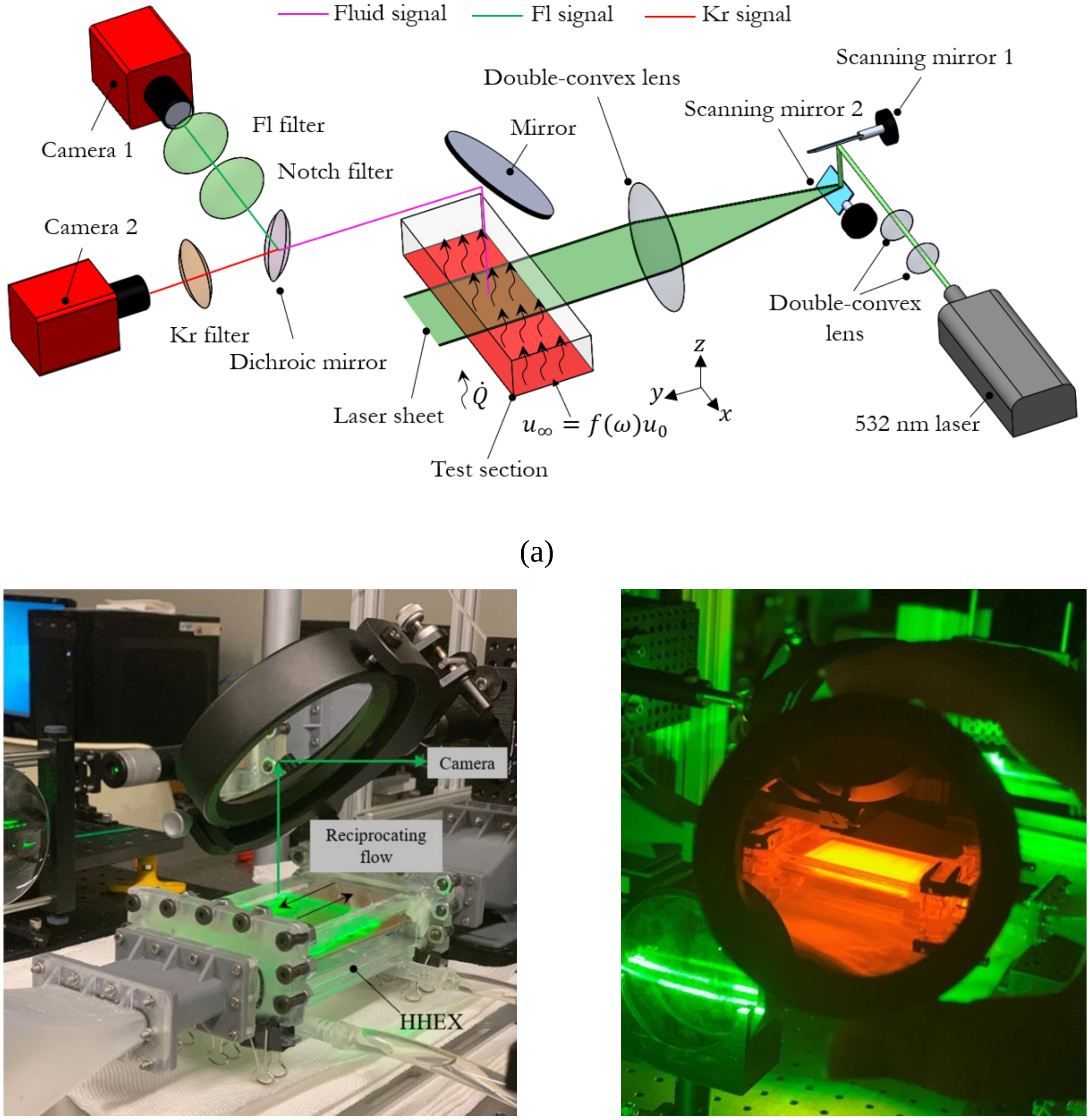

(a)

(b) (c)

Figure 7-3. (a) Schematic of the optical measurement system used to apply two-colour two-dye PLIF. (b) Shows the test section and emitted light from the two-dye while it is illuminated by the 532 nm laser sheet. (c) Indicates the illuminated test section visualized by a long-pass (orange) filter.

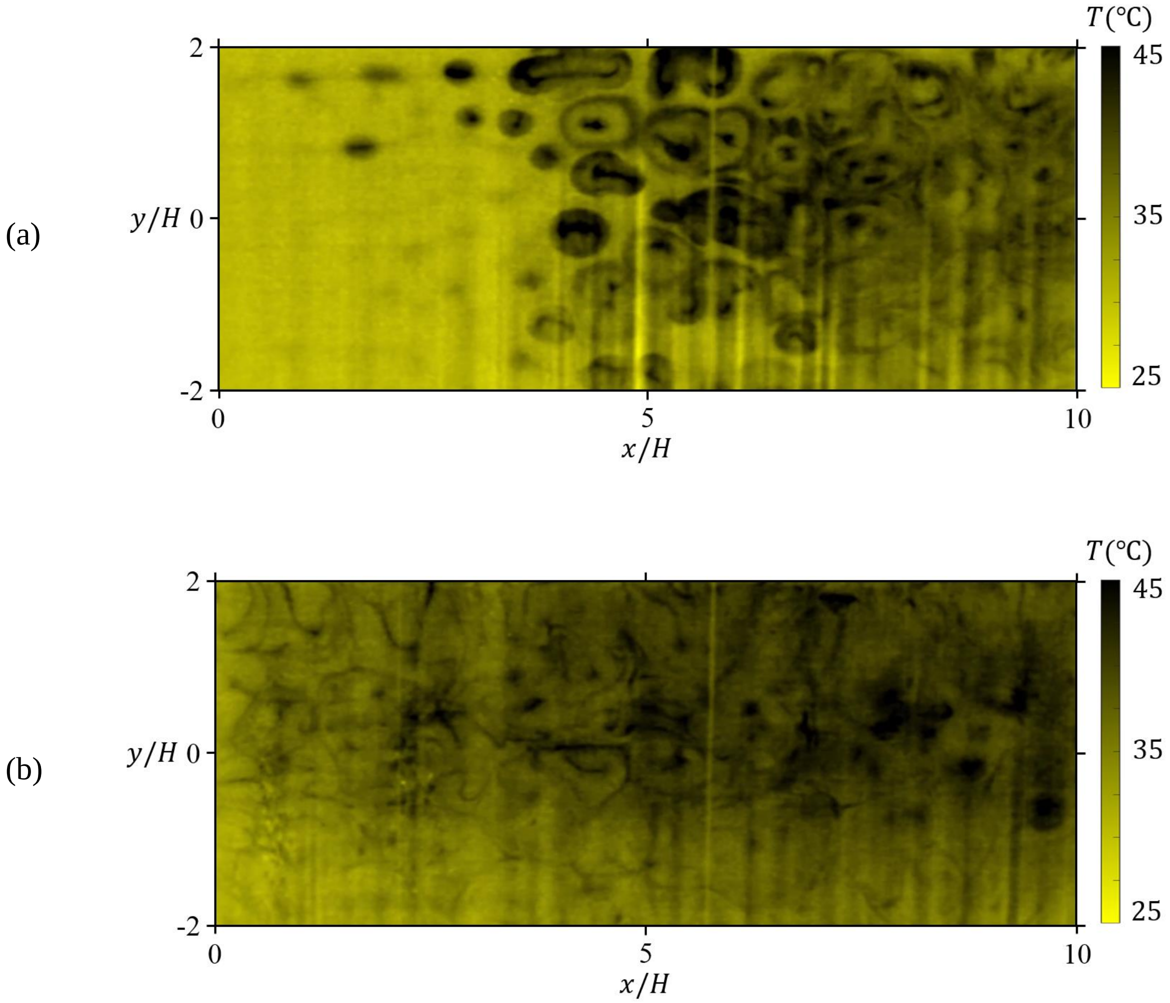

Figure 7-4. Temperature map of the PRBC flow at the test section height of $z = 9$ mm. $Ra = 4.5 \times 10^5$ and $Re = 0$. (a) $t \approx 6$ s (b) $t \approx 28$ s.

Experiments were conducted for three different Richardson numbers of $Ri = 2.2$, 3.2, and 5. In previous chapter it was shown that for Richardson numbers $Ri < 10$, heat transfer coefficient, Nusselt number, can be estimated based on the vertical temperature gradient with vertical flows being negligible in comparison to the higher Richardson numbers. Hence, the three Richardson numbers that were investigated in previous chapters are investigated in this chapter as well. The other conditions of the experiment including the Rayleigh number and Reynolds number which is controlled by the variation of the cross-flow velocity is listed in Table 7-1. For these three

Richardson numbers, experiments were conducted once without swirler representing the basic PRBC flow, which was introduced and discussed in previous chapter, and once with the swirler, PRBC-SW, being placed right before the test section inducing large-scale flow structures to the flow. All the parameters in the experiments for both of these scenarios are exactly the same.

Table 7-1. Flow properties of the PRBC investigated flow.

Ri	5	3.2	2.2
Re	133	167	200
$Ra \times 10^{-5}$	4.5	4.5	4.5
Pr	5	5	5
$U_\infty \times 10^{-3}$ (m/s)	20	25	30
T_H (℃)	45	45	45
T_∞	25	25	25

7.3 Results and discussion

To evaluate the variation of the heat transfer along the test section i.e. x-direction, the mean heat transfer, $\partial\langle\bar{T}^*\rangle_y/\partial z^*$ is plotted in Figure 7-5. This mean heat transfer coefficient presents both ensemble average highlighted as $\bar{\cdot}$ and spatial average in y-direction highlighted as $\langle\cdot\rangle_y$ where $\cdot$ denotes a random parameter such as temperature, T. The plot in Figure 7-5 indicates the variation of the heat transfer coefficient, $\partial\langle\bar{T}^*\rangle_y/\partial z^*$ along the channel for three different Richardson numbers of $Ri = 2.2$, 3.2, and 5 for the PRBC without the implementation of the swirler i.e. basic PRBC shown with blue colour and with implementation of the swirler highlighted in red colour.

As can be seen in Figure 7-5, for the basic PRBC and for all the three Richardson numbers, heat transfer decreases along the channel due to increase in the temperature near the bottom boundary (hot wall). However, for $x/H > 7$, it can be seen that heat transfer increases slightly. This increase in the heat transfer indicates the start of the development of the flow rolling structures which is a characteristic of the PRBC flow lead to the increase in heat transfer along the channel. By implementing the swirler, it can be seen that the overall heat transfer is increased relative to the same Richardson number but without having the swirler. The difference between the heat transfer of the basic PRBC and PRBC-SW is higher for higher Richardson numbers. However, in case of PRBC, it can be seen that in PRBC-SW, the heat transfer decreases constantly along the channel and it does not increase similar to PRBC for $x/H > 7$.

For each Richardson number, the overall heat transfer coefficient defined as the magnitude of $\partial\langle\overline{T}^*\rangle_{x,\,y}/\partial z^*$ is plotted in Figure 7-6. This is necessary for comparison of PRBC with PRBC-SW and to investigate the influence of inducing large-scale flow structures on heat transfer. The overall heat transfer is defined as the ensemble average highlighted as $\bar{\cdot}$ and spatial average in $x - y$ plane defined as $\langle\cdot\rangle_{x,y}$ where $\cdot$ is a random parameter such as temperature, T. As can be seen in this figure for both cases of PRBC and PRBC-SW heat transfer increases by decreasing the Richardson number which is along with the increase in the Reynolds number by increasing the velocity of Poiseuille flow. Regarding the influence of the implementation of swirler, an enhancement can be observed when the swirler is employed. This increase in the heat transfer can be seen that increases by decreasing the Richardson number. The heat transfer enhancement is also listed in Table 7-2. For lowest Richardson number, $Ri = 2.2$, the heat transfer increases by around 20% which is significant.

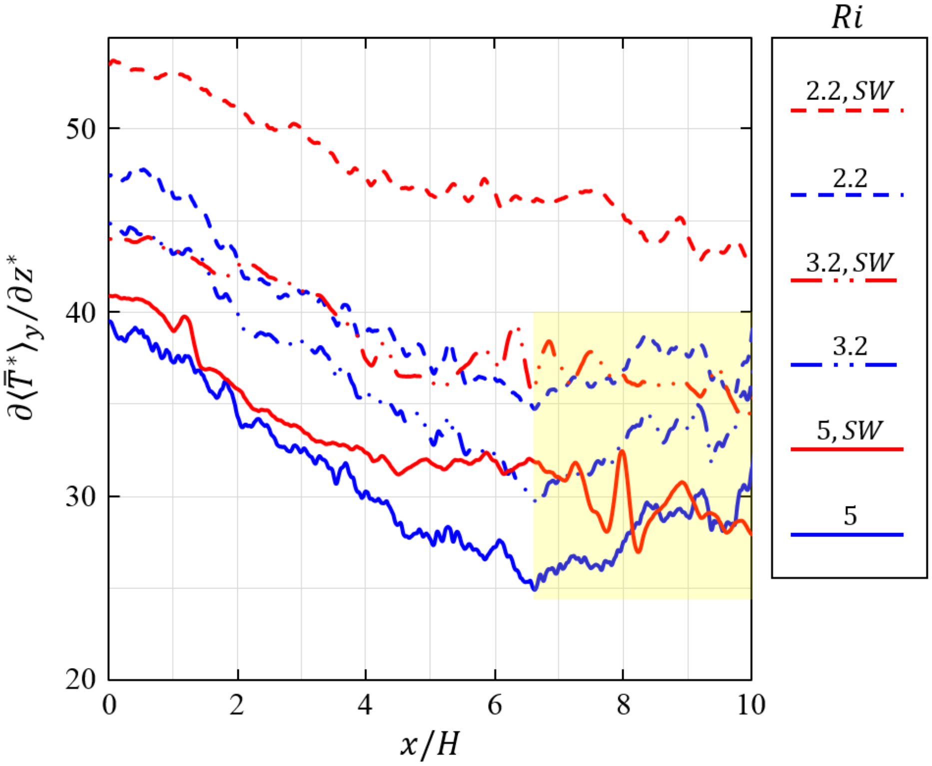

Figure 7-5. Variation of the mean heat transfer coefficient, $\partial\langle\bar{T}^*\rangle_y/\partial z^*$along the x-axis for the case with the swirler highlighted as SW with red colour and base case PRBC highlighted in blue colour.

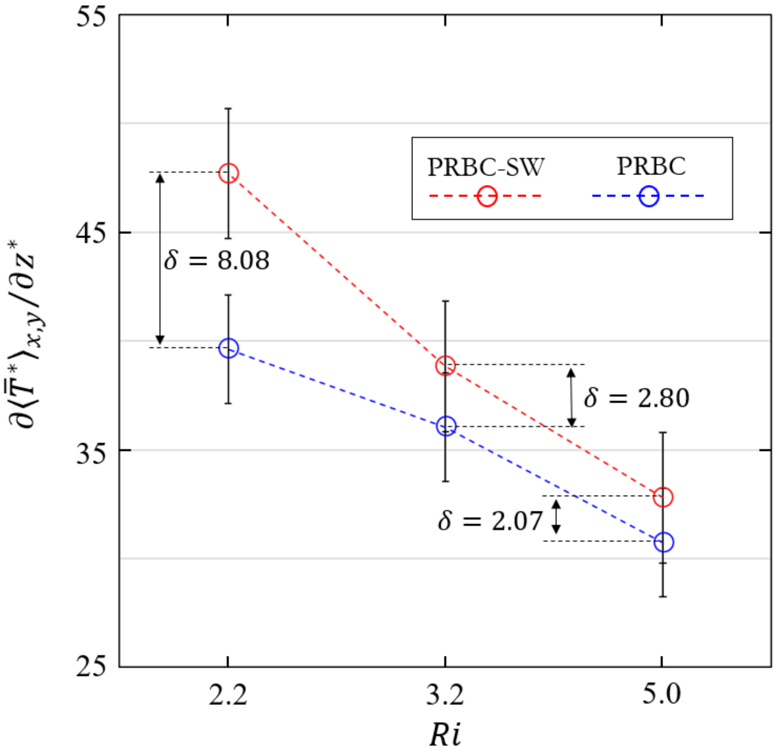

Figure 7-6. Spatio-temporal mean heat transfer for Richardson numbers of $Ri = 2.2$, 3.2, and 5 for the basic PRBC highlighted in red and the PRBC with swirler highlighted in blue. The error bar indicates the spatio-temporal standard deviation of the heat transfer coefficient.

Table 7-2. Mean heat transfer coefficient for the basic PRBC and the PRBC with swirler. The enhancement is also listed for all the studied Richardson numbers.

Ri	5	3.2	2.2
Nu_{PRBC}	30.73	36.04	39.62
$Nu_{PRBC-SW}$	32.8	38.84	47.7
$(\delta/Nu_{PRBC})(\%)$	6.73	7.77	20.39

The temperature map near the bottom boundary (hot wall) for two cases of PRBC and PRBC-SW are indicated in Figure 7-7 and Figure 7-8, respectively. Figure 7-7(a) and (b) shows two instantaneous temperature fields of PRBC both at Richardson number of $Ri = 2.2$ and Figure 7-8

(a) and (b) indicate instantaneous temperature fields for PRBC-SW at the same Richardson number as Figure 7-7. It is worth noting that upstream is at the left side of these temperature maps. Comparing the PRBC cases with PRBC-SW, it can be observed that generally the temperature is higher for PRBC, indicating higher heat transfer in PRBC-SW. Furthermore, it can be seen that thermal plumes are more pronounced in PRBC highlighted by strong white regions within the temperature field. In contrast, in PRBC-SW, thermal plumes are less pronounced indicating lower temperature regions. This observations suggest the influence of the induced LSCs to suppress the vertical motion of thermal plumes and hence, lowering the high temperature zones near the solid boundary which leads to higher heat transfer coefficient. The influence of the induce LSCs are also relatively effective along the channel with and not limited only to the beginning of the channel as the elongation of the high temperature streaks can be observed in the case of PRBC-SW.

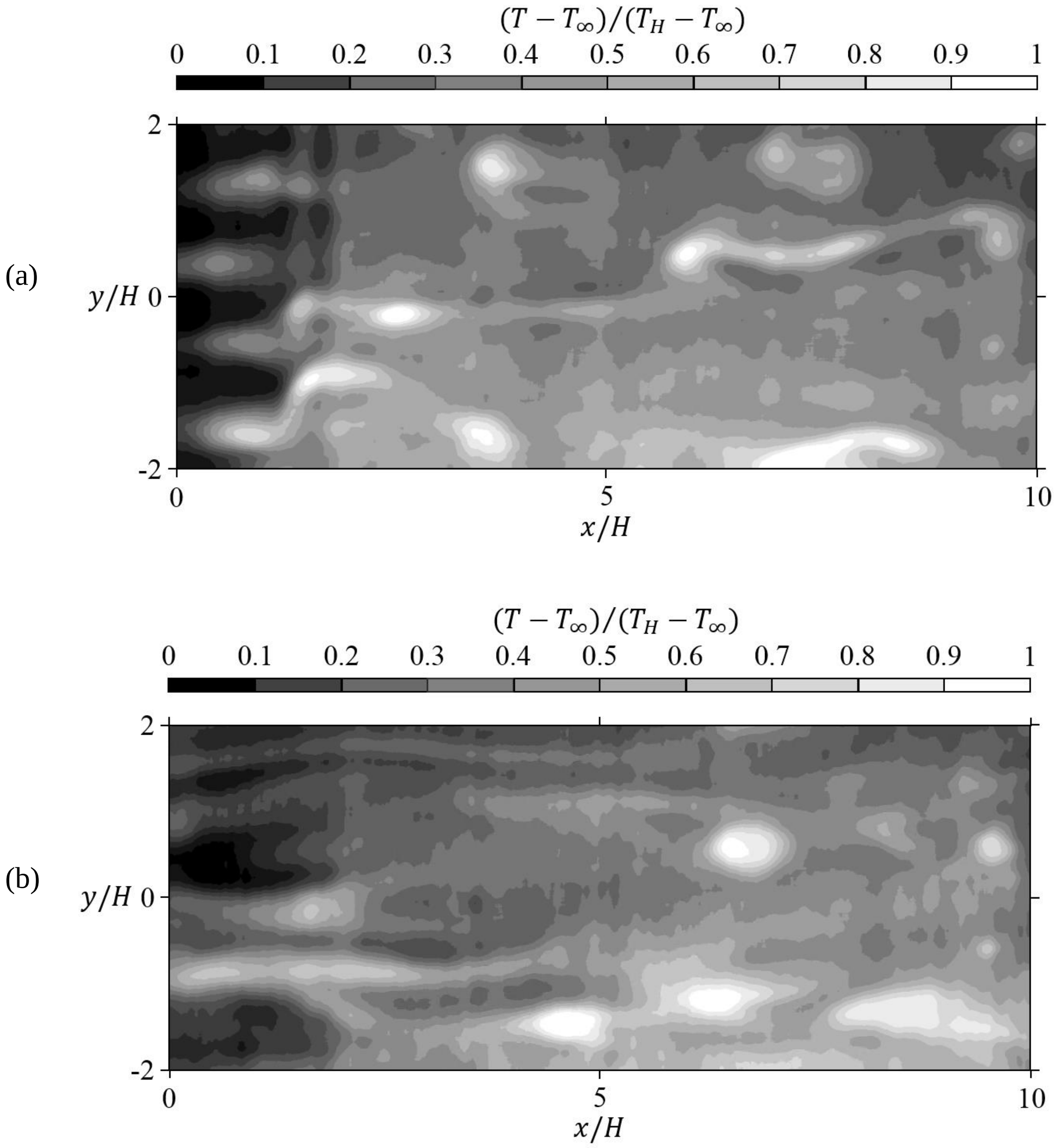

Figure 7-7. Instantaneous temperature fields near the bottom boundary (hot wall) for basic case of PRBC flow when the flow is fully developed and for the Richardson number of $Ri = 2.2$.

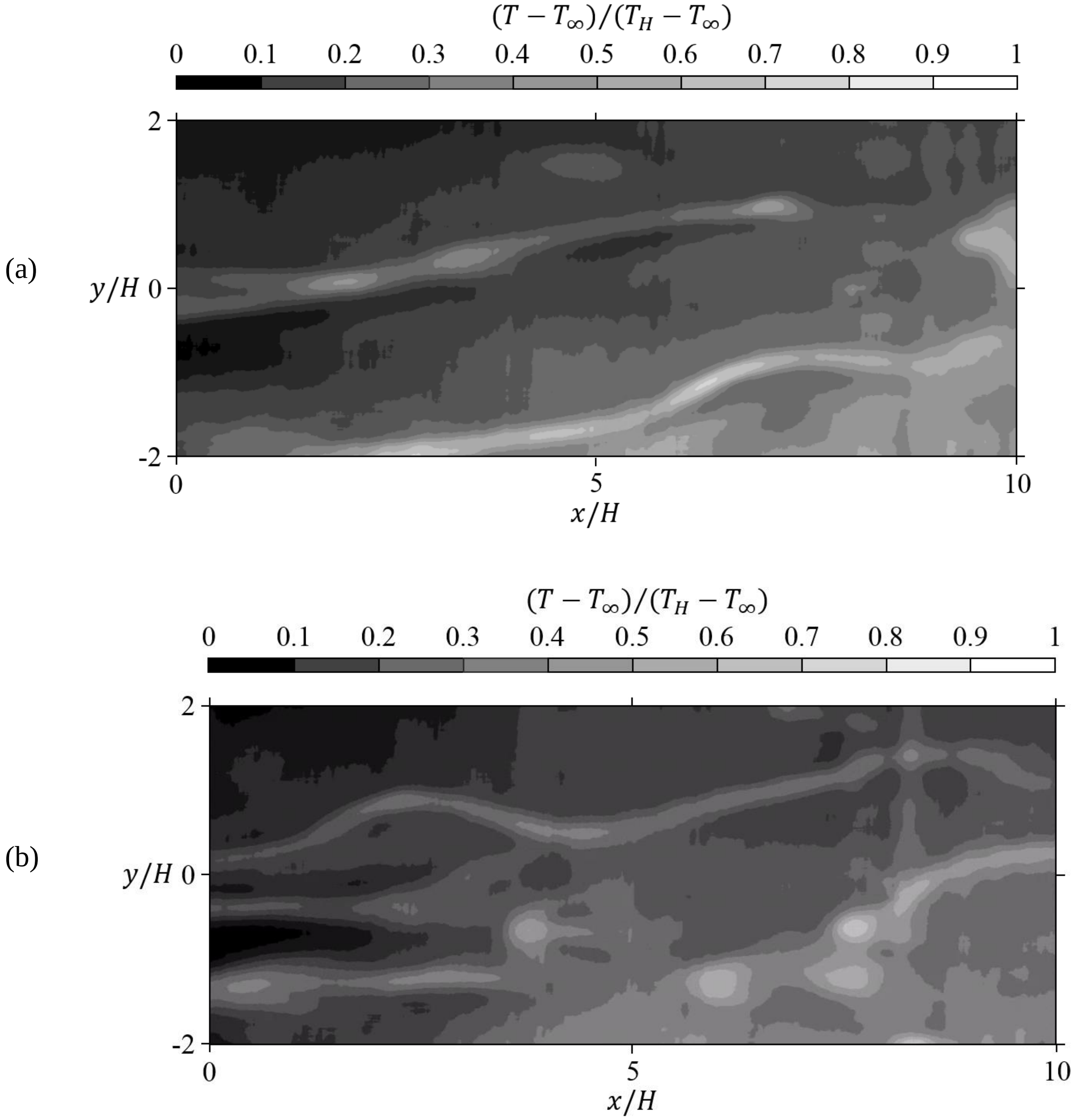

Figure 7-8. Instantaneous temperature fields near the bottom boundary (hot wall) for basic case of PRBC flow with the swirler and for the Richardson number of $Ri = 2.2$.

7.4 Conclusion

This chapter has explored the potential of employing large-scale circulating structures (LSC) to enhance heat transfer in mixed convection, particularly within Poiseuille-Rayleigh-Bénard Convection (PRBC) flow. The results of the experimental work, involving the introduction of a custom-designed swirler to induce LSC, demonstrate a significant improvement in heat transfer, particularly at lower Richardson numbers. Compared to traditional approaches like vortex generators used in purely forced convection and high Reynolds numbers, $Re = O(10^5)$, the implementation of LSC within PRBC shows greater promise, offering up to 20% enhancement in heat transfer for mixed convection regime with very low Reynolds numbers, $Re = O(10^2)$. The data gathered from two-colour two-dye laser-induced fluorescence (PLIF) thermometry confirms that the presence of LSC modifies the temperature distribution and flow structure within the PRBC system. The observed reduction in lower boundary temperatures in the PRBC-SW case confirms the hypothesis that LSC can improve heat transfer by promoting more efficient mixing and circulation of the fluid. These findings align with previous studies on Rayleigh-Bénard convection provide further evidence that large-scale flow structures play a critical role in enhancing thermal transport in mixed convection scenarios.

References

[1] B. Adrian, *CONVECTION HEAT TRANSFER*. John Wiley and Sons, Inc, 2013.

[2] R. B. Pérez, A. M. Pérez, and D. S. Suárez, “Influence of the punched holes on thermohydraulic performance and flow pattern of rectangular channels with a pair of perforated vortex generators,” *Int J Heat Mass Transf*, vol. 184, 2022, doi: 10.1016/j.ijheatmasstransfer.2021.122291.

[3] Y. Xu, M. D. Islam, and N. Kharoua, “Experimental study of thermal performance and flow behaviour with winglet vortex generators in a circular tube,” *Appl Therm Eng*, vol. 135, no. January, pp. 257–268, 2018, doi: 10.1016/j.applthermaleng.2018.01.112.

[4] G. Zhou and Q. Ye, “Experimental investigations of thermal and flow characteristics of curved trapezoidal winglet type vortex generators,” 2011, doi: 10.1016/j.applthermaleng.2011.11.024.

[5] H. Huisseune, C. T’joen, P. De Jaeger, B. Ameel, S. De Schampheleire, and M. De Paepe, “Performance enhancement of a louvered fin heat exchanger by using delta winglet vortex generators,” 2012, doi: 10.1016/j.ijheatmasstransfer.2012.09.004.

[6] G. Ahlers, S. Grossmann, and D. Lohse, “Heat transfer and large scale dynamics in turbulent Rayleigh-Bénard convection,” *Rev Mod Phys*, vol. 81, no. 2, pp. 503–537, 2009, doi: 10.1103/RevModPhys.81.503.

[7] X. Chen, D. P. Wang, and H. D. Xi, “Reduced flow reversals in turbulent convection in the absence of corner vortices,” *J Fluid Mech*, no. March, 2020, doi: 10.1017/jfm.2020.202.

[8] D. G. Osborne and F. P. Incropera, “Laminar, mixed convection heat transfer for flow between horizontal parallel plates with asymmetric heating,” 1985.

[9] Sina Kashanj and David S. Nobes. "Application of 4D two-colour LIF to explore the temperature field of laterally confined turbulent Rayleigh–Bénard convection." Experiments in Fluids 64.3 (2023): 46.

Chapter 8: Conclusion

The role of large-scale circulation (LSC) and flow rolling structures on heat and momentum transfer of wall-bounded natural and mixed convection were studied experimentally. This study was conducted for the cases which are paradigms in studying wall-bounded natural convection i.e. Rayleigh-Bénard convection (RBC) and wall-bounded mixed convection i.e. Poiseuille-Rayleigh-Bénard convection (PRBC). The condition of the experiments was defined within the Non-Oberbeck-Boussinesq (NOB) regime with relatively high temperature gradients up to $40\ ℃$ and working fluid of water.

For measuring and visualizing the flow velocity field particle image velocimetry (PIV) was employed in different forms of 2D and 3D by using a scanning approach. For measuring and visualizing the temperature field and estimating the heat transfer, a high sensitive two-colour two-dye laser-induced fluorescence (LIF) was also developed in both 2D and 3D forms. A simultaneous velocimetry and thermometry technique was also developed mainly to investigate the influence of vertical convection and temperature gradient in PRBC flow. These techniques were developed based on combination of the one-colour planar LIF (PLIF) and PIV using fluorescent seeding particles.

As discussed in chapter 2, to investigate the organization of the flow in RBC flow and identify the role of LSC in momentum transfer in comparison to the smaller flow structures, time-resolved 2D PIV was applied for whole field velocimetry of an RBC enclosure with a unit aspect ratio. With a working fluid of water and within NOB condition, a combinatorial algorithm was used to detect flow rolling structures sized from the start of the convection and for the developed RBC flow. It was found that within the experiment condition i.e. $= 5.3 \times 10^7$, $Pr = 7$, flow was dominated by small-scale flow structures for both states. Statistics showed that flow structures were much larger in the developed state in comparison with the start of the convection. The formation of larger flow structures in the developed state was found to be associated with higher momentum transfer. For both states of the flow, it was also found that there was an inverse correlation between the numbers of flow rolling structures and momentum transfer. The results indicated that in RBC formation of fewer but larger flow rolling structures can improve the momentum transfer which could improve the heat transfer.

Based on the results of the inverse correlation between the momentum transfer with the size and number of the flow structures, it could be determined that the formation of a single large-scale flow structure e.g. LSC, can improve the heat transfer of a system significantly. Hence, in chapter 3, the influence of the lateral confinement of the convection cell of RBC flow on the formation of LSC was investigated. This part of the study was performed within a convection cell with an aspect ratio of $\Gamma = 1/10$. The flow was measured and visualized by applying long-time time-resolved 2D PIV and 3D scanning PIV. The measurements of the flow from the start of the convection indicated that the severe lateral confinement such as in this case, can form a prolonged single stable LSC at a Rayleigh number, $Ra = 2.3 \times 10^7$, that usually forms multiple, unstable LSCs. Results also highlighted that increasing the Rayleigh number up to $Ra = 8.8 \times 10^7$ the prolonged stable single LSC persisted and remained stable by damping the elliptical instability. However, increasing the Rayleigh number would increase the vertical inertia of the flow leading to the formation of a twisted regime with up to double twist for $Ra = 8.8 \times 10^7$.

In chapter 4 and 5, to study the temperature field of RBC flow with a severe lateral confinement i.e. $\Gamma = 1/10$, long-time time-resolved PLIF and time-resolved 3D scanning LIF were applied. Results indicated that within this convection cell, only single thermal plumes were generated. Both hot and cold thermal plumes were found that had a scale of the convection cell. These results were also observed in the 3D temperature field confirming the 2D observations of the temperature field. For the Rayleigh number in which prolonged single double twist LSC was observed, it was found that temperature oscillated due to the generation of thermal plumes with a frequency similar to the non-confined RBC flow, $f \approx 0.028$ Hz , but with the same working fluid. This finding suggests that the formation of the single LSC was driven by the formation of thermal plumes. Increasing the Rayleigh number to higher values, however, showed that the oscillations occured with a different frequency, $f \approx 0.006$ Hz, showing the formation of a more pronounced set of thermal plumes that dominated the flow organization. The results of the heat transfer coefficient, Nusselt number, also indicated that although the spatio-temporal variation of the temperature gradient near the boundaries (both hot and cold) are different when derived from 3D or 2D measurements, the same trend could be found. This suggests that 2D measurement of the temperature could represent most aspects of the physics.

The next question which was investigated in chapter 6 was to see if the LSC also formed and influenced the a PRBC, i.e. flow within a channel heated from below, since it has more hypothetical engineering applications due to the introduction of the cross flow. For this study, a test section with limited length was designed and fabricated. The limited length was considered in the design since most of the applications e.g. heater and coolers, have limited length. To investigate the flow, temperature field and heat transfer, the simultaneous PIV/PLIF system was employed. This investigation was conducted for Rayleigh number of 4.5×10^5 and Reynolds numbers of 0 to 200, which resulted in the variation of Richardson number from $Ri = 2.2$ to $Ri = \infty$ which indicates mixed to natural convection. It was found that development of the flow did not lead to the formation of LSC and the flow was dominated by the Poiseuille flow and only influenced by the generation of thermal plumes, adding vertical convection to the flow field. Heat transfer was also investigated by considering two terms of vertical convection which was influence by vertical motion present in the flow mainly due to the formation of thermal plumes and the vertical temperature gradient. Results indicated that for higher Richardson numbers i.e. $Ri > 10$ vertical convection had a significant influence on the heat transfer. However, for $Ri < 10$, heat transfer was dominated by the temperature gradient and the influence of the vertical convection was negligible.

Since LSC does not form within PRBC flow with limited channel length, the idea of inducing the LSC for heat transfer enhancement purposes was investigated in chapter 7. This investigation was performed on the PRBC flow that was investigated earlier and for Richardson numbers of $Ri = 2.2$, 3.2, and 5 in which it was found that the heat transfer was dominated by the temperature gradient. Investigations were conducted by measuring the temperature distribution near the bottom boundary (hot wall) of the whole test section by applying the temperature sensitivity enhanced two-colour two-dye PLIF. Multiple side by side LSCs were induced passively to the flow by using a simple geometry swirler at the inlet of the flow. The study demonstrated that inducing the LSC to the PRBC flow can enhance the heat transfer significantly up to around $\sim 20\%$, for a Richardson number of $Ri = 2.2$. The heat transfer in the PRBC flow is very important since it is a relatively low Reynolds number flow with $Re = O(10^2)$ while in many applications inducing small eddies to the turbulent boundary layer can improve the heat transfer for $Re = O(10^5)$ and higher. It was also found that the heat transfer enhancement improves by increasing the Reynolds number which suggest a hypothetical significant heat transfer enactment in turbulent flows.

Future work

This study investigates the properties of flow rolling structures specifically the LSC in RBC flow and PRBC flow. The application of inducing of LSC for heat transfer enhancement was also briefly investigated showing promising techniques for future heat transfer applications, especially those with dominated mixed convection regime due to low velocity, small geometries, or high temperature differences. More research is required to investigate the influence of inducing LSC to flows with different properties to see the influence of LSC on heat transfer. The LSC could be induced in different either passive or active techniques which would depend on the application and flow properties that could be adjusted. Furthermore, the passive inducement of the LSC could be optimized and investigated to study the relation between the different types of swirler and their parameters on the induced LSC and the resultant heat transfer and temperature distribution. The application of introducing LSC into the flow in a wall-bounded turbulent flow as LSC could also influence the turbulent RBC flow.

Bibliography

[1] B. Adrian, CONVECTION HEAT TRANSFER. John Wiley and Sons, Inc, 2013.

[2] G. Ahlers, S. Grossmann, and D. Lohse, “Heat transfer and large scale dynamics in turbulent Rayleigh-Bénard convection,” Rev Mod Phys, vol. 81, no. 2, pp. 503–537, 2009, doi: 10.1103/RevModPhys.81.503.

[3] I. V. Miroshnichenko and M. A. Sheremet, “Turbulent natural convection heat transfer in rectangular enclosures using experimental and numerical approaches: A review,” Renewable and Sustainable Energy Reviews, vol. 82, no. December 2016, pp. 40–59, 2018, doi: 10.1016/j.rser.2017.09.005.

[4] R. Krishnamurti and L. N. Howard, “Large-scale flow generation in turbulent convection,” Proceedings of the National Academy of Sciences, vol. 78, no. 4, pp. 1981–1985, Apr. 1981, doi: 10.1073/PNAS.78.4.1981.

[5] L. Zwirner, A. Tilgner, and O. Shishkina, “elliptical instability and multiple-roll flow modes of the large-scale circulation in confined turbulent Rayleigh-Bénard convection,” Phys Rev Lett, vol. 125, no. 5, Jul. 2020, doi: 10.1103/PhysRevLett.125.054502.

[6] E. P. Van Der Poel, R. J. A. M. Stevens, and D. Lohse, “Connecting flow structures and heat flux in turbulent Rayleigh- Bénard convection,” Phys Rev E Stat Nonlin Soft Matter Phys, vol. 84, no. 4, pp. 1–4, 2011, doi: 10.1103/PhysRevE.84.045303.

[7] H. D. Xi and K. Q. Xia, “Flow mode transitions in turbulent thermal convection,” Physics of Fluids, vol. 20, no. 5, pp. 1–15, 2008, doi: 10.1063/1.2920444.

[8] Z. Wang, H. Xu, C. Chen, G. Hong, Z. Song, and Y. Zhang, “Numerical analysis of Poiseuille-Rayleigh-Bénard convection in supercritical carbon dioxide,” Nuclear Engineering and Technology, vol. 54, no. 9, pp. 3540–3550, Sep. 2022, doi: 10.1016/j.net.2022.04.010.

[9] R. Taher, M. M. Ahmed, Z. Haddad, and C. Abid, “Poiseuille-Rayleigh-Bénard mixed convection flow in a channel: Heat transfer and fluid flow patterns,” Int J Heat Mass Transf, vol. 180, Dec. 2021, doi: 10.1016/j.ijheatmasstransfer.2021.121745.

[10] D. G. Osborne and F. P. Incropera, “Laminar, mixed convection heat transfer for flow between horizontal parallel plates with asymmetric heating,” 1985.

[11] T. Meuel, M. Coudert, P. Fischer, C.-H. Bruneau, and H. Kellay, Effects of rotation on temperature fluctuations in turbulent thermal convection on a hemisphere, Scientific Reports 8, 1 (2018).

[12] M. Krishnan, V. M. Ugaz, and M. A. Burns, PCR in a Rayleigh-Bénard convection cell, Science 298, 793 (2002).

[13] D. Khodakov, J. Li, J. X. Zhang, and D. Y. Zhang, Highly multiplexed rapid DNA detection with single-nucleotide specificity via convective PCR in a portable device, Nature Biomedical Engineering 5, 702 (2021).

[14] O. Shishkina, Rayleigh-Bénard convection: The container shape matters, Physical Review Fluids 6, 090502(2021).

[15] G. Ahlers, E. Bodenschatz, R. Hartmann, X. He, D. Lohse, P. Reiter, R. J. Stevens, R. Verzicco, M. Wedi, S. Weiss, et al., Aspect ratio dependence of heat transfer in a cylindrical Rayleigh-Bénard cell, Physical Review Letters 128, 084501 (2022).

[16] H. D. Xi, S. Lam, and K. Q. Xia, From laminar plumes to organized flows: the onset of large-scale circulation in turbulent thermal convection, Journal of Fluid Mechanics 503, 47 (2004).

[17] J.-Q. Zhong and G. Ahlers, Heat transport and the large- scale circulation in rotating turbulent Rayleigh-Bénard convection, Journal of Fluid Mechanics 665, 300 (2010).

[18] R. Hartmann, K. L. Chong, R. J. Stevens, R. Verzicco, and D. Lohse, Heat transport enhancement in confined Rayleigh-Bénard convection feels the shape of the container, Epl 135, 10.1209/0295-5075/ac19ed (2021).

[19] D. Funfschilling, E. Brown, A. Nikolaenko, and G. Ahlers, Heat transport by turbulent Rayleigh-Bénard convection in cylindrical samples with aspect ratio one and larger, Journal of Fluid Mechanics 536, 145 (2005).

[20] A. Nikolaenko, E. Brown, D. Funfschilling, and G. Ahlers, Heat transport by turbulent Rayleigh-Bénard convection in cylindrical cells with aspect ratio one and less, Journal of Fluid Mechanics 523, 251 (2005).

[21] C. Sun, L.-Y. Ren, H. Song, and K.-Q. Xia, Heat transport by turbulent Rayleigh-Bénard convection in 1 m diameter cylindrical cells of widely varying aspect ratio, Journal of Fluid Mechanics 542, 165 (2005).

[22] S. Weiss and G. Ahlers, Effect of tilting on turbulent convection: cylindrical samples with aspect ratio, Journal of Fluid Mechanics 715, 314 (2013).

[23] E. P. van der Poel, R. J. Stevens, K. Sugiyama, and D. Lohse, Flow states in two-dimensional Rayleigh- Bénard convection as a function of aspect ratio and Rayleigh number, Physics of Fluids 24, 085104 (2012), 1206.3823.

[24] L. Zwirner and O. Shishkina, Confined inclined thermal convection in low-Prandtl number fluids, Journal of Fluid Mechanics 850, 984 (2018).

[25] H. Xia, M. Shats, and G. Falkovich, Spectrally condensed turbulence in thin layers, Physics of Fluids 21 (2009).

[26] X. Chen, D. P. Wang, and H. D. Xi, Reduced flow reversals in turbulent convection in the absence of corner vortices, Journal of Fluid Mechanics 891, 10.1017/jfm.2020.202 (2020).

[27] Z.-H. Wan, Q. Wang, B. Wang, S.-N. Xia, Q. Zhou, and D.-J. Sun, On non-Oberbeck-Boussinesq effects in Rayleigh-Bénard convection of air for large temperature differences, Journal of Fluid Mechanics 889, A10 (2020).

[28] V. Valori, G. Elsinga, M. Rohde, M. Tummers, J. Westerweel, and T. Van Der Hagen, Experimental velocity study of non-Boussinesq Rayleigh-Bénard convection, Physical Review E 95, 53113 (2017).

[29] G. Ahlers, E. Brown, F. F. Araujo, D. Funfschilling, S. Grossmann, and D. Lohse, Non-Oberbeck–Boussinesq effects in strongly turbulent Rayleigh–Bénard convection, Journal of Fluid Mechanics 569, 409 (2006).

[30] A. D. Demou and D. G. Grigoriadis, Direct numerical simulations of Rayleigh–Bénard convection in water with non-Oberbeck–Boussinesq effects, Journal of Fluid Mechanics 881, 1073 (2019).

[31] S. Kashanj and D. S. Nobes, Temperature field of non-Oberbeck–Boussinesq Rayleigh–Bénard convection in a low aspect ratio cell, Physics of Fluids 36 (2024).

[32] S. Horn, O. Shishkina, and C. Wagner, On non-Oberbeck–Boussinesq effects in three-dimensional Rayleigh–Bénard convection in glycerol, Journal of Fluid Mechanics 724, 175 (2013).

[33] S. Horn and O. Shishkina, Rotating non-Oberbeck–Boussinesq Rayleigh–Bénard convection convection in water, Physics of Fluids 26 (2014).

[34] V. Valori, G. E. Elsinga, M. Rohde, J. Westerweel, and T. H. van Der Hagen, Particle image velocimetry measurements of a thermally convective supercritical fluid, Experiments in Fluids 60, 1 (2019).

[35] M. Bussiére, G. M. Bessa, C. R. Koch, and D. S. Nobes, Application of a combinatorial vortex detection algorithm on 2 component 2 dimensional particle image velocimetry data to characterize the wake of an oscillating wing, Fluids 9, 53 (2024).

[36] M. Jiang, R. Machiraju, and D. Thompson, Detection and visualization of, The visualization handbook 295 (2005).

[37] I. A. Sadarjoen and F. H. Post, Detection, quantification, and tracking of vortices using streamline geometry, Computers & Graphics 24, 333 (2000).

[38] E. Brown and G. Ahlers, Rotations and cessations of the large-scale circulation in turbulent non-Oberbeck–Boussinesq Rayleigh– Bénard convection, Journal of Fluid Mechanics 568, 351 (2006).

[39] F. F. Araujo, S. Grossmann, and D. Lohse, Wind reversals in turbulent Rayleigh-Bénard convection, Physical Review Letters 95, 084502 (2005).

[40] K. Sugiyama, R. Ni, R. J. Stevens, T. S. Chan, S. Q. Zhou, H. D. Xi, C. Sun, S. Grossmann, K. Q. Xia, and D. Lohse, Flow reversals in thermally driven turbulence, Physical Review Letters 105, 1 (2010).

[41] K. Q. Xia, C. Sun, and S. Q. Zhou, Particle image velocimetry measurement of the velocity field in turbulent thermal convection, Physical Review E 68, 1 (2003).

[42] K. Sugiyama, E. Calzavarini, S. Grossmann, and D. Lohse, Flow organization in two-dimensional non-Oberbeck-Boussinesq Rayleigh-Bénard convection in water, Journal of Fluid Mechanics 637, 105 (2009).

[43] Gray, D.D. and Giorgini, A., 1976. The validity of the Boussinesq approximation for liquids and gases. International Journal of Heat and Mass Transfer, 19(5), pp.545-551.

[44] G. Ahlers et al., “Aspect Ratio Dependence of Heat Transfer in a Cylindrical Rayleigh-Bénard Cell,” Phys Rev Lett, vol. 128, no. 8, p. 84501, 2022, doi: 10.1103/PhysRevLett.128.084501.

[45] R. Hartmann, R. Verzicco, L. Klein Kranenbarg, D. Lohse, and R. J. A. M. Stevens, “Multiple heat transport maxima in confined-rotating Rayleigh-Bénard convection,” J Fluid Mech, vol. 939, pp. 1–27, 2022, doi: 10.1017/jfm.2021.1031.

[46] Y. C. Xie, G. Y. Ding, and K. Q. Xia, “Flow Topology Transition via Global Bifurcation in Thermally Driven Turbulence,” Phys Rev Lett, vol. 120, no. 21, May 2018, doi: 10.1103/PhysRevLett.120.214501.

[47] G. Paolillo, C. S. Greco, T. Astarita, and G. Cardone, “Experimental determination of the 3-D characteristic modes of turbulent Rayleigh-Bénard convection in a cylinder,” J Fluid Mech, vol. 922, 2021, doi: 10.1017/jfm.2021.554.

[48] S. Kashanj and D. S. Nobes, “Application of 4D two-colour LIF to explore the temperature field of laterally confined turbulent Rayleigh–Bénard convection,” Exp Fluids, vol. 64, no. 3, Mar. 2023, doi: 10.1007/s00348-023-03589-9.

[49] R. E. Ecke and O. Shishkina, “Annual review of fluid mechanics turbulent rotating Rayleigh-Bénard convection,” 2022, doi: 10.1146/annurev-fluid-120720.

[52] Q. Wang, R. Verzicco, D. Lohse, and O. Shishkina, “Multiple states in turbulent large-aspect-ratio thermal convection: what determines the number of convection rolls?,” Phys Rev Lett, vol. 125, no. 7, Aug. 2020, doi: 10.1103/PhysRevLett.125.074501.

[54] N. Fujisawa, S. Funatani, and N. Katoh, ‘Scanning liquid-crystal thermometry and stereo velocimetry for simultaneous three-dimensional measurement of temperature and velocity field in a turbulent Rayleigh-Bérnard convection’, Exp Fluids, vol. 38, no. 3, pp. 291–303, Mar. 2005, doi: 10.1007/s00348-004-0891-2.

[55] S. Zhou, C. Sun, and K. Xia, ‘Measured oscillations of the velocity and temperature fields in turbulent Rayleigh-Bénard convection in a rectangular cell’, pp. 28–30, 2007, doi: 10.1103/PhysRevE.76.036301.

[56] S. Ding, H. Li, W. Yan, and J. Zhong, ‘PHYSICAL REVIEW FLUIDS 4 , 023501 (2019) Temperature fluctuations relevant to thermal-plume dynamics in turbulent rotating Rayleigh-Bénard convection’, vol. 023501, pp. 1–11, 2019, doi: 10.1103/PhysRevFluids.4.023501.

[57] E. P. Van Der Poel, R. Verzicco, S. Grossmann, and D. Lohse, ‘Plume emission statistics in turbulent Rayleigh–Bénard convection’, J Fluid Mech, vol. 772, pp. 5–15, Jun. 2015, doi: 10.1017/JFM.2015.176.

[58] X. L. Qiu and P. Tong, ‘Large-scale velocity structures in turbulent thermal convection’, Phys Rev E Stat Phys Plasmas Fluids Relat Interdiscip Topics, vol. 64, no. 3, p. 13, 2001, doi: 10.1103/PhysRevE.64.036304.

[59] S. Q. Zhou, Y. C. Xie, C. Sun, and K. Q. Xia, ‘Statistical characterization of thermal plumes in turbulent thermal convection’, Phys Rev Fluids, vol. 1, no. 5, p. 054301, Sep. 2016

[60] Q. Zhou and K. Q. Xia, ‘Physical and geometrical properties of thermal plumes in turbulent Rayleigh–Bénard convection’, New J Phys, vol. 12, no. 7, p. 075006, Jul. 2010, doi: 10.1088/1367-2630/12/7/075006.

[62] J. Salort et al., ‘Thermal boundary layer near roughnesses in turbulent Rayleigh-Bénard convection: Flow structure and multistability’, Physics of Fluids, vol. 26, no. 1, Jan. 2014, doi: 10.1063/1.4862487.

[63] Q. Zhou, R. J. A. M. Stevens, K. Sugiyama, S. Grossmann, D. Lohse, and K. Q. Xia, ‘Prandtl–Blasius temperature and velocity boundary-layer profiles in turbulent Rayleigh–Bénard convection’, J Fluid Mech, vol. 664, pp. 297–312, Dec. 2010, doi: 10.1017/S0022112010003824.

[64] X. He, E. Bodenschatz, and G. Ahlers, ‘Aspect ratio dependence of the ultimate-state transition in turbulent thermal convection’, Proc Natl Acad Sci U S A, vol. 117, no. 48, pp. 30022–30023, 2020, doi: 10.1073/pnas.2007399117.

[65] K. P. Iyer, J. D. Scheel, J. Schumacher, and K. R. Sreenivasan, ‘The dependence of heat transport law on aspect ratio is still unclear’, Proc Natl Acad Sci U S A, vol. 117, no. 48, p. 30024, 2020, doi: 10.1073/pnas.2007913117.

[66] K. L. Chong, S. Di Huang, M. Kaczorowski, and K. Q. Xia, ‘Condensation of coherent structures in turbulent flows’, Phys Rev Lett, vol. 115, no. 26, Dec. 2015, doi: 10.1103/PhysRevLett.115.264503.

[67] X. J. Huang, Y. P. Hu, and Y. R. Li, ‘Aspect ratio dependence of Rayleigh-Bénard convection of cold water near its maximum density in box-shaped containers’, Physics of Fluids, vol. 31, no. 7, Jul. 2019, doi: 10.1063/1.5097964.

[68] K. L. Chong and K. Q. Xia, ‘Exploring the severely confined regime in Rayleigh-Bénard convection’, J Fluid Mech, vol. 805, p. R4, Oct. 2016, doi: 10.1017/jfm.2016.578.

[69] Y. P. Hu, Y. R. Li, C. M. Wu, S. Z. Li, and M. H. Li, ‘Flow pattern and heat transfer in Rayleigh-Bénard convection of cold water near its density maximum in a rectangular cavity’, Int

J Heat Mass Transf, vol. 107, pp. 1065–1075, Apr. 2017, doi: 10.1016/j.ijheatmasstransfer.2016.11.013.

[70] H. Yik, V. Valori, and S. Weiss, ‘Turbulent Rayleigh-Bénard convection under strong non-Oberbeck-Boussinesq conditions’, Phys Rev Fluids, vol. 5, no. 10, Oct. 2020, doi: 10.1103/PhysRevFluids.5.103502.

[71] C. A. L. Y. and J. F. F. eds. Tropea, Springer Handbook of Experimental Fluid Mechanics. Berlin: Berlin: Springer, 2007.

[72] A. S. Nebuchinov, Y. A. Lozhkin, A. V. Bilsky, and D. M. Markovich, ‘Combination of PIV and PLIF methods to study convective heat transfer in an impinging jet’, Exp Therm Fluid Sci, vol. 80, pp. 139–146, 2017, doi: 10.1016/j.expthermflusci.2016.08.009.

[73] H. Hu, M. Koochesfahani, C. Lum, J. Coppeta, and C. Rogers, ‘Molecular tagging thermometry with adjustable temperature sensitivity’, Exp Fluids, vol. 40, no. 5, pp. 753–763, May 2006, doi: 10.1007/s00348-006-0112-2.

[74] D. Schiepel, D. Schmeling, and C. Wagner, ‘Simultaneous tomographic particle image velocimetry and thermometry of turbulent Rayleigh-Bénard convection’, Meas Sci Technol, vol. 32, no. 9, 2021, doi: 10.1088/1361-6501/abf095.

[75] S. Moller, C. Resagk, and C. Cierpka, ‘Long-time experimental investigation of turbulent superstructures in Rayleigh–Bénard convection by noninvasive simultaneous measurements of temperature and velocity fields’, Exp Fluids, vol. 62, no. 4, pp. 1–18, 2021, doi: 10.1007/s00348-020-03107-1.

[76] J. P. Crimaldi, ‘Planar laser induced fluorescence in aqueous flows’, Exp Fluids, vol. 44, no. 6, pp. 851–863, 2008, doi: 10.1007/s00348-008-0496-2.

[77] J. Sakakibara, K. Hishida, and M. Maeda, ‘Measurements of thermally stratified pipe flow using image-processing techniques’, Exp Fluids, vol. 16, no. 2, pp. 82–96, 1993, doi: 10.1007/BF00944910.

[78] M. B. Shafii, C. L. Lum, and M. M. Koochesfahani, ‘In situ LIF temperature measurements in aqueous ammonium chloride solution during uni-directional solidification’, in Experiments in Fluids, 2010, pp. 651–662. doi: 10.1007/s00348-009-0758-7.

[79] J. A. Sutton, B. T. Fisher, and J. W. Fleming, ‘A laser-induced fluorescence measurement for aqueous fluid flows with improved temperature sensitivity’, Exp Fluids, vol. 45, no. 5, pp. 869–881, 2008, doi: 10.1007/s00348-008-0506-4.

[80] H. Rochlitz and P. Scholz, ‘Application of laser-induced fluorescence technique in a duct flow with one heated wall’, Exp Fluids, vol. 59, no. 3, pp. 1–20, 2018, doi: 10.1007/s00348-018-2508-1.

[81] S. Moller, T. Käufer, A. Pandey, J. Schumacher, and C. Cierpka, ‘Combined particle image velocimetry and thermometry of turbulent superstructures in thermal convection’, J Fluid Mech, vol. 945, Aug. 2022, doi: 10.1017/jfm.2022.538.

[82] T. Käufer and C. Cierpka, ‘Volumetric Lagrangian temperature and velocity measurements with thermochromic liquid crystals’, Meas Sci Technol, vol. 35, no. 3, p. 035301, Mar. 2024, doi: 10.1088/1361-6501/ad16d1.

[83] A. Eghtesad, M. A. Bijarchi, M. B. Shafii, and H. Afshin, ‘A state-of-the-art review on laser-induced fluorescence (LIF) method with application in temperature measurement’, Feb. 01, 2024, Elsevier Masson s.r.l. doi: 10.1016/j.ijthermalsci.2023.108686.

[84] W. Chaze, O. Caballina, G. Castanet, and F. Lemoine, ‘Spatially and temporally resolved measurements of the temperature inside droplets impinging on a hot solid surface’, Exp Fluids, vol. 58, no. 8, Aug. 2017, doi: 10.1007/s00348-017-2375-1.

[85] H. Ulrich, S. Sigl, M. Möhnle, E. Berrocal, and L. Zigan, ‘Droplet thermometry based on an optimized two dye two-color laser-induced fluorescence concept’, Front Phys, vol. 11, 2023, doi: 10.3389/fphy.2023.1235847.

[86] E. Villermaux, ‘Memory-induced low frequency oscillations in closed convection boxes’, Physical review letters 75, no. 25 (1995): 4618. 1995.

[87] H. D. Xi, S. Q. Zhou, Q. Zhou, T. S. Chan, and K. Q. Xia, ‘Origin of the temperature oscillation in turbulent thermal convection’, Phys Rev Lett, vol. 102, no. 4, Jan. 2009, doi: 10.1103/PhysRevLett.102.044503.

[88] Q. Zhou, H. D. Xi, S. Q. Zhou, C. Sun, and K. Q. Xia, ‘Oscillations of the large-scale circulation in turbulent Rayleigh-Bénard convection: The sloshing mode and its relationship with

the torsional mode', J Fluid Mech, vol. 630, pp. 367–390, 2009, doi: 10.1017/S0022112009006764.

[89] Y. Zhang et al., 'Statistics of velocity and temperature fluctuations in two-dimensional Rayleigh-Bénard convection', Phys Rev E, vol. 96, no. 2, Aug. 2017, doi: 10.1103/PhysRevE.96.023105.

[90] O. Shishkina and C. Wagner, 'Analysis of thermal dissipation rates in turbulent Rayleigh-Bénard convection', J Fluid Mech, vol. 546, pp. 51–60, Jan. 2006, doi: 10.1017/S0022112005007408.

[91] V. T. Vishnu, A. K. De, and P. K. Mishra, 'Statistics of thermal plumes and dissipation rates in turbulent Rayleigh-Bénard convection in a cubic cell', Int J Heat Mass Transf, vol. 182, Jan. 2022, doi: 10.1016/j.ijheatmasstransfer.2021.121995.

[92] H. Yang, Y. Wei, Z. Zhu, H. Dou, and Y. Qian, 'Statistics of heat transfer in two-dimensional turbulent rayleigh-bénard convection at various prandtl number', Entropy, vol. 20, no. 8, Aug. 2018, doi: 10.3390/e20080582.

[93] D. Lohse and K. Q. Xia, "Small-scale properties of turbulent Rayleigh-Benard convection," Annu Rev Fluid Mech, vol. 42, pp. 335–364, 2010, doi: 10.1146/annurev.fluid.010908.165152.

[94] W. V. R. Malkus, "The heat transport and spectrum of thermal turbulence," Proc R Soc Lond A Math Phys Sci, vol. 225, no. 1161, pp. 196–212, Aug. 1954, doi: 10.1098/RSPA.1954.0197.

[95] C. H. B. Priestley, "Convection from a large horizontal surface," Australian Journal of Physics, vol. 7, pp. 176–201, 1954, doi: https://doi.org/10.1071/PH540176.

[96] C. R. Doering, "Turning up the heat in turbulent thermal convection," Proc Natl Acad Sci U S A, vol. 117, no. 18, pp. 9671–9673, 2020, doi: 10.1073/pnas.2004239117.

[97] R. H. Kraichnan, "Turbulent thermal convection at arbitrary prandtl number," Physics of Fluids, vol. 5, p. 1374, 1962, doi: 10.1063/1.1706533.

[98] S. Grossmann and D. Lohse, "Multiple scaling in the ultimate regime of thermal convection," Phys. Fluids, vol. 23, p. 45108, 2011, doi: 10.1063/1.3582362.

[99] C. R. Doering, “Thermal forcing and ‘classical’ and ‘ultimate’ regimes of Rayleigh–Bénard convection,” J Fluid Mech, vol. 868, pp. 1–4, Jun. 2019, doi: 10.1017/JFM.2019.118.

[100] J. Sakakibara and R. J. Adrian, “Whole field measurement of temperature in water using two-color laser induced fluorescence,” Exp Fluids, vol. 26, no. 1–2, pp. 7–15, 1999, doi: 10.1007/s003480050260.

[101] H. Hu and M. M. Koochesfahani, “Molecular tagging velocimetry and thermometry and its application to the wake of a heated circular cylinder,” Meas Sci Technol, vol. 17, no. 6, pp. 1269–1281, 2006, doi: 10.1088/0957-0233/17/6/S06.

[102] J. Sakakibara and R. J. Adrian, “Measurement of temperature field of a Rayleigh-Bénard convection using two-color laser-induced fluorescence,” Exp Fluids, vol. 37, pp. 331–340, 2004, doi: 10.1007/s00348-004-0821-3.

[103] X. Song and D. S. Nobes, “Experimental investigation of evaporation-induced convection in water using laser based measurement techniques,” Exp Therm Fluid Sci, vol. 35, no. 6, pp. 910–919, Sep. 2011, doi: 10.1016/j.expthermflusci.2011.01.010.

[104] H. J. Kim and K. D. Kihm, “Application of a two-color laser induced fluorescence (LIF) technique for temperature mapping,” American Society of Mechanical Engineers, Heat Transfer Division, (Publication) HTD, vol. 369, no. 7, pp. 335–341, 2001.

[105] C. E. Estrada-Pérez, Y. A. Hassan, and S. Tan, “Experimental characterization of temperature sensitive dyes for laser induced fluorescence thermometry,” Review of Scientific Instruments, vol. 82, no. 7, p. 74901, 2011, doi: 10.1063/1.3590929.

[106] D. A. Walker, “A fluorescence technique for measurement of concentration in mixing liquids,” J Phys E, vol. 20, no. 2, pp. 217–224, 1987, doi: 10.1088/0022-3735/20/2/019.

[107] T. Nakajima, M. Utsunomiya, and Y. Ikeda, “Simultaneous Measurement of Velocity and Temperature of Water Using LDV and Fluorescence Technique,” Applications of Laser Techniques to Fluid Mechanics, pp. 34–53, 1991, doi: 10.1007/978-3-642-61254-1_3.

[108] M. C. J. Coolen, R. N. Kieft, C. C. M. Rindt, and A. A. Van Steenhoven, “Application of 2-D LIF temperature measurements in water using a Nd : YAG laser,” Springer-Verlag, 1999.

[109] A. Abdelghany, K. Kuribayashi, and M. Tange, “Ratiometric laser-induced fluorescence for liquid-phase thermometry around boiling bubbles at extended temperatures above 70 °C,” Exp Fluids, vol. 63, no. 2, pp. 1–9, 2022, doi: 10.1007/s00348-022-03397-7.

[110] J. Coppeta and C. Rogers, “Dual emission laser induced fluorescence for direct planar scalar behavior measurements,” Exp Fluids, vol. 25, no. 1, pp. 1–15, 1998, doi: 10.1007/s003480050202.

[111] P. S. Karasso and M. G. Mungal, “PLIF measurements in aqueous flows using the Nd: YAG laser,” Exp Fluids, vol. 23, no. 5, pp. 382–387, 1997, doi: 10.1007/s003480050125.

[112] S. Liu et al., “From Rayleigh-Bénard convection to porous-media convection: How porosity affects heat transfer and flow structure,” J Fluid Mech, vol. 895, 2020, doi: 10.1017/jfm.2020.309.

[113] J. A. Letelier, N. Mujica, and J. H. Ortega, “Perturbative corrections for the scaling of heat transport in a Hele-Shaw geometry and its application to geological vertical fractures,” J Fluid Mech, vol. 864, pp. 746–767, 2019, doi: 10.1017/jfm.2019.3.

[114] H. V. Mahaney, F. P. Incropera, and S. Ramadhyani, “Development of laminar mixed convection flow in a horizontal rectangular duct with uniform bottom heating,” Numerical Heat Transfer, vol. 12, no. 2, pp. 137–155, 1987, doi: 10.1080/10407788708913578.

[115] I. Catton, “Convection in a Closed Rectangular Region: The Onset of Motion,” J Heat Transfer, vol. 92, no. 1, pp. 186–188, Feb. 1970, doi: 10.1115/1.3449626.

[116] S. Kashanj and D. S. Nobes, “Experimental evidence of the correlation between the flow rolling structures and momentum transfer in Rayleigh–Bénard convection,” Physics of Fluids, vol. 36, no. 10, Oct. 2024, doi: 10.1063/5.0225406.

[117] S. Pirozzoli, M. Bernardini, R. Verzicco, and P. Orlandi, “Mixed convection in turbulent channels with unstable stratification,” J Fluid Mech, vol. 821, pp. 482–516, Jun. 2017, doi: 10.1017/jfm.2017.216.

[118] J. R. Maughan and F. P. Incropera, “Experiments on mixed convection heat transfer for airflow in a horizontal and inclined channel,” 1987.

[119] J. R. Maughan and F. P. Incropera, “Experiments in Fluids Secondary flow in horizontal channels heated from below,” 1987.

[120] D. G. Osborne and F. P. Incropera, “Experimental study of mixed convection heat transfer for transitional and turbulent flow between horizontal, parallel plates,” 1985.

[121] G. Zhou and Z. Feng, “Experimental investigations of heat transfer enhancement by plane and curved winglet type vortex generators with punched holes,” International Journal of Thermal Sciences, vol. 78, pp. 26–35, Apr. 2014, doi: 10.1016/j.ijthermalsci.2013.11.010.

[122] T. Y. Chen and H. T. Shu, “Flow structures and heat transfer characteristics in fan flows with and without delta-wing vortex generators,” Exp Therm Fluid Sci, vol. 28, no. 4, pp. 273–282, 2004, doi: 10.1016/S0894-1777(03)00107-9.

[123] U. Akdag and A. F. Ozguc, “Experimental investigation of heat transfer in oscillating annular flow,” Int J Heat Mass Transf, vol. 52, no. 11–12, pp. 2667–2672, 2009, doi: 10.1016/j.ijheatmasstransfer.2009.01.006.

[124] J. D. Patil and B. S. Gawali, “Experimental study of heat transfer characteristics in oscillating fluid flow in tube,” Experimental Heat Transfer, vol. 30, no. 4, pp. 328–340, 2017, doi: 10.1080/08916152.2016.1258018.

[125] M. Mommert, D. Schiepel, D. Schmeling, and C. Wagner, “Reversals of coherent structures in turbulent mixed convection,” J Fluid Mech, vol. 904, no. October, 2020, doi: 10.1017/jfm.2020.705.

[127] M. Koochesfahani, R. Cohn, and C. Mackinnon, “Simultaneous whole-field measurements of velocity and concentration fields using a combination of MTV and LIF,” 2000.

[128] B. Stier and M. M. Koochesfahani, “Molecular Tagging Velocimetry (MTV) measurements in gas phase flows,” Springer-Verlag, 1999.

[129] K. Hishida and J. Sakakibara, “Combined planar laser-induced fluorescence-particle image velocimetry technique for velocity and temperature fields,” in Experiments in Fluids, 2000. doi: 10.1007/s003480070015.

[130] S. Grafsronningen and A. Jensen, “Simultaneous PIV/LIF measurements of a transitional buoyant plume above a horizontal cylinder,” Int J Heat Mass Transf, vol. 55, no. 15–16, pp. 4195–4206, 2012, doi: 10.1016/j.ijheatmasstransfer.2012.03.060.

[131] S. Funatani, N. Fujisawa, and H. Ikeda, “Simultaneous measurement of temperature and velocity using two-colour LIF combined with PIV with a colour CCD camera and its application to the turbulent buoyant plume,” Meas Sci Technol, vol. 15, no. 5, pp. 983–990, 2004, doi: 10.1088/0957-0233/15/5/030.

[132] R. B. Pérez, A. M. Pérez, and D. S. Suárez, “Influence of the punched holes on thermohydraulic performance and flow pattern of rectangular channels with a pair of perforated vortex generators,” Int J Heat Mass Transf, vol. 184, 2022, doi: 10.1016/j.ijheatmasstransfer.2021.122291.

[133] Y. Xu, M. D. Islam, and N. Kharoua, “Experimental study of thermal performance and flow behaviour with winglet vortex generators in a circular tube,” Appl Therm Eng, vol. 135, no. January, pp. 257–268, 2018, doi: 10.1016/j.applthermaleng.2018.01.112.

[134] G. Zhou and Q. Ye, “Experimental investigations of thermal and flow characteristics of curved trapezoidal winglet type vortex generators,” 2011, doi: 10.1016/j.applthermaleng.2011.11.024.

[135] H. Huisseune, C. T’joen, P. De Jaeger, B. Ameel, S. De Schampheleire, and M. De Paepe, “Performance enhancement of a louvered fin heat exchanger by using delta winglet vortex generators,” 2012, doi: 10.1016/j.ijheatmasstransfer.2012.09.004.

Appendix A: Uncertainty Estimation

To estimate uncertainty, a spatio-temporal analysis was conducted under stationary conditions. For PIV, velocity was measured in a stationary fluid where the theoretical velocity is zero. While for PLIF, temperature was measured in a uniform region with a constant temperature. The uncertainty is quantified by calculating the probability density function (PDF), mean and standard deviation of the measured fields. This method captures both random and systematic uncertainties by analyzing deviations from the expected values. The advantages of this approach include a comprehensive assessment of uncertainty across spatial and temporal dimensions and clear statistical reporting that aids in comparing uncertainty with the actual physical characteristics of the flow or temperature fields. This method ensures a robust and detailed understanding of measurement uncertainty since it represents an *in situ* estimation specifically for each experiment.

Random Uncertainty in PIV

In this work, PIV was used to measure the velocity field of the fluid flow. To estimate the uncertainty in the velocity measurement, both random and systematic uncertainties were considered. The random uncertainty was captured by evaluating the standard deviation of the velocity field, while systematic uncertainty (bias) is assessed by comparing the mean of the measured values with the expected theoretical value.

Random uncertainty in PIV arises due to various factors such as noise in image acquisition, particle tracking errors and small fluctuations in the system. To calculate this uncertainty, measurements were conducted in a stationary fluid, where the theoretical velocity should be zero. Any deviation from zero was attributed to random noise and system imperfections in both measurement system i.e. PIV and fluid test rig parameters relevant to the velocity measurements such as vibration and buoyancy effects on the seeding particles. The random uncertainty,σ_u, was quantified as the standard deviation of the measured velocity values and is calculated using:

$$\sigma_u = \sqrt{\frac{1}{N}\sum_{i=1}^{N}(u_i - \bar{u})^2} \tag{1}$$

where u_i represents the individual velocity measurements, $\bar{u}$ is the mean velocity, and N is the number of measurements. This approach allows for an estimation of the random fluctuations in the measured velocity field, providing insight into the variability of the data due to noise and other factors.

Systematic Uncertainty (Bias) in PIV

The systematic uncertainty, or bias, in velocity measurement was assessed by calculating the deviation of the mean measured velocity from the expected theoretical value of zero. Since the stationary fluid should exhibit no flow, any non-zero average velocity suggests a systematic error, likely due to calibration, optical misalignment, or slight vibrations in the experimental setup. The bias in velocity,δ_u , was calculated as:

$$\delta_u = |\bar{u}| \tag{2}$$

This equation captures the extent to which the measured velocity deviates from the expected zero value, indicating systematic errors that need to be accounted for in the uncertainty estimation.

Total Uncertainty in PIV

To combine both random and systematic uncertainties, the total uncertainty in velocity measurement was calculated as:

$$\epsilon_u = \sqrt{{\delta_u}^2 + {\sigma_u}^2} \tag{3}$$

This equation provides the overall uncertainty in the velocity measurement by considering both the variability of the data (random uncertainty) and any systematic deviations from the expected value (bias).

Velocity in RBC with $\boldsymbol{\Gamma = 1/10}$

The probability density function (PDF) of the velocity (theoretically zero) are shown in below Figure A-1.

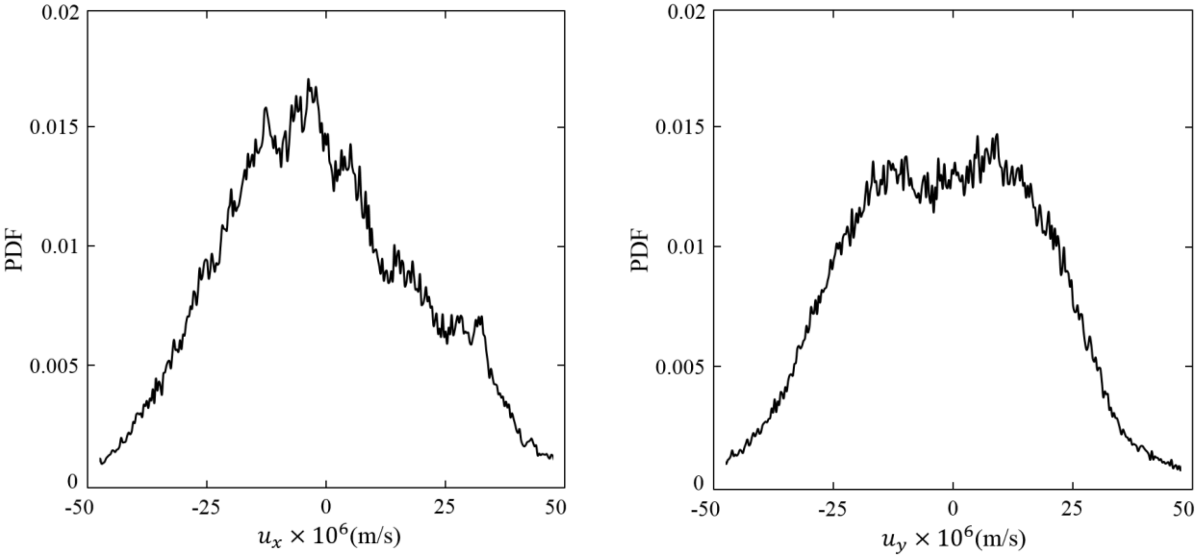

(a) (b)

Figure A-1. Probability density function (PDF) of velocity in (a) x-direction and (b) y-direction.

The random, bias and total uncertainties in both x-direction and y-direction are listed in Table A-1. The uncertainties values are also compared with the velocity scale of the flow. As can be seen, the total uncertainty in the velocity in both directions is negligible in comparison with the velocity scale of the flow, U.

Table A-1. List of the estimated uncertainties in velocity in both x-direction, u_x and y-direction, u_y for random σ, bias δ, and total ϵ, uncertainties compared with the velocity scale U.

σ_{u_x}	δ_{u_x}	ϵ_{u_x}	$\sigma_{u_x}/U(\%)$	$\delta_{u_x}/U(\%)$	$\epsilon_{u_x}/U(\%)$
0.020	0.035	0.040	0.006	0.011	0.012
σ_{u_y}	δ_{u_y}	ϵ_{u_y}	$\sigma_{u_y}/U(\%)$	$\delta_{u_y}/U(\%)$	$\epsilon_{u_y}/U(\%)$
0.020	0.040	0.045	0.006	0.012	0.014

Velocity in RBC with $\Gamma = 1$

The probability density function (PDF) of the velocity (theoretically zero) are shown in Figure A-2.

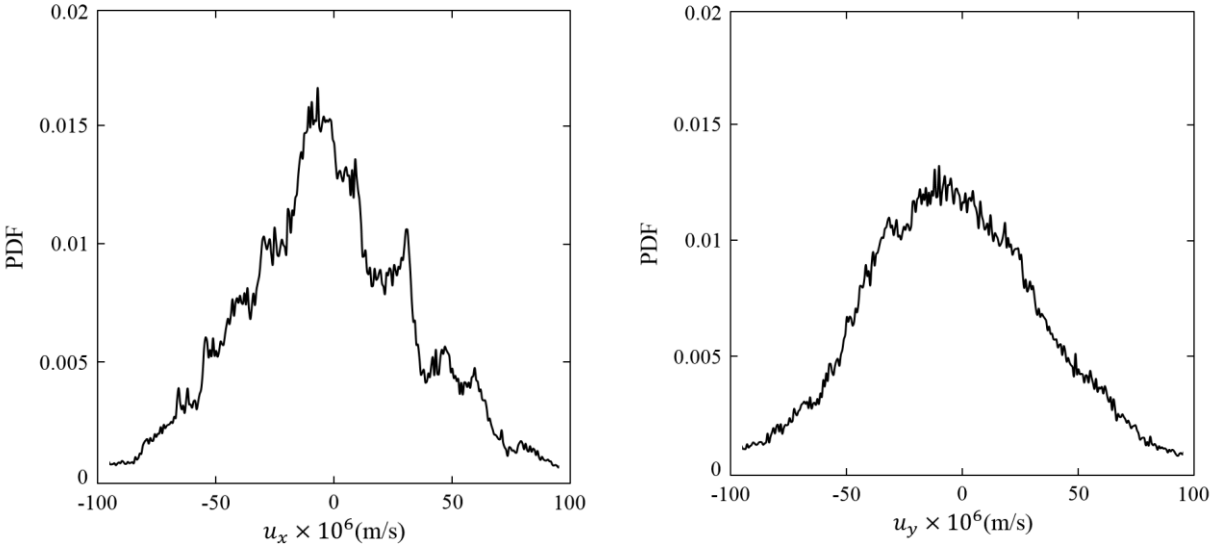

(a) (b)

Figure A- 2. Probability density function (PDF) of velocity in (a) x-direction and (b) y-direction.

The random, bias and total uncertainties in both x-direction and y-direction are listed in Table A-2. The uncertainties values are also compared with the velocity scale of the flow. As can be seen, the total uncertainty in the velocity in both directions is negligible in comparison with the velocity scale of the flow, U.

Table A-2. List of the estimated uncertainties in velocity in both x-direction, u_x and y-direction, u_y for random σ, bias δ, and total ϵ, uncertainties compared with the velocity scale U.

σ_{u_x}	δ_{u_x}	ϵ_{u_x}	$\sigma_{u_x}/U(\%)$	$\delta_{u_x}/U(\%)$	$\epsilon_{u_x}/U(\%)$
0.041	0.071	0.082	0.074	0.129	0.149
σ_{u_y}	δ_{u_y}	ϵ_{u_y}	$\sigma_{u_y}/U(\%)$	$\delta_{u_y}/U(\%)$	$\epsilon_{u_y}/U(\%)$
0.031	0.052	0.060	0.056	0.094	0.109

Velocity in PRBC

The probability density function (PDF) of the velocity (theoretically zero) are shown in Figure A-3.

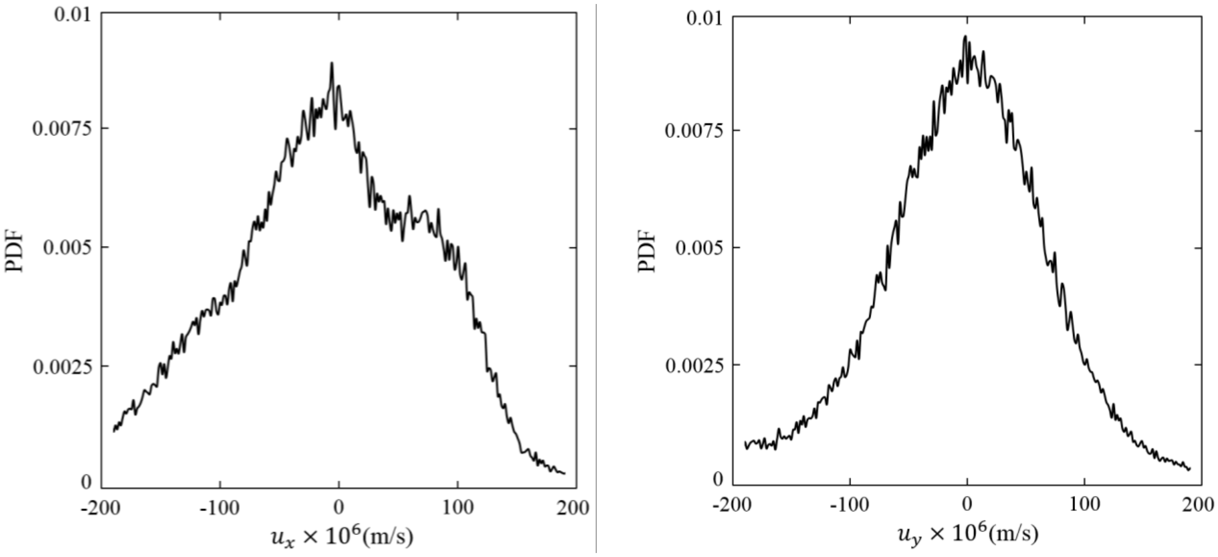

(a) (b)

Figure A-3. Probability density function (PDF) of velocity in (a) x-direction and (b) y-direction.

The random, bias and total uncertainties in both x-direction and y-direction are listed in Table A-3. The uncertainties values are also compared with the velocity scale of the flow. As can be seen, the total uncertainty in the velocity in both directions is negligible, $\epsilon_{u_x}/U < 1$ (%) and $\epsilon_{u_y}/U < 1$ (%), in comparison with the velocity scale of the flow, U.

Table A-3. List of the estimated uncertainties in velocity in both x-direction, u_x and y-direction, u_y for random σ, bias δ, and total ϵ, uncertainties compared with the velocity scale U.

σ_{u_x}	δ_{u_x}	ϵ_{u_x}	$\sigma_{u_x}/U(\%)$	$\delta_{u_x}/U(\%)$	$\epsilon_{u_x}/U(\%)$
0.066	0.114	0.132	0.101	0.175	0.203
σ_{u_y}	δ_{u_y}	ϵ_{u_y}	$\sigma_{u_y}/U(\%)$	$\delta_{u_y}/U(\%)$	$\epsilon_{u_y}/U(\%)$
0.062	0.108	0.125	0.095	0.166	0.192

Uncertainty Estimation in PLIF (Temperature Measurement)

In this work, PLIF was used to measure the temperature field of the fluid. Similar to PIV, uncertainty estimation in PLIF includes both random and systematic components.

Random Uncertainty in PLIF

Random uncertainty in PLIF arises from factors such as fluctuations in laser power, image noise, and camera sensitivity. To assess this, the measured intensity field in a region where the temperature was constant was considered. Any variation in the measured intensity was attributed to random noise. The temperature T is linearly related to the image intensity I through the calibration factor β, where $T = \beta I$. The random uncertainty in intensity, σ_I, was calculated using:

$$\sigma_I = \sqrt{\frac{1}{N}\sum_{i=1}^{N}(I_i - \bar{I})^2} \tag{4}$$

where I_i represents the individual intensity measurements, $\bar{I}$ is the mean intensity, and N is the number of measurements. The uncertainty in temperature due to intensity fluctuations was then propagated to the temperature field using the calibration factor β. Hence the random uncertainty was estimated as:

$$\sigma_T = \beta \sigma_I \tag{5}$$

Systematic Uncertainty (Bias) in PLIF

The systematic uncertainty, or bias, in PLIF was assessed by calculating the deviation of the mean measured temperature from the expected theoretical value of a known constant temperature. Since the temperature in a constant region should not fluctuate, any deviation from the expected temperature suggests a systematic error, likely due to camera noises, laser intensity variation, or optical misalignment in the experimental setup. The bias in temperature, δ_T, was calculated as:

$$\delta_T = |T - \bar{T}| \tag{6}$$

where $\bar{T}$ was the mean measured temperature calculated as $\bar{T} = \beta \bar{I}$, and T is the known constant temperature.

Total Uncertainty in PIV

To combine both random and systematic uncertainties, the total uncertainty in PLIF is calculated as:

$$\epsilon_T = \sqrt{{\delta_T}^2 + {\sigma_T}^2} \tag{7}$$

This equation provides the overall uncertainty in the temperature measurement by considering both the variability of the data (random uncertainty) and any systematic deviations from the expected value (bias).

Temperature in RBC with $\Gamma = 1/10$

The probability density function (PDF) of the fluorescent intensity (theoretically constant) is shown Figure A-4.

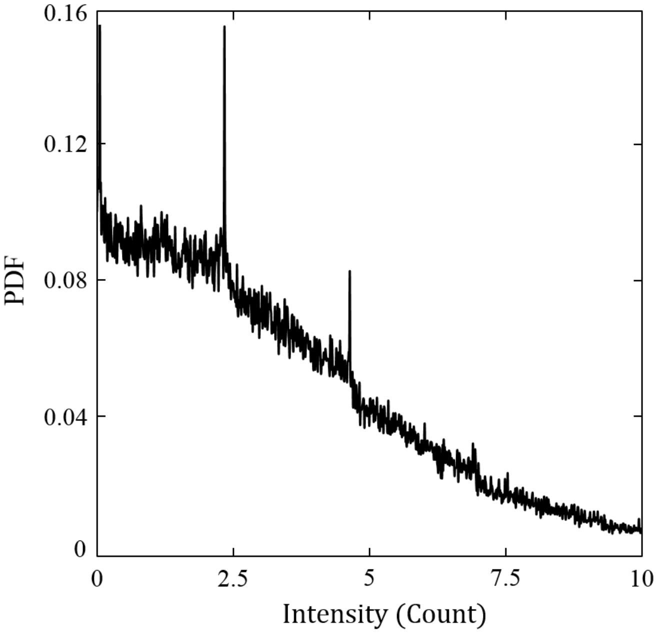

Figure A-4. Probability density function (PDF) of intensity of the fluorescent signal.

The random, bias and total uncertainties of the temperature are listed in Table A-4. The uncertainties values are also compared with the temperature gradient of the flow. As can be observed, the total uncertainty, ϵ_T is negligible in comparison with the temperature difference within the flow, ΔT.

Table A-4. List of the estimated uncertainties in temperature for random σ, bias δ, and total ϵ, uncertainties compared with the temperature gradient ΔT.

σ_T (°C)	δ_T (°C)	ϵ_T (°C)	$\sigma_T/\Delta T(\%)$	$\delta_\mathrm{T}/\Delta T(\%)$	$\epsilon_T/\Delta T(\%)$
0.188	0.326	0.377	0.470	0.815	0.942

Temperature in PRBC

The probability density function (PDF) of the fluorescent intensity (theoretically constant) are shown in Figure A-5:

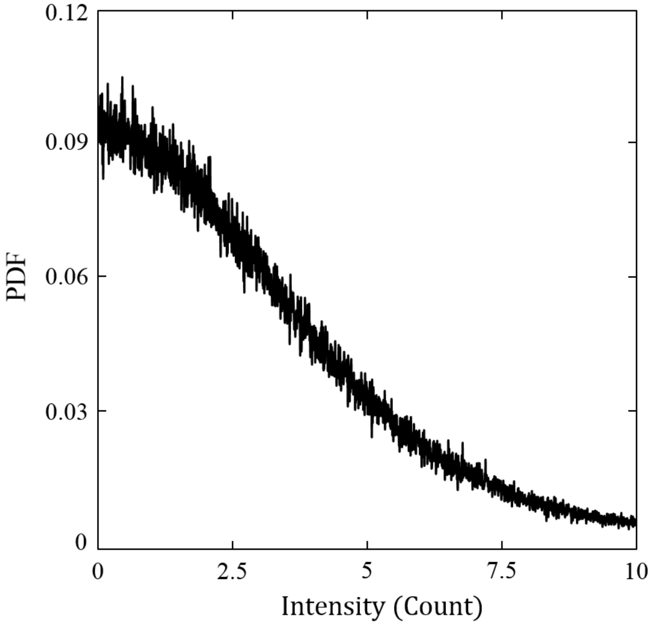

Figure A-5. Probability density function (PDF) of intensity of the fluorescent signal.

The random, bias and total uncertainties of the temperature is listed in Table A-5. The uncertainties values are also compared with the temperature gradient of the flow. As can be observed, the total uncertainty, ϵ_T is higher than the one in RBC flow but still negligible in comparison with the temperature difference within the flow, ΔT. The higher value in uncertainty in PRBC case is mainly due to application of PLIF simultaneous with PIV which is influenced by the background noise of the seeding particles.

Table A-5. List of the estimated uncertainties in temperature for random σ, bias δ, and total ϵ, uncertainties compared with the temperature gradient ΔT.

σ_T (℃)	δ_T (℃)	ϵ_T (℃)	$\sigma_T/\Delta T(\%)$	$\delta_\mathrm{T}/\Delta T(\%)$	$\epsilon_T/\Delta T(\%)$
0.436	0.755	0.872	2.18	3.77	4.36

Appendix B: Fluid Test Rig Drawing

In this section the drawing of the assembled fluid test rig for generating the PRBC flow is represented. Solid models and drawings are provided using a commercial software, i.e. SolidWorks, Dassault Systèmes. The drawings include the assembly of the PRBC fluid test rig and the assembly of the test section.

ITEM NO.	PART NUMBER	QTY.
1	Test Section	1
2	Traverse	1
3	Cylinder-Piston	1
4	Elbow	1
5	Vertical Duct	1
6	Adaptor	2
7	Motor	1
8	Converging Nozzle	2
9	Vertical Duct Adaptor	1

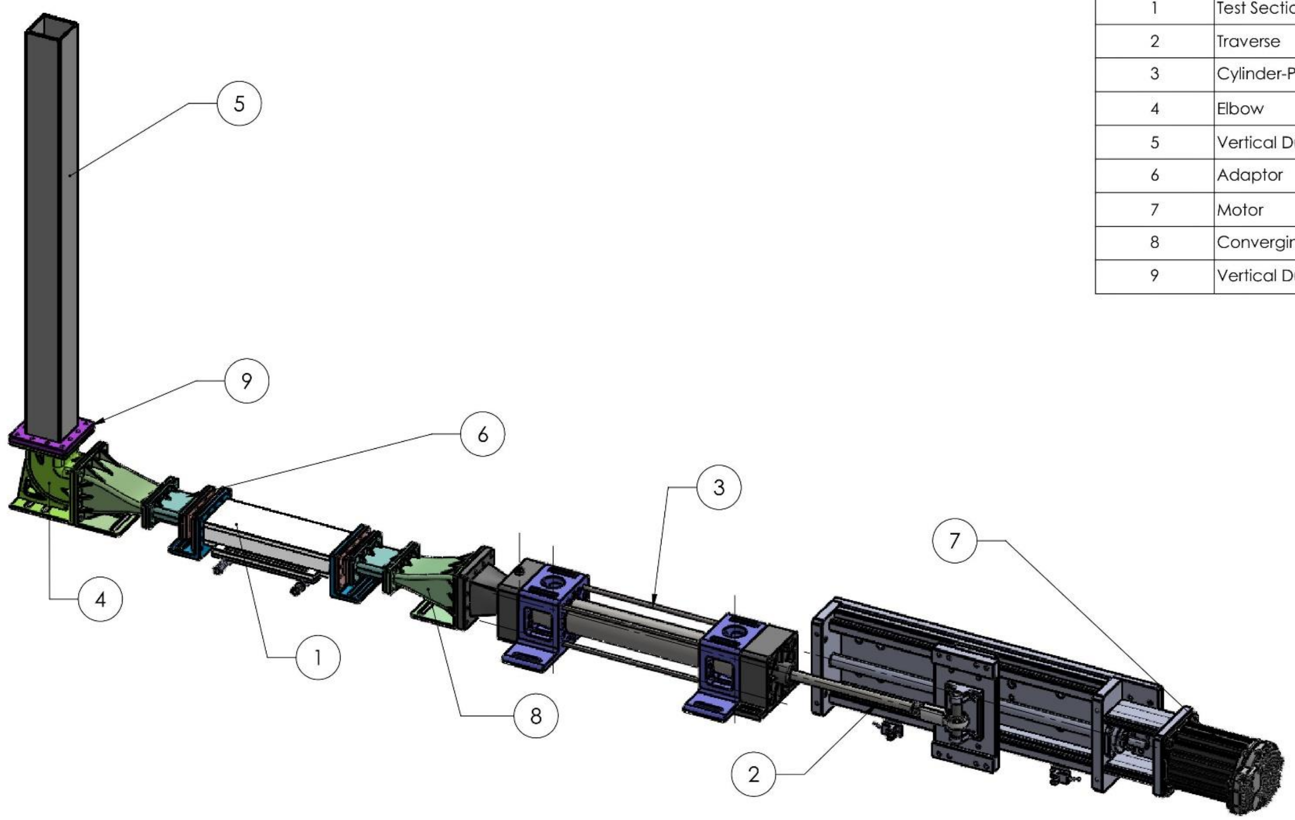

Nobes Lab
Contact
Sina Kashanj
Email
kashanj@ualberta.ca

UNLESS OTHERWISE SPECIFIED:
DIMENSIONS ARE IN MM
TOLERANCES:
ANGULAR: ± 0.5°
LINEAR
X = ± 0.5
X.X = ± 0.1
X.XX = ± 0.025
SURFACE FINISH µm 0.6
DO NOT SCALE DRAWING

MATERIAL:
Various

FILE NAME:
Fluid Test Rig

DRAWN BY:
Sina Kashanj

SM By	Sina Kashanj
Review	Dr. David S. Nobes
Rev2	

kashanj
Thursday, October 24, 2024 3:39:40 PM
Wednesday, August 25, 2021 9:00:21 AM

The Department of Mechanical Engineering
UNIVERSITY OF ALBERTA

TITLE:
Fluid Test Rig

SIZE **B**
Project
PhD Thesis
REV

SCALE: 1:6
Mass:
SHEET 1 OF 3

SOLIDWORKS Educational Product. For Instructional Use Only.

ITEM NO.	PART NUMBER	QTY.
1	Test Section	1
2	Traverse	1
3	Cylinder-Piston	1
4	Elbow	1
5	Vertical Duct	1
6	Vertical Duct Adaptor	1
7	Adaptor	2
8	Converging Nozzle	2
9	Motor	1

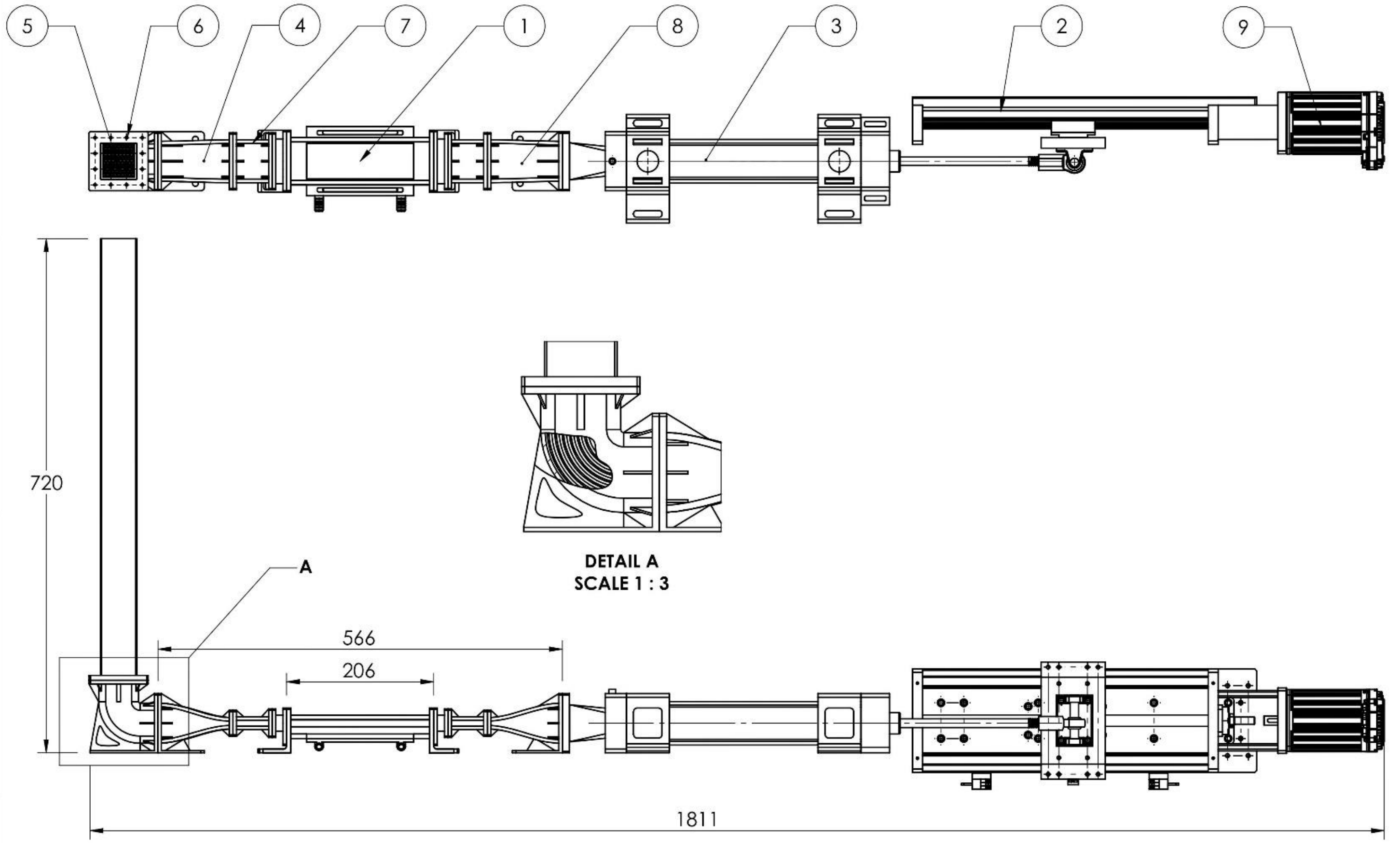

Nobes Lab
Contact
Sina Kashanj
Email
kashanj@ulaberta.ca

UNLESS OTHERWISE SPECIFIED:
DIMENSIONS ARE IN MM
TOLERANCES:
ANGULAR: ± 0.5°
LINEAR
X = ± 0.5
X.X = ± 0.1
X.XX = ± 0.025
SURFACE FINISH µm 0.6
DO NOT SCALE DRAWING

MATERIAL:
Various
FILE NAME:
Fluid Test Rig

DRAWN BY:
Sina Kashanj
SM by Sina Kashanj
Review Dr. David S. Nobes
Review
kashanj
Thursday, October 24, 2024 3:39:40 PM
Wednesday, August 25, 2021 9:00:21 AM

The Department of Mechanical Engineering
UNIVERSITY OF ALBERTA
TITLE:
Fluid Test Rig
SIZE
B
Project
PhD Thesis
REV
SCALE: 1:6
Mass:
SHEET 2 OF 3

ITEM NO.	PART NUMBER	QTY.
1	Window_top	1
2	Window_side	2
3	Window_connction	1
4	Heat Exchanger	1
5	Copper Sheet	1
6	Connection	2

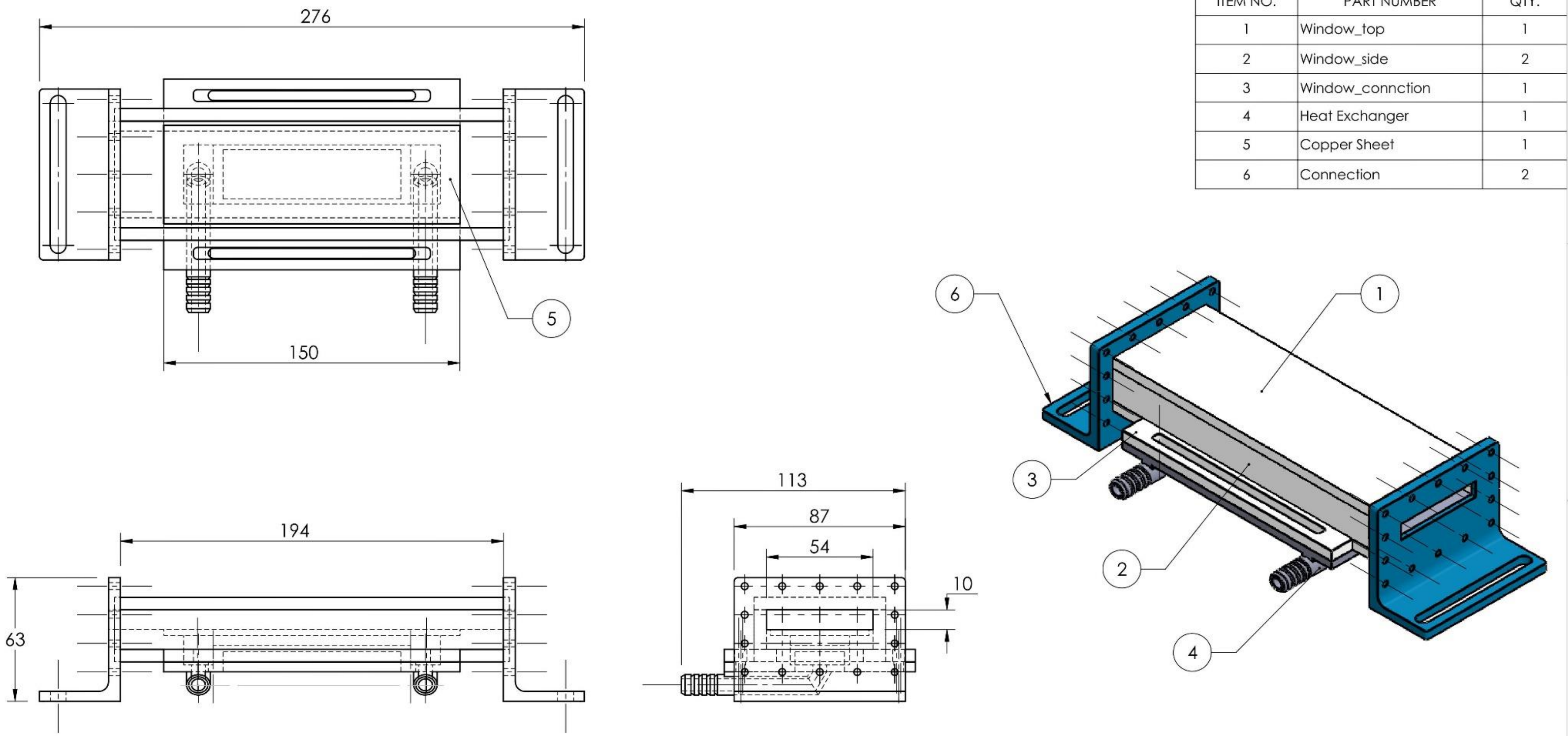

Nobes Lab Contact Sina Kashanj Email kashanj@ualberta.ca	UNLESS OTHERWISE SPECIFIED: DIMENSIONS ARE IN MM TOLERANCES: ANGULAR: ± 0.5° LINEAR X = ± 0.5 X.X = ± 0.1 X.XX = ± 0.025 SURFACE FINISH µm 0.6 DO NOT SCALE DRAWING	DRAWN BY: **Sina Kashanj** SM By: Sina Kashanj Review: Dr. David S. Nobes Review: kashanj Thursday, October 24, 2024 3:39:39 PM Sunday, April 4, 2021 7:44:01 PM	The Department of Mechanical Engineering UNIVERSITY OF ALBERTA TITLE: Test Section SIZE B Project: PhD Thesis REV
MATERIAL: Various			
FILE NAME: Test Section			SCALE: 1:2 Mass: SHEET 3 OF 3